



Universiteit
Leiden
The Netherlands

Supramolecular host-guest chemistry for applications in theranostics

Spa, S.J.

Citation

Spa, S. J. (2019, May 9). *Supramolecular host-guest chemistry for applications in theranostics*. Retrieved from <https://hdl.handle.net/1887/72514>

Version: Not Applicable (or Unknown)

License: [Leiden University Non-exclusive license](#)

Downloaded from: <https://hdl.handle.net/1887/72514>

Note: To cite this publication please use the final published version (if applicable).

Cover Page



Universiteit Leiden



The handle <http://hdl.handle.net/1887/72514> holds various files of this Leiden University dissertation.

Author: Spa, S.J.

Title: Supramolecular host-guest chemistry for applications in theranostics

Issue Date: 2019-05-09

SUPRAMOLECULAR HOST-GUEST CHEMISTRY

for applications in theranostics

Silvia Spa

Supramolecular host-guest chemistry for applications in theranostics

© S.J. Spa, 2019

ISBN: 978-94-6380-276-5

Design and lay-out: Wendy Schoneveld || www.wenzid.nl

Printed: ProefschriftMaken || Proefschriftmaken.nl

The research leading to these results has received funding from the European Research Council (ERC) under the European Union's Seventh Framework Program FP7/2007-2013 (Grant No. 2012-306890).

Supramolecular host-guest chemistry for applications in theranostics

Proefschrift

ter verkrijging van
de graad van Doctor aan de Universiteit Leiden
op gezag van Rector Magnificus Prof. mr. C. J. J. M. Stolker,
volgens besluit van het College voor Promoties
te verdedigen op donderdag 9 mei 2019
klokke 11.15 uur

door

Silvia Johara Spa

Geboren te 's-Gravenhage
In 1988

Promotor

Prof. Dr. M.A. van Buchem

Co-promotoren

Dr. F.W.B. van Leeuwen

Prof. R.C. Hoeben

Leden promotiecommissie

Prof. Dr. J.A. van der Hage

Prof. Dr. E. Bouwman

Prof. Dr. A.H. Velders (Universiteit Wageningen)

Dr. B. Cornelissen (Universiteit Oxford)



Shining light upon the unknown

Table of Contents

| | | |
|------------------|---|-----|
| CHAPTER 1 | Introduction and outline | 8 |
| CHAPTER 2 | Obtaining control of cell surface functionalizations via Pre-targeting and Supramolecular host guest interactions | 15 |
| CHAPTER 3 | A Supramolecular Approach for Liver Radioembolization | 71 |
| CHAPTER 4 | In vivo stability of supramolecular host-guest complexes monitored by dual- isotope multiplexing in a pre-targeting model of experimental liver radioembolization | 99 |
| CHAPTER 5 | Orthogonal Functionalization of Ferritin via Supramolecular Re-Assembly | 127 |
| CHAPTER 6 | The influence of systematic structure alterations on the photophysical properties and conjugation characteristics of asymmetric cyanine 5 dyes | 157 |
| CHAPTER 7 | Future perspectives | 193 |
| CHAPTER 8 | Summary | 197 |
| CHAPTER 9 | Nederlandse samenvatting | 204 |
| | List of publications | 207 |
| | Curriculum Vitae | 209 |
| | Dankwoord | 209 |



CHAPTER 1

Introduction and Outline

In the last few decades our knowledge in the fields of molecular biology and medicine has vastly increased. Serious illnesses are being tackled with the help of a large selection of pharmaceuticals and clinical procedures. However, with the increase in therapeutic know-how, the insight has grown in the fact that current therapies are far from perfect and that sometimes the side-effects of the cure are worse than the disease itself. To reduce collateral damage and side effects, increasing effort is being spent on the development of personalized medicine and the integration of diagnostics and therapy into one treatment plan, giving rise to the field of theranostics.

With the idea of personalized medicine, the demand for the availability of a generic chemical toolbox that supports refinement of therapeutic strategies has risen. Such a chemical toolbox could, for example, include interchangeable targeting groups and/or therapeutic entities allowing the target (e.g. specificity) and doses of the therapy to be adjusted to the patient's needs. Furthermore, theranostic approaches often demand for new drug/tracer designs, where both imaging labels (fluorescence and/or radio-label) and therapeutic agents are either combined in one tracer, or their location and action can be linked.

There has already been a lot of research towards combining different functional features into one targeting tracer in the field of nanomedicine.^{2,3} One prime example is the combined integration of a radioactive and fluorescent signature in the clinically applied multimodal nanoparticle Indocyanine green-^{99m}Tc-nanocolloid.⁴ Unfortunately, controlling the amount and number of labels on the nanoparticles remains challenging.

Nature's way to introduce complex functionalizations is presented by supramolecular interactions.^{5,6} For example: the folding and replication of DNA, the formation of protein capsids (e.g. ferritin, viruses), and the specific binding of proteins to cellular receptors. When analyzing the basis of these systems, many are based on multivalent host-guest interactions. Zooming in, these interactions occur with the help of hydrogen bonding, metal coordination, hydrophobic forces, van der Waals forces and/or electrostatic effects.⁷ On their own these chemical interactions are relatively weak, their strength however, lies in their numbers. Through multiple interactions strong but still revisable binding is accomplished leading to highly specific interactions.

A well-described supramolecular system is the host-guest interaction between adamantane (Ad) and β -cyclodextrin (β -CD)(hydrophobic forces⁷). One CD-Ad interaction has a relative low binding strength ($K_D = 5 \cdot 10^4 \text{ M}^{-1}$),^{8,9} but three or more of such interactions increases the binding strength significantly ($K_D = 1 \cdot 10^7 - 1 \cdot 10^{10} \text{ M}^{-1}$).^{10,11} Hence in the field of supramolecular chemistry/nanotechnology, CD-Ad interactions are utilized as driving

forces for compound aggregation.^{12,13}

In this thesis supramolecular host-guest interactions and self-assembly processes are investigated in relation to the development of theranostic and diagnostic drugs/tracers.

Chapter 2 explores the possibility of utilizing the supramolecular host-guest chemistry between β -CD and Ad to drive cell functionalization and cell-cell interaction in an *in vitro* environment. To this end cellular surfaces are functionalized in a two-step pre-targeting set-up and the effects were monitored using fluorescence imaging.

After exploring the CD-Ad interaction *in vitro*, the supramolecular host-guest interaction was further tested *in vivo*, as described in **chapter 3**. Here a pre-targeting setup for liver radioembolization is discussed, again exploring the interaction between the β -CD and Ad-functionalized protein microparticles. Radiolabeling with ^{99m}Tc supported *in vivo* SPECT imaging and quantitative biodistribution studies (%ID/g; 2h post injection). In **chapter 4** the pre-targeting principle for radioembolization is further explored by using the two radioisotopes: ^{99m}Tc and ¹¹¹In. Via dual-isotope multiplexing and by monitoring the individual components via dual-isotope SPECT and %ID/g analysis more light is shed on the *in vivo* co-localization of β -cyclodextrin polymers and Ad-functionalized protein microparticles.

In **chapter 5**, use of a self-assembled protein for drug/tracer development is described. The supramolecular self-assembly interaction of (apo)ferritin was utilized to obtain control over multi-functionalization of these bionanoparticles. Re-assembly of stoichiometric mixtures of functionalized (apo)ferritin subunits, was combined with tests that underline the preservation of ferritins natural iron mineralization properties.

As fluorescence plays an important part in the analysis technologies used in this thesis, and can provide clinical theranostic value in the form of fluorescence guided surgery, **chapter 6** was devoted to the photophysical properties of different fluorophores. Through systematic alteration of the Cy5-dye structure more insight was obtained in the structure/chemical- and photo-physical-property relationships.

In **chapter 7** the future of supramolecular interactions in theranostic procedures is discussed and a summary of the thesis is provided in **chapter 8**.

REFERENCES

1. Patra M, Zarschler K, Pietzsch H-J, et al., New insights into the pretargeting approach to image and treat tumours. *Chem Soc Rev.* **2016**, 45 (23), 6415-6431.
2. Re F, Moresco R, Masserini M. Nanoparticles for neuroimaging. *J Phys D Appl Phys.* **2012**, 45 (7), 1-12.
3. Bhaskar S, Tian F, Stoeger T, et al., Multifunctional Nanocarriers for diagnostics, drug delivery and targeted treatment across blood-brain barrier: perspectives on tracking and neuroimaging. *Part Fibre Toxicol.* **2010**, 7 (1), 3.
4. Kleinjan GH, Werkhoven E Van, Berg NS Van Den, et al., The best of both worlds : a hybrid approach for optimal pre- and intraoperative identification of sentinel lymph nodes. *Eur J Nucl Med Mol Imaging.* **2018**, 10.1007/s00259-018-4028-x
5. Crabb E, Moore E. *Metals and Life.* 1st ed. Cambridge: RSC Publishing; 2010.
6. Nelson david L, Cox MM. *Lehninger Principles of Biochemistry.* 5th ed. Winconsin: Freeman; 2008.
7. Steed JW, Atwood JL. *Supramolecular Chemistry.* 2nd ed. United Kingdom: wiley; 2009.
8. Gade M, Paul A, Alex C, et al., Supramolecular scaffolds on glass slides as sugar based rewritable sensors for bacteria. *Chem Commun (Camb).* **2015**, 51 (29), 6346-6349.
9. Granadero D, Bordello J, Perez-Alvite MJ, et al., Host-guest complexation studied by fluorescence correlation spectroscopy: Adamantane-cyclodextrin inclusion. *Int J Mol Sci.* **2010**, 11 (1), 173-188.
10. Huskens J, Mulder A, Auletta T, et al., A model for describing the thermodynamics of multivalent host-guest interactions at interfaces. *J Am Chem Soc.* **2004**, 126 (21), 6784-6797.
11. Mulder A, Auletta T, Sartori A, et al., Divalent binding of a bis(adamantyl)-functionalized calix[4]arene to β -cyclodextrin-based hosts: An experimental and theoretical study on multivalent binding in solution and at self-assembled monolayers. *J Am Chem Soc.* **2004**, 126 (21), 6627-6636.
12. Nikura K, Sugimura N, Musashi Y, et al., Virus-like particles with removable cyclodextrins enable glutathione-triggered drug release in cells. *Mol Biosyst.* **2013**, 9 (3), 501-507.
13. Osman SK, Brandl FP, Zayed GM, et al., Cyclodextrin based hydrogels: Inclusion complex formation and micellization of adamantane and cholesterol grafted polymers. *Polymer (Guildf).* **2011**, 52 (21), 4806-4812.





Adapted from: Rood MTM, Spa SJ, Welling MM, ten Hove JB, van Willigen DM, Buckle T, Velders AH, van Leeuwen FWB.

Sci Rep 2017;7:39908-39918



CHAPTER 2

**Obtaining control of cell surface functionalization
via Pre-targeting and Supramolecular host guest
interactions**

ABSTRACT

The use of mammalian cells for therapeutic applications is finding its way into modern medicine. However, modification or “training” of cells to make them suitable for a specific application remains complex. By envisioning a chemical toolbox that enables specific, but straight-forward and generic cellular functionalization, we investigated how membrane-receptor (pre)targeting could be combined with supramolecular host-guest interactions based on β -cyclodextrin (CD) and adamantane (Ad). The feasibility of this approach was studied in cells with membranous overexpression of the chemokine receptor 4 (CXCR4). By combining specific targeting of CXCR4, using an adamantane (Ad)-functionalized Ac-TZ14011 peptide (guest; $K_D = 56$ nM), with multivalent host molecules that entailed fluorescent β -CD-Poly(isobutylene-alt-maleic-anhydride)-polymers with different fluorescent colors and number of functionalities, host-guest cell-surface modifications could be studied in detail. A second set of Ad-functionalized entities enabled introduction of additional surface functionalities. In addition, the attraction between CD and Ad could be used to drive cell-cell interactions. Combined we have shown that supramolecular interactions, that are based on specific targeting of an overexpressed membrane receptor, allow specific and stable, yet reversible, surface functionalization of viable cells and how this approach can be used to influence the interaction between cells and their surroundings.

INTRODUCTION

Cells are the cornerstones of mammalian life forms, their versatile surfaces are naturally evolved to express molecules which provide a refined means to interact with their surroundings, e.g. functionalizations.¹ These functionalities can stimulate and/or respond to cellular activity,² regulate vital processes such as hormone balance^{3,4} and induce immune responses.^{5,6} The strength of using cells for therapeutic purposes is progressively being recognized in medicine and is (among others) exploited in the form of immunotherapy and (stem) cell transplantations.⁷⁻⁹ The implantation of (stem) cells allows regeneration of the impaired tissue, however therapy efficiency is limited by low engraftment of the cells at the site of interest.¹⁰ Furthermore, such cell-based therapies often go hand-in-hand with relatively complex biological modification processes such as genetic modification¹¹ or metabolic labelling.¹² As each medical application desires specialized features and functions, these modification processes match an individual cell type to a specific application. To enhance delivery and local retention to the site of interest, ideally an interaction-enhancing functionalization can be introduced in a cell-type specific manner, using well defined and generic (chemical) functionalization approaches.¹³ By recognizing the cell surface as a (complex) chemical scaffold, one can reason that its functionality and interactions can be altered via bio-orthogonal conjugations.¹⁴⁻¹⁶ Known examples are the introduction of polyelectrolyte polymers^{14,17-19} and the insertion of lipophilic anchors containing a functional group such as integrins or reactive handles.²⁰⁻²⁴ Alternatively, one could approach cell functionalization in a way similar to the functionalization of inorganic surfaces. The opposite has been used extensively; hereby inorganic surfaces with simulated cell surfaces have been applied to mimic interactions that occur in nature.²⁵⁻²⁷ When controllable and reversible inorganic-surface modifications are desired in aqueous environments, supramolecular host-guest interactions, e.g. using beta-cyclodextrin (β -CD) and adamantane (Ad), provide outcome.²⁸⁻³³ Especially when one considers that CD based host-guest interactions also play a key role in the preparation of biomedical materials and in drug delivery.³³⁻³⁵

Membrane-expressed biomarkers provide a unique fingerprint for cell populations and allow efficient and specific targeting using vectors such as antibody-derivatives and peptides.³⁶ Such vectors are routinely used for applications in imaging and therapy.³⁷ Not only can specificity be achieved by direct targeting of the receptor, indirect targeting can also be applied in a pre-targeting setup.³⁸ Here a receptor-targeting vector is first directed towards the membrane-receptor. This first targeting step is then followed by a secondary functionalization, using an agent that contains e.g. a diagnostic or a therapeutic label.³⁸⁻⁴⁰

Other than applying the pre-targeting concept to introduce such diagnostic/therapeutic labels, potentially the same concept could also be utilized to introduce other functionalities on the cell surfaces.

We reasoned that it would be possible to functionalize cell surfaces in a similar way to what is known for inorganic surfaces. To realize this, a combination of membrane receptor-(pre)targeting and supramolecular surface functionalization techniques were used. Herein the chemokine receptor 4 (CXCR4),⁴¹ a receptor that plays a key role in cellular motility as result of chemotaxis, served as the membrane receptor. Specific functionalization of CXCR4 was achieved via the use of an adamantane functionalized Ac-TZ14011 peptide (Figure 1a1). Further surface functionalization was based on the host-guest interaction between beta-cyclodextrin host molecules on fluorescent beta-cyclodextrin-Poly(isobutylene-alt-maleic-anhydride)-polymers and the adamantane functionality (Figure 1a2). We also illustrate how such an approach enables the introduction of additional surface functionalities (e.g. diagnostic labels) and can even be used to drive cell-cell interactions.

EXPERIMENTAL

General

For information on the materials used and more in depth experimental descriptions (including compound synthesis and analysis, determination of the receptor affinity of Ac-TZ14011-Ad, cell culture and confocal microscopy), see the Supporting information (SI).

Polymer synthesis

Poly(isobutylene-alt-maleic anhydride) (PIBMA₃₉, M_w 6,000) or PIBMA₃₈₉ (M_w 60,000) were dissolved in dry DMSO together with DIPEA and the appropriate Cy5- or Cy3-dye. The reaction was left to stir for at least 7 h. Then 6-monodeoxy-6-monoamine-β-cyclodextrin (β-CD) was added and the mixture was stirred at 80 °C for another 12 h. After cooling to RT, the polymer was dialyzed against H₂O for 1 day, then against 100 mM phosphate buffer pH 9.0 for another day, and finally against H₂O for 5 days. The dialysis medium was refreshed every day. The remaining solution was then lyophilized to obtain the product. The number of CD groups per polymer, was estimated via ¹H NMR analysis and the number of dyes per polymer was estimated via UV/Vis absorbance (see Supporting information). Prior to use, a solution of 1 mg/mL in H₂O each polymer was prepared and stored at 4 °C.

Cy5_{0,4}PIBMA₃₉ (Compound 2)

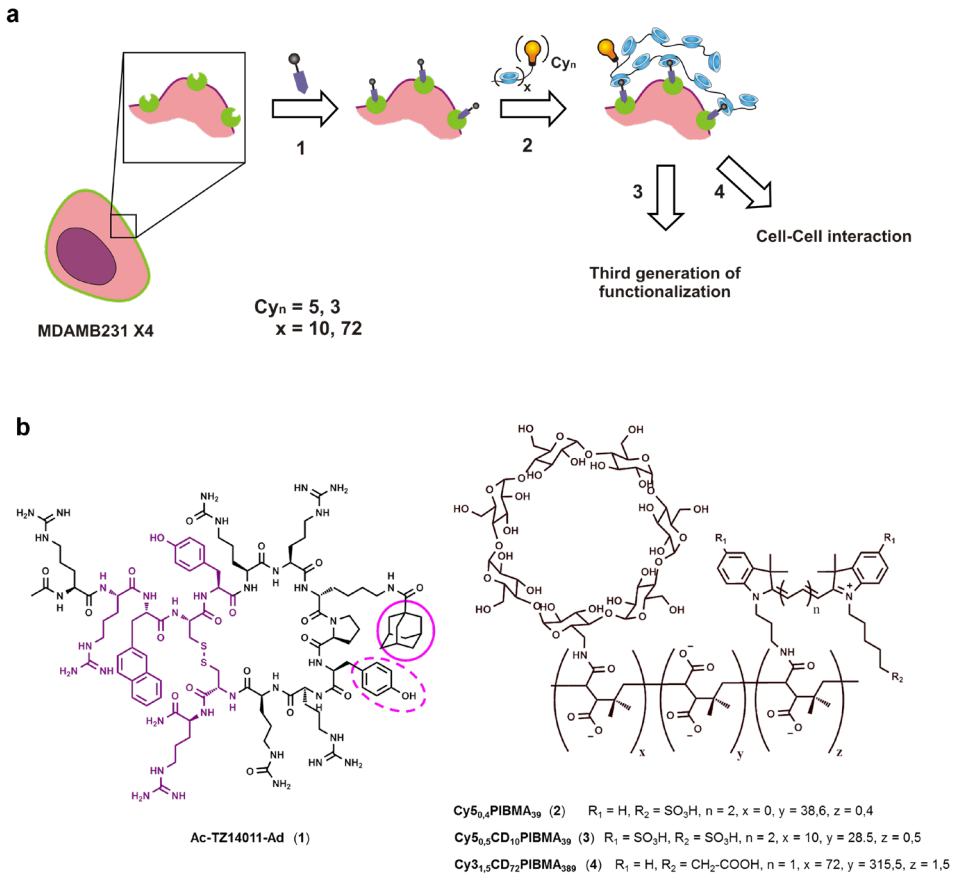


Figure 1. (a) Schematic representation of the supramolecular functionalization of cell surfaces via targeting of the membrane-receptor CXCR4 (green). As first step, cellular specificity is introduced by using **Ac-TZ14011-Ad** (1) peptide to target CXCR4 (step 1). This provides an Ad-functionality on the surface that can be used as basis for more generic functionalization with β -CD polymers containing variable fluorescent labels and β -CD; **Cy_{0.5}CD₁₀PIBMA₃₉** (3), **Cy_{3.15}CD₇₂PIBMA₃₈₉** (4) (step 2; $x = 10$ or 72). The then artificially generated CD-surfaces can be used to drive cellular interactions with entities containing matching guest functionalities. Hereby a third generation of functionalization can be introduced such as Ad-functionalized fluorescent dye (step 3) or cell-cell interactions can be induced with Ad-functionalized cells (step 4). (b) Chemical structures of the key compounds; **Ac-TZ14011-Ad** (1), **Cy_{0.5}CD₁₀PIBMA₃₉** (3), **Cy_{3.15}CD₇₂PIBMA₃₈₉** (4), **Cy_{0.4}PIBMA₃₉** (2), the polymer-units containing different functionalities are randomly distributed within the polymer. In **Ac-TZ14011-Ad** the pharmacophore of Ac-TZ14011 is indicated in purple. The main guest for β -CD; Ad is indicated by a pink solid line, together with a possible second guest: Tyr10 (pink dotted line).

PIBMA₃₉ (9.1 mg, 1.5 μmol) and Cy5-Sulfonate-Amine (**10**) (1 mg, 1.8 μmol) were dissolved in 0.6 mL dry DMSO, DIPEA (13 μL, 74 μmol) was added and the mixture was stirred at RT overnight. Subsequently, the reaction mixture was directly dialyzed and after lyophilization, the product was obtained as a blue powder (2 mg, 0.3 μmol).

Average number of Cy5 dye/polymer according UV/vis absorbance: 0.4

Estimated molecular weight: 7.8 kDa (Table S1).

Cy5_{0.5}CD₁₀PIBMA₃₉ (Compound **3**)

PIBMA₃₉ (30 mg, 5 μmol) and Cy5-(SO₃)Sulfonate-(SO₃)Amine (**9**) (5.0 mg, 5.6 μmol) were dissolved in 3 mL dry DMSO and DIPEA (50 μL, 250 μmol) was added. The reaction was stirred at 80 °C for 7 h, then 6-monodeoxy-6-monoamino-β-cyclodextrin (95 mg, 80 μmol) was added and the solution was stirred for another 72 h at 80 °C. After dialysis and lyophilization, the product was obtained as a blue powder (87 mg, 5 μmol).

Average number of CD groups/polymer according ¹H NMR: 10

Average number of Cy5 dye/polymer according UV/vis absorbance: 0.5

Estimated molecular weight: 18.8 kDa (Table S1).

Cy3_{1.5}CD₇₂PIBMA₃₈₉ (Compound **4**)

PIBMA₃₈₉ (10 mg, 0.17 μmol) and DIPEA (15 μL, 85 μmol) were dissolved in 1.7 mL dry DMSO and a solution of Cy3-Amine-COOH (**11**) in dry DMSO (0.25 mM, 800 μL, 0.2 μmol) was added. The reaction was stirred overnight at RT, then, 6-monodeoxy-6-monoamino-β-cyclodextrin (31.6 mg, 27 μmol) was added and the solution was stirred for another night at 80 °C. After dialysis and lyophilization the product was obtained as a bright pink powder (22.3 mg, 0.16 μmol).

Average number of CD groups/polymer according ¹H NMR: 72

Average number of Cy3 dye/polymer according UV/vis absorbance: 1.5

Estimated molecular weight: 155 kDa (Table S2).

Cell experiments

Functionalization of cells

MDAMB231 X4, were seeded onto culture dishes (80,000 per dish) and brought to 0 °C, followed by incubation with **Ac-TZ14011-Ad** (10 μM) in 1 mL DMEM for 1 h at 0 °C. Subsequently, either **Cy5_{0.5}CD₁₀PIBMA₃₉** or **Cy3_{1.5}CD₇₂PIBMA₃₈₉** was added (10 μM final β-CD concentration). After 1 h of incubation at 0 °C, cells were washed twice with PBS and confocal images were taken.

Functionalization of cells in a mixed cell-culture

A mixed-cell set-up was used to determine the specificity of the cell functionalization. A mixture of 40,000 cells of each strain of MDAMB231 X4 and MDAMB231 cells were seeded. The next day, the cells were brought to 0 °C and subsequently they were functionalized with either **Cy5_{0.5}CD₁₀PIBMA₃₉** or **Cy3_{1.5}CD₇₂PIBMA₃₈₉** (see functionalization of the cells). During confocal analysis discrimination between the fluorescence of the outer membrane of the two cell lines was based on the GFP signal, only present in the MDAMB231 X4 strain. To determine the difference in polymer binding to **Ac-TZ14011-Ad** functionalized MDAMB231 X4 and MDAMB231 cells. The experiment was performed twice and for each cell type the average gray value/m² of 25 cells in total was measured (see SI for further details).

Ac-TZ14011-Ad induced cell functionalization analyzed by confocal microscopy

The receptor-mediated functionalization of cells was examined by confocal microscopy and flow cytometry (see also '**Ac-TZ14011-Ad** induced cell functionalization analyzed by flow cytometry'). For Confocal microscopy MDAMB231 X4 cells (80,000 per well) were incubated with either Ac-TZ14011 (10 μM), **Ac-TZ14011-Ad** (10 μM), or none, for 1 h at 0 °C in 1 mL DMEM. Subsequently, either **Cy5_{0.4}PIBMA₃₉** or **Cy5_{0.5}CD₁₀PIBMA₃₉** was added (10 μM β-CD; 1 μM polymer final concentration) and another hour at 0 °C of incubation followed. Thereafter, the cells were washed twice with PBS and confocal images were acquired. All experiments were performed in 6-fold and for each condition per experiment at least 10 cells were included in the study. The Cy5 signal present on the cell in each sample was quantified to analyze differences between the amounts of binding of the polymers to the cells when either, no peptide, Ac-TZ14011, or **Ac-TZ14011-Ad** was present. For normalization all results were divided by the average fluorescence value obtained when just the polymer was added. The significance of the obtained differences was determined by student T-test (two tailed, unpaired).

Cy5-Ad and **Cy5-Ad₂** functionalization of polymer modified cell surfaces

A third functionalization on the β-CD-polymer functionalized cells was introduced, by first functionalizing adherent MDAMB231 X4 cells with **Cy3_{1.5}CD₇₂PIBMA₃₈₉**. Subsequently, the cells were washed once with DMEM, followed by incubation with **Cy5-Ad_n** (n = 1 or 2, 5 μM) in 1 mL DMEM for 1 h at 0 °C. Before confocal images were taken, the cells were washed twice with PBS. As a control experiment, the cells were incubated with **Cy5-Ad₂** (5 μM final concentration) while the polymer was omitted in the first incubation step.

Table 1. Tested cell mixtures of adhered and suspended MDAMB231 X4 cells and their functionalization.

| Cell mixture | Adherent MDAMB231 | In suspension MDAMB231 + Hoechst labelled |
|--------------|---|---|
| 1 | Ac-TZ14011-Ad + Cy3_{1.5}CD₇₂PIBMA₃₈₉ | Ac-TZ14011-Ad |
| 2 | Ac-TZ14011-Ad + Cy3_{1.5}CD₇₂PIBMA₃₈₉ | None |
| 3 | None | Ac-TZ14011-Ad |
| 4 | None | None |

Cell-cell interactions

To study cell-cell interactions, variable combinations of functionalized MDAMB231 X4 cells were evaluated. MDAMB231 X4 cells (300,000 per tube) in suspension were incubated with Hoechst 33342 (1 µg/mL) for 30 minutes in 1 mL DMEM at 0 °C. Subsequently, they were washed once with PBS (centrifuged 3 min, 3000 x g, 4 °C), cooled on ice and either incubated with **Ac-TZ14011-Ad** (11 µM) or none, in DMEM (500 µL) for 1 h at 0 °C. After washing twice with PBS (centrifuged 3 min, 3000 x g, 4 °C), cells were resuspended in 300 µL PBS and added to a separate batch of adherent MDAMB231 X4 target cells (80,000 cells per dish). The latter were either functionalized with **Cy3_{1.5}CD₇₂PIBMA₃₈₉** or none, or subsequently washed with PBS. The variable cell mixtures, see Table S1, were allowed to incubate in 1 mL PBS for 15 to 30 min at RT. Prior to imaging, the excess of unbound cells in suspension were gently washed away with PBS (2 x 1 mL, RT). The samples were examined under confocal microscopy in a culture dish and of each sample approximately 10 images were acquired at randomly chosen locations. All experiments were performed in 5-fold, resulting in the analysis of 223 ± 30 cells per cell combination. For each image obtained, the ratio between Hoechst stained cells that had an interaction with a target cell and the total number of Hoechst-stained cells in the image, was calculated. Obtained ratio's for each cell combination (Table 1) were averaged and statistical significance of differences between each cell combination determined using student T-test (two tailed, unpaired).

Ac-TZ14011-Ad induced cell functionalization analyzed by flow cytometry

Besides examining the receptor-mediated functionalization of cells by confocal microscopy (see '**Ac-TZ14011-Ad** induced cell functionalization analyzed by confocal microscopy') the

functionalization was also examined by flow cytometry to quantify the rate of functionalization. For this purpose, MDAMB231 X4 cells were trypsinized and divided into aliquots (300,000 cells per tube), centrifuged for three minutes ($3000 \times g$, $4\text{ }^{\circ}\text{C}$), and supernatant was decanted. The cells were incubated with 50 μL PBS containing either Ac-TZ14011 (10 μM), **Ac-TZ14011-Ad** (10 μM), or none for 1 h at $0\text{ }^{\circ}\text{C}$. Subsequently, 50 μL of either **Cy5_{0.4}PIBMA₃₉** or **Cy5_{0.5}CD₁₀PIBMA₃₉** in PBS was added (10 μM $\beta\text{-CD}$; 1 μM polymer final concentration) and another hour at $0\text{ }^{\circ}\text{C}$ of incubation followed. The cells were washed twice with PBS (centrifuged 3 min, $3000 \times g$, $4\text{ }^{\circ}\text{C}$), resuspended in 300 μL PBS and the intensity of Cy5 fluorescence related to the cells was measured by flow cytometry (see ESI for further details). All experiments were performed in 8-fold. For data normalization, all results were divided by the average fluorescence value obtained when only the polymer was added. The significance of the obtained differences was determined by student T-test (two tailed, unpaired).

RESULTS AND DISCUSSION

Design and synthesis of the chemical components

The cyclic Ac-TZ14011 peptide, a well-known targeting ligand for the CXCR4 receptor,⁴¹ was functionalized using an Ad-group (Figure 1b). Hereby the Ad-group pointed outwards from the pharmacophore,⁴² making the Ad-group available for interactions with the cell's environment. Flow cytometry-based competition experiments on viable CXCR4 expressing cells (MDAMB231 X4), revealed a K_D of 56 nM for **Ac-Tz14011-Ad** (Figure S11), using the fluorescent Ac-TZ14011-MSAP ($K_D = 187\text{ nM}$) as a reference. Unmodified Ac-TZ14011 has an affinity of 8.6 nM,⁴³ which indicates that the introduction of the Ad functionality only has a relatively small adverse effect on the receptor affinity.⁴¹

Poly(isobutylene-alt-maleic-anhydride) (PIBMA) with different lengths (PIBMA₃₉ and PIBMA₃₈₉) were used for the polymer backbone, as the anhydrides allow easy grafting with nucleophiles such as $\beta\text{-CD-NH}_2$, Cy3-NH₂ and Cy5-NH₂. Furthermore, hydrolyzing the non-reacted anhydrides to carboxylates, provides good solubility in aqueous solutions ($\text{p}K_a = 4$).^{44,45} This approach resulted in the synthesis of two fluorescent $\beta\text{-CD-PIBMA}$ -polymers and one solely fluorescent PIBMA₃₉-polymer without $\beta\text{-CD}$ for control experiments. After conjugation, absorption spectroscopy revealed that on average 0.5 Cy5, 1.5 Cy3, and 0.4 Cy5 fluorophores were conjugated to the respective polymers. ¹H-NMR and NMR Diffusion Ordered Spectroscopy (DOSY) were used to determine the

degree of CD-functionalization and to estimate the hydrodynamic diameter of the respective polymers. This yielded one polymer with 10 β -CD-units with diameter \sim 2.8 nm (\sim 18.8 kDa; **Cy5_{0.5}CD₁₀PIBMA₃₉**), one polymer with 72 β -CD-units with diameter \sim 11.7 nm (\sim 155 kDa; **Cy3_{1.5}CD₇₂PIBMA₃₈₉**), and one polymer without β CD-units with diameter \sim 2.7 nm (\sim 7.8 kDa; **Cy5_{0.4}PIBMA₃₉**)(Figure 1b).

Functionalization of cell surfaces

To prove that (supramolecular) cell-surface modification becomes possible via specific functionalization of the membrane-receptors, CXCR4 overexpressing MDAMB231 X4 cells were functionalized in two steps; first with **Ac-TZ14011-Ad** (1 h; 0 °C), to allow for CXCR4 receptor targeting (Figure 1,1) and secondly with either **Cy5_{0.5}CD₁₀PIBMA₃₉** or **Cy3_{1.5}CD₇₂PIBMA₃₈₉** (1 h; 0 °C) to allow further surface functionalization (Figure 1,2). Cell analysis using confocal microscopy indicated that cell functionalization was accomplished using both polymer types (Figure S12). MTT cell-viability tests performed 24 h after the (supramolecular) cell-surface functionalization (Figure S13) showed that the cells were not negatively affected by the functionalization with **Ac-TZ14011-Ad** and either one of the two polymers (0–16 μ M β -CD).

To further study the CXCR4-receptor specificity of the functionalization process, the experiments were repeated with a mixed cell culture of viable MDAMB231 X4 (with overexpressed CXCR4 receptor and with CXCR4-linked GFP-tag) and as a control MDAMB231 cells (with basal CXCR4 expression and without CXCR4-linked GFP-tag). We have demonstrated previously that a fluorescent variant of the Ac-TZ14011 peptide allows for differentiation between the two cell lines, using their difference in CXCR4 expression levels⁴⁶. Confocal microscopy (Figure 2) and intensity analysis revealed that the average signal intensities of **Cy5_{0.5}CD₁₀PIBMA₃₉** and **Cy3_{1.5}CD₇₂PIBMA₃₈₉** were respectively 5 and 8 times higher on the MDAMB231 X4 cells, compared to the signal intensities observed on the cells with basal CXCR4 expression (MDAMB231), which indicates receptor specificity.

The influence of host-guest interactions on the degree of cell surface functionalization was examined on MDAMB231 X4 cells. Here for the conditions of the first incubation step were varied as follows; (1) by omitting the use of a CXCR4-binding peptide, (2) by using non-Ad functionalized Ac-TZ14011 (includes a lower affinity tyrosine (Tyr10) guest moiety^{47,48}) or (3) via the standard procedure by using **Ac-TZ14011-Ad**. Differences in functionalization using **Cy5_{0.5}CD₁₀PIBMA₃₉** or **Cy5_{0.4}PIBMA₃₉** were analyzed using both semi-quantitative (confocal microscopy) and quantitative (flow cytometry) methods. Under a direct comparison at baseline the non-specific uptake of **Cy5_{0.5}CD₁₀PIBMA₃₉** is about

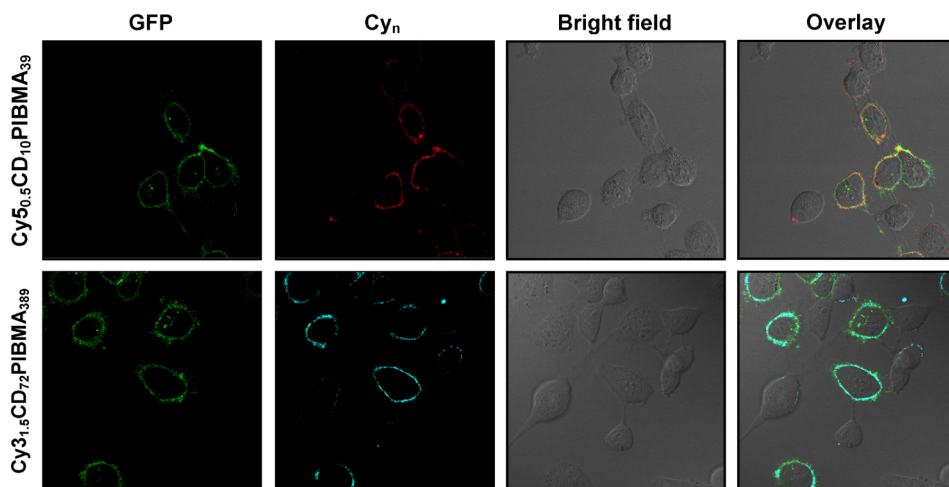


Figure 2. Supramolecular surface modification of viable MDAMB231 X4 (with CXCR4-linked GFP-Tag) and MDAMB231 cells (without GFP-Tag) in mixed cell culture. Modification was accomplished via specific functionalization of the CXCR4 receptor with Ac-TZ14011-Ad, followed by host-guest interaction between β -CD molecules on fluorescent **Cy5_{0.5}CD₁₀PIBMA₃₉** or **Cy3_{1.5}CD₇₂PIBMA₃₈₉** polymers and the Ad functionality. Functionalization mainly occurs on the CXCR4 overexpressing MDAMB231 X4 cells. For clarity, both the (overlay) image and the same image at the individual channels are displayed, with GFP in green, Cy5 (**Cy5_{0.5}CD₁₀PIBMA₃₉**) in red, and Cy3 (**Cy3_{1.5}CD₇₂PIBMA₃₈₉**) in blue.

one-and-a-half times that of **Cy5_{0.4}PIBMA₃₉**, which indicates that β -CD can interact with cell-surface residues. Pre-targeting based introduction of guest moieties on the CXCR4 receptors yielded statistically significant ($p < 0.01$) increases in **Cy5_{0.5}CD₁₀PIBMA₃₉** binding (Figure 3a). The middle column of Figure 3a, indicates that the Tyr10 residue on the Ac-TZ14011 peptide (Figure 1b) already induces enhanced binding of the CD-polymer.⁴¹ The introduction of the higher affinity Ad-guest molecule (**Ac-TZ14011-Ad**), further enhances this effect (Figure 3a, last column).

When the polymer did not include β -CD (host) functionalizations (**Cy5_{0.4}PIBMA₃₉**), binding was not induced by the presence of **Ac-TZ14011**, or **Ac-TZ14011-Ad** (Figure 3b). Figure S15 further illustrates that the availability of multiple CD-moieties on the polymer backbone enhances the binding considerably. On average **Cy5_{0.5}CD₁₀PIBMA₃₉** displayed two-fold higher binding than **Cy5_{0.4}PIBMA₃₉**. The findings of Figure 3a,b and Figure S15 combined suggest that both guest and host moieties play an instrumental role in the cell functionalization process.

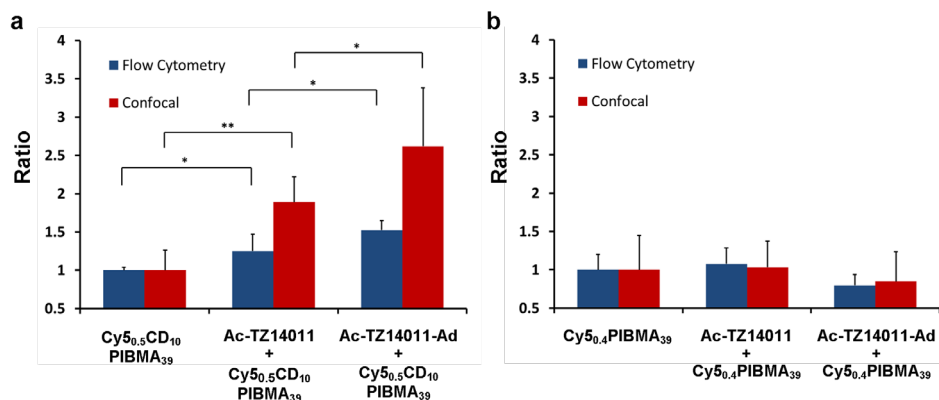


Figure 3. Host-guest interaction dependent cellular functionalization: (a) Binding of **Cy5_{0.5}CD₁₀PIBMA₃₉** increases in a statistically significant manner when the guest moieties **Ac-TZ14011** and **Ac-TZ14011-Ad** become available at the cell surface. (b) **Cy5_{0.5}CD₁₀PIBMA₃₉** functionalization is not influenced by the availability of guest moieties. These values remain at baseline. The degree of functionalization was quantified by Flow cytometry (blue) or Confocal microscopy (red). Graphs show the normalized data with the error bars indicating the standard deviations ($n = 6$) and the significance of differences marked with * ($p < 0.05$) or ** ($p < 0.01$).

During the (supramolecular) cell surface modification it is expected that one polymer interacts with multiple **Ac-TZ14011-Ad** moieties to establish functionalization. Individual CXCR4 receptors have a diameter of approximately 4 to 5 nm, based on the crystal structure of CXCR4 obtained from the RCSB protein data bank (PDB code 3OE0).⁴¹ Although the distance between CXCR4 receptors on the membrane is unknown, it is reported that they can cluster in groups.^{49,50} When assuming a spherical structure, **Cy5_{0.5}CD₁₀PIBMA₃₉** has a hydrodynamic diameter of 2.8 nm in water but, when unfolded, the polymer length is approximately 24 nm (based on the estimated bond lengths of one subunit, times the number of subunits in the polymer). Hypothetically, this should allow simultaneous interactions with multiple (clustered) **Ac-TZ14011-Ad** functionalized CXCR4 receptors. The longer **Cy3_{1.5}CD₇₂PIBMA₃₈₉** polymer (hydrodynamic diameter ~11.7 nm; unfolded > 200 nm) should allow such multivalent interactions even more. To test this theory, the functionalization was also performed using monovalent **Cy5-CD (5)** instead of a CD_nPIBMA_m polymer, which resulted in a substantial lower degree of functionalization (Figure S14). These findings show that multivalent interactions between β -CD-host molecules and different Ad-guest molecules are indeed required. Furthermore it confirms the assumption that each polymer interacts with at least two or more **Ac-TZ14011-Ad** functionalized CXCR4 receptors.

Since **Cy3_{1.5}CD₇₂PIBMA₃₈₉** differs considerably from **Cy5_{0.5}CD₁₀PIBMA₃₉** in length (unfolded; 24 vs. > 200 nm) and in CD number (10 vs. 72), **Cy3_{1.5}CD₇₂PIBMA₃₈₉** can, in theory, bind to more **Ac-TZ14011-Ad** groups than **Cy5_{0.5}CD₁₀PIBMA₃₉**. This difference was indeed reflected in the affinity of both polymers for the Ad-functionalized cell surfaces. In competition experiments (see supporting information for more detailed description and discussion), **Cy3_{1.5}CD₇₂PIBMA₃₈₉** bound in slightly larger quantities to the cells surface than **Cy5_{0.5}CD₁₀PIBMA₃₉** (Figure S17). Competition followed over time by confocal microscopy, revealed that under competitive conditions **Cy3_{1.5}CD₇₂PIBMA₃₈₉** could replace **Cy5_{0.5}CD₁₀PIBMA₃₉** cell functionalizations, while the reverse proved to be difficult (Figures S18 and S19).

To investigate if the observed replacement is indeed based on host-guest interactions, the same longitudinal competition experiment was repeated with **Cy5_{0.4}PIBMA₃₉**. This experiment demonstrated that **Cy5_{0.4}PIBMA₃₉** was not replaced by **Cy3_{1.5}CD₇₂PIBMA₃₈₉**, which displayed increased binding to the cell surface over time (see supporting information for more detailed description and discussion; Figures S18 and S19). When the reverse was attempted, **Cy3_{1.5}CD₇₂PIBMA₃₈₉** could also not be replaced by **Cy5_{0.4}PIBMA₃₉** while the backbone polymer already displayed binding at an early time-point. These results indicate that the non-specific binding of **Cy5_{0.4}PIBMA₃₉** occurs at a different location than where **Cy3_{1.5}CD₇₂PIBMA₃₈₉** binds in a specific manner. These control experiments underline that the observed replacement between **Cy5_{0.5}CD₁₀PIBMA₃₉** and **Cy3_{1.5}CD₇₂PIBMA₃₈₉** (Figures S18 and S19) represent competition observed in the host-guest interactions between the CD-moieties on the polymers and the **Ac-TZ14011-Ad** ligands.

Using cells as chemical scaffold for further functionalization

β -CD based binding of the PIBMA-polymers to the **Ac-TZ14011-Ad** functionalized cell surface is dynamic and occurs with the presence of an excess of β -CD groups on the polymers (Figure 4a, step 1, 2). Hence, it is expected that non-bound β -CD groups remain available that can be used for consecutive supramolecular functionalization steps. This concept was initially studied using **Cy5-Ad** (6) and **Cy5-Ad₂** (7). The monovalent **Cy5-Ad** showed very little staining of cells that were pre-functionalized with **Cy3_{1.5}CD₇₂PIBMA₃₈₉** (Figure S20). In contrast, the bivalent **Cy5-Ad₂** showed clear staining under identical conditions, providing co-localization of the CXCR4 receptor (GFP), **Cy3_{1.5}CD₇₂PIBMA₃₈₉** (Cy3), and **Cy5-Ad₂** (Cy5) (Figure 4b). Use of **Cy5** (8) alone did not result in staining (Figure S20). Moreover, experiments where **Cy5-Ad₂** was added in the absence of **Cy3_{1.5}CD₇₂PIBMA₃₈₉** did not yield non-specific staining which is a clear indication that the

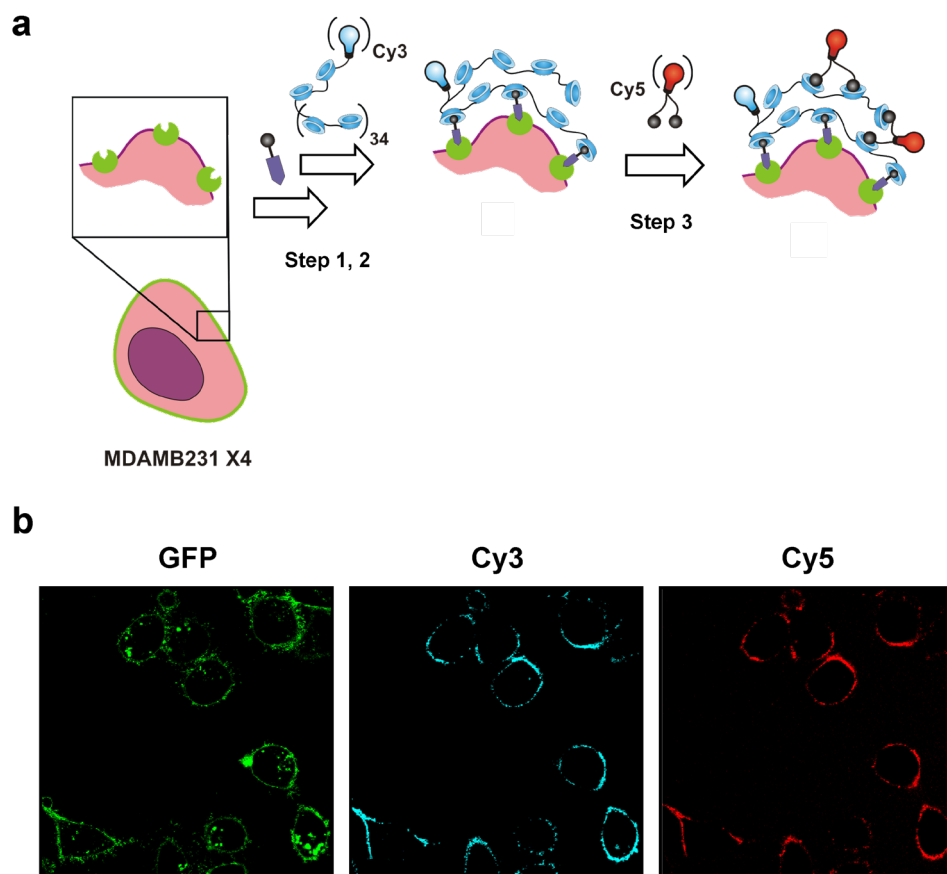


Figure 4. (a) Schematic illustration of introducing a third-generation of surface modification, e.g. **Cy5-Ad₂**. The host-guest interaction of CD-Ad is dynamic and after functionalizing the cell surface with $\text{CD}_n\text{-PIBMA}_m$ polymers, e.g. **Cy3_{1,5}CD₇₂PIBMA₃₈₉** (step 1,2), non-bound β -CD groups should be available to host the second fluorescent label (step 3). (b) Confocal images visualizing the introduction of **Cy5-Ad₂** on **Cy3_{1,5}CD₇₂PIBMA₃₈₉** functionalized MDAMB231 X4 cells. For clarity, both the (overlay) image and the same image at the individual channels are displayed, with GFP in green, Cy3 (**Cy3_{1,5}CD₇₂PIBMA₃₈₉**) in blue and Cy5 (**Cy5-Ad₂**) in red.

polymer is essential for functionalization (Figure S21). When looking at the binding constant of mono- and bivalent Ad with multivalent β -CD hosts in general,⁵¹⁻⁵⁴ a difference of at least a factor 200 is found. The binding constant of bis-adamantane (e.g. **Cy5-Ad₂**) with multivalent β -CD hosts lies between $1 \cdot 10^7$ – $1 \cdot 10^{10}$ M⁻¹ (depending on the host and its environment),^{52,53} while the **Cy5-Ad** interaction with **Cy3_{1,5}CD₇₂PIBMA₃₈₉** can be seen as

a monovalent interaction of which the binding constant lies around $5 \cdot 10^4 \text{ M}^{-1}$.^{51,54} Again multivalency seems to be a key component for facilitating stable interactions under *in vitro* conditions. The ability to utilize β -CD functionalized cell surfaces to introduce a third-generation of functionalization opens up a scale of functionalization types to tailor a wide range of applications. For example, diagnostic labels for cell-tracking⁵⁵ could be introduced via this route. Alternatively, the introduction of therapeutic agents or a combination of both is possible. Hereby cells are converted into functional scaffolds that can be applied for delivery applications.

Given the fact that the $\text{CD}_n\text{PIBMA}_m$ polymers interact with **Ac-TZ14011-Ad** functionalization on the cell surface and that the secondary polymer surface functionalization enables a third-generation of surface modifications, we reasoned that it would be of interest to use such technology to drive the interactions between MDAMB231 X4 cells that are either functionalized with $\text{CD}_n\text{PIBMA}_m$ polymers or **Ac-TZ14011-Ad** (Figure 5a).

To study the induction of cell-cell interactions, **Ac-TZ14011-Ad** + **Cy3_{1,5}CD₇₂PIBMA₃₈₉** functionalized adhered MDAMB231 X4 cells were incubated with a solution containing **Ac-TZ14011-Ad** functionalized MDAMB231 X4 cells in suspension (see Figure 5a for a schematic representation). In the latter the nucleus was stained with Hoechst in order to enable discrimination between the two. After 15–30 min of incubation, cell-cell interactions were quantified using confocal microscopy (Figure 5b). Analysis of the obtained images revealed that on average 61% of the Hoechst stained suspended cells within the field of view interacted with non-Hoechst stained adherent cells. Control experiments where the adherent cells were not functionalized using **Cy3_{1,5}CD₇₂PIBMA₃₈₉** and/or in which the cells in suspension were not functionalized with **Ac-TZ14011-Ad** resulted in significantly ($p < 0.01$ and $p < 0.05$ respectively) lower percentages of cell-cell interactions, as is depicted in Figure 5. This made us conclude that the introduced cell-surface modifications and underlying supramolecular chemistry opens the perspective to drive cell-cell interactions.

Synthetic control on cell-cell enhancing interactions could be beneficial for cell-based therapies.^{7–9} For example, a challenge in (heart) stem-cell transplantation is to make the cells reside at the site of interest long enough to deliver a therapeutic effect.¹⁰ In the current clinical set-up, for example, cardiac stem cells are quickly cleared from location after intramyocardial injection.⁵⁶ If the interaction of a transplanted cell with its surrounding could be enhanced, e.g. by providing a “temporary glue-like” adhesion of the cells at the injection site, the local retention could be improved. By allowing the cells time to engraft to the host tissue using natural transmembrane receptor interactions, the cellular retention

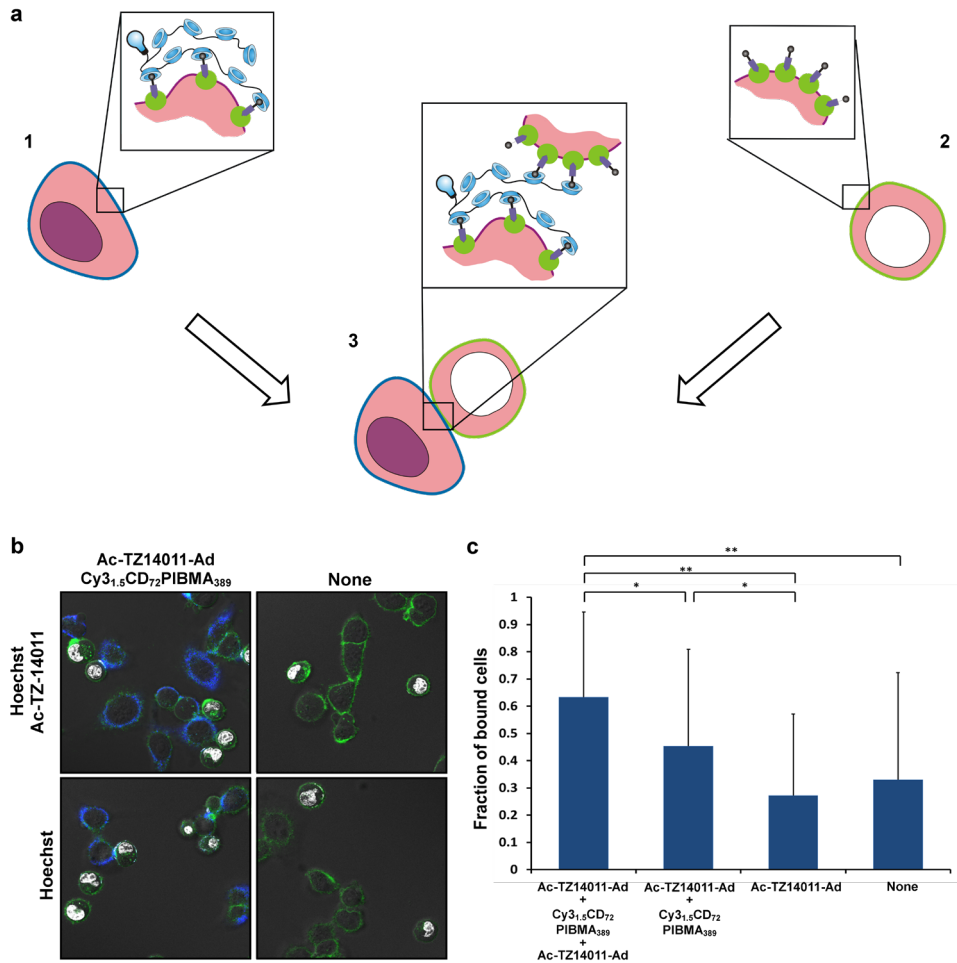


Figure 5. (a) Schematic overview of inducing cell-cell interactions (3) between β -CD polymer (Cy3_{1,5}CD₇₂PIBMA₃₈₉) functionalized cells (1) and Ad (Ac-TZ14011-Ad) functionalized cells (2) with Hoechst staining (white) (b) Representative confocal images of inducing supramolecular cell-cell interactions between variable functionalized MDAMB231 X4 cells. With GFP in green, Cy3 in blue and Hoechst in white. (c) Average values of the fraction of cell-cell interactions in each test condition. Significance of differences is marked with * ($p < 0.05$) or ** ($p < 0.01$).

and thus the therapeutic efficacy is likely to be enhanced. Alternatively, the same mechanism could be applied to temporarily adhere cells that excrete therapeutic substances such as enzymes.⁵⁷ To demonstrate that the technology described is not limited to cancer cells we successfully applied this technology on CXCR4 expressing human cardiac

stem cells (Figure S22), which are currently applied in stem cell-therapy. After having established all the chemical requirements for the supramolecular cell-surface modification, studies regarding the biological efficacy of functionalized stem cells will be initiated.

The cell-surface modification approach as described in this manuscript, obtains its cell-type specificity from the specific targeting of membrane receptors, in this case being CXCR4 (Figure 1, 1). While polymer modification of the cell surface is a generic step (Figure 1, 2), the introduction of functionalities for e.g. adhesion can again be tailored if required. This provides a large degree of (synthetic) freedom and possibilities. With the many membrane-receptor targeting vectors available on the market these days,^{38,40,43,58,59} and the huge variety of functionalities that could be of value, the proposed approach can be made compatible with a whole scale of cells and cell-therapy applications. The most critical part herein seems to be a high local density of one, or a combination of, membrane-receptors so that multivalent interactions with the host polymer are possible.

Based on the possibility of introducing specificity via the membrane-receptors (Figure 2, 3) it may be postulated that the supramolecular approach provides a good alternative for current cell surface functionalization methods, such as the layer by layer (LBL) α -specific cell coating by polyelectrolyte polymers¹⁸ or the insertion of lipophilic anchors.²⁰ While the LBL technique has proven its applicability as cell coating on different sturdy cell membranes, e.g. bacteria and pancreatic islets,⁶⁰ the supramolecular functionalization is more subtle and allows cell surface modification in more sensitive cell types without harming the cell viability (Figure S13).

CONCLUSIONS

In this study we have shown that cell specific sequential surface functionalization could be accomplished by pre-targeting cells with an Ad-containing targeting vector such as **Ac-TZ14011-Ad**. This pre-targeting approach provides the possibility of tailoring this first step towards other cell types. Subsequently, host-guest interactions between fluorescent labeled CD_n PIBMA_m host polymers and the introduced Ad-guest functionality not only enable surface coating, but also formed a basis for further hierarchical functionalization. The described host-guest approach adds the possibility to introduce specific functionalizations on the CD_n PIBMA_m modified cell surface. There are always non-bound β -CD groups available for further functionalization, since the polymers contain an excess of β -CD groups. The specific functionalizations can be in the form of diagnostic- and/or

therapeutic-labels, so that the cells become vehicles for imaging and/or drug-delivery applications. In addition, we have shown that these supramolecular functionalizations provide a basis to drive cell-cell interactions that could prove to be of future benefit for cell based therapies.

Acknowledgments

The research leading to these results has received funding from the European Research Council (ERC) under the European Union's Seventh Framework Program FP7/2007-2013 (Grant No. 2012-306890), from the NWO nanogrant (Grant No. STW 11435), a Netherlands Organization for Scientific Research STW-VIDI grant (Grant No. STW BGT11272) and the 2015-2016 Post-Doctoral Molecular Imaging Scholar Program Grant granted by the Society of Nuclear Medicine and Molecular imaging (SNMMI) and the Education and Research Foundation for Nuclear Medicine and Molecular Imaging.

REFERENCES

1. B. Alberts; A. Johnson; D. Morgan, et al., *Molecular biology of the cell*. 6 ed.; Garland science: New York, 2014.
2. H. Lodish; A. Berk; C. A. Kaiser, et al., *Molecular Cell Biology*. 7 ed.; W. H. Freeman: New York, 2012.
3. S. Barja-Fernandez; C. Folgueira; C. Castelao, et al., Regulation of growth hormone by the splanchnic area. *Prog Mol Biol Transl Sci* **2016**, *138*, 41-60.
4. J. Vriend; R. J. Reiter, Melatonin, bone regulation and the ubiquitin-proteasome connection: a review. *Life Sciences* **2016**, *145*, 152-160.
5. O. T. Burton; H. C. Oettgen, Beyond immediate hypersensitivity; evolving roles for IgE antibodies in immune homeostasis and allergic diseases. *Immunol Rev* **2011**, *242*, 128-143.
6. C. M. Alexander; K. N. Xiong; K. Velmurugan, et al., Differential innate immune cell signatures and effects regulated by toll-like receptor 4 during murine lung tumor promotion. *Exp Lung Res* **2016**, *42* (3), 154-173.
7. J. A. M. Shapiro; J. R. T. Lakey; E. A. Ryan, Islet transplantation in seven patients with type 1 diabetes mellitus using a glucocorticoid-free immunosuppressive regimen. *New. Eng. J. Med.* **2000**, *343*, 230-238.
8. H. Felfly; G. G. Haddad, Hematopoietic stem cells: potential new applications for translational medicine. *J Stem Cells* **2014**, *9* (3), 163-197.
9. A. Gratwohl; H. Baldomero; M. Aljurf, Hematopoietic stem cell transplantation. *J. Am. Med. Assoc.* **2010**, *303*, 1617-1624.
10. M. C. den Haan; R. W. Grauss; A. M. Smits, et al., Cardiomyogenic differentiation-independent improvement of cardiac function by human cardiomyocyte progenitor cell injection in ischaemic mouse hearts. *J Cell Mol Med* **2012**, *16* (7), 1508-1521.
11. C. C. Liu; P. G. Schultz, Adding new chemistries to the genetic code. *Annu. Rev. Biochem* **2010**, *79*, 413-444.
12. Z. J. Gartner; C. R. Bertozzi, Programmed assembly of 3-dimensional microtissues with defined cellular connectivity. *Proc Natl Acad Sci U S A* **2009**, *106* (12), 4606-4610.
13. M. D. Mager; V. LaPointe; M. M. Stevens, Exploring and exploiting chemistry at the cell surface. *Nat Chem* **2011**, *3* (8), 582-589.
14. B. G. Mathapa; V. N. Paunov, Fabrication of viable cyborg cells with cyclodextrin functionality. *Biomater. Sci.* **2014**, *2* (2), 212-219.

15. M. T. Stephan; J. J. Moon; S. H. Um, et al., Therapeutic cell engineering with surface-conjugated synthetic nanoparticles. *Nat Med* **2010**, *16* (9), 1035-1041.
16. C. S. McKay; M. G. Finn, Click chemistry in complex mixtures: bioorthogonal bioconjugation. *Chem Biol* **2014**, *21* (9), 1075-1101.
17. S. Krol; S. Del Guerra; M. Grupillo, Multilayer nanoencapsulation. new approach for immune protection of human pancreatic islets. *Nano Lett.* **2006**, *6*, 1933-1939.
18. J. T. Wilson; W. Cui; V. Kozlovskaya, et al., Cell surface engineering with polyelectrolyte multilayer thin films. *J. Am. Chem. Soc.* **2011**, *133* (18), 7054-7064.
19. Y. Teramura; Y. Kaneda; T. Totani, et al., Behavior of synthetic polymers immobilized on a cell membrane. *Biomaterials* **2008**, *29* (10), 1345-1355.
20. D. Rabuka; M. Forstner; J. Groves, Noncovalent cell surface engineering: Incorporation of bioactive synthetic glycopolymers into cellular membranes. *J. Am. Chem. Soc.* **2008**, *130*, 5947-5953.
21. H. R. Jia; H. Y. Wang; Z. W. Yu, et al., Long-time plasma membrane imaging based on a two-step synergistic cell surface modification strategy. *Bioconjugate Chem.* **2016**, *27* (3), 782-789.
22. S. Goennenwein; M. Tanaka; B. Hu, Functional incorporation of integrins into solid supported membranes on ultrathin films of cellulose: impact on adhesion. *Biophys. J.* **2003**, *85*, 646-655.
23. D. Dutta; A. Pulsipher; W. Luo, et al., Synthetic chemoselective rewiring of cell surfaces: generation of three-dimensional tissue structures. *J. Am. Chem. Soc.* **2011**, *133* (22), 8704-8713.
24. D. A. Blake; N. V. Bovin; D. Bess, et al., FSL constructs: a simple method for modifying cell/virion surfaces with a range of biological markers without affecting their viability. *J. Vis. Exp.* **2011**, *54* (54), 1-9.
25. S. Kaufmann; M. Tanaka, Cell adhesion onto highly curved surfaces: one-step immobilization of human erythrocyte membranes on silica beads. *Chemphyschem* **2003**, *4* (7), 699-704.
26. H. R. Marsden; I. Tomatsu; A. Kros, Model systems for membrane fusion. *Chem. Soc. Rev.* **2011**, *40* (3), 1572-1585.
27. Q. An; J. Brinkmann; J. Huskens, et al., A supramolecular system for the electrochemically controlled release of cells. *Angew. Chem. Int. Ed. Engl.* **2012**, *51* (49), 12233-12237.
28. G. V. Dubacheva; T. Curk; R. Auzely-Velty, et al., Designing multivalent probes for tunable superselective targeting. *Proc Natl Acad Sci U S A* **2015**, *112* (18), 5579-5584.
29. R. de la Rica; R. M. Fratila; A. Szarpak, et al., Multivalent nanoparticle networks as

- ultrasensitive enzyme sensors. *Angew. Chem. Int. Ed. Engl.* **2011**, *50* (25), 5704-5707.
30. A. Gonzalez-Campo; S. H. Hsu; L. Puig, et al., Orthogonal covalent and noncovalent functionalization of cyclodextrin-alkyne patterned surfaces. *JACS* **2010**, *132* (33), 11343-11436.
31. P. Neiryneck; J. Brinkmann; Q. An, et al., Supramolecular control of cell adhesion via ferrocene-cucurbit[7]uril host-guest binding on gold surfaces. *Chem Commun (Camb)* **2013**, *49* (35), 3679-3681.
32. M. Oikonomou; J. Wang; R. R. Carvalho, et al., Ternary supramolecular quantum-dot network flocculation for selective lectin detection. *Nano Research* **2016**, *9* (7), 1904-1912.
33. C. B. Rodell; J. E. Mealy; J. A. Burdick, Supramolecular guest-host interactions for the preparation of biomedical materials. *Bioconjugate Chem.* **2015**, *26* (12), 2279-2289.
34. N. Li; Y. Chen; Y. M. Zhang, et al., Polysaccharide-gold nanocluster supramolecular conjugates as a versatile platform for the targeted delivery of anticancer drugs. *Sci Rep* **2014**, *4*, 4164.
35. Y. Yang; Y. M. Zhang; Y. Chen, et al., Polysaccharide-based noncovalent assembly for targeted delivery of taxol. *Sci Rep* **2016**, *6*, 19212.
36. L. Carlred; A. Gunnarsson; S. Sole-Domenech, et al., Simultaneous imaging of amyloid-beta and lipids in brain tissue using antibody-coupled liposomes and time-of-flight secondary ion mass spectrometry. *J. Am. Chem. Soc.* **2014**, *136* (28), 9973-9981.
37. A. Hellebust; R. Richards-Kortum, Advances in molecular imaging: targeted optical contrast agents for cancer diagnostics. *Nanomedicine (Lond)* **2012**, *7* (3), 429-445.
38. S. M. van Duijnhoven; R. Rossin; S. M. van den Bosch, et al., Diabody pretargeting with click chemistry in vivo. *J Nucl Med* **2015**, *56* (9), 1422-1428.
39. F. C. van de Watering; M. Rijpkema; M. Robillard, et al., Pretargeted imaging and radioimmunotherapy of cancer using antibodies and bioorthogonal chemistry. *Front Med (Lausanne)* **2014**, *1* (44), 1-11.
40. M. Millard; S. Odde; N. Neamati, Integrin targeted therapeutics. *Theranostics* **2011**, *1*, 154-188.
41. J. Kuil; T. Buckle; F. W. van Leeuwen, Imaging agents for the chemokine receptor 4 (CXCR4). *Chem. Soc. Rev.* **2012**, *41* (15), 5239-5261.
42. J. Kuil; P. Steunenber; P. T. K. Chin, et al., Peptide-Functionalized Luminescent Iridium Complexes for Lifetime Imaging of CXCR4 Expression. *ChemBiochem* **2011**, *12* (12), 1896-1902.
43. J. Kuil; T. Buckle; J. Oldenburg, et al., Hybrid peptide dendrimers for imaging of

- chemokine receptor 4 (CXCR4) expression. *Mol Pharm* **2011**, *8* (6), 2444-2453.
44. M. Weickenmeier; G. Wenz; J. Huff, Association thickener by host guest interaction of a beta-cyclodextrin polymer and a polymer with hydrophobic side-groups. *Macromolecular Rapid Communications* **1997**, *18* (12), 1117-1123.
45. L. Grana-Suarez; W. Verboom; J. Huskens, Cyclodextrin-based supramolecular nanoparticles stabilized by balancing attractive host-guest and repulsive electrostatic interactions. *Chem Commun (Camb)* **2014**, *50* (55), 7280-7282.
46. Tessa Buckle; Steffen van der Wal; Stijn J.M. van Malderen, et al., Hybrid imaging labels; providing the link between mass spectrometry-based molecular pathology and theranostics. *Theranostics* **2017**, *7* (3), 624-633
47. F. Achmann; D. Otzen; K. Larsen, Structural background of cyclodextrin-protein interactions. *Protein Eng.* **2003**, *16*, 905-912.
48. K. Uekama; F. Hirayama; T. Irie, Cyclodextrin drug carrier systems. *Chem. Rev.* **1998**, *98*, 2045-2076.
49. Singer, II; S. Scott; D. W. Kawka, et al., CCR5, CXCR4, and CD4 are clustered and closely apposed on microvilli of human macrophages and T cells. *J Virol* **2001**, *75* (8), 3779-3790.
50. G. L. Nicolson, The fluid-mosaic model of membrane structure: still relevant to understanding the structure, function and dynamics of biological membranes after more than 40 years. *Biochim. Biophys. Acta* **2014**, *1838* (6), 1451-1466.
51. M. Gade; A. Paul; C. Alex, et al., Supramolecular scaffolds on glass slides as sugar based rewritable sensors for bacteria. *Chem Commun (Camb)* **2015**, *51* (29), 6346-6349.
52. J. Huskens; A. Mulder; T. Auletta, et al., A model for describing the thermodynamics of multivalent host-guest interactions at interfaces. *JACS* **2004**, *126*, 6784-6797.
53. A. Mulder; T. Auletta; A. Sartori, et al., Divalent binding of a bis(adamantyl)-functionalized calix[4]arene to B-cyclodextrin-based hosts: an experimental and theoretical study on multivalent binding in solution and at self-assembled monolayers. *JACS* **2004**, *126*, 6627-6636.
54. D. Granadero; J. Bordello; M. J. Perez-Alvite, et al., Host-guest complexation studied by fluorescence correlation spectroscopy: adamantane-cyclodextrin inclusion. *Int J Mol Sci* **2010**, *11* (1), 173-818.
55. E. Cassette; M. Helle; L. Bezdetnaya, et al., Design of new quantum dot materials for deep tissue infrared imaging. *Adv Drug Deliv Rev* **2013**, *65* (5), 719-731.
56. W. Hudson; M. C. Collins; D. deFreitas, et al., Beating and arrested intramyocardial injections are associated with significant mechanical loss: implications for cardiac cell

- transplantation. *J Surg Res* **2007**, *142* (2), 263-267.
57. M. K. Danks; K. J. Yoon; R. A. Bush, et al., Tumor-targeted enzyme/prodrug therapy mediates long-term disease-free survival of mice bearing disseminated neuroblastoma. *Cancer Res* **2007**, *67* (1), 22-25.
58. A. Bunschoten; D. M. van Willigen; T. Buckle, et al., Tailoring fluorescent dyes to optimize a hybrid RGD-tracer. *Bioconjugate Chem.* **2016**, *27* (5), 1253-1258.
59. B. Bakhshinejad, Phage display and targeting peptides: surface functionalization of nanocarriers for delivery of small non-coding RNAs. *Front Genet* **2015**, *6*, 178.
60. R. F. Fakhrullin; A. I. Zamaleeva; R. T. Minullina, et al., Cyborg cells: functionalisation of living cells with polymers and nanomaterials. *Chem. Soc. Rev.* **2012**, *41* (11), 4189-41206.





SUPPORTING INFORMATION CHAPTER 2

**Obtaining control of cell surface
functionalizations via Pre-targeting and
Supramolecular host guest interactions**

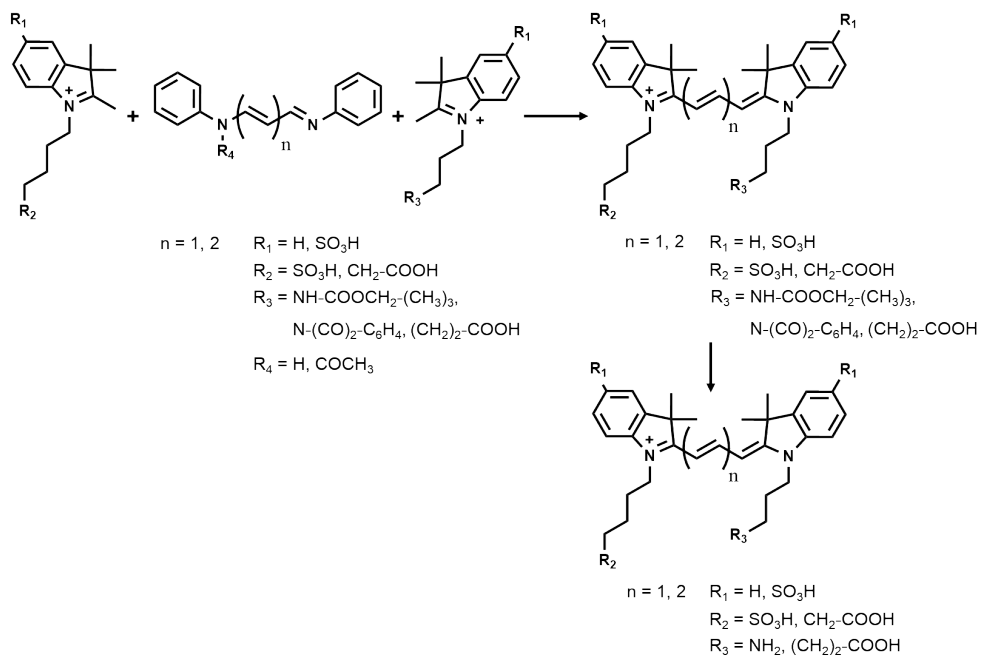


Figure S1. Synthesis of Cy5-(SO₃)Sulfonate-(SO₃)COOH (compound **8**) ($n = 1$, $R_1 = \text{SO}_3\text{H}$, $R_2 = \text{SO}_3\text{H}$, $R_3 = (\text{CH}_2)_2\text{-COOH}$), Cy5-(SO₃)Sulfonate-(SO₃)Amine (compound **9**), Cy5-Sulfonate-Amine (compound **10**) ($n = 1$, $R_1 = \text{H}$, $R_2 = \text{SO}_3\text{H}$, $R_3 = \text{NH}_2$), and Cy3-Amine-COOH (compound **11**) ($n = 0$, $R_1 = \text{H}$, $R_2 = \text{CH}_2\text{-COOH}$, $R_3 = \text{NH}_2$), ($n = 1$, $R_1 = \text{SO}_3\text{H}$, $R_2 = \text{SO}_3\text{H}$, $R_3 = \text{NH}_2$).

EXPERIMENTAL

General

All chemicals were obtained from commercial sources and used without further purification. ISOBAM-04 was kindly supplied by Kuraray Europe GmbH free of charge. NMR spectra were recorded using a Bruker DPX 300 spectrometer (300 MHz ^1H NMR) or a Bruker AVANCE III 500 MHz with a TXI gradient probe and are referenced to residual solvent signal or TMS. HPLC was performed on a Waters system by using a 1525EF pump and a 2489 UV detector. For the MTT assay the Perkin Elmer plate reader 1420 Multilabel Counter was applied. For preparative HPLC a Dr. Maisch GmbH, Reprosil-Pur 120 C18-AQ 10 μm (250 \times 20 mm) column was used and a gradient of 0.1 % TFA in $\text{H}_2\text{O}/\text{CH}_3\text{CN}$ (95:5) to 0.1 % TFA in $\text{H}_2\text{O}/\text{CH}_3\text{CN}$ (5:95) in 40 min was employed. For analytical HPLC a Dr. Maisch GmbH, Reprosil-Pur C18-AQ 5 μm (250 \times 4.6 mm) column was used and a gradient of 0.1 % TFA in $\text{H}_2\text{O}/\text{CH}_3\text{CN}$ (95:5) to 0.1 % TFA in $\text{H}_2\text{O}/\text{CH}_3\text{CN}$ (5:95) in 40 min was employed. MALDI-TOF measurements were performed on a Bruker Microflex. For dialysis Sigma Pur-A-Lyzer™ Mega 3500 tubes were used.

Synthesis of the cyanine-dye building blocks

Indole

The indole-based building blocks; Indole-Sulfonate, Indole-COOH, sulfoindole-Sulfonate and sulfoindole-COOH were synthesized according a previously reported procedure,^{1,2} while the indole-based building blocks; indole-Phth, Indole-AmineBoc, and sulfoindole-AmineBoc were synthesized according an adjusted synthesis method based on published procedure.^{2,3} The crude product of the Indole building blocks could be directly used in the next reaction step, except for sulfoindole-AmineBoc, which was purified first.

Indole-Phth

A mixture of 2,3,3-trimethylindolenine (504 μL , 3.1 mmol) and N-(3-Bromopropyl) phthalimide (843 mg, 3.1 mmol) in 5 mL MeCN was stirred for 4 h at 100 $^\circ\text{C}$, followed by 72 h at 60 $^\circ\text{C}$. The resulting red precipitate was collected, dissolved in acetone and precipitated in Et_2O . The suspension was filtrated and the residue was washed with Et_2O yielding the crude product as an orange solid (1.2 g)

Indole-AmineBoc

A solution of 2,3,3-trimethylindolenine (3.7 ml, 22.8 mmol) and tert-butyl-(3- bromopropyl) carbamate (5.4 g, 22.8 mmol) in 25 mL dry MeCN was stirred for 72 h at 60 $^\circ\text{C}$. The mixture was concentrated under vacuum, re-dissolved in a small amount of MeOH and precipitated in Et_2O while stirring. The precipitate was filtered off and washed with Et_2O until the filtrate was colorless, yielding the product as a pink solid (3.5 g).

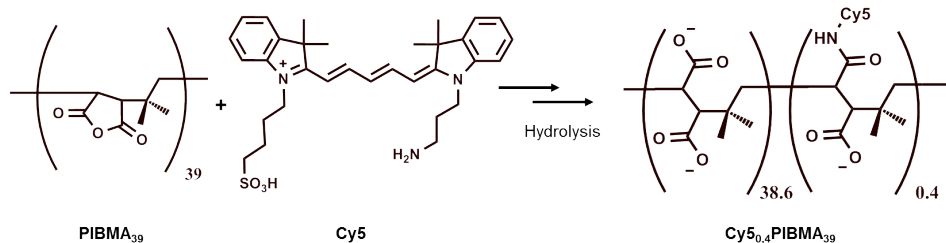


Figure S2. Conjugation of PIBMA₃₉ with Cy5-Sulfonate-Amine (10).

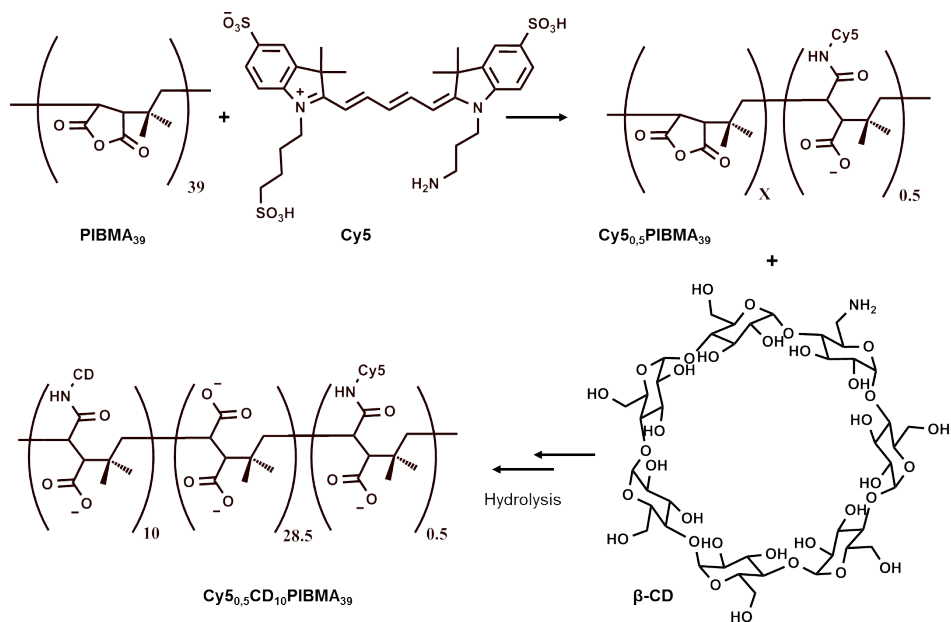


Figure S3. Conjugation of PIBMA₃₉ with Cy3-Amine-COOH (9) and subsequently with β -CD.

Sulfoindole-AmineBoc

A solution of 2,3,3-trimethyl-3H-indole-5-sulfonate potassium salt (1.1 g, 4 mmol) and 3-propylamine-HBr (0.87 g, 4 mmol) in 10 mL 1,2-dichlorobenzene was stirred for 30 min at 110 °C, followed by 10 min at 150 °C. The resulting purple precipitate was collected and dispersed in 15 mL MeOH. Di-tert-butylidicarbonate (1.7 g, 8 mmol) and DIPEA (1.4 mL, 8 mmol) were added and the reaction mixture was refluxed for 30 minutes. The mixture was concentrated in vacuo and purified by column chromatography (MeOH:CH₂Cl₂ 1:3), yielding the product as a pink solid (81 mg).

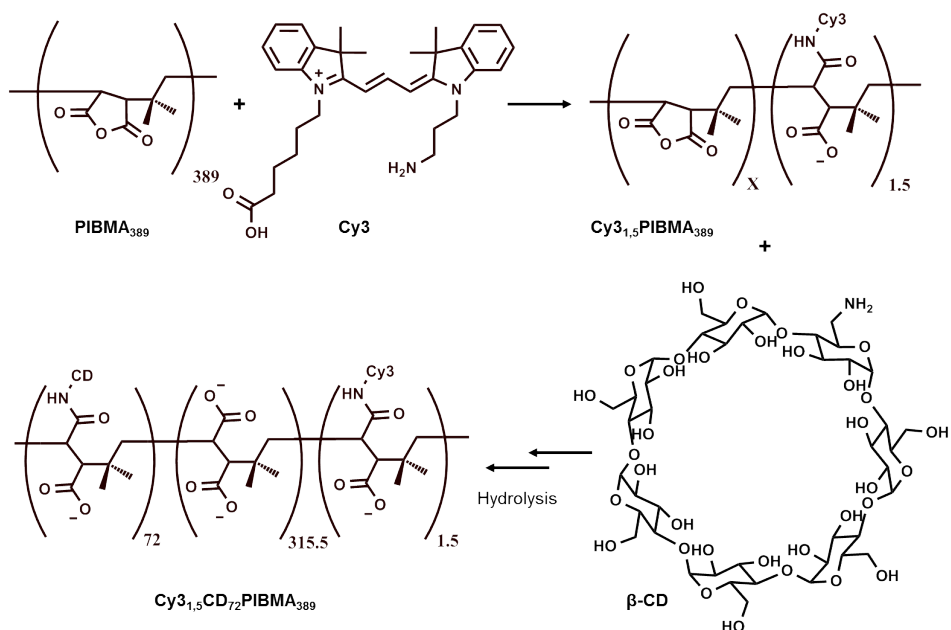


Figure S4. Conjugation of PIBMA₃₈₉ with Cy3-(Sulfonate-(SO₃)Amine (**11**) and subsequently with β-CD.

SYNTHESIS OF THE CYANINE-DYES

Cy5-(SO₃)Sulfonate-(SO₃)COOH (compound **8**)

Cy5-(SO₃)Sulfonate-(SO₃)COOH was synthesized according to a previously reported method.^{2,4}

MS (MALDI-TOF): [C₃₅H₄₅N₂O₁₁S₃]⁺ calcd 765.2, found 765.7. ¹H NMR spectrum as previously described.^{2,4}

Cy5-(SO₃)Sulfonate-(SO₃)Amine (compound **9**)

Sulfoindole-Sulfonate (41 mg, 0.1 mmol) and 3-anilinoacraldehyde anil hydrochloride (28 mg, 0.1 mmol) were dissolved in 4 mL HOAc:Ac₂O (1:1). After 30 minutes at 110 °C, the compound was precipitated in 50 mL diethyl ether. The obtained solid was dissolved in a mixture of 8 mL Ac₂O:Pyridine (1:1) and sulfoindole-AmineBoc (40 mg, 0.1 mmol) was added. After stirring at RT overnight, the product was concentrated under vacuo and purified by preparative HPLC. The product containing fraction was collected and lyophilized to give 5.0 mg (6.2 μmol) of Cy5-(SO₃)Sulfonate-(SO₃)AmineBoc. Subsequently, Cy5-(SO₃)

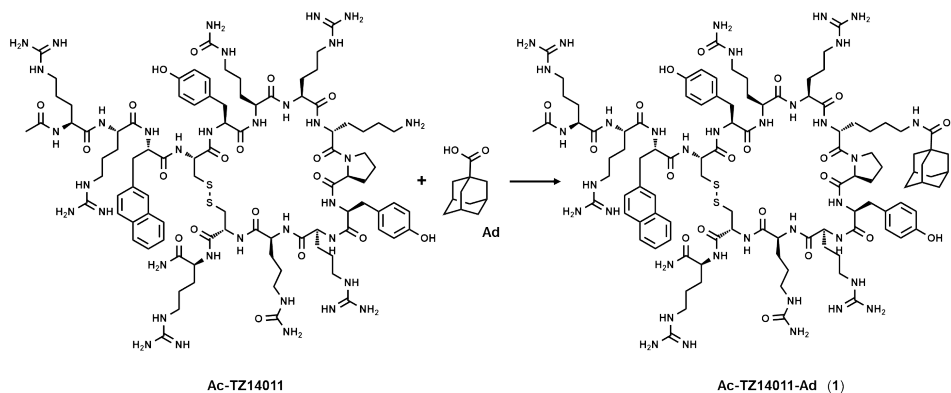


Figure S5. Conjugation of Ac-TZ14011 with 1-adamantanecarboxylic acid

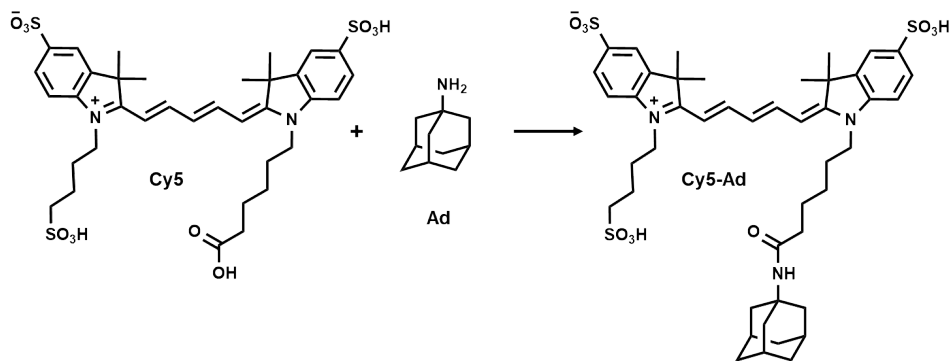


Figure S6. Conjugation of Cy5-(SO₃)Sulfonate-(SO₃)COOH (Cy5, **8**) with aminoadamantane (Ad).

Sulfonate-(SO₃)AmineBoc was deprotected by stirring in TFA:MeCN:CH₂Cl₂ 2:2:1 overnight at RT. After evaporation of the solvents, Cy5-(SO₃)Sulfonate-(SO₃)Amine was obtained as a dark blue powder (4.4 mg, 6.2 μmol, 6% yield)

MS (MALDI-TOF): [C₃₂H₄₂N₃O₉S₃]⁺ calcd 708.1, found 708.2. ¹H NMR (300 MHz, D₂O): 8.00 (m, 2H, CH), 7.83-7.74 (dd, 4H, Ar-H), 7.34 (d, 1H, Ar-H), 7.20 (d, 1H, Ar-H), 6.54 (t, 1H, CH), 6.34 (d, 1H, CH), 6.16 (d, 1H, CH), 4.09 (m, 4H, N-CH₂), 3.10 (t, 2H, CH₂-NH₂), 2.96 (t, 2H, CH₂-SO₃), 2.15- 1.91 (m, 6H, 3CH₂), 1.61 (d, 12H, C-(CH₃)₂) ppm.

Cy5-Sulfonate-Amine (compound **10**)

Indole-Sulfonate (100 mg, 0.34 mmol) and 3-anilinoacraldehyde anil hydrochloride (88

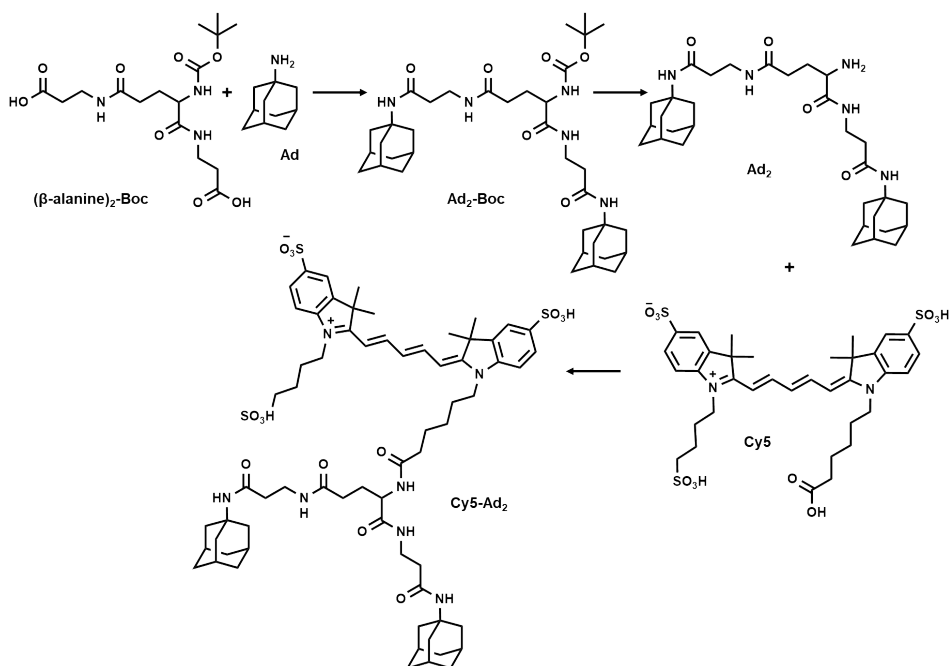


Figure S7. Synthesis of Cy5-Ad₂ (**7**) by conjugating Cy5-(SO₃)Sulfonate-(SO₃)COOH (Cy5, **8**) with bis-adamantane (Ad₂). The two Ad compounds are connected to each other via a previously synthesized β-alanine spacer.⁷

mm, 0.34 mmol) were dissolved in 10 mL HOAc:AC₂O (1:1). After 60 min stirring at 110 °C the mixture was cooled down and a solution of Indole-AmineBoc (161 mg, 0.51 mmol) in 10 mL pyridine was added. After stirring for 2 h at 140 °C, the blue solution was concentrated under vacuo and purified by column chromatography (MeOH:CH₂Cl₂ 1:10 to 1:1 gradient) and preparative HPLC. Product containing fractions were collected and lyophilized to yield a black solid. Subsequently, the obtained solid was dissolved in 30 mL DCM:TFA (1:1) and a few drops of H₂O were added. After 3 h stirring, the reaction mixture was concentrated under vacuo, redissolved in H₂O and lyophilized to yield the product as a blue powder (11.6 mg, 21 μmol, 4.2% yield)

MS (MALDI-TOF): [C₃₂H₄₂N₃O₃S]⁺ calcd 548.7, found 548.5. ¹H NMR (300 MHz, MeOD): 8.28 (m, 2H, CH), 7.53-7.23 (qt, 8H, Ar-H), 6.69 (t, 1H, CH), 6.47 (d, 1H, CH), 6.26 (d, 1H, CH), 4.18 (m, 4H, N-CH₂), 3.12 (t, 1H, CH₂-NH₂), 2.93 (t, 2H, CH₂-SO₃), 2.16-1.99 (m, 6H, 3CH₂), 1.73 (s, 12H, C-(CH₂)₂) ppm.

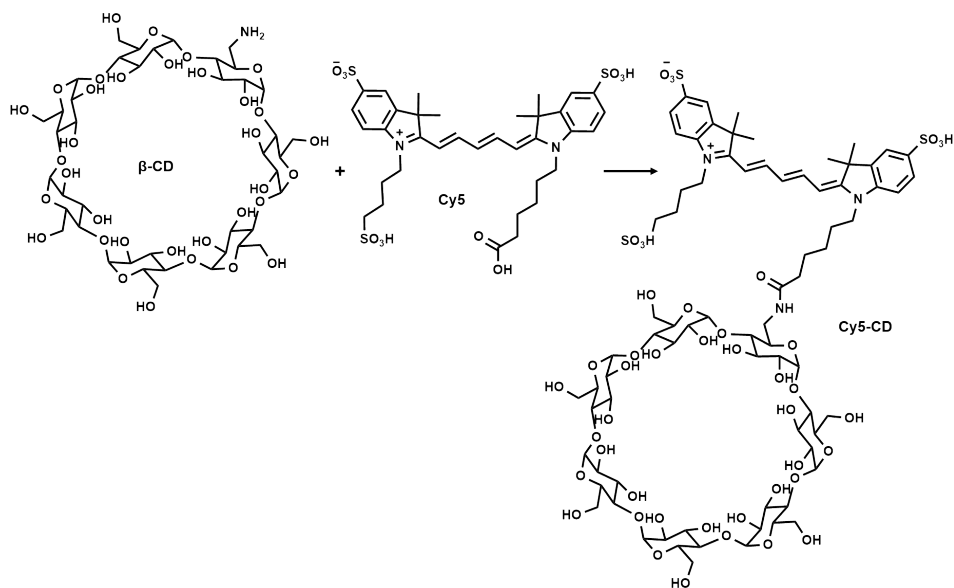


Figure S8. Conjugation of β -CD with Cy5-(SO_3^-)Sulfonate-(SO_3^-)COOH (Cy5, **8**).

Cy3-Amine-COOH (compound **11**)

Synthesis of Cy3-Amine-COOH was adapted from previously described asymmetric cyanine synthesis.⁵ N,N'-Diphenylformamidine (102 mg, 0.52 mmol) was dissolved in cold DCM (50 mL). DIPEA (181 μL , 1.04 mmol) and acetic anhydride (59 μL , 0.63 mmol) were added and the mixture was stirred for 2 h at room temperature. The mixture was concentrated under vacuum yielding a colorless oil. The oil was re-dissolved in 20 mL EtOH together with indole-COOH (127 mg, 0.46 mmol), indole-Phth (197 mg, 0.46 mmol) and pyridine (169 μL , 2.10 mmol). The solution was refluxed for 3 h and stirred overnight at 60 $^\circ\text{C}$. Acetic anhydride (60 μL) was added, and the reaction mixture turned pink. After refluxing for 4 h, the crude product was concentrated in vacuo and purified by column chromatography (eluents: MeOH). The product fractions were combined, concentrated and lyophilized to give a pink solid of impure compound Cy3-Phth-COOH. A portion of Cy3-Phth-COOH (100 mg, 0.16 mmol) was further purified by preparative HPLC. After lyophilization of the product fractions, Cy3-Phth-COOH was deprotected by adding 2 mL of CH_3NH_2 (33% in EtOH). The solution was stirred for 5 h, after which the reaction was concentrated in vacuo to give Cy3-Amine-COOH as a pink solid. Subsequently the compound was purified by preparative HPLC. Fraction containing product was collected and lyophilized and gave the pure product as a pink solid (4 mg, 7.99 μmol , 5% yield).

MS (MALDI-TOF): $[\text{C}_{32}\text{H}_{42}\text{N}_3\text{O}_2]^+$ calcd 500.3, found 499.3. ^1H NMR (500 MHz, DMSO- d_6): 8.36 (t, 1H, CH), 7.66 (d, 2H, Ar-H), 7.51 (d, 2H, Ar-H), 7.46 (t, 2H, Ar-H), 7.32 (q, Ar-H), 6.55 (d, CH), 6.46 (d, 1H, CH), 4.21 (m, 2H, N-CH₂), 4.12 (m, 2H, N-CH₂), 2.94 (m, 2H, CH₂-NH₂), 2.22 (t, 2H, CH₂-SO₃), 2.03 (m, 2H, CH₂), 1.74 (m, 2H, CH₂), 1.71 (d, 12H, C-(CH₃)₂), 1.56 (m, 2H, CH₂), 1.43 (m, 2H, CH₂) ppm.

Polymer synthesis

*Cy5*_{0.4}*PIBMA*₃₉ (compound **2**), *Cy5*_{0.5}*CD*₁₀*PIBMA*₃₉ (compound **3**), and *Cy3*_{1.5}*CD*₇₂*PIBMA*₃₈₉ (compound **4**)

For detailed description of the polymers synthesis, see main manuscript

Synthesis of Ad-functionalized compounds

Ac-TZ14011-Ad (compound **1**)

PyBOP (2.8 mg, 5.4 μmol), 1-adamantanecarboxylic acid (1.1 mg, 6 μmol) and DIPEA (5.1 μL , 30 μmol) were dissolved in 1 mL dry DMF and stirred for 5 minutes at RT. This was added to a solution of *Ac-TZ14011* (9.8 mg, 3.5 μmol), synthesized as previously described,⁶ in 1 mL dry DMF. The reaction mixture was stirred for 48 h at RT. Subsequently, 2.5 mL of 0.1% TFA (H₂O) was added to the reaction mixture to purify the reaction mixture directly by preparative HPLC. The product fraction was lyophilized to give the product as a white powder (8 mg, 2.7 μmol , 77% yield).

MS (MALDI-TOF): $[\text{C}_{103}\text{H}_{158}\text{N}_{35}\text{O}_{20}\text{S}_2]^+$ calcd 2270.7, found 2271.3. The analytical HPLC chromatogram is shown in Figure S9.

Cy5-Ad (compound **6**)

1-Aminoadamantane hydrochloride (7.5 mg, 40 μmol), *Cy5*-(SO₃)Sulfonate-(SO₃)COOH (**8**) (8.2 mg, 10 μmol) and PyBOP (31 mg, 60 μmol) were dissolved in 2 mL dry DMF. DIPEA (50 μL , 300 μmol) was added and the reaction was stirred overnight, in the dark, at RT. Solvents were evaporated in vacuo and the product was purified by preparative HPLC. The product containing fraction was lyophilized to give the product as a blue powder (5.4 mg, 5.7 μmol , 57 % yield).

MS (MALDI-TOF): $[\text{C}_{45}\text{H}_{60}\text{N}_3\text{O}_{10}\text{S}_3]^+$ calcd 898.3, found 898.9. ^1H -NMR (300 MHz, DMSO- d_6): 8.36 (t, 2H, CH), 7.80 (s, 2H, Ar-H), 7.61 (d, 2H, Ar-H), 7.31 (dd, 2H, Ar-H), 6.59 (t, 1H, CH), 6.34 (t, 2H, CH), 4.08 (m, 4H, N-CH₂), 2.03 – 1.95 (m, 6H, 3CH₂), 1.84 (s, 3H, 3CH), 1.80-1.69 (m, 2H, CH₂), 1.68 (s, 12H, C-(CH₃)₂), 1.56 (s, 6H, 3CH₂), 1.46 (m, 2H, CH₂), 1.23 (s, 6H, 3CH₂) ppm.

Cy5-Ad₂ (compound 7)

Cy5-Ad₂ was synthesized in multiple steps using standard peptide coupling chemistry. Boc-Glu-(β-Ala)₂ (101 mg, 0.26 mmol), synthesized as described before,⁸ PyBOP (676 mg, 1.3 mmol) and DIPEA (530 μL, 3 mmol) were dissolved in 5 mL dry DMF. After 5 min, adamantan-1-amine hydrochloride (244 mg, 1.3 mmol) was added and the mixture was stirred for 3 h at RT. The product was purified by column chromatography (CH₂Cl₂:MeOH 9:1) and the product containing fractions were collected and concentrated under vacuo. The obtained compound was dissolved in 4 mL TFA:DCM (1:4) and stirred overnight at RT. After evaporation of the solvents in vacuo, the obtained H-Glu-(β-Ala-Ad)₂ was dissolved in H₂O:MeCN and lyophilized to give the product as a white solid (111 mg, 0.17 mmol). Subsequently, H-Glu-(β-Ala-Ad)₂ (20 mg, 30 μmol) was dissolved in 2 mL dry DMF and Cy5-(SO₃)Sulfonate-(SO₃)COOH (**8**) (25 mg, 30 μmol), PyBOP (16 mg, 30 μmol) and DIPEA (17 μL, 100 μmol) were added. After stirring overnight at RT, 2 mL of 0.1 % TFA in H₂O was added to purify the product directly by preparative HPLC. The product containing fractions were collected and lyophilized to give Cy5-Ad₂ as a blue solid (9.0 mg, 6.9 μmol, 2.6 %).

MS (MALDI-TOF): [C₆₆H₉₂N₇O₁₄S₃]⁺ calcd 1303.7, found 1303.9. ¹H NMR (300 MHz, DMSO-D₆): 8.35 (t, 2H, CH), 7.80 (s, 4H, Ar-H), 7.60 (d, 2H, Ar-H), 7.33 (d, 2H, Ar-H), 6.58 (t, 1H, CH), 6.42 (d, 1H, CH), 6.31 (d, 1H, CH), 4.07 (m, 4H, N-CH₂), 3.36 - 3.15 (m, 5H, CH and 2CH₂, semi covered under solvent peak), 2.29-2.02 (m, 6H, 3CH₂), 2.01 - 1.19 (m, 10H, 5CH₂), 1.88 (s, 6H, 6CH), 1.80-1.69 (m, 4H, 2CH₂) 1.68 (s, 12H, C-(CH₂)₂), 1.57 (s, 12H, 6CH₂), 1.23 (s, 12H, 6CH₂) ppm.

Synthesis of Cy5-CD (compound 5)

Cy5-(SO₃)Sulfonate-(SO₃)COOH (**8**) (4.2 mg, 5 μmol), 6-monodeoxy-6-monoamino-β-cyclodextrin (5.9 mg, 5 μmol), and PyBOP (5.2 mg, 10 μmol) were dissolved in 1 mL dry DMSO. DIPEA (3.5 μL, 20 μmol) was added and the mixture was stirred overnight at RT. The products were precipitated in CH₂Cl₂ and purified by preparative HPLC. The product fraction was lyophilized to give a blue powder (5.2 mg, 2.7 μmol, 53%).

MS (MALDI-TOF): [C₇₇H₁₁₃N₃O₄₄S₃]⁺ calcd 1880.8, found 1882.0. ¹H NMR (300 MHz, D₂O): 8.03 (m, 2H, CH), 7.79-7.74 (m, 4H, Ar-H), 7.29 (t, 2H, Ar-H), 6.6-6.2 (m, 3H, CH), 4.97 (m, 7H, O-CH-O-CH of β-CD), 4.05 (m, 4H, N-CH₂), 3.90-3.49 (m, 42H, all other β-CD protons), 2.91 (t, 2H, CH₂-COOH), 2.17 (t, 2H, CH₂-SO₃), 2.0-1.0 (m, 10H, 5CH₂), 1.65 (s, 12H, C-(CH₂)₂) ppm.

Analysis of the CD-polymers

The grafting efficiency of β -CD and the fluorophores was determined by a combination of $^1\text{H-NMR}$ and UV/Vis absorption measurements. The grafting of the β -CD was determined by $^1\text{H-NMR}$, by integrating the polymer peaks at 1.38 - 1.00 ppm (both methyl and CH_2 moieties) and the β -CD peaks at 5.1 ppm (anomeric carbon CH) and 4.00 - 3.50 ppm (all other β -CD protons). The integral of the peaks corresponding to the polymer was then set at 8 (Supplementary Figure S10B). The obtained integral for the β -CD peaks at 5.1 ppm and 4.00 - 3.50 ppm were divided by 7 and 42 respectively (in theory, if one β -CD per subunit would have been present, their integrals would have been 7 and 42). The resulting ratio is the approximated percentage of β -CD per subunit. Both ratios obtained for the peak at 5.0 and 4.0 - 3.5 ppm were averaged and then multiplied by the number of subunits in the polymer.

To determine the number of fluorophores per polymer, first the fluorophore concentration of the sample was calculated by measuring the absorbance at 650 nm (Cy5) or at 550 nm (Cy3) and applying the Beer-Lambert law (equation (1)). Then the concentration of the fluorophore was correlated with the calculated concentration of the polymer, based on its estimated molecular weight.

$$A = l \cdot \varepsilon \cdot C \quad (\text{eq.1})$$

Where: A = absorbance, l = path length in cm, ε = absorption coefficient, C = Molar concentration

The molecular weight (MW) of the polymer was first estimated by adding together: the starting MW of the polymer (6,000 or 60,000 g/mol), the MW of β -CD (1133 g/mol) times the numbers of β -CD per polymer (0, 10, or 72), and the MW of H_2O (18 g/mol) times the number of carboxylates per polymer (78.0, 67.5, or 705.5). Then the number of fluorophores per polymer was calculated and the resulting number of fluorophore per polymer (0.4, 0.5, or 1.5) times the MW of the fluorophore was added to obtain the final MW of the polymers

The hydrodynamic radii of the polymers were determined using dynamic light scattering (DLS) and diffusion-ordered NMR spectroscopy (DOSY). Based on the diffusion constants, the hydrodynamic radii could be calculated using the Stokes-Einstein equation (Equation (2)).

$$D = \frac{k_B T}{6\pi\eta r} \quad (\text{eq. 2})$$

Where: D = diffusion constant, K_b = boltzmann's constant, T = absolute temperature, η = dynamic viscosity of the medium and r = radius of the particles /compound.

Cell culture

Human MDAMB231 cells, transfected with human CXCR4 conjugated GFP (MDAMB231 X4), were kindly provided by Dr. Gary Luker (Center for Molecular Imaging, University of Michigan, USA).⁵ Native MDAMB231 cells with basal CXCR4 expression were used as control.⁶ Cells were maintained in Dulbecco's minimum essential medium (DMEM) enriched with 10% fetal bovine serum and 5 mL Penicillin/Streptomycin (1,000 units/mL Penicillin; 1,000 $\mu\text{g}/\text{mL}$ Streptomycin) (all Life Technologies Inc.). Cell lines were cultured and maintained under standard conditions (37 °C and 5% CO_2).

Confocal microscopy

One day prior the experiment, cells were trypsinized, seeded onto culture dishes with glass insert ($\varnothing 35\text{mm}$ glass bottom dishes No. 15, poly-d-lysine coated, γ -Irradiated, MatTek corporation) and incubated overnight in 2 mL DMEM. After incubation of the compounds (see below for the conditions of each experiment), live cell images were taken on a Leica SP5 or SP8 WLL confocal microscope under 63x magnification. The intrinsic GFP signal in the MDAMB231 X4 cells was measured with excitation at 488 nm and emission was collected at 500-525 nm. Cy3 fluorescence was measured with excitation at 514 nm, emission was collected at 550-570 nm. Cy5 fluorescence was measured with excitation at 633 nm, emission was collected at 650-700 nm. Any Hoechst 33342 fluorescence was measured using 405 nm excitation and emission was collected at 420-470 nm. Images and signal quantifications were obtained using Leica Application Suite software, by applying the polygon function and calculating the average gray value/ m^2 for each cell. For quantifications; background signal (amount of grey value/ m^2 when no compounds are added) was subtracted from the fluorescence signal obtained for the samples.

Comparison of multivalent and monovalent functionalization

To study the differences in binding of multivalent- and monovalent β -CD compounds to **Ac- TZ14011-Ad** functionalized cells, adhering MDAMB231 X4 cells were functionalized with either **Cy5_{0.5}CD₁₀PIBMA₃₉**, **Cy5_{0.4}PIBMA₃₉**, or **Cy5-CD** (according described procedure; 'Functionalization of cells', see main manuscript), in such a way that the polymer concentration was 1 μM (**Cy5_{0.5}CD₁₀PIBMA₃₉** and **Cy5_{0.4}PIBMA₃₉**) and the β -CD concentration was 10 μM (**Cy5_{0.5}CD₁₀PIBMA₃₉** and **Cy5-CD**). After washing twice with PBS,

confocal images were taken. For quantification, for each condition of 25 cells the average grey value/m² was measured (Figure S14 and S15).

*Competition between **Cy5_{0.5}CD₁₀PIBMA₃₉** and **Cy3_{1.5}CD₇₂PIBMA₃₈₉** (monitored using microscopy)*

To compare the binding strength between **Cy5_{0.5}CD₁₀PIBMA₃₉** and **Cy3_{1.5}CD₇₂PIBMA₃₈₉** MDA231 X4 cells were functionalized with either **Cy5_{0.5}CD₁₀PIBMA₃₉** (10 μM final β-CD concentration), **Cy3_{1.5}CD₇₂PIBMA₃₈₉** (10 μM final β-CD concentration), or a mixture of **Cy5_{0.5}CD₁₀PIBMA₃₉** and **Cy3_{1.5}CD₇₂PIBMA₃₈₉** (20 μM final β-CD concentration; 10 μM each). After washing twice with PBS confocal images were taken of the different samples. To determine the degree of binding of the polymers under the different conditions the average grey value/m² was determined for 25 cells in the individual samples (Figure S17)

To follow the competition over time, adherent MDAMB231 X4 cells were functionalized with either **Cy5_{0.5}CD₁₀PIBMA₃₉** or **Cy3_{1.5}CD₇₂PIBMA₃₈₉** (10 μM final β-CD concentration). Subsequently, they were imaged at RT (without washing first) and either **Cy5_{0.5}CD₁₀PIBMA₃₉** or **Cy3_{1.5}CD₇₂PIBMA₃₈₉** (10 μM final β-CD concentration) was added. The change in fluorescence was followed for 18 minutes, while taking images each minute (Figure S18 and S19).

*Replacement between **Cy5_{0.4}PIBMA₃₉**, **Cy5_{0.5}CD₁₀PIBMA₃₉** and **Cy3_{1.5}CD₇₂PIBMA₃₈₉** (monitored using microscopy)*

The replacement between **Cy5_{0.5}CD₁₀PIBMA₃₉** and **Cy3_{1.5}CD₇₂PIBMA₃₈₉** was performed according the same procedure as described for the competition experiment followed over time. Only now the excess of binding polymer was washed away with PBS (2 x 1 mL) before imaging. As a control, a sample was included where only medium was added after washing away the excess of the first polymer. The change in fluorescence was followed for 18 minutes, while taking images each minute (Figures S18 and S19).

The replacement of the non-host containing **Cy5_{0.4}PIBMA₃₉** polymer by **Cy3_{1.5}CD₇₂PIBMA₃₈₉** and the reverse were performed according the same procedure as described above. The cells were incubated with **Cy5_{0.4}PIBMA₃₉** (1 μM polymer) or **Cy3_{1.5}CD₇₂PIBMA₃₈₉** (10 μM final β-CD concentration) and during imaging **Cy3_{1.5}CD₇₂PIBMA₃₈₉** (10 μM final β-CD concentration) or **Cy5_{0.4}PIBMA₃₉** (1 μM polymer) was added (Figures S18 and S19).

Functionalization of human stem cells

Human fetal heart stem cells, with CXCR4 expression, (17 weeks after gestation) were

grown in M199 -/- on gelatin-coated glass-bottom dishes (100,000 cells per dish). These cells were functionalized with **Ac-TZ14011-Ad** and **Cy3_{1,5}CD₇₂PIBMA₃₈₉** according described procedure (see ‘functionalization of cells’, main manuscript). Subsequently, they were carefully washed with colorless DMEM (2 x 1 mL) and analyzed by confocal microscopy (Figure S22).

Flow cytometry

MDAMB231 X4 cells were trypsinized (using 0.5% trypsin/EDTA, BD Biosciences) and counted. Hereafter cells were divided into aliquots (300,000 cells per tube), centrifuged for three minutes (3000 x g, 4 °C), and the supernatant was decanted. After incubation of the compounds (see experimental description for detailed conditions) flow cytometry measurements were performed on a BD FACS Canto™ II. Live cells were gated using forward scatter and side scatter, and 10,000 viable cells were analyzed for each sample. Cy5 fluorescence was measured on the APC channel and Cy5.5 fluorescence (for Ac-TZ14011-MSAP) was measured on the APC-Cy7 channel. For quantification; background signal (amount of fluorescence when no functionalizations were added) was subtracted from the fluorescence signal obtained for all samples.

*Determination of the receptor affinity of **Ac-TZ14011-Ad***

The affinity (KD) of **Ac-TZ14011-Ad** was calculated from flow cytometry measurements, using an earlier described procedure.⁸ In short: Different concentrations of Ac-TZ14011-Ad, ranging between 0.5 – 15,000 nM in 120 µL PBS, were added to MDAMB231 X4 cells in the presence of Ac-TZ14011-MSAP (250 nM), a compound with well-defined receptor affinity.⁸ After one hour of incubation on ice, the cells were washed two times with PBS (centrifuged 3 min, 3000 x g, 4 °C), and resuspended in 300 µL PBS. The fluorescence of the reference compound was measured as described in the flow cytometry section. All experiments were performed in duplicate (n = 2). The mean fluorescence was normalized and fitted with equations in the GraphPad Prism 6 software (Figure S11). The KD values were calculated using the “Binding-Competitive, One site-Fit Ki” nonlinear regression equation (Equation (3) and (4)), where the used KD value of Ac-TZ14011-MSAP (187 nM) has previously been reported.⁸

$$\log IC_{50} = \log \left(10^{\log KD} * \left(1 + \frac{[MSAP]}{[K_{D,MSAP}]} \right) \right) \quad (\text{eq.3})$$

$$y = \frac{1}{1 + 10^{x - \log IC_{50}}} \quad (\text{eq.4})$$

IC50 = concentration of the competitor that results in 50% binding, K_D = dissociation constant of the competitor in nM, [MSAP] = concentration of Ac-TZ14011-MSAP (250 nM), K_D , MSAP = dissociation constant of Ac-TZ14011-MSAP (187 nM), y = normalized fluorescence, x = concentration of peptide-Ad in nM.

*Competition between **Cy5_{0.5}CD₁₀PIBMA₃₉** and **Cy3_{1.5}CD₇₂PIBMA₃₈₉** (monitored using flow cytometry)*

To analyze the degree of binding of **Cy5_{0.5}CD₁₀PIBMA₃₉** to **Ac-TZ14011-Ad** functionalized MDA231 X4 cells in the presence of a competitor or DMEM, MDAMB231 X4 cells were trypsinized and divided into aliquots (300,000 cells per tube). The aliquots were centrifuged for four minutes (3000 x g, 4 °C), the supernatant was decanted and the cells were resuspended in 50 μ L **Ac-TZ14011-Ad** (10 μ M) in DMEM. After 1 h incubation at 0 °C the cells were centrifuged again for four minutes (3000 x g, 4 °C), the supernatant was decanted and 100 μ L of either **Cy5_{0.5}CD₁₀PIBMA₃₉** (10 μ M β -CD) or a mixture of **Cy5_{0.5}CD₁₀PIBMA₃₉** and **Cy3_{1.5}CD₇₂PIBMA₃₈₉** (each 10 μ M β -CD) in DMEM was added. Another hour at 0 °C followed. The cells were then washed twice with PBS (centrifuged 3 min, 3000 x g, 4 °C), resuspended in 150 μ L PBS and the intensity of Cy5 fluorescence related to the cells was measured by flow cytometry. Due to presence of GFP, the intensity of Cy3 fluorescence could not be monitored. This experiment was performed in two-fold (Figure S17).

Replacement between **Cy5_{0.5}CD₁₀PIBMA₃₉ and **Cy3_{1.5}CD₇₂PIBMA₃₈₉** quantified by radioactivity**

Radiolabeling of **Cy5_{0.5}CD₁₀PIBMA₃₉** and **Cy3_{1.5}CD₇₂PIBMA₃₈₉** with technetium-99m was performed as follows: **Cy5_{0.5}CD₁₀PIBMA₃₉** (75 μ L, 43.8 nmol β -CD) or **Cy3_{1.5}CD₇₂PIBMA₃₈₉** (75 μ L, 38 nmol β -CD), was mixed with SnCl₂·2H₂O (4 μ L of 1 mg/mL saline solution, 17.7 nmol, Technescan PYP Kit, Mallinckrodt Medical B.V., Petten, The Netherlands) and freshly eluted ^{99m}Tc-Na-pertechnetate (200 μ L, Technekow, Mallinckrodt Medical B.V.) and gently stirred for 1 h at RT. Thereafter, the reaction mixture was purified from free ^{99m}Tc by size exclusion chromatography using sterile PBS as mobile phase on Sephadex™ G-25 desalting columns (PD-10, GE Healthcare Europe GmbH, Freiburg, Germany). Fractions containing radiolabeled **Cy5_{0.5}CD₁₀PIBMA₃₉** (^{99m}Tc-Cy5_{0.5}CD₁₀PIBMA₃₉) or **Cy3_{1.5}CD₇₂PIBMA₃₈₉** (^{99m}Tc-Cy3_{1.5}CD₇₂PIBMA₃₈₉) were collected and directly applied in the assembly studies at a final concentration of 13 μ M β -CD).

MDAMB231 X4 cells were harvested, counted and diluted to 80,000 cells/mL using DMEM. Of this solution, 200 μ L (16,000 cells) fractions were transferred to polystyrene

tube (FACS) and the cells were cooled on ice for 15 minutes. Subsequently, **Ac-Tz14011-Ad** (100 μ L, 11 μ M) was added and another incubation of 15 minutes followed. Thereafter, the mixture was centrifuged (5 min, 1250 \times g, 4 $^{\circ}$ C) and the supernatant was aspirated. The cells were resuspended in 200 μ L DMEM and either $^{99m}\text{Tc-Cy5}_{0.5}\text{CD}_{10}\text{PIBMA}_{39'}$, $^{99m}\text{Tc-Cy3}_{1.5}\text{CD}_{72}\text{PIBMA}_{389'}$, $\text{Cy5}_{0.5}\text{CD}_{10}\text{PIBMA}_{39'}$ or $\text{Cy3}_{1.5}\text{CD}_{72}\text{PIBMA}_{389}$ (100 μ L, 13 μ M β -CD) was added, and incubation followed for 15 min at 0 $^{\circ}$ C. Thereafter, the mixture was centrifuged as described before. After aspiration of the supernatant and suspension of the cells in 200 μ L DMEM, either $\text{Cy5}_{0.5}\text{CD}_{10}\text{PIBMA}_{39'}$, $\text{Cy3}_{1.5}\text{CD}_{72}\text{PIBMA}_{389}$, $^{99m}\text{Tc-Cy5}_{0.5}\text{CD}_{10}\text{PIBMA}_{39'}$ or $^{99m}\text{Tc-Cy3}_{1.5}\text{CD}_{72}\text{PIBMA}_{389}$ (100 μ L, 13 μ M β -CD) was added and the samples were shortly vortexed. To challenge the strength of the binding of the fluorescent β -CD polymers to MDAMB231 X4 cells, incubation of 1 h at 0 $^{\circ}$ C followed. After centrifugation of the cells and aspiration of the supernatant both were counted for radioactivity in a dose-calibrator or gamma counter to assess the amount of cellular-bound $^{99m}\text{Tc-Cy}_n\text{-CD}_x\text{-PIBMA}_y$ activity. Data was expressed as the mean % (\pm SD, n = 6) of the total amount of $^{99m}\text{Tc-Cy}_n\text{-CD}_x\text{-PIBMA}_y$ activity added to the cells (Figure S16).

Cell viability assay

To determine the effect of polymer functionalization on the cell viability, after cell functionalization a MTT test was performed according to a described procedure.^{9,10} MDAMB231 X4 cells (16,000 cells per tube) in 200 μ L DMEM were cooled on ice for 15 minutes. **Ac-Tz14011-Ad** (100 μ L, 10 μ M) was added and incubation of 15 minutes followed. Thereafter, the mixture was centrifuged (5 min, 1250 \times g, 4 $^{\circ}$ C) and the supernatant was aspirated. The cells were resuspended in 200 μ L DMEM and variable concentrations of either $\text{Cy5}_{0.5}\text{CD}_{10}\text{PIBMA}_{39}$ or $\text{Cy3}_{1.5}\text{CD}_{72}\text{PIBMA}_{389}$ (100 μ L, 0-16 μ M final β -CD concentration) were added. After 15 min incubation on ice, the cells were washed twice with PBS (centrifuged 5 min, 1250 \times g, 4 $^{\circ}$ C), resuspended in 400 μ L DMEM (16,000 cells per tube) and transferred in 200 μ L duplicates to a 96-wells plate (CellStar®, Greiner Bio-One, Alphen a/d Rijn, The Netherlands) with 8,000 cells per well. After 24 h incubation at 37 $^{\circ}$ C, 20 μ L (0.1 mg) of a MTT (3-(4,5-dimethylthiazol-2-yl)-2,5-diphenyltetrazolium bromide) solution in PBS (5 mg/mL) was added to each well, followed by gently shaking the plate and then by incubation for 4 h at 37 $^{\circ}$ C. Thereafter, cells were optically checked under a light microscope to determine the uptake and colouring of MTT. The medium was carefully removed and 100 μ L of DMSO was added to each well to extract the insoluble formazan product from the cells. After 10-15 minutes at 37 $^{\circ}$ C, the uptake of MTT in each well was determined by measuring the absorbance at 545 nm. Measurements were normalized to

those of untreated cells which were kept on ice during the entire procedure of polymer functionalization (Figure S13)

RESULTS AND DISCUSSION

Synthesis of Cy5-CD, Cy5-Ad and Cy5-Ad₂

To compare cell functionalization with multivalent β -CD groups (**Cy5_{0.5}CD₁₀PIBMA₃₉**, **Cy3_{1.5}CD₇₂PIBMA₃₈₉**) to monovalent β -CD, a Cy5 fluorophore was conjugated to β -CD via amide bond formation to give **Cy5-CD** (52% yield). By the same synthesis strategy **Cy5-Ad** was synthesized (57% yield), as mode to investigate if polymer coated cells could further be functionalized via de CD-Ad host-guest interaction. To strengthen this interaction also a **Cy5-Ad₂** was synthesized (2.6% yield). Both Ad molecules were connected to the Cy5 and each other via a short spacer consisting of 2 beta alanines,⁷ again functionalization could be established via multiple amide bond formations.

Functionalization: mono vs multivalent β -CD hosts

Comparing the fluorescence signal intensities after functionalization with **Cy5-CD** (monovalent host) or **Cy5_{0.5}CD₁₀PIBMA₃₉** (multivalent host), reveals substantial more binding to Ad functionalized cell surfaces by **Cy5_{0.5}CD₁₀PIBMA₃₉** (Figure S14 and S15). As a control the same functionalization was also performed with **Cy5_{0.4}PIBMA₃₉** (Figure S7). While **Cy5_{0.4}PIBMA₃₉** binds slightly more to the cell surface compared to **Cy5-CD**, it are the multiple CD groups on **Cy5_{0.5}CD₁₀PIBMA₃₉** that considerably increases the amount of binding.

Radiolabeling of the polymers

Cy5_{0.5}CD₁₀PIBMA₃₉ and **Cy3_{1.5}CD₇₂PIBMA₃₈₉** were radiolabeled with technetium-99m according to a modification of a previously described labeling technique (described above).¹¹ We propose that the carboxylates, formed after hydrolysis, and possibly also the side chains of β -CD could function as chelate for the technetium-99m ions after reduction with SnCl₂. Since no significant release of radioactivity from the polymer was observed until 24 hours after radiolabeling, the interaction was stable under the *in vitro* conditions here applied.

Exchange and competition between CD_nPIBMA_m polymers

To monitor the strength and reversibility of the PIBMA surface modifications, exchange experiments were performed between radiolabeled and non-radiolabeled CD_nPIBMA_m polymers. After functionalizing MDAMB231 X4 cells with either ^{99m}Tc-Cy5_{0.5}CD₁₀PIBMA₃₉

or ^{99m}Tc -**Cy3**_{1.5}**CD**₇₂**PIBMA**₃₈₉, both polymers remained attached to the cell membrane for at least 1 hour in PBS. However, the use of either **Cy5**_{0.5}**CD**₁₀**PIBMA**₃₉ or **Cy3**_{1.5}**CD**₇₂**PIBMA**₃₈₉ as competitor resulted in a decrease in signal (Figure S16A and C). Binding of the competitors was confirmed when the experiment was performed with non-radioactive **Cy5**_{0.5}**CD**₁₀**PIBMA**₃₉ or **Cy3**_{1.5}**CD**₇₂**PIBMA**₃₈₉ functionalized MDAMB231 X4 cells and using ^{99m}Tc -labeled competitors, indicating an exchange between the two polymers (Figure S16B and D).

The polymer exchange was visually confirmed using confocal microscopy experiments performed over time (0 – 18 min), at the same β -CD concentrations (Figure S18B and S19B). Figure S18B shows a decrease in **Cy5**_{0.5}**CD**₁₀**PIBMA**₃₉ signal, while at the same time the **Cy3**_{1.5}**CD**₇₂**PIBMA**₃₈₉ signal increases, indicating an exchange between the two polymers. In these images the signal of **Cy5**_{0.5}**CD**₁₀**PIBMA**₃₉ is nearly gone after 18 minutes. In the absence of **Cy3**_{1.5}**CD**₇₂**PIBMA**₃₈₉, this decrease in **Cy5**_{0.5}**CD**₁₀**PIBMA**₃₉ was not observed (Figure S18A). This confocal experiment was repeated, using **Cy5**_{0.4}**PIBMA**₃₉ (Figure S18D). The signal of **Cy5**_{0.4}**PIBMA**₃₉ did not decrease over time, indicating a clear difference of interaction compared to **Cy5**_{0.5}**CD**₁₀**PIBMA**₃₉ (with CD-moieties). In the presence of **Cy5**_{0.4}**PIBMA**₃₉ the signal of **Cy3**_{1.5}**CD**₇₂**PIBMA**₃₈₉ still increased over time, although it was less intense (Figure S18D). To validate these findings the experiment was also performed in reversed order (**Cy3**_{1.5}**CD**₇₂**PIBMA**₃₈₉ as initial binder and **Cy5**_{0.4}**PIBMA**₃₉ as competitor (Figure S19D)). Here initial non-specific binding of **Cy5**_{0.4}**PIBMA**₃₉ occurred, but no further increase in binding could be observed over time. The **Cy3**_{1.5}**CD**₇₂**PIBMA**₃₈₉ signal only showed a drop following initial non-specific **Cy5**_{0.4}**PIBMA**₃₉ binding. When the cells are only washed and no Cy5 polymer is added, no such decrease in Cy3 signal was observed (Figure S19A). These results suggest that **Cy5**_{0.4}**PIBMA**₃₉ binds on a different location and via a different type of interaction than **Cy3**_{1.5}**CD**₇₂**PIBMA**₃₈₉ (non-specific vs. specific host-guest). These same results also indicate that the non-specific binding of **Cy5**_{0.4}**PIBMA**₃₉ hinders **Cy3**_{1.5}**CD**₇₂**PIBMA**₃₈₉ via electrostatic repulsion, thereby influencing the binding equilibrium.

To further explore the difference in affinity of the two CD-polymers for Ad functionalized cell surfaces, competition experiments were performed. **Ac-TZ14011-Ad** functionalized MDAMB231 X4 cells were incubated with a mixture of both polymers at equal β -CD concentration. This resulted in more **Cy3**_{1.5}**CD**₇₂**PIBMA**₃₈₉ bound to the cell surface than **Cy5**_{0.5}**CD**₁₀**PIBMA**₃₉ (Figure S17). According to these results **Cy3**_{1.5}**CD**₇₂**PIBMA**₃₈₉ seems to have higher affinity for **Ac-TZ14011-Ad** functionalized MDAMB231 X4 cells than **Cy5**_{0.5}**CD**₁₀**PIBMA**₃₉. Exchange was also attempted following functionalization, in the

presence of an excess of the initial binder revealed that **Cy5_{0.5}CD₁₀PIBMA₃₉** can partly be competed off the surface by **Cy3_{1.5}CD₇₂PIBMA₃₈₉** (Figure S18C), while **Cy3_{1.5}CD₇₂PIBMA₃₈₉** cannot visibly be replaced by **Cy5_{0.5}CD₁₀PIBMA₃₉** (Figure S19C). This data provides a further indication that **Cy3_{1.5}CD₇₂PIBMA₃₈₉** is the better binder of the two.

Combined, these data suggest that the polymer functionalization is stable when no competition occurs, but is reversible under competitive conditions. Furthermore, the data confirms that there is a different mode of action for polymers that contain β -CD vs. those that don't.

Table S1. Determined parameters of the synthesized polymers

| | MW start (kDa) | Repeating units | CD/polymer | Carboxylates/olymer | Dye/polymer | MW final (kDa) | \emptyset (DLS) (nm) | \emptyset (DOSY) (nm) |
|--|----------------|-----------------|------------|---------------------|-------------|----------------|------------------------|-------------------------|
| Cy5 _{0.4} PIBMA ₃₉ | 6 | 39 | 0 | 78 | 0.4 Cy5 | 7.8 | a | 2.7 |
| Cy5 _{0.5} CD ₁₀ PIBMA ₃₉ | 6 | 39 | 10 | 67.5 | 0.5 Cy5 | 18.8 | a | 2.8 |
| Cy3 _{1.5} CD ₇₂ PIBMA ₃₈₉ | 60 | 389 | 72 | 704.5 | 1.5 Cy3 | 155.0 | 18.4 | 11.7 |

^a Values could not be determined due to Cy5 influence.

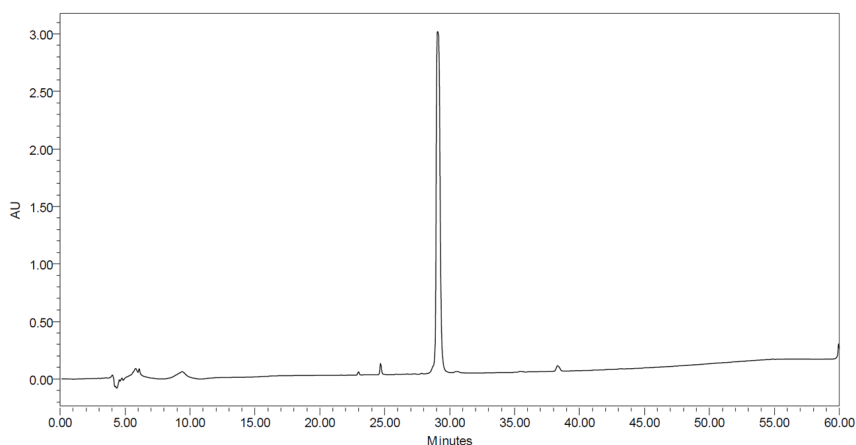


Figure S9. Analytical HPLC of **Ac-TZ14011-Ad**

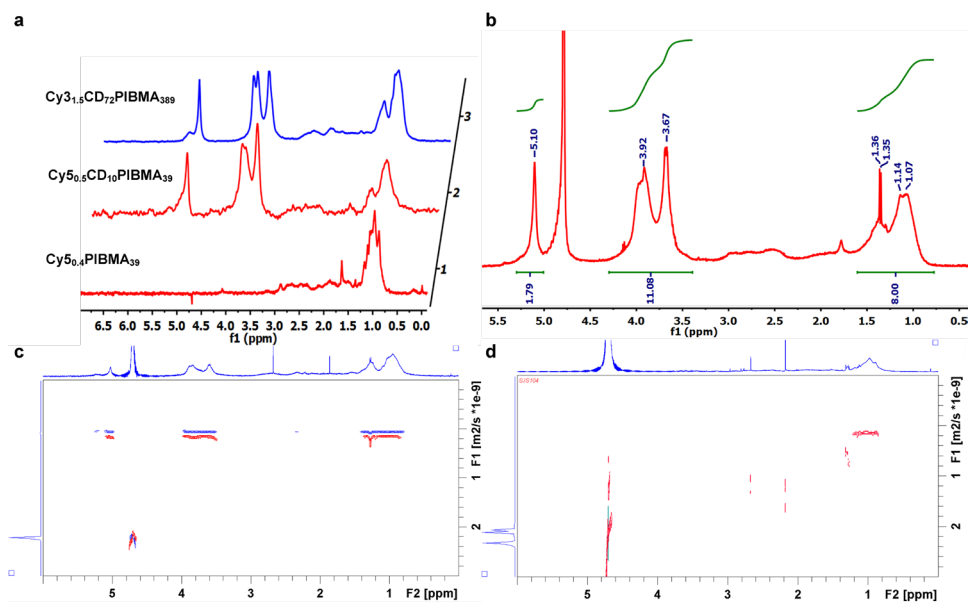


Figure S10. **a)** Diffusion-filtered NMR spectra of $\text{Cy}_{3_{1.5}}\text{CD}_{72}\text{PIBMA}_{389}$, $\text{Cy}_{5_{0.5}}\text{CD}_{10}\text{PIBMA}_{39}$ and $\text{Cy}_{5_{0.4}}\text{PIBMA}_{39}$. Represented in red the Cy5 polymers and in blue the Cy3. **b)** 1H-NMR spectrum of $\text{Cy}_{5_{0.5}}\text{CD}_{10}\text{PIBMA}_{39}$ showing integration of the β -CD peaks at 5.1 ppm (anomeric carbon CH) and at 3.92 - 3.67 ppm (all other β -CD protons), and the polymer peaks at 1.36 - 1.07 ppm (both methyl and CH₂ moieties). The later integral was set at 8 to calculate the β -CD per polymer ratio by dividing the integrals at 5.1 and 3.92 - 3.67 ppm by 7 and 42 respectively (see 'analysis of the polymers'). **c)** DOSY spectra of $\text{Cy}_{5_{0.5}}\text{CD}_{10}\text{PIBMA}_{39}$ (red) and $\text{Cy}_{3_{1.5}}\text{CD}_{72}\text{PIBMA}_{389}$ (blue). Vertical axis shows diffusion coefficient, with the largest molecules appearing at the top of the graph. **d)** DOSY spectrum of $\text{Cy}_{5_{0.4}}\text{PIBMA}_{39}$.

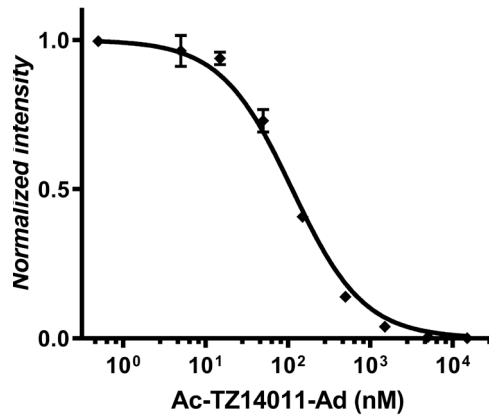


Figure S11. Competition assay curve of **Ac-TZ14011-MSAP** with **Ac-TZ14011-Ad**, acquired by flow cytometry, to determine binding constant (K_D).

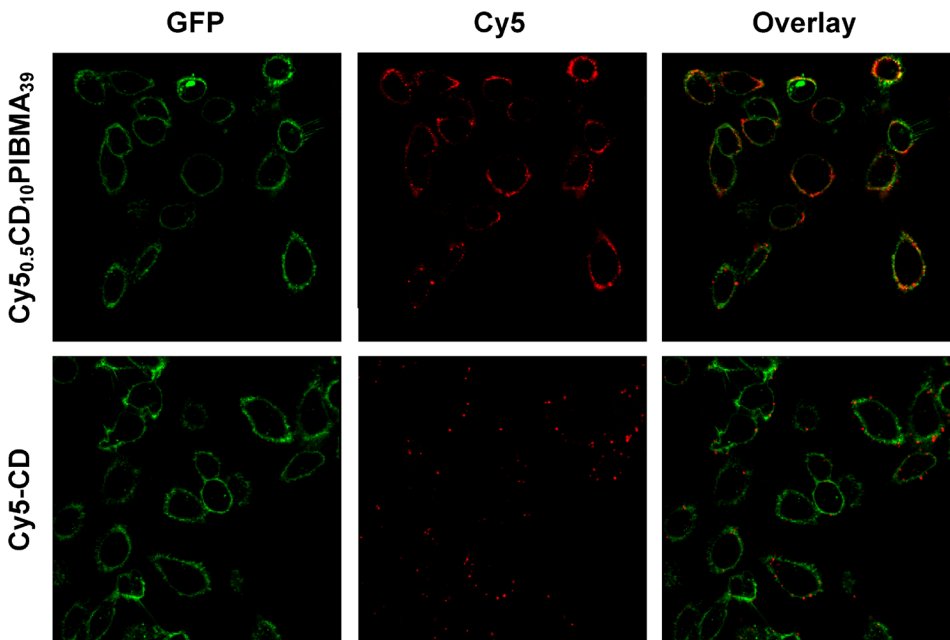


Figure S12. Viable CXCR4 overexpressing MDAMB231 X4 cells (with GFP-Tag) functionalized with either **Cy5_{0.5}CD₁₀PIBMA₃₉** or **Cy3_{1.5}CD₇₂PIBMA₃₈₉**. The CXCR4 receptor was first targeted with **Ac-TZ14011-Ad**, followed by functionalization with fluorescent **Cy5_{0.5}CD₁₀PIBMA₃₉** or **Cy3_{1.5}CD₇₂PIBMA₃₈₉** via the host-guest interaction between the β -CD molecules and the Ad functionality. For clarity, both the (overlay) image and the same image at the individual channels are displayed, with GFP in green, Cy5 (**Cy5_{0.5}CD₁₀PIBMA₃₉**) in red, and Cy3 (**Cy3_{1.5}CD₇₂PIBMA₃₈₉**) in blue.

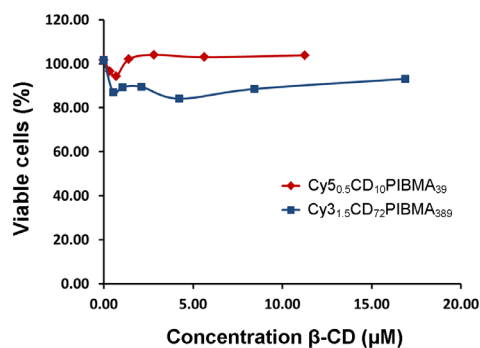


Figure S13. Viability of MDAMB231 X4 cells measured 24 h after functionalization with either $Cy5_{0.5}CD_{10}PIBMA_{39}$ (red) or $Cy3_{1.5}CD_{72}PIBMA_{389}$ (blue) at variable polymer concentrations (0 – 16 μ M).

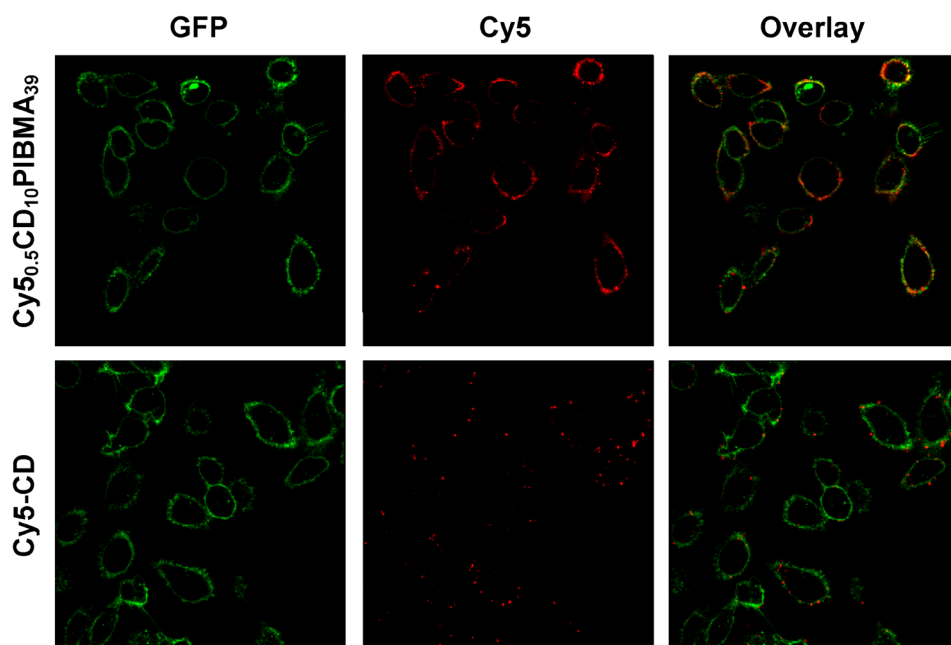


Figure S14. Comparison of multivalent and monovalent functionalization of viable cell surfaces. MDAMB231 X4 cells incubated with **Ac-TZ14011-Ad**, and subsequently with $Cy5_{0.5}CD_{10}PIBMA_{39}$ or **Cy5-CD**. For clarity, both the (overlay) image and the same image at the individual channels are displayed, with GFP in green and Cy5 in red.

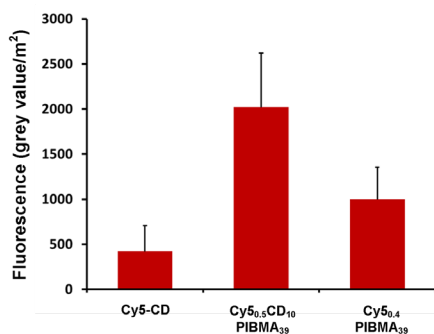


Figure S15. Comparison in binding of **Cy5-CD** (monovalent host), **Cy5_{0.5}CD₁₀PIBMA₃₉** (multivalent host), and **Cy5_{0.4}PIBMA₃₉** (no host) to **Ac-TZ14011-Ad** functionalized MDAMB231 X4 cells. The degree of binding was quantified by confocal microscopy, the graph shows the normalized data with the error bars indicating the standard deviation (25 cells analyzed for each condition).

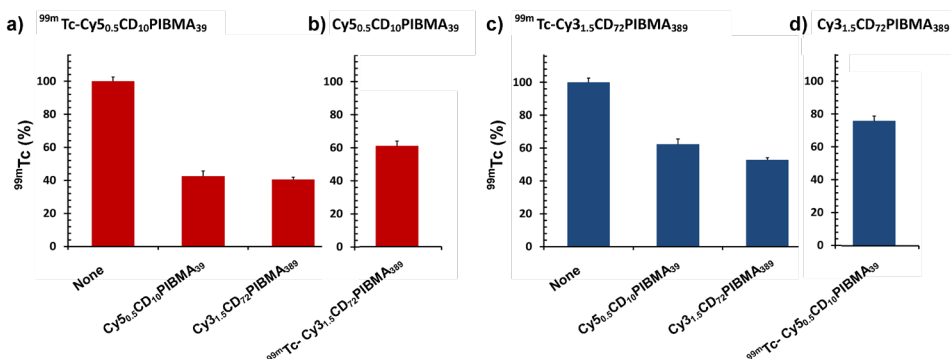


Figure S16. Exchange experiments between radiolabeled and non-radiolabeled CD_nPIBMA_m polymers on MDAMB231 cells, monitored by radioactivity after 1 h of incubation with the competitor (**a-d**). **a - b**) MDAMB231 X4 cells functionalized with **Cy5_{0.5}CD₁₀PIBMA₃₉**, either radiolabeled (**a**) or non-radiolabeled (**b**). **c - d**) MDAMB231 X4 cells functionalized with radiolabeled **Cy3_{1.5}CD₇₂PIBMA₃₈₉** (**c**) or non-radiolabeled **Cy3_{1.5}CD₇₂PIBMA₃₈₉** (**d**). As competitor, **Cy5_{0.5}CD₁₀PIBMA₃₉** or **Cy3_{1.5}CD₇₂PIBMA₃₈₉** were added to the cells functionalized with ^{99m}Tc-CD_nPIBMA_m polymers (**a** and **c**), showing partial replacement of the original polymer. In **b** and **d**, ^{99m}Tc-**Cy5_{0.5}CD₁₀PIBMA₃₉** or ^{99m}Tc-**Cy3_{1.5}CD₇₂PIBMA₃₈₉** were added as competitor to cells functionalized with non-radioactive CD_nPIBMA_m polymers, showing binding of the competitor.

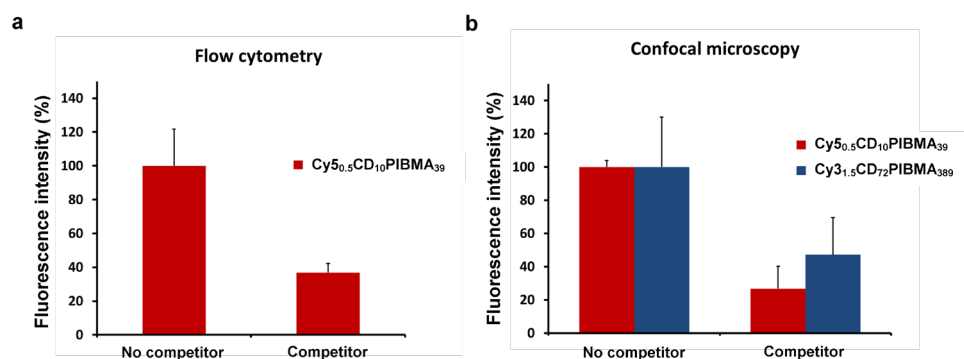
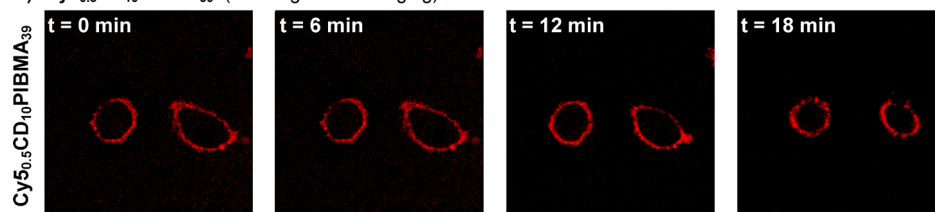
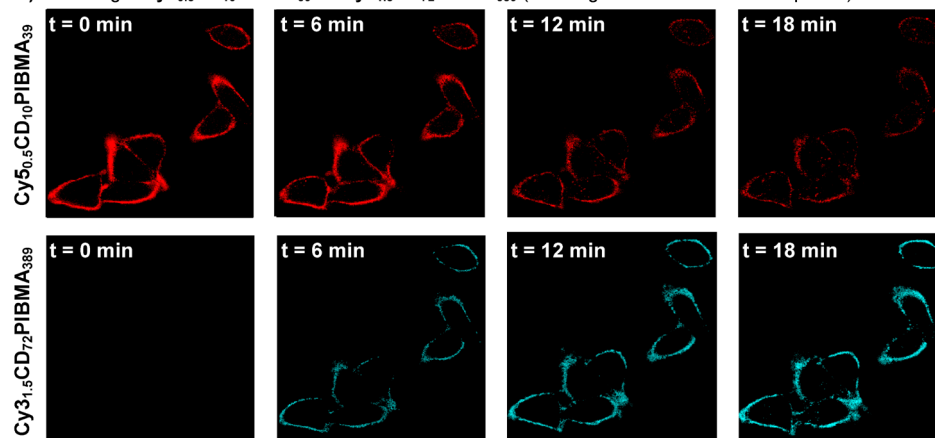


Figure S17. Fluorescence intensities obtained after incubation of **Ac-TZ14011-Ad** functionalized MDAMB231 X4 cells with a mixture of **Cy5_{0.5}CD₁₀PIBMA₃₉** and **Cy3_{1.5}CD₇₂PIBMA₃₈₉** (equal β -CD concentration). **a)** Fluorescence intensity of **Cy5_{0.5}CD₁₀PIBMA₃₉** measured by flow cytometry, showing the reduction in **Cy5_{0.5}CD₁₀PIBMA₃₉** binding when **Cy3_{1.5}CD₇₂PIBMA₃₈₉** was present during incubation. **b)** Fluorescence intensity of **Cy5_{0.5}CD₁₀PIBMA₃₉** and **Cy3_{1.5}CD₇₂PIBMA₃₈₉** measured by confocal microscopy, showing the reduction in **Cy5_{0.5}CD₁₀PIBMA₃₉** (in red) and **Cy3_{1.5}CD₇₂PIBMA₃₈₉** binding (in blue) when both polymers are present during incubation. **Cy3_{1.5}CD₇₂PIBMA₃₈₉** binds stronger as the binding of **Cy5_{0.5}CD₁₀PIBMA₃₉** is more reduced. The error bars indicate the standard deviation ($n = 2$).

a) Cy5_{0.5}CD₁₀PIBMA₃₉ (washing before imaging)



b) Exchange: Cy5_{0.5}CD₁₀PIBMA₃₉ vs **Cy3_{1.5}CD₇₂PIBMA₃₈₉** (washing before addition of competitor)



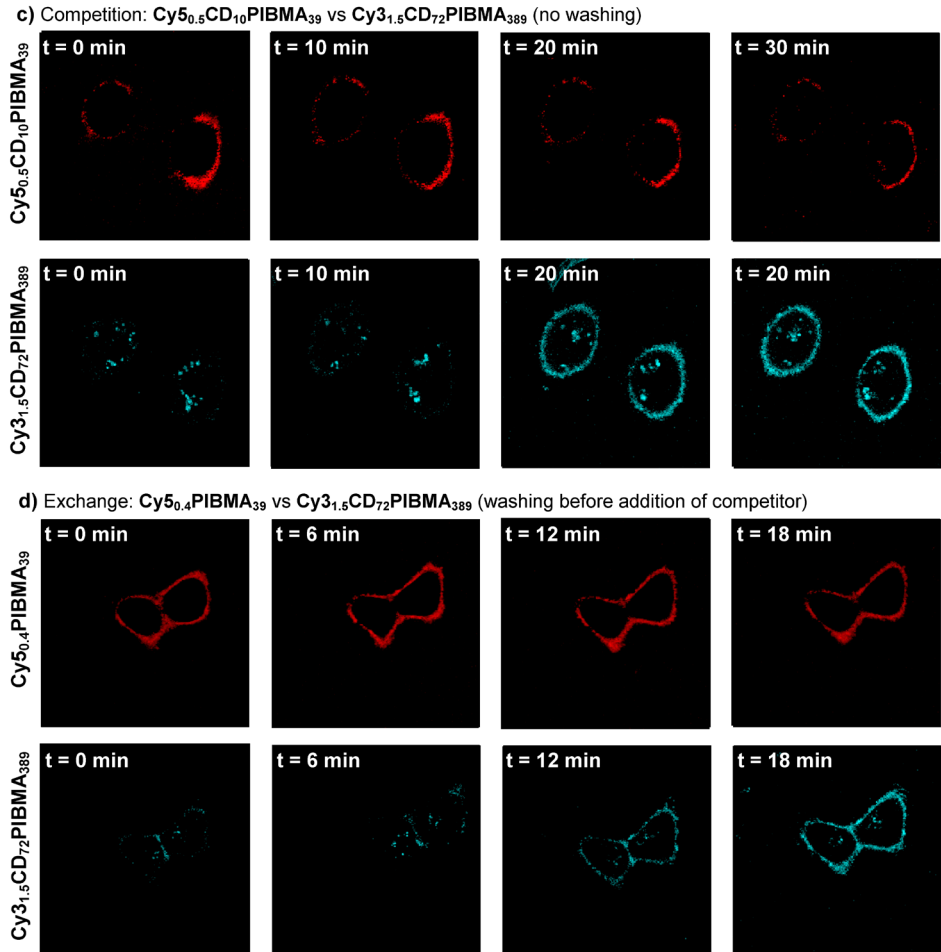
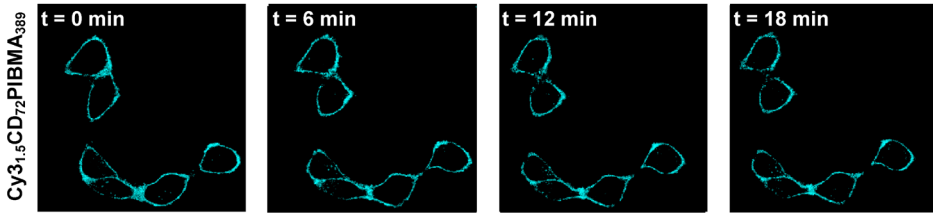
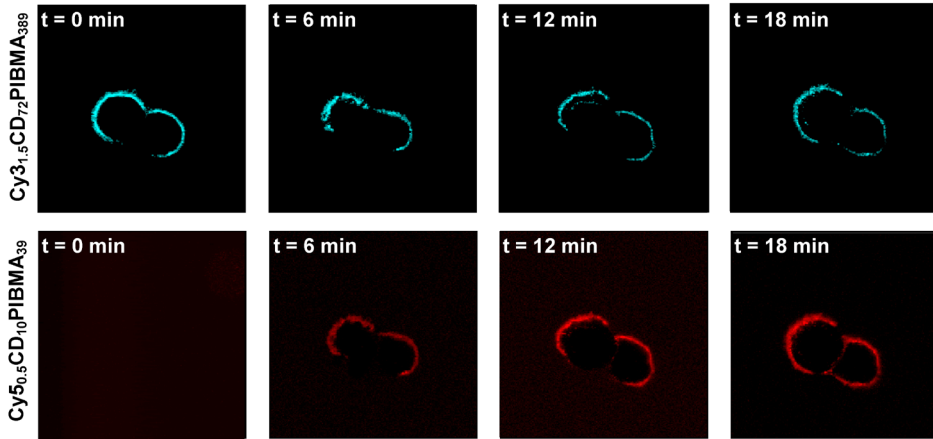


Figure S18. Reduction in Cy5 signal ($\text{Cy5}_{0.5}\text{CD}_{10}\text{PIBMA}_{39}$ or $\text{Cy5}_{0.4}\text{PIBMA}_{39}$) under various conditions. **Ac-TZ14011-Ad** functionalized MDAMB231 X4 cells were incubated with $\text{Cy5}_{0.5}\text{CD}_{10}\text{PIBMA}_{39}$ or $\text{Cy5}_{0.4}\text{PIBMA}_{39}$ (1 h), subsequently either a competitor or nothing was added and the cells were imaged over time for a duration of 18 minutes. **a)** $\text{Cy5}_{0.5}\text{CD}_{10}\text{PIBMA}_{39}$ functionalized cells were washed, but no competitor was added. **b)** $\text{Cy5}_{0.5}\text{CD}_{10}\text{PIBMA}_{39}$ functionalized cells were washed and $\text{Cy3}_{1.5}\text{CD}_{72}\text{PIBMA}_{389}$ was added. **c)** $\text{Cy3}_{1.5}\text{CD}_{72}\text{PIBMA}_{389}$ was directly added to $\text{Cy5}_{0.5}\text{CD}_{10}\text{PIBMA}_{39}$ functionalized cells, with both polymers in solution the exchange took more time and cells were imaged up to 30 min. **d)** $\text{Cy5}_{0.4}\text{PIBMA}_{39}$ functionalized cells were washed and $\text{Cy3}_{1.5}\text{CD}_{72}\text{PIBMA}_{389}$ was added. With Cy5 ($\text{Cy5}_{0.5}\text{CD}_{10}\text{PIBMA}_{39}$ or $\text{Cy5}_{0.4}\text{PIBMA}_{39}$) in red and Cy3 ($\text{Cy3}_{1.5}\text{CD}_{72}\text{PIBMA}_{389}$) in blue.

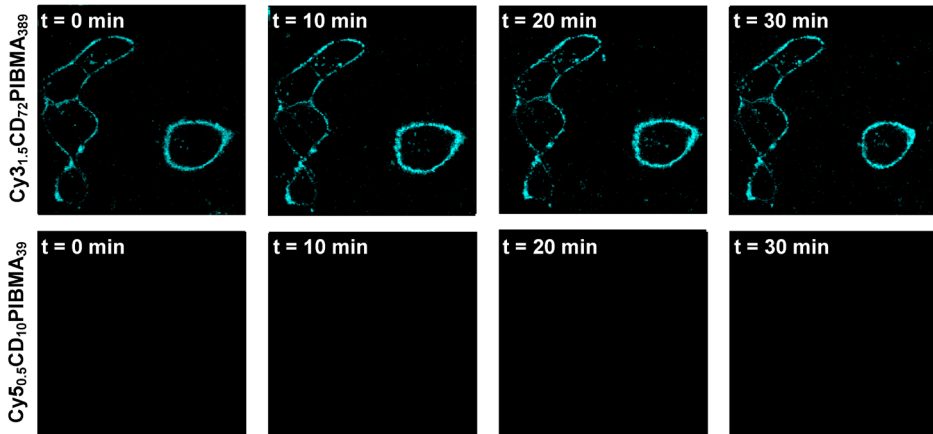
a) **Cy3_{1.5}CD₇₂PIBMA₃₈₉** (washed before imaging)



b) Exchange: **Cy3_{1.5}CD₇₂PIBMA₃₈₉** vs **Cy5_{0.5}CD₁₀PIBMA₃₉** (washing before addition of competitor)



c) Competition: **Cy3_{1.5}CD₇₂PIBMA₃₈₉** vs **Cy5_{0.5}CD₁₀PIBMA₃₉** (no washing)



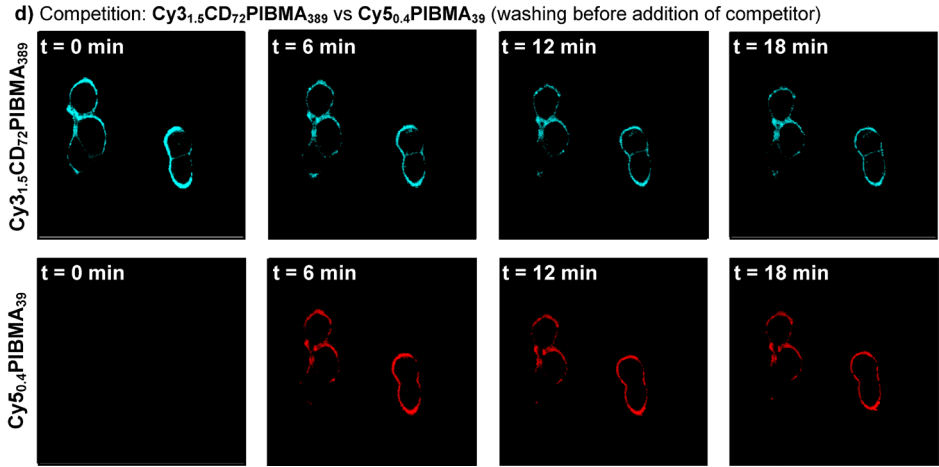


Figure S19. Reduction in Cy3 signal ($\text{Cy3}_{1.5}\text{CD}_{72}\text{PIBMA}_{389}$) under various conditions. **Ac-TZ14011-Ad** functionalized MDAMB231 X4 cells were incubated with $\text{Cy3}_{1.5}\text{CD}_{72}\text{PIBMA}_{389}$ (1 h), subsequently either a competitor or nothing was added and the cells were imaged over time for a duration of 18 minutes. **a)** Cells were washed, but no competitor was added. **b)** Cells were washed and $\text{Cy5}_{0.5}\text{CD}_{10}\text{PIBMA}_{39}$ was added. **c)** $\text{Cy5}_{0.5}\text{CD}_{10}\text{PIBMA}_{39}$ was directly added to $\text{Cy3}_{1.5}\text{CD}_{72}\text{PIBMA}_{389}$ functionalized cells. With both polymers in solution the exchange took more time and cells were imaged up to 30 min. **d)** Cells were washed and $\text{Cy5}_{0.4}\text{PIBMA}_{39}$ was added. With Cy5 ($\text{Cy5}_{0.5}\text{CD}_{10}\text{PIBMA}_{39}$ or $\text{Cy5}_{0.4}\text{PIBMA}_{39}$) in red and Cy3 ($\text{Cy3}_{1.5}\text{CD}_{72}\text{PIBMA}_{389}$) in blue.

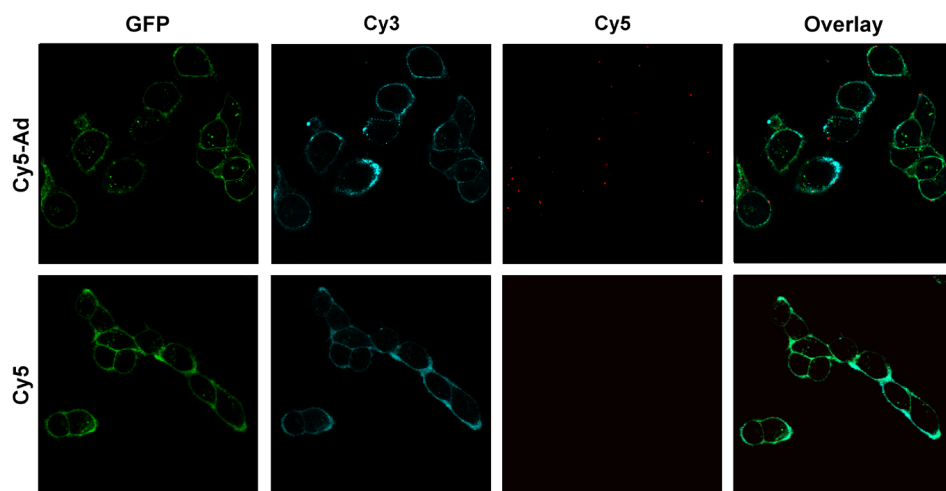


Figure S20. Binding of **Cy5-Ad** or **Cy5** to **Cy3_{1.5}-CD₇₂-PIBMA₃₈₉** functionalized MDAMB231 X4 cells analyzed by confocal microscopy. For clarity, both the (overlay) image and the same image at the individual channels are displayed, with GFP in green, Cy3 (**Cy3_{1.5}-CD₇₂-PIBMA₃₈₉**) in blue and Cy5 (**Cy5-Ad** or **Cy5**) in red.

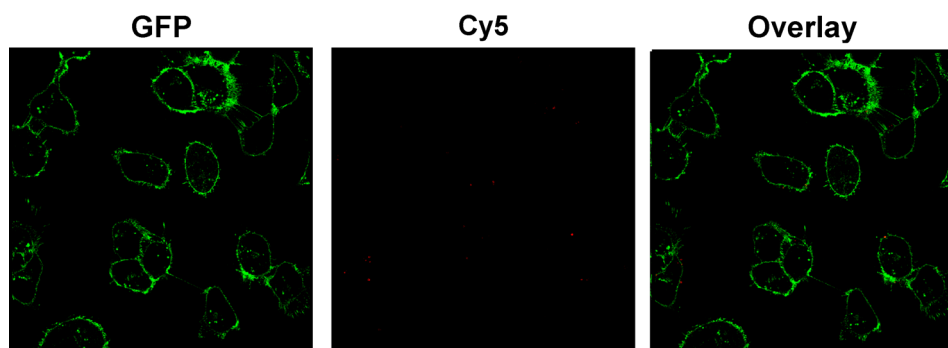


Figure S21. Binding of **Cy5-Ad₂** to non-functionalized MDAMB231 X4 cells. **Cy5-Ad₂** poorly binds to the cell surfaces when CD_nPIBMA_m functionalization is absent. For clarity, both the (overlay) image and the same image at the individual channels are displayed, with GFP in green, and Cy5 (**Cy5-Ad₂**) in red.

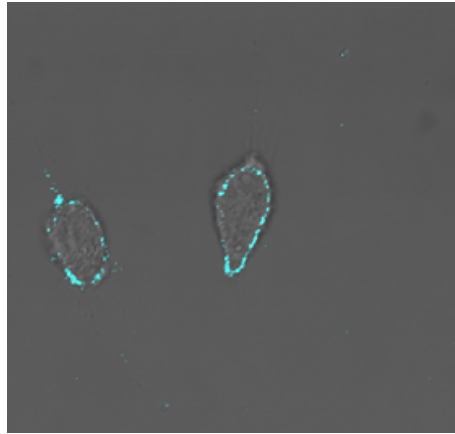


Figure S22. Functionalization of CXCR4 expressing human fetal heart stem cell with **Cy3_{1.5}CD₇₂PIBMA₃₈₉** (blue) analyzed by confocal microscopy.

REFERENCES

1. A. Bunschoten; D. M. van Willigen; T. Buckle, et al., Tailoring fluorescent dyes to optimize a hybrid RGD-tracer. *Bioconjugate Chem.* **2016**, 27 (5), 1253-1258.
2. R. B. Mujumdar; L. A. Ernst; S. R. Mujumdar, et al., Cyanine dye labeling reagents: sulfoindocyanine succinimidyl esters. *Bioconjugate Chem.* **1993**, 4, 105-111.
3. V. E. Shershov; M. A. Spitsyn; V. E. Kuznetsova, et al., Near-infrared heptamethine cyanine dyes. Synthesis, spectroscopic characterization, thermal properties and photostability. *Dyes and Pigments* **2013**, 97 (2), 353-360.
4. S. Huvneers; I. van den Bout; P. Sonneveld, et al., Integrin alpha v beta 3 controls activity and oncogenic potential of primed c-Src. *Cancer Res* **2007**, 67 (6), 2693-2700.
5. J. W. Song; S. P. Cavnar; A. C. Walker, et al., Microfluidic endothelium for studying the intravascular adhesion of metastatic breast cancer cells. *PLoS One* **2009**, 4 (6), e5756.
6. N. S. van den Berg; T. Buckle; J. Kuil, et al., Immunohistochemical detection of the CXCR4 expression in tumor tissue using the fluorescent peptide antagonist Ac-TZ14011-FITC. *Transl Oncol* **2011**, 4 (4), 234-240.
7. J. Kuil; T. Buckle; J. Oldenburg, et al., Hybrid peptide dendrimers for imaging of chemokine receptor 4 (CXCR4) expression. *Mol Pharm* **2011**, 8 (6), 2444-2453.
8. J. Kuil; T. Buckle; H. Yuan, et al., Synthesis and Evaluation of a Bimodal CXCR4 Antagonistic Peptide. *Bioconjugate Chemistry* **2011**, 22 (5), 859-864.
9. T. Mosmann, Rapid colorimetric assay for cellular growth and survival: application to proliferation and cytotoxicity assays. *J Immunol Methods* **1983**, 65, 55-63.
10. D. Gerlier; N. Thomasset, Use of MTT colorimetric assay to measure cell activation. *J Immunol Methods* **1986**, 94, 57-63.
11. E. K. J. Pauwels; M. M. Welling; R. I. J. Feitsma, The labeling of proteins and LDL with ^{99m}Tc: a new direct method employing KBH₄ and stannous chloride. *Nucl Med Biol* **1993**, 20, 825-833.





Adapted from: Spa SJ, Welling MW, van Oosterom MN, Rietbergen DDD, Burgmans MC, Verboom W, Huskens J, Buckle T, van Leeuwen FWB.

Theranostics 2018;8:2377-2386



CHAPTER **3**

**A Supramolecular Approach for
Liver Radioembolization**

ABSTRACT

Hepatic radioembolization therapies can suffer from discrepancies between diagnostic planning (scout-scan) and the therapeutic delivery itself, resulting in unwanted side-effects such as pulmonary shunting. We reasoned that a nanotechnology-based pre-targeting strategy could help overcome this shortcoming by directly linking pre-interventional diagnostics to the local delivery of therapy.

Methods

The host-guest interaction between adamantane and cyclodextrin was employed in an *in vivo* pre-targeting set-up. Adamantane (guest)-functionalized macro albumin aggregates (MAA-Ad; $d = 18 \mu\text{m}$) and (radiolabeled) Cy5 and β -cyclodextrin (host)-containing PIBMA polymers ($^{99\text{m}}\text{Tc-Cy5}_{0.5}\text{CD}_{10}\text{PIBMA}_{39}$; MW ~ 18.8 kDa) functioned as the reactive pair. Following liver or lung embolization with ($^{99\text{m}}\text{Tc}$)-MAA-Ad or ($^{99\text{m}}\text{Tc}$)-MAA (control), the utility of the pre-targeting concept was evaluated after intravenous administration of $^{99\text{m}}\text{Tc-Cy5}_{0.5}\text{CD}_{10}\text{PIBMA}_{39}$.

Results

Interactions between MAA-Ad and $\text{Cy5}_{0.5}\text{CD}_{10}\text{PIBMA}_{39}$ could be monitored in solution using confocal microscopy and were quantified by radioisotope-based binding experiments. *In vivo* the accumulation of the MAA-Ad particles in the liver or lungs yielded an approximate ten-fold increase in accumulation of $^{99\text{m}}\text{Tc-Cy5}_{0.5}\text{CD}_{10}\text{PIBMA}_{39}$ in these organs (16.2 %ID/g and 10.5 %ID/g, respectively) compared to the control. Pre-targeting with MAA alone was shown to be only half as efficient. Uniquely, for the first time, this data demonstrates that the formation of supramolecular interactions between cyclodextrin and adamantane can be used to drive complex formation in the chemically challenging *in vivo* environment.

Conclusion

The *in vivo* distribution pattern of the cyclodextrin host could be guided by the pre-administration of the adamantane guest, thereby creating a direct link between the scout-scan (MAA-Ad) and delivery of therapy.

INTRODUCTION

Radioembolization is a radiation-based therapeutic method that is applied for primary liver tumors and metastases that are untreatable via surgery or chemotherapy. During these interventions, microspheres that contain therapeutic radioisotopes (β -emitters such as yttrium-90 or holmium-166) are intrahepatically delivered.¹ While the clinical benefit of this approach has been demonstrated in large randomized controlled trials,²⁻⁴ the preclusion of hepatopulmonary shunting remains an unsolved challenge. Shunting results in the displacement of a fraction of the administered particles towards the microvasculature of the lung instead of the liver, leading to ineffective dose distribution and serious adverse effects such as radiation pneumonitis.⁵⁻⁷ To predict the likelihood of shunting prior to initiation of the therapeutic intervention, technetium-99m labelled macro albumin aggregates (^{99m}Tc-MAA; d = 18 μ m) can be administered as a diagnostic “scout” procedure. Besides insight into the degree of shunting, SPECT/CT-based ^{99m}Tc-MAA uptake monitoring also helps to provide a dosimetric (distribution) model for the therapeutic isotopes.^{6,8} Differences in particle composition and pharmacokinetics, however, do not fully exclude discrepancies between the “scout” procedure and the therapeutic delivery. As a result, hepatopulmonary shunting still occurs in over 13% of therapeutic interventions.⁹⁻¹¹ Unfortunately, when this occurs the implementation of preventive measures is no longer an option.

In an attempt to provide a more advanced theranostic solution for this problem, we investigated a two-step pre-targeting concept *in vivo*. The potential of an *in vivo* pre-targeting setup has been shown in radioimmunotherapy of cancer which has relied on, for example, the interactions between complementary oligonucleotides,¹² or bispecific- or avidin/biotinantibodies.¹³ However, this setup suffered from slow pharmacokinetics (at least 2 days between the first two injections), possible internalization of the antibody, and/or requires multiple (3-5) injection steps.¹³ To overcome these issues a different pre-targeting approach based on multivalent supramolecular host-guest interactions between adamantane (Ad) and β -cyclodextrin (CD; Figure 1A) was investigated. While CD has been utilized to form nanoparticles for drug delivery^{14,15} the host-guest chemistry was always performed beforehand, and not *in situ*. Recently, we successfully employed CD-Ad host-guest chemistry *in vitro*^{16,17} and, to the best of our knowledge, we now employ these chemical CD-Ad host-guest interactions *in vivo* for the first time.

Using Ad_x-guest-functionalized MAA microspheres (Figure 1A), the diagnostic MAA compound was converted into a pre-targeting vector for an intravenously (i.v.) administered

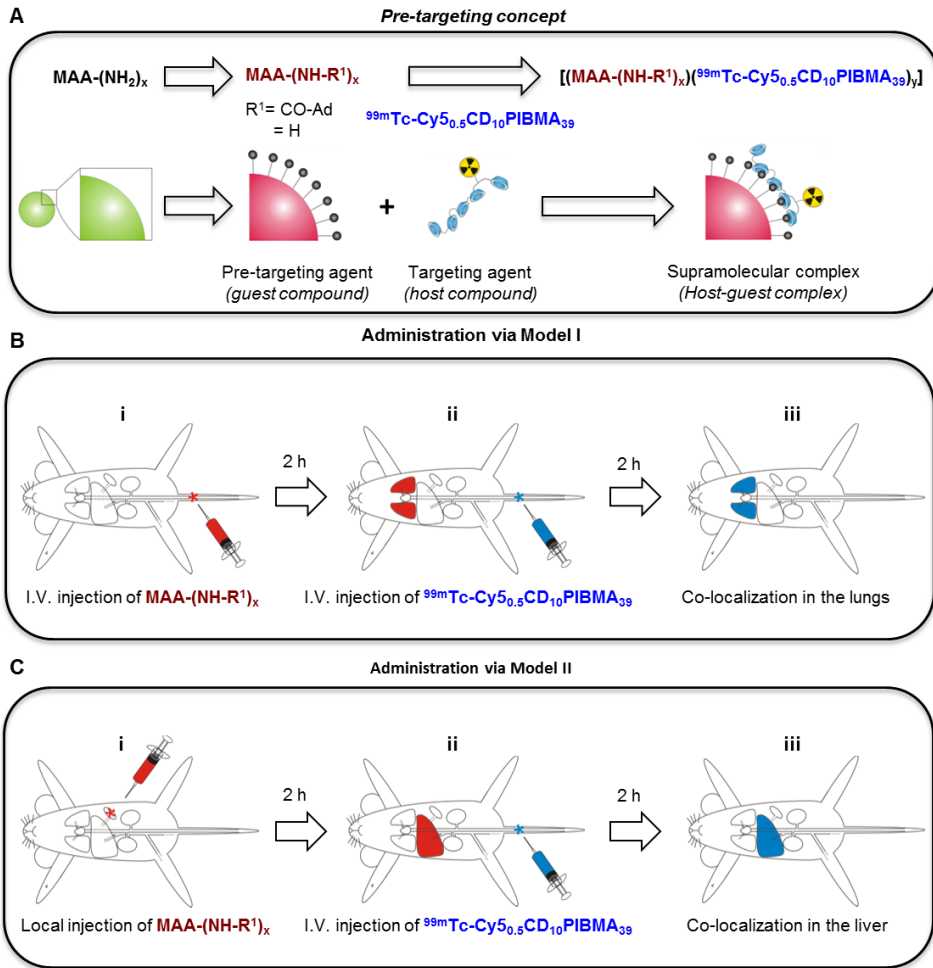


Figure 1. The radioembolization tailored pre-targeting concept is schematically illustrated by the chemical and functional steps involved. **A)** Representation of the different chemical functionalities and components. **B)** I.v. pre-administered MAA-Ad (Bi) accumulated in the lungs (Bii). Subsequent i.v. administration of ${}^{99m}\text{Tc-Cy}5_{0.5}\text{CD}_{10}\text{PIBMA}_{39}$ (Bii) resulted in pulmonary co-localization of MAA-Ad and ${}^{99m}\text{Tc-Cy}5_{0.5}\text{CD}_{10}\text{PIBMA}_{39}$ (Biii). **C)** Local pre-administered MAA-Ad (Ci) accumulated in the liver (Cii). Following i.v. administration of ${}^{99m}\text{Tc-Cy}5_{0.5}\text{CD}_{10}\text{PIBMA}_{39}$ (Cii) hepatic co-localization of both compounds was observed (Ciii).

radiolabeled β -cyclodextrin-PIBMA-polymer (host, Figure 1A). The β -cyclodextrin-polymer provides a platform for future functionalization with therapeutic radioisotopes. The pre-targeted radioembolization concept was tested via the use of two different pre-clinical

models that were either in line with: 1) the routine clinical use of ^{99m}Tc -MAA for lung staining, wherein MAA is administered intravenously (i.v.; Model I, Figure 1B), or 2) the current clinical set-up for locally administered hepatic radioembolization wherein MAA is administered locally (Model II, Figure 1C).

EXPERIMENTAL

General

For the stability of the compounds please see the Supplementary Material section. All chemicals were obtained from commercial sources and used without further purification. NMR spectra were obtained using a Bruker DPX 300 spectrometer (300 MHz, ^1H NMR) or a Bruker AVANCE III 500 MHz with a TXI gradient probe. All spectra were referenced to residual solvent signal or TMS. HPLC was performed on a Waters system using a 1525EF pump and a 2489 UV detector. For preparative HPLC, a Dr. Maisch GmbH, Reprosil-Pur 120 C18-AQ 10 μm column and a gradient of 0.1 % TFA in $\text{H}_2\text{O}/\text{CH}_3\text{CN}$ (95:5) to 0.1 % TFA in $\text{H}_2\text{O}/\text{CH}_3\text{CN}$ (5:95) in 40 min were used. For analytical HPLC, a Dr. Maisch GmbH, Reprosil-Pur C18-AQ 5 μm (250 \times 4.6 mm) column and a gradient of 0.1 % TFA in $\text{H}_2\text{O}/\text{CH}_3\text{CN}$ (95:5) to 0.1 % TFA in $\text{H}_2\text{O}/\text{CH}_3\text{CN}$ (5:95) in 40 min were used. MALDI-ToF measurements were performed on a Bruker Microflex. High-resolution mass spectra were measured on an Exactive orbitrap high-resolution mass spectrometer (Thermo Fisher Scientific, San Jose, CA) and processed with the use of Thermo Scientific Xcalibur software (V2.1.0.1139). For dialysis, Sigma Pur-ALyzerTM Mega 3,500 units were used.

Synthesis

Adamantane-tetrafluorophenol (Ad-TFP)

1-Adamantanecarboxylic acid (500 mg, 2.8 mmol) and 2,3,5,6-tetrafluorophenol (TFP) (718 mg, 4.3 mmol) were dissolved in 10 mL dry dichloromethane (DCM) and stirred for 10 min. Subsequently, *N,N*-dicyclohexylcarbodiimide (858 mg, 4.3 mmol), dissolved in 5 mL dry DCM, was added drop-wise. After stirring for 2 days at RT, the reaction mixture was filtered and the filtrate was concentrated in vacuo. The resulting yellow product was purified by silica column chromatography (DCM:Hexane, 1:1). Pure fractions were pulled and concentrated under vacuum to obtain the product as a white crystalline powder (785 mg, 86%). ^1H NMR (300 MHz, CDCl_3 , 25 $^\circ\text{C}$) = δ 7.06 – 6.89 (m, 1H, CH of TFP), 2.09 (s, 9H, C-CH₂-CH and CH₂-CH-CH₂), 1.78 (s, 6H, CH-CH₂-CH). High resolution mass: $[\text{C}_{17}\text{H}_{17}\text{F}_4\text{O}_2]^+$ calculated 329.3, found 328.1 (Figure S1).

Cy5-(SO₃)Sulfonate-(SO₃)COTFP

Cy5-(SO₃)Sulfonate-(SO₃)COOH was synthesized according to an earlier published procedure.¹⁸

Cy5_{0.5}CD₁₀PIBMA₃₉

The synthesis of Cy5_{0.5}CD₁₀PIBMA₃₉ was performed according to a recently described procedure.¹⁶

Functionalization of macro-aggregates with adamantane (MAA-Ad)

Albumin macro-aggregates (TechneScan®, MAA) were obtained from Mallinckrodt Medical B.V., Petten, The Netherlands. Lyophilized macroaggregates (2 mg) were dissolved in 1 mL of saline (0.9% NaCl, sterile and pyrogen-free, B. Braun Medical Supplies, Inc., Oss, The Netherlands) and portions of 0.1 mL (containing 0.2 mg MAA) were stored in Eppendorf tubes at -20 °C until further use. For functionalization, one portion was defrosted and 20 µL of Ad-TFP (10 mg/mL DMSO) was added. After agitation in a shaking water bath for 1 h at 37 °C, the solution was washed 2 times with phosphate buffered saline (PBS) by 2 centrifugation steps (3 min, 3000 ×g). The obtained MAA-Ad was diluted in 1 mL of PBS to 0.2 mg/mL.

To estimate the number of Ad conjugated to MAA, the MAA functionalization was also performed with Cy5-TFP according to the same procedure as for Ad-TFP. Subsequently, the absorbance at 650 nM of the MAA-Cy5 constructs was measured using a NanoDrop Spectrophotometer (Thermo Fisher Scientific Inc. Wilmington, DE, USA). The dye concentration was calculated using the absorbance following the law of Lambert Beer ($A = \epsilon \cdot l \cdot C$) with $\epsilon_{\text{Cy5}} = 250 \times 10^3 \text{ mol}^{-1}\text{cm}^{-1}$. The number of Cy5/MAA aggregates was then calculated by dividing the calculated Cy5 concentration by the known MAA concentration, resulting in a ratio of $3.07(\pm 0.24) \times 10^8$ Cy5/MAA particle on average. Assuming that Ad-TFP reacts in a similar fashion as Cy5-TFP, it was estimated that the ratio of Ad/MAA would be of the same order of magnitude.

Radiolabeling of Cy5_{0.5}CD₁₀PIBMA₃₉

Radiolabeling of Cy5_{0.5}CD₁₀PIBMA₃₉ was performed as follows: to 10 mL of Cy5_{0.5}CD₁₀PIBMA₃₉ (1 mg/mL in PBS), 4 mL of SnCl₂·2H₂O (0.44 mg/mL saline, Technescan PYP, Mallinckrodt Medical B.V.), and 100 mL of a freshly eluted ^{99m}Tc-Na-pertechnetate solution (500 MBq/mL, Mallinckrodt Medical B.V.) were added, and the mixture was gently stirred in a shaking water bath for 1 h at 37 °C.¹⁹ Subsequently, the labeling yield

was estimated over time by ITLC analysis according to the following procedure: 2 mL of the reaction mixture was applied on 1x7 cm ITLC-SG paper strips (Agilent Technologies, USA) for 10 min at RT with PBS as the mobile phase. After 1 h, the highest labeling yield of $\text{Cy5}_{0.5}\text{CD}_{10}\text{PIBMA}_{39}$ with $^{99\text{m}}\text{Tc}$ was assessed (49.6%) and the reaction mixture was purified by size exclusion chromatography with sterile PBS as the mobile phase using Sephadex™ G-25 (desalting columns PD-10, GE Healthcare Europe GmbH, Freiburg, Germany). Fractions containing $^{99\text{m}}\text{Tc-Cy5}_{0.5}\text{CD}_{10}\text{PIBMA}_{39}$ were collected and directly applied in the imaging experiments.

Radiostability in PBS

To assess the stability of the radiolabeling in PBS, after 24 h the release of radioactivity from PD-10-purified $^{99\text{m}}\text{Tc-Cy5}_{0.5}\text{CD}_{10}\text{PIBMA}_{39}$ was determined with ITLC (according to the same method described in 'Radiolabeling of $\text{Cy5}_{0.5}\text{CD}_{10}\text{PIBMA}_{39}$ ').

Supramolecular interaction between MAA-Ad and $^{99\text{m}}\text{Tc-Cy5}_{0.5}\text{CD}_{10}\text{PIBMA}_{39}$

To determine the supramolecular interaction between MAA-Ad and $\text{Cy5}_{0.5}\text{CD}_{10}\text{PIBMA}_{39}$ *in vitro*, 0.1 mL of MAA-Ad in PBS (0.2 mg/mL) and 0.1 mL of $^{99\text{m}}\text{Tc-Cy5}_{0.5}\text{CD}_{10}\text{PIBMA}_{39}$ in PBS (1 mg/mL, 1 MBq) were mixed and the solution was incubated for 1 h in a shaking water bath at 37 °C. Thereafter, the radioactivity of the total amount added and the radioactivity of the pellet after two washing steps with PBS were measured in a dose-calibrator to determine the amount of binding of $^{99\text{m}}\text{Tc-Cy5}_{0.5}\text{CD}_{10}\text{PIBMA}_{39}$ to MAA-Ad. After correction for background activity, the amount of binding was expressed as the percentage of the total amount of radioactivity (%binding). To assess the effect of the Ad moieties, the same experiment was also performed with non-functionalized MAA and the resulting %binding of $^{99\text{m}}\text{Tc-Cy5}_{0.5}\text{CD}_{10}\text{PIBMA}_{39}$ to MAA and MAA-Ad were compared (Figure 2B). Significance between the two conditions was calculated using a two-tailed student's t-Test with $n = 4$.

The supramolecular interaction between MAA-Ad and $\text{Cy5}_{0.5}\text{CD}_{10}\text{PIBMA}_{39}$ was also visualized by confocal microscopy, employing the Cy5 component of the polymer.¹⁶ For this purpose, the same experiment was repeated, but this time non-radioactive $\text{Cy5}_{0.5}\text{CD}_{10}\text{PIBMA}_{39}$ was added to the MAA and MAA-Ad solutions. After washing, 10 mL of MAA (with or without-Ad) $\text{Cy5}_{0.5}\text{CD}_{10}\text{PIBMA}_{39}$ solution was pipetted onto culture dishes with glass inserts (ø35mm glass bottom dishes No. 15, poly-d-lysine coated, γ -irradiated, MatTek corporation). Images were taken on a Leica SP5 WLL confocal microscope under 63x magnification using Leica Application Suite software. Cy5 fluorescence was measured with excitation at 633 nm and emission was collected at 650-700 nm.

In vivo studies

Animals

All *in vivo* studies were performed using 10-12 week old Swiss mice (20-25 g, Crl:OF1 strain, Charles River Laboratories, USA). All animal studies were approved by the institutional Animal Ethics Committee (DEC permit 12160) of the Leiden University Medical Center. All mice were kept under specific pathogen-free conditions in the animal housing facility of the LUMC. Food and water were given *ad libitum*.

General SPECT imaging and biodistribution protocol

SPECT imaging was performed at 2 h after injection of ^{99m}Tc -labeled compounds. Mice were placed onto a dedicated positioning bed of a three-headed U-SPECT-2 (MILabs, Utrecht, the Netherlands) under continuous 1-2% isoflurane anesthesia.²⁰ Radioactivity counts from total body scans or selected regions of interest (ROI) were acquired for 60 min using a 0.6 mm mouse multi-pinhole collimator in list mode data. For reconstruction from list mode data, the photo peak energy window was centered at 140 keV with a window width of 20%. Side windows of 5% were applied to correct for scatter and down scatter corrections. The image was reconstructed using 24 Pixel based Ordered Subset Expectation Maximization iterations (POSEM) with 4 subsets, 0.2 mm isotropic voxel size and with decay and triple energy scatter correction integrated into the reconstruction with a post filter setting of 0.25 mm.²¹ Volume rendered images were generated from 2-4 mm slices and analyzed using Matlab R2014a software (version 8.3.0.532, MathWorks® Natick, MA). Images were generated from maximum intensity protocols (MIP) adjusting the color scale threshold to optimal depiction of the tissues of interest.²² After imaging, the mice were euthanized by an intraperitoneal injection of 0.25 mL Euthasol (ASTfarma, Oudewater, The Netherlands).

To determine the biodistribution of the tracer, organs were collected from mice and counted for radioactivity in a dose-calibrator (VDC 101, Veenstra Instruments, Joure, the Netherlands) or a gamma counter (Wizard2 2470 automatic gamma scintillation counter, Perkin Elmer). After collecting and counting all tissues together with the remaining activity in the carcass, the total amount of remaining radioactivity in the animal was counted and, after correction for physical decay, the urinary excretion expressed as the percentage of the total injected dose (%ID) was calculated. Radioactivity counts in tissues were expressed as the percentage of the total injected dose of radioactivity per gram tissue (%ID/g). Additionally, reconstructed images were generated and analyzed using Amide 1.0.2 software (<http://amide.sourceforge.net/documentation.html>).²³

Mapping the distribution of $^{99m}\text{Tc-Cy5}_{0.5}\text{CD}_{10}\text{PIBMA}_{39}$ in mice

To determine the natural distribution of $^{99m}\text{Tc-Cy5}_{0.5}\text{CD}_{10}\text{PIBMA}_{39}$, 0.1 mL of PBS containing $^{99m}\text{Tc-Cy5}_{0.5}\text{CD}_{10}\text{PIBMA}_{39}$ (1 mg/mL, 20 MBq) was injected i.v. 2 h after injection, SPECT imaging and biodistribution studies were performed as described above (Figure 3A, D).

Mapping the distribution of ^{99m}Tc -labeled MAA-Ad in mice via:

i.v. administration, Model I

To determine whether MAA embolizations are tolerated by mice and whether MAA-Ad is delivered to the capillaries of the lungs, MAA-Ad was radiolabeled according to the manufacturer's instructions, and 0.1 mL of $^{99m}\text{Tc-MAA-Ad}$ in PBS (0.02 mg, 2 mg/mL) was injected into the tail vein. At 2 h after injection, the organ distribution of the tracer in mice was imaged using SPECT and quantified with biodistribution studies (see SPECT imaging protocol and biodistribution studies described above (Figure 3 B, D).

Local administration, model II

An embolization setup in the liver was performed to mimic the clinical setup for liver radioembolization.²⁴ For this purpose, animals were anesthetized by intraperitoneal injection of a mixture containing Hypnorm (Vetapharma, Leeds, United Kingdom), dormicum (Roche, Basel, Switzerland), and water (1:1:2). After shaving and cleaning with ethanol (70%), the abdominal cavity was incised for 0.5 cm and the spleen was exposed outside the mouse. Of the $^{99m}\text{Tc-MAA-Ad}$ solution (2 mg/mL), 100 μL was injected into the spleen using a Myjector U-100 insulin syringe (29G x $\frac{1}{2}$ " 0.33 x12 mm, Terumo Europe, Leuven, Belgium) and after 5 s the needle was removed and the spleen was positioned inside the peritoneal cavity. The incision was sutured by 2-4 stitches and the animals were placed under a heating lamp to maintain the body temperature at 37 °C. At 2 h after injection, the organ distribution of the tracer in mice was imaged using SPECT and quantitated with biodistribution studies as described above (Figure 3C, D).

Mapping the distribution of $^{99m}\text{Tc-Cy5}_{0.5}\text{CD}_{10}\text{PIBMA}_{39}$ after MAA(-Ad) pre-administration

The influence of MAA or MAA-Ad on the distribution of $^{99m}\text{Tc-Cy5}_{0.5}\text{CD}_{10}\text{PIBMA}_{39}$ was evaluated as follows: first, 0.1 mL containing MAA-Ad or non-functionalized MAA in 0.1 mL (0.02 mg, 2 mg/mL) was injected by either i.v. administration (Figure 1B, Model I) or local administration (Figure 1C, Model II). After 2 h, 0.1 mL of $^{99m}\text{Tc-Cy5}_{0.5}\text{CD}_{10}\text{PIBMA}_{39}$ in PBS (1 mg/mL, 20 MBq) was i.v. injected and another 2 h later SPECT imaging and biodistribution studies were performed as described above (Figure 4).

RESULTS AND DISCUSSION

To allow for initial diagnostics of the particle distribution and to provide a guest-particle that can act as an *in vivo* target, clinical grade MAA particles were functionalized with Ad guest moieties (Figure 1A) via amide bond formation. This yielded MAA-Ad with, on average, 10^8 Ad molecules per MAA particle. Especially for these experiments a fluorescent β -cyclodextrin-poly(isobutylene-alt-maleic-anhydride)-polymer host molecule (Cy5_{0.5}CD₁₀PIBMA₃₉, ~18.8 kDa, diameter, ~11.7 nm) was synthesized (Figure 1A),¹⁶ that contained (on average) ten β -CD compounds. Besides CD, various carboxylic acid groups were present on the backbone of the polymer that could serve as the chelating ligand for a range of metal ion-based radio-isotopes, such as ⁹⁰Y, ¹⁶⁶Ho, and ^{99m}Tc.

The interaction between CD and Ad is well-known, with a binding affinity of $\sim 5 \times 10^4$ M⁻¹ for a monovalent interaction.²⁵ Increasing the number of host and guest moieties drives multivalent interactions, which effectively increases the binding affinity.²⁶ Evidence that individual compounds effectively form complexes based on intended Ad-CD binding interactions was demonstrated *in vitro*. While MAA alone did induce some Cy5_{0.5}CD₁₀PIBMA₃₉ accumulation, clearly a higher level of Cy5_{0.5}CD₁₀PIBMA₃₉ accumulation was obtained with MAA-Ad (Figure 2A). The difference in accumulation was quantified by a radioisotope-based binding experiment with ^{99m}Tc-Cy5_{0.5}CD₁₀PIBMA₃₉. This experiment revealed a significant ($p < 0.01$) 5.7-fold increase (Figure 2B) in ^{99m}Tc-Cy5_{0.5}CD₁₀PIBMA₃₉ accumulation with MAA-Ad (49.2%) versus MAA (8.6%), underlining that the observed complex formation is indeed facilitated by the intended Ad-CD host-guest interactions.

To create a reference for the *in vivo* binding between Cy5_{0.5}CD₁₀PIBMA₃₉ and MAA-Ad, first the biodistribution of *i.v.* administered ^{99m}Tc-Cy5_{0.5}CD₁₀PIBMA₃₉ was studied without any pre-targeting vector present. This yielded a low overall organ uptake (~ 1.5 %ID/g, Figure 3A, D). Secondly, the distribution of the pre-targeting vector ^{99m}Tc-MAA-Ad in both the *i.v.* and local administration model was determined. SPECT imaging and biodistribution studies at 2 h post tracer administration revealed a distinct distribution pattern of ^{99m}Tc-MAA-Ad for Model I (*i.v.*) and Model II (local, Figure 3A, 3B). In agreement with previous reports on the distribution of ^{99m}Tc-MAA after *i.v.* injection,²⁷ Model I showed high levels of accumulation of ^{99m}Tc-MAA-Ad in the lungs (335 %ID/g). Local administration of ^{99m}Tc-MAA-Ad, whereby hepatic tracer delivery was realized through injection into parenchymal tissue of the spleen (Model II),²⁸ resulted in high uptake levels in the liver (50.4 %ID/g).

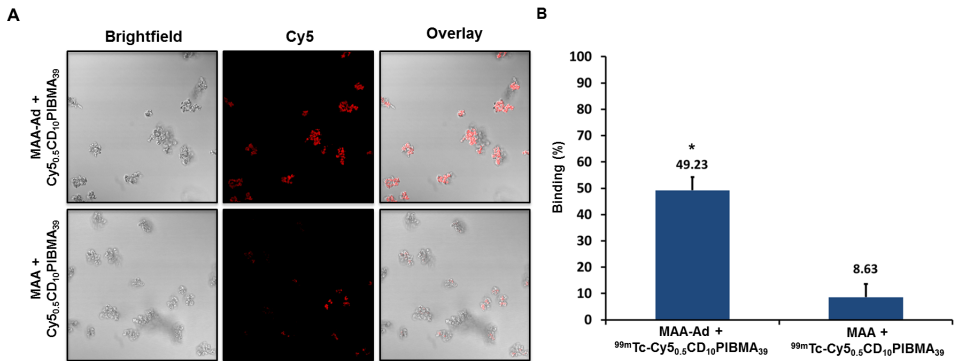


Figure 2. **A**) Fluorescence confocal microscopy-based evaluation of $\text{Cy5}_{0.5}\text{CD}_{10}\text{PIBMA}_{39}$ (Cy5) binding to MAA-Ad (top) and non-functionalized MAA (bottom). The MAA-Ad localized particles (brightfield) reveal a higher degree of staining compared to MAA alone, indicated by the higher Cy5-related fluorescence intensities (in red). **B**) The binding of $^{99m}\text{Tc-Cy5}_{0.5}\text{CD}_{10}\text{PIBMA}_{39}$ to MAA-Ad and MAA quantified by radioactivity and expressed as a percentage of the total amount of radioactivity ($^{99m}\text{Tc-Cy5}_{0.5}\text{CD}_{10}\text{PIBMA}_{39}$) added. Showing 5.7 times more binding to MAA functionalized with the Ad guest moiety compared to non-functionalized MAA, with a significance of difference of $P < 0.01$.

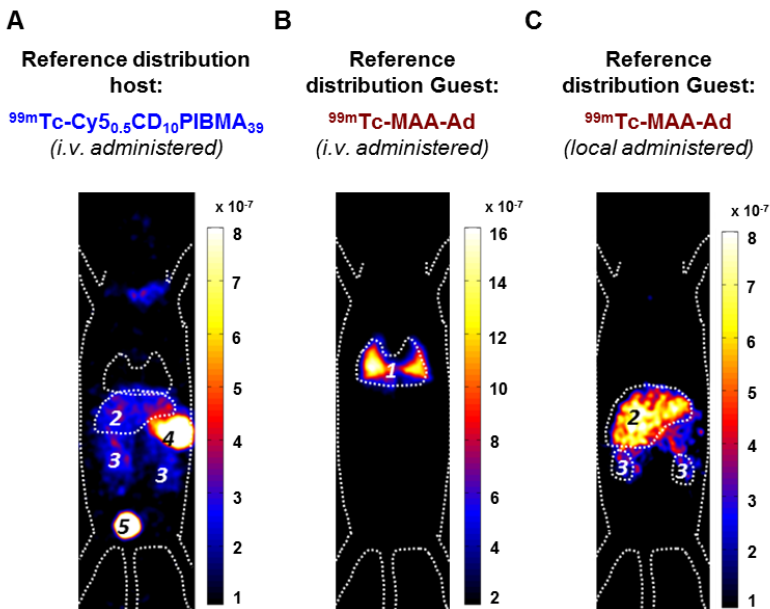


Figure 3. Reference SPECT and biodistribution data of i.v.-administered $^{99m}\text{Tc-Cy5}_{0.5}\text{CD}_{10}\text{PIBMA}_{39}$ and i.v.- or locally administered $^{99m}\text{Tc-MAA-Ad}$. **A**) Following i.v. administration of the targeted (host) agent $^{99m}\text{Tc-Cy5}_{0.5}\text{CD}_{10}\text{PIBMA}_{39}$ no prominent distribution to the kidneys, liver or lungs was observed. **B** and **C**) The pre-targeting (guest) agent $^{99m}\text{Tc-MAA-Ad}$ displayed either pulmonary (B) or hepatic (C) accumulation depending on the route of administration (i.v. or local). Organs are marked as (1) lungs, (2) liver, (3) kidneys, (4) stomach, and (5) urinary bladder.

Table 1. Reference biodistributions of i.v.-administered $^{99m}\text{Tc-Cy5}_{0.5}\text{CD}_{10}\text{PIBMA}_{39}$ and i.v.- or locally administered $^{99m}\text{Tc-MAA-Ad}$. Data (expressed as the mean of the percentage of the injected dose per gram tissue (%ID/g) of 5 observations) were calculated based on the radioactive counts measured in various tissues at 2 h post-injection of the radioactive tracer.

| Tissue | Reference distribution host | Reference distribution guest | |
|----------------|---|--|---|
| | $^{99m}\text{Tc-Cy5}_{0.5}\text{CD}_{10}\text{PIBMA}$ mean | Model I: $^{99m}\text{Tc-MAA-Ad}$ mean | Model II: $^{99m}\text{Tc-MAA-Ad}$ mean |
| Blood | 2.4 ± 1.3 | 2.7 ± 0.9 | 1.0 ± 0.6 |
| Lungs | 1.7 ± 0.5 | 335.8 ± 38.7 | 4.4 ± 1.2 |
| Spleen | 0.9 ± 0.4 | 0.9 ± 0.2 | 6.1 ± 2.4 |
| Liver | 1.0 ± 0.2 | 1.3 ± 0.4 | 50.4 ± 15.4 |
| Kidneys | 4.7 ± 1.3 | 1.8 ± 0.6 | 15.3 ± 2.7 |
| Muscle | 0.4 ± 0.2 | 0.3 ± 0.1 | 0.9 ± 0.3 |
| Brain | 0.1 ± 0.0 | 0.1 ± 0.1 | 0.2 ± 0.1 |

The influence of local MAA(-Ad) deposits on the distribution of i.v.-administered $^{99m}\text{Tc-Cy5}_{0.5}\text{CD}_{10}\text{PIBMA}_{39}$ was studied via Model I (Figure 1B). Here the biodistribution of $^{99m}\text{Tc-Cy5}_{0.5}\text{CD}_{10}\text{PIBMA}_{39}$ after i.v. pre-administration of MAA and MAA-Ad (Figure 4A, B) was compared with the reference distribution of $^{99m}\text{Tc-Cy5}_{0.5}\text{CD}_{10}\text{PIBMA}_{39}$ (no MAA(-Ad) administered, Figure 3A, S2). Pre-targeting with non-functionalized MAA did not lead to changes in the distribution of $^{99m}\text{Tc-Cy5}_{0.5}\text{CD}_{10}\text{PIBMA}_{39}$ (Figure 4A, S2). More specifically, uptake levels in both the lungs and liver remained around 1.5 %ID/g (Figure 4E, 5A). Pre-targeting with MAA-Ad, however, did induce clear alterations in the distribution pattern of $^{99m}\text{Tc-Cy5}_{0.5}\text{CD}_{10}\text{PIBMA}_{39}$ (Figure 4B) as uptake in the lungs increased 6.2-fold (10.5 %ID/g, Figure 4E, 5A). Interestingly, the uptake in the liver also increased towards 5.7 %ID/g, while both the i.v. administration of $^{99m}\text{Tc-MAA-Ad}$ and $^{99m}\text{Tc-Cy5}_{0.5}\text{CD}_{10}\text{PIBMA}_{39}$ alone did not lead to significant liver uptake. It appears that the presence of $^{99m}\text{Tc-Cy5}_{0.5}\text{CD}_{10}\text{PIBMA}_{39}$ influenced the retention of MAA-Ad, causing partial displacement of the (complexed) compounds towards the liver. Alternatively, Ad-labeled metabolites of MAA-Ad could have migrated to the liver, thereby providing a platform for $^{99m}\text{Tc-Cy5}_{0.5}\text{CD}_{10}\text{PIBMA}_{39}$ binding.

To assess the value of pre-targeting in the liver, which is representative of the clinical radioembolization procedure, the same host-guest setup was applied following intrahepatic deposition (Model II; Figure 1C). In this model, the influence of MAA-Ad was even more profound. The presence of low quantities of uptake in the salivary glands and the stomach (Table S1, Figure S2) is indicative for the presence of some free ^{99m}Tc (see Supplementary Material for further stability details).²⁹ Compared to the control, pre-targeting with non-

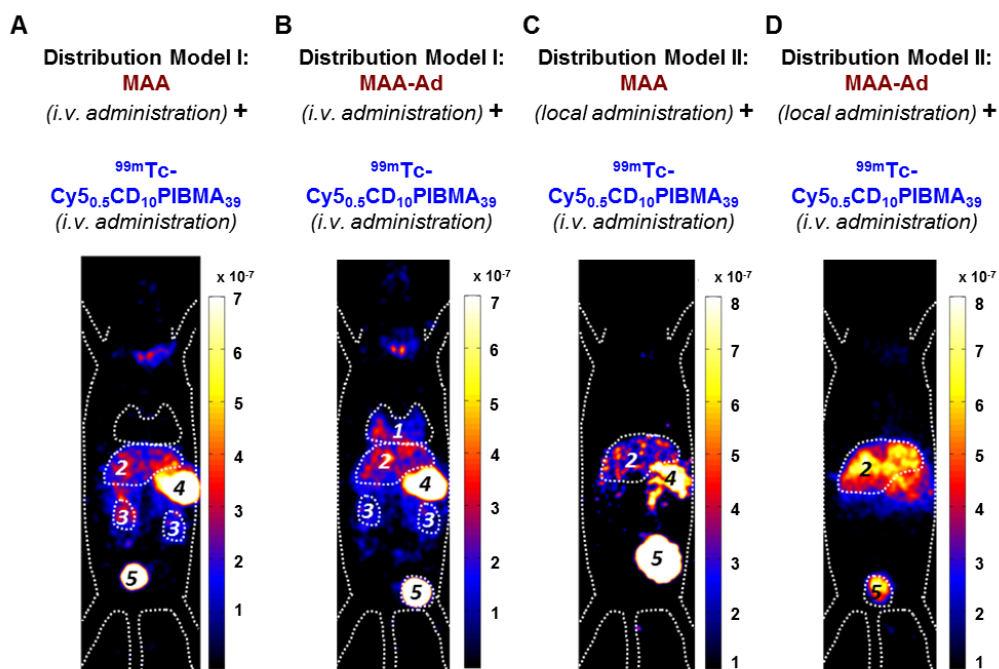


Figure 4. SPECT and biodistribution data of i.v.-administered $^{99m}\text{Tc-Cy}_{5.0.5}\text{CD}_{10}\text{PIBMA}_{39}$ after pre-targeting with MAA or MAA-Ad either i.v. (Model I) or locally (Model II) administered. **A)** Following i.v. administration of MAA, no pulmonary accumulation of $^{99m}\text{Tc-Cy}_{5.0.5}\text{CD}_{10}\text{PIBMA}_{39}$ was observed. **B)** i.v. pre-administered Ad-functionalized MAA did lead to pulmonary accumulation of $^{99m}\text{Tc-Cy}_{5.0.5}\text{CD}_{10}\text{PIBMA}_{39}$. **C)** Following local administration of MAA, slight uptake in liver and kidneys occurred. **D)** After pre-targeting with MAA-Ad, the hepatic accumulation of $^{99m}\text{Tc-Cy}_{5.0.5}\text{CD}_{10}\text{PIBMA}_{39}$ was even more profound. Organs are marked as (1) lungs, (2) liver, (3) kidneys, (4) stomach, and (5) urinary bladder.

functionalized MAA resulted in increased uptake levels of $^{99m}\text{Tc-Cy}_{5.0.5}\text{CD}_{10}\text{PIBMA}_{39}$ in the liver (8.7 %ID/g) and kidneys (10.7 %ID/g), but not in the lungs (1.4 %ID/g, Table 1 vs. Figure 4C, Table 2). This complex formation is in line with that observed during the radioisotope-based in vitro binding experiments in solution (Figure 2). After pre-targeting with MAA-Ad, the differences became more distinct, yielding a 15.7-fold increase in liver uptake (16.2 %ID/g) and a 4.5-fold increase in kidney uptake (19.6 %ID/g) (Figure 4D, E, 5B). Both uptake profiles are in accordance with the distribution pattern of locally administered $^{99m}\text{Tc-MAA-Ad}$ (Figure 3C). As was concluded from the in situ binding, the liver uptake induced by MAA-Ad was nearly double that observed using MAA only. Clearly the host-guest complex formation is more efficient in the liver than in the lungs (see Figure 5). This is likely to be related to the 1,000-fold reduction in particle velocity experienced as they traverse the

Table 2. Biodistribution of $^{99m}\text{Tc-Cy5}_{0.5}\text{CD}_{10}\text{PIBMA}_{39}$ after pre-targeting with i.v.- (Model I) or locally (Model II) administered MAA or MAA-Ad. Data (expressed as the mean of the percentage of the injected dose per gram tissue (%ID/g) of 5 observations) were calculated based on the radioactive counts measured in various tissues at 2 h post-injection of the radioactive tracer.

| Distribution of host ($^{99m}\text{Tc-Cy5}_{0.5}\text{CD}_{10}\text{PIBMA}_{39}$) following injection of indicated guest | | | | |
|--|-----------------------------|--------------------------------|------------------------------|---------------------------------|
| Tissue | Model I: MAA Mean | Model I: MAA-Ad Mean | Model II: MAA Mean | Model II: MAA-Ad mean |
| Blood | 2.1 ± 1.0 | 1.9 ± 0.5 | 1.9 ± 0.3 | 3.8 ± 0.6 |
| Lungs | 1.6 ± 0.7 | 10.5 ± 4.6 | 1.4 ± 0.7 | 2.6 ± 0.2 |
| Spleen | 1.2 ± 0.4 | 4.7 ± 2.3 | 4.7 ± 1.3 | 10.4 ± 1.4 |
| Liver | 2.2 ± 0.9 | 5.7 ± 0.9 | 8.7 ± 1.0 | 16.2 ± 0.7 |
| Kidneys | 4.1 ± 1.7 | 6.6 ± 2.0 | 10.7 ± 0.8 | 19.6 ± 3.8 |
| Muscle | 0.5 ± 0.2 | 0.5 ± 0.2 | 0.5 ± 0.1 | 0.8 ± 0.4 |
| Brain | 0.3 ± 0.4 | 0.2 ± 0.2 | 0.1 ± 0.1 | 0.1 ± 0.0 |

vasculature of the liver, a feature that was said to result in 7.5-times higher interaction rates between particles and hepatic cells.³⁰ The flow reduction may also be enhanced further following partial blockage (embolization) of capillary vessels by MAA(-Ad).

Taken together, the combined distribution data for Model I and Model II clearly indicate that the *in vivo* distribution pattern of the multimeric $^{99m}\text{Tc-Cy5}_{0.5}\text{CD}_{10}\text{PIBMA}_{39}$ host molecule, which served as a model for a future therapeutic agent, can be guided by a pre-targeting approach that makes use of Ad-functionalized microspheres. The fact that the supramolecular interactions in the liver are stronger than those in the lungs indicates that in this pre-targeting model, pulmonary shunting during liver embolization procedures would only result in limited unwanted side-effects. Furthermore, although not yet explored in this study, in the future the polymer-based building blocks can be synthetically modified to: i) optimize their pharmacokinetics and ii) act as carriers for other (therapeutic) isotopes or drugs, e.g., for chemo-embolization.^{29,31,32} Alternatively, local (e.g. intratumoral) deposits of albumin-based particles could not only be used to mark tumors for surgical resection.³³ In a pre-targeting approach such particles could also help provide local therapy.

In previous studies we have demonstrated that supramolecular chemistry can be used to generate clinical grade imaging agents, such as indocyanine green (ICG)- ^{99m}Tc -nanocolloid.^{31,32} This multimodal nanoparticle has helped to connect pre- and intraoperative imaging, and as such, realized image-guided surgery of infected lymph nodes. In the present study, we successfully applied a different supramolecular interaction *in vivo* to advance a theranostic medical intervention, namely radioembolization.

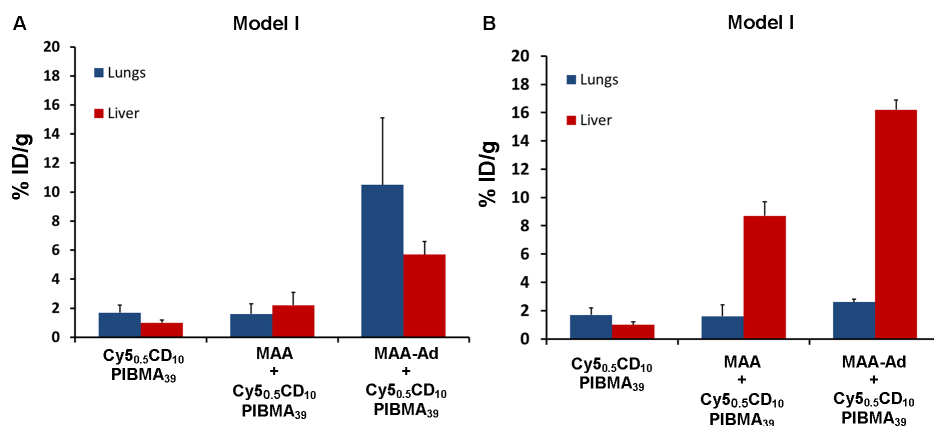


Figure 5. Influence of MAA(-Ad) on the uptake of $^{99m}\text{Tc-Cy}_{5.0,5}\text{CD}_{10}\text{-PIBMA}_{39}$ in the lungs and liver (Table 1 and 2). **A)** Uptake in the lungs increased when MAA-Ad was administered i.v. (Method I). **B)** Increasing uptake in the liver was seen when MAA-Ad was administered locally (Method II). The significance of difference ($P < 0.01$) is indicated with *

CONCLUSION

The initial proof-of-concept data presented demonstrates that despite the chemically complex in vivo environment, multivalent host-guest interactions between Ad and CD can still be formed. Depending on the route of MAA-Ad administration (i.v. or local), the degree and location of $^{99m}\text{Tc-Cy}_{5.0,5}\text{CD}_{10}\text{-PIBMA}_{39}$ accumulation could be guided. For future radioembolization applications this would mean that the distributions observed in the scout scan would directly correlate to those of the therapeutic radioisotope delivery (e.g., ^{90}Y or ^{166}Ho). Overall, a versatile new chemical platform for translational theranostic pre-targeting has been generated.

Acknowledgements

The research leading to these results was funded with grants from: the European Research Council (ERC) under the European Union's Seventh Framework Program FP7/2007-2013 (grant agreement number 2012-306890), from the Netherlands Organization for Scientific Research (NWO nano-Grant STW 11435 and VIDI-grant - STW BGT11272) and the 2015-2016 Postdoctoral Molecular Imaging Scholar Program Grant granted by the Society of Nuclear Medicine and Molecular Imaging (SNMMI) and the Education and Research Foundation (ERF) for Nuclear Medicine and Molecular Imaging. We acknowledge Mark T. M. Rood for providing $\text{Cy}_{5.0,5}\text{CD}_{10}\text{-PIBMA}_{39}$.

REFERENCES

1. R. Hickey; R. J. Lewandowski; T. Prudhomme, et al., 90Y Radioembolization of Colorectal Hepatic Metastases Using Glass Microspheres: Safety and Survival Outcomes from a 531-Patient Multicenter Study. *Journal of nuclear medicine : official publication, Society of Nuclear Medicine* **2016**, 57 (5), 665-71.
2. P. Hilgard; M. Hamami; A. E. Fouly, et al., Radioembolization with yttrium-90 glass microspheres in hepatocellular carcinoma: European experience on safety and long-term survival. *Hepatology* **2010**, 52 (5), 1741-9.
3. A. Kennedy; D. Coldwell; B. Sangro, et al., Radioembolization for the treatment of liver tumors general principles. *American journal of clinical oncology* **2012**, 35 (1), 91-9.
4. C. E. Rosenbaum; H. M. Verkooijen; M. G. Lam, et al., Radioembolization for treatment of salvage patients with colorectal cancer liver metastases: a systematic review. *Journal of nuclear medicine : official publication, Society of Nuclear Medicine* **2013**, 54 (11), 1890-5.
5. M. Cremonesi; C. Chiesa; L. Strigari, et al., Radioembolization of hepatic lesions from a radiobiology and dosimetric perspective. *Frontiers in oncology* **2014**, 4, 210.
6. A. J. A. T. Braat; M. L. J. Smits; M. N. G. J. A. Braat, et al., 90Y Hepatic Radioembolization: An Update on Current Practice and Recent Developments. *J. Nucl. Med.* **2015**, 56 (7), 1079-1087.
7. A. F. van den Hoven; C. E. Rosenbaum; S. G. Elias, et al., Insights into the Dose-Response Relationship of Radioembolization with Resin 90Y-Microspheres: A Prospective Cohort Study in Patients with Colorectal Cancer Liver Metastases. *Journal of nuclear medicine : official publication, Society of Nuclear Medicine* **2016**, 57 (7), 1014-9.
8. S. Shanehsazzadeh; A. Lahooti; H. Yousefnia, et al., Comparison of estimated human dose of (68)Ga-MAA with (99m)Tc-MAA based on rat data. *Annals of nuclear medicine* **2015**, 29 (8), 745-53.
9. E. Garin; Y. Rolland; S. Laffont, et al., Clinical impact of (99m)Tc-MAA SPECT/CT-based dosimetry in the radioembolization of liver malignancies with (90)Y-loaded microspheres. *European journal of nuclear medicine and molecular imaging* **2016**, 43 (3), 559-75.
10. T. W. Leung; W. Y. Lau; S. K. Ho, et al., Radiation pneumonitis after selective internal radiation treatment with intraarterial 90yttrium-microspheres for inoperable hepatic tumors. *Int. J. Radiat. Oncol. Biol. Phys.* **1995**, 33 (4), 919-24.
11. A. K. Jha; N. Purandare; S. A. Shah, et al., Is there a correlation between planar scintigraphy after Tc-99m-MAA and Y-90 administration? *Nucl. Med. Commun.* **2016**, 37 (2), 107-109.

12. M. Patra; K. Zarschler; H. J. Pietzsch, et al., New insights into the pretargeting approach to image and treat tumours. *Chemical Society reviews* **2016**, *45* (23), 6415-6431.
13. O. C. Boerman; F. G. van Schaijk; W. J. G. Oyen, et al., Pretargeted Radioimmunotherapy of Cancer: Progress Step by Step. *Journal of nuclear medicine : official publication, Society of Nuclear Medicine* **2003**, *44*, 400-411.
14. S. Gaur; Y. Wang; L. Kretzner, et al., Pharmacodynamic and pharmacogenomic study of the nanoparticle conjugate of camptothecin CRLX101 for the treatment of cancer. *Nanomedicine : nanotechnology, biology, and medicine* **2014**, *10* (7), 1477-86.
15. Z. Dan; H. Cao; X. He, et al., Biological stimuli-responsive cyclodextrin-based host-guest nanosystems for cancer therapy. *International journal of pharmaceutics* **2015**, *483* (1-2), 63-8.
16. M. T. Rood; S. J. Spa; M. M. Welling, et al., Obtaining control of cell surface functionalizations via Pre-targeting and Supramolecular host guest interactions. *Scientific reports* **2017**, *7*, 39908.
17. M. Oikonomou; J. Wang; R. R. Carvalho, et al., Ternary supramolecular quantum-dot network flocculation for selective lectin detection. *Nano Res* **2016**, *9* (7), 1904-1912.
18. S. J. Spa; A. Bunschoten; M. T. M. Rood, et al., Orthogonal Functionalization of Ferritin via Supramolecular Re-Assembly. *Eur J Inorg Chem* **2015**, *2015* (27), 4603-4610.
19. M. M. Welling; A. Paulusma-Annema; H. S. Balter, et al., Technetium-99m labelled antimicrobial peptides discriminate between bacterial infections and sterile inflammations. *European journal of nuclear medicine* **2000**, *27* (3), 292-301.
20. M. M. Welling; A. Bunschoten; J. Kuil, et al., Development of a Hybrid Tracer for SPECT and Optical Imaging of Bacterial Infections. *Bioconjugate Chem.* **2015**, *26* (5), 839-849.
21. W. Branderhorst; B. Vastenhouw; F. J. Beekman, Pixel-based subsets for rapid multipinhole SPECT reconstruction. *Phys. Med. Biol.* **2010**, *55* (7), 2023-34.
22. M. N. van Oosterom; R. Kreuger; T. Buckle, et al., U-SPECT-BioFluo: an integrated radionuclide, bioluminescence, and fluorescence imaging platform. *EJNMMI Res.* **2014**, *4* (1), 56-56.
23. A. M. Loening; S. S. Gambhir, AMIDE: a free software tool for multimodality medical image analysis. *Mol. Imaging* **2003**, *2* (3), 131-7.
24. H. Kasuya; D. K. Kuruppu; J. M. Donahue, et al., Mouse models of subcutaneous spleen reservoir for multiple portal venous injections to treat liver malignancies. *Cancer. Res.* **2005**, *65* (9), 3823-7.
25. M. R. Eftink; M. L. Andy; K. Bystrom, et al., Cyclodextrin Inclusion Complexes: Studies of the Variation in the Size of Alicyclic Guests. *Journal of the American Chemical Society* **1989**, *111* (17), 6765-6772.

26. A. Mulder; T. Auletta; A. Sartori, et al., Divalent binding of a Bis(adamantyl)-functionalized calix[4]arene to cyclodextrin-based hosts: An Experimental and Theoretical Study on Multivalent Binding in Solution and at Self-Assembled Monolayers. *Journal of the American Chemical Society* **2004**, 126 (21), 6627-6636.
27. R. Chandra; J. Shamoun; P. Braunstein, et al., Clinical Evaluation of an Instant Kit for Preparation of ^{99m}Tc-MAA for Lung Scanning. *Journal of nuclear medicine : official publication, Society of Nuclear Medicine* **1973**, 14, 702-705.
28. H. Kasuya; D. K. Kuruppu; J. M. Donahue, et al., Mouse Models of Subcutaneous Spleen Reservoir for Multiple Portal Venous Injections to Treat Liver Malignancies. *Cancer Res* **2005**, 65 (9), 3823-3827.
29. R. S. Irwin; P. W. Doherty; T. Bartter, et al., Evaluation of Technetium Pertechnetate as a Radionuclide Marker of Pulmonary Aspiration of Gastric Contents in Rabbits. *Chest* **1988**, 93 (6), 1270-1275.
30. K. M. Tsoi; S. A. MacParland; X. Z. Ma, et al., Mechanism of hard-nanomaterial clearance by the liver. *Nature materials* **2016**, 15 (11), 1212-1221.
31. O. R. Brouwer; N. S. van den Berg; H. M. Matheron, et al., A hybrid radioactive and fluorescent tracer for sentinel node biopsy in penile carcinoma as a potential replacement for blue dye. *European urology* **2014**, 65 (3), 600-9.
32. N. S. van den Berg; O. R. Brouwer; B. E. Schaafsma, et al., Multimodal Surgical Guidance during Sentinel Node Biopsy for Melanoma: Combined Gamma Tracing and Fluorescence Imaging of the Sentinel Node through Use of the Hybrid Tracer Indocyanine Green-^{99m}Tc-Nanocolloid. *Radiology* **2015**, 275, 521-529.
33. G. H. Kleinjan; O. R. Brouwer; H. M. Matheron, et al., Hybrid radioguided occult lesion localization (hybrid ROLL) of (18)F-FDG-avid lesions using the hybrid tracer indocyanine green-(^{99m}Tc)-nanocolloid. *Revista espanola de medicina nuclear e imagen molecular* **2016**, 35 (5), 292-7.





SUPPORTING INFORMATION CHAPTER 3

**A Supramolecular Approach for
Liver Radioembolization**

EXPERIMENTAL SECTION

Stability of $^{99m}\text{Tc-Cy5}_{0.5}\text{CD}_{10}\text{PIBMA}_{39}$ in FCS

$^{99m}\text{Tc-Cy5}_{0.5}\text{CD}_{10}\text{PIBMA}_{39}$ was dissolved in FCS (2.5 $\mu\text{g}/\text{mL}$) and shaken in a water bath at 37 °C for 44 h. After 2, 20, and 44 h 0.1 mL samples were taken and their composition was analyzed by PD-10-SEC.

Stability of $^{99m}\text{Tc-Maa-Ad}$ in FCS

Lyophilized MAA (2 mg) was dissolved in 1 mL of saline (0.9% NaCl, sterile and pyrogen-free, B. Braun Medical Supplies, Inc., Oss, The Netherlands). To one portion 100 mL of a freshly eluted $^{99m}\text{Tc-Na-pertechnetate}$ solution (500 MBq/mL, Mallinckrodt Medical B.V.) was added and the mixture was gently stirred in a shaking water bath for 1 h at 37 °C. Thereafter, the solution was washed 2 times PBS by 2 centrifugation steps (3 min, 1,200 rpm). Next, 20 mL of Ad-TFP (10 mg/mL DMSO) was added. After allowing it to react in a shaking water bath for 1 h at 37 °C, the reaction mixture was washed 2 times with PBS by 2 centrifugation steps (3 min, 1,200 rpm) and the pellet was dissolved in 1 mL PBS. Of this solution, 0.1 mL was added to 0.9 mL of FCS and was shaken in a water bath at 37 °C up to 44 h. At 2, 20, and 44 h after incubation 0.1 mL samples were taken and their composition analysed by PD-10 SEC.

Stability of $\text{Cy5}_{0.5}\text{CD}_{10}\text{PIBMA}_{39}$ and MAA-Ad complexes in FCS

Mixtures of either MAA-Ad (0.2 mg/mL) with $^{99m}\text{Tc-Cy5}_{0.5}\text{CD}_{10}\text{PIBMA}_{39}$ (10 $\mu\text{g}/\text{mL}$, 1 MBq) or $^{99m}\text{Tc-MAA-Ad}$ (0.2 mg/mL, 1 MBq) with $\text{Cy5}_{0.5}\text{CD}_{10}\text{PIBMA}_{39}$ (10 $\mu\text{g}/\text{mL}$) were prepared in 0.2 mL PBS and the solutions were incubated for 1 h in a shaking water bath at 37 °C. Thereafter, the formed complexes were washed twice with PBS by centrifugation (5 min, 3,000 g) and resuspended in 0.2 mL PBS. Subsequently, 0.1 mL thereof was mixed with 1 mL FCS and shaken at 37 °C in a shaking water bath up to 44 h. At 2, 20, and 44 h after incubation 0.1 mL samples were taken and diluted in 1 mL of PBS and after spinning for 5 min at 7,000 rpm, the decay corrected radioactivity of the pellet and supernatant was measured in a dose-calibrator. Hereby a reduction, in the radioactivity of the pellet represents dissociation or instability (% of binding).

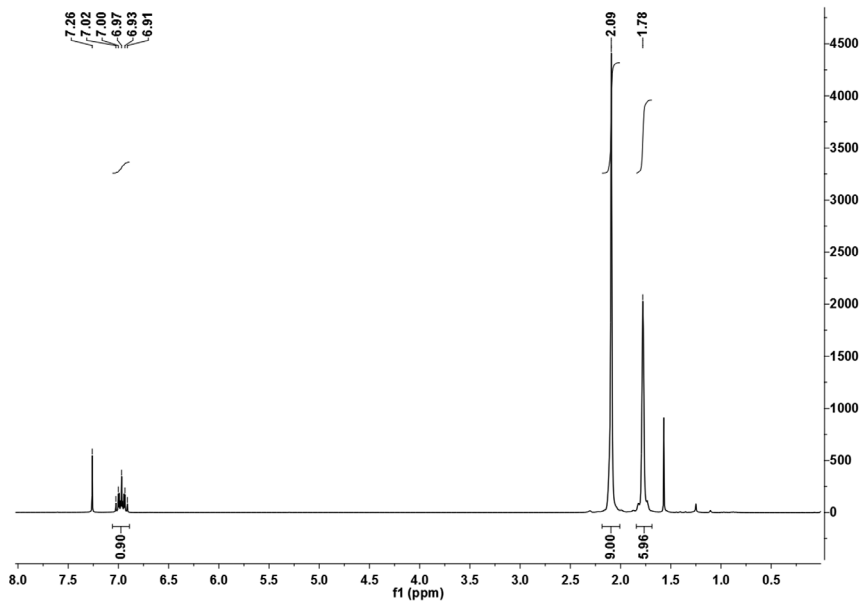
RESULTS AND DISCUSSION

To quantify the difference of $^{99m}\text{Tc-Cy5}_{0.5}\text{CD}_{10}\text{PIBMA}_{39}$ accumulation after pre-administration of nothing, MAA or MAA-Ad for all the investigated organs (Table 1 and Table S1), the relative increase of $^{99m}\text{Tc-Cy5}_{0.5}\text{CD}_{10}\text{PIBMA}_{39}$ accumulation with regard to the $^{99m}\text{Tc-Cy5}_{0.5}\text{CD}_{10}\text{PIBMA}_{39}$ reference distribution (Figure 3) was calculated (Figure S2). If there was a significant increase with $p < 0.01$ this was indicated with a *. When MAA or MAA-Ad was administered i.v. the uptake in the lungs was found highest (but this difference was not significant due to large variations). While locally administered MAA or MAA-Ad resulted in significant increases in spleen, liver and kidneys; pre-administration of MAA or MAA-Ad was performed via the spleen. With the i.v. pre-administration method (Model I) the polymer accumulation increased in more organs compared to the local pre-administration method (Model II), underlining once more the fact that the system works best for the clinically more relevant model i.e. local administration. The significance data can be slightly misleading since increases from e.g. 0.1 %ID/g to 0.3 %ID/g in the brain will be displayed as significant (Table 1 and Table S1).

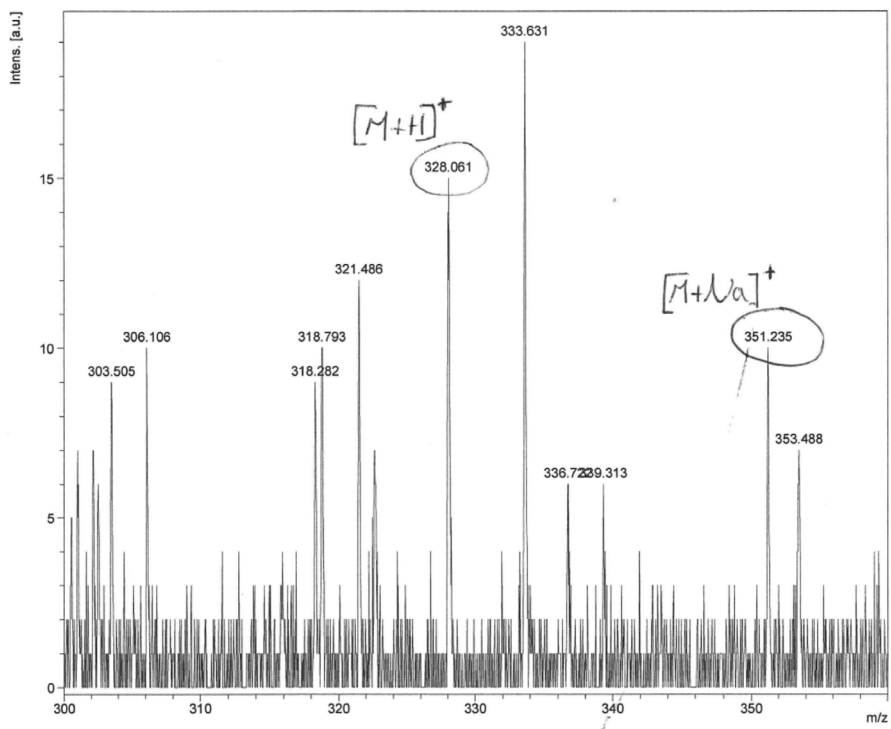
Table S1. The biodistribution of $^{99m}\text{Tc-Cy5}_{0.5}\text{CD}_{10}\text{PIBMA}_{39}$ following injection of: none (reference distribution), MAA, or MAA-Ad and the biodistribution of $^{99m}\text{Tc-MAA-Ad}$ administered via Models I and II. Data (expressed as the mean \pm SD of the percentage of the injected dose per gram tissue (%ID/g) of 5 observations) are calculated from radioactivity counts in various tissues at 2 h post-injection of the tracer.

| Tissue | Reference distribution host | Distribution of host ($^{99m}\text{Tc-Cy5}_{0.5}\text{CD}_{10}\text{PIBMA}_{39}$) following injection of indicated guest | | | | Reference distribution guest | |
|----------------|---|--|-----------------|---------------|------------------|-----------------------------------|------------------------------------|
| | $^{99m}\text{Tc-Cy5}_{0.5}\text{CD}_{10}\text{PIBMA}$ | Model I: MAA | Model I: MAA-Ad | Model II: MAA | Model II: MAA-Ad | Model I: $^{99m}\text{Tc-MAA-Ad}$ | Model II: $^{99m}\text{Tc-MAA-Ad}$ |
| | mean | Mean | Mean | Mean | mean | mean | mean |
| Salivary gland | 3.5 \pm 0.4 | 9.1 \pm 3.3 | 17.3 \pm 3.5 | 3.0 \pm 0.6 | 3.9 \pm 0.1 | N.A. | 8.9 \pm 1.9 |
| Stomach | 4.4 \pm 0.8 | 19.8 \pm 7.6 | 10.8 \pm 1.4 | 3.0 \pm 0.6 | 2.3 \pm 0.8 | 11.5 \pm 9.1 | 12.7 \pm 3.1 |
| Intestines | 0.8 \pm 0.3 | 1.5 \pm 0.6 | 1.5 \pm 0.3 | 0.9 \pm 0.0 | 0.7 \pm 0.3 | 0.6 \pm 0.3 | 1.8 \pm 0.5 |

A



B



◀ **Figure S1. A)** NMR of Ad-TFP measured in CDCl_3 . **B)** Mass spectra of Ad-TFP, only low signals could be obtained as the compound is hard to ionize. Signals corresponding to the mass matrix are therefore clearly visible as well.

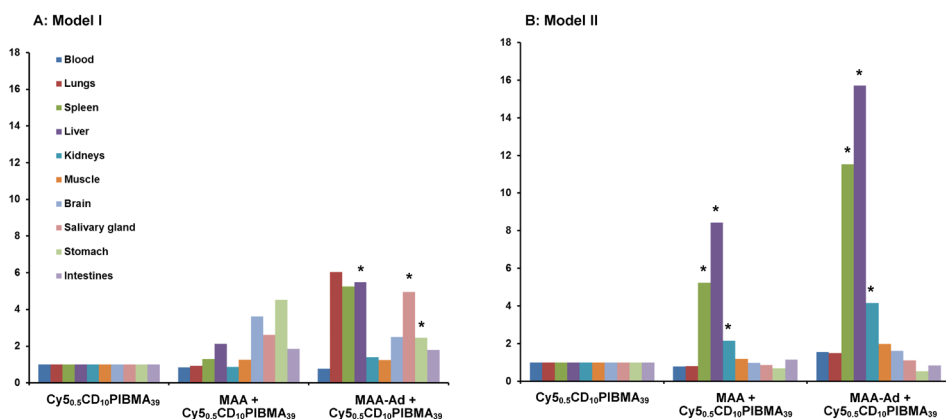


Figure S2. Relative increase of $^{99\text{m}}\text{Tc-Cy5.5CD}_{10}\text{PIBMA}_{39}$ after i.v. (A) or Local (B) administration of MAA or MAA-Ad with respect to $^{99\text{m}}\text{Tc-Cy5.5CD}_{10}\text{PIBMA}_{39}$ accumulation in the indicated organ when no particles are pre-administered. With significance of difference ($p < 0.01$) indicated by *.

Both the individual components and the complexes formed demonstrated a high serum stability (Figure S3). No clear metabolites of the individual components could be defined. This said some dissociation of $^{99\text{m}}\text{Tc}$ was observed both from the individual components as from the complexes formed. Nevertheless, the complex yielded around a 80% stability at 44 h.

As the $\text{Cy5.5CD}_{10}\text{PIBMA}_{39}$ polymer was not optimized for $^{99\text{m}}\text{Tc}$ chelation, but merely provided coordination sides by its free $-\text{COOH}$ moieties, some dissociation of $^{99\text{m}}\text{Tc}$ was observed *in vivo* (Table S1, Figure S3). When this occurred, characteristic uptake in the salivary glands and stomach could be observed. As these findings did not complicate the assessment of the pre-targeting ability, no attempts were made to optimize the chelation stability.

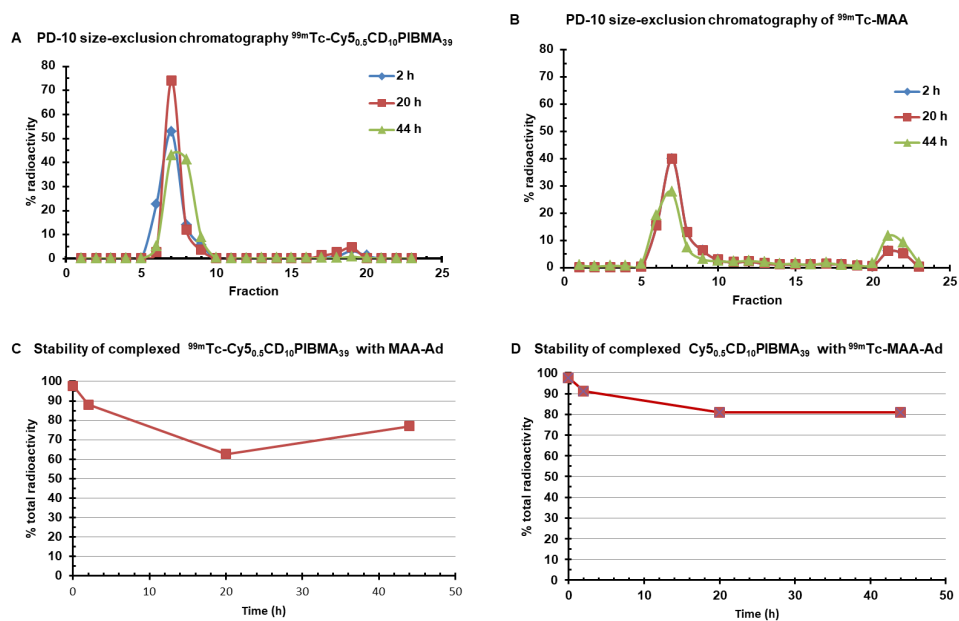


Figure S3. A) Serum stability of $^{99m}\text{Tc-Cy}_{5.0.5}\text{CD}_{10}\text{PIBMA}_{39}$ (peak around fraction 18 indicated smaller fragments), **B)** Serum stability of $^{99m}\text{Tc-MAA}$ (peak around fraction 22 indicated some free ^{99m}Tc), **C)** Serum stability of $[^{99m}\text{Tc-Cy}_{5.0.5}\text{CD}_{10}\text{PIBMA}_{39} * \text{MAA-Ad}]$ complexes, **D)** Serum stability of $[\text{Cy}_{5.0.5}\text{CD}_{10}\text{PIBMA}_{39} * ^{99m}\text{Tc-MAA-Ad}]$ complexes.





Adapted from: Welling MM, Spa SJ, van Willigen DM, Rietbergen DDD, Roestenberg M, Buckle T, van Leeuwen FWB.

J Control Release. 2019;293:126-134



CHAPTER 4

***In vivo* stability of supramolecular host-guest complexes monitored by dual-isotope multiplexing in a pre-targeting model of experimental liver radioembolization**

ABSTRACT

Introduction

Cyclodextrin (CD) based supramolecular interactions have been proposed as nanocarriers for drug delivery. We previously explored the use of supramolecular interactions to perform targeted hepatic radioembolization. In a two-step procedure the appropriate location of the diagnostic pre-targeting vector can first be confirmed, after which the therapeutic vector will be targeted through multivalent host-guest interactions. Such a procedure would prevent therapeutic errors due to a mismatch between diagnostic and therapeutic procedures. In the current study we explored the use of dual-isotope imaging to assess the *in vivo* stability of the formed complex and individual components.

Methods

Dual-isotope imaging of the host and guest vectors was performed after labeling of the pre-targeted guest vector, being adamantane (Ad) functionalized macro-aggregated albumin (MAA) particles, with technetium-99m (^{99m}Tc -MAA-Ad). The host vector, $\text{Cy5}_{0.5}\text{CD}_9\text{PIBMA}_{39}$, was labeled with indium-111 (^{111}In - $\text{Cy5}_{0.5}\text{CD}_9\text{PIBMA}_{39}$). The *in situ* stability of both the individual vectors and the resulting $[\text{MAA-Ad-}^{111}\text{In-Cy5}_{0.5}\text{CD}_9\text{PIBMA}_{39}]$ complexes was studied over 44 h at 37 °C in a serum protein-containing buffer. *In vivo*, the host vector $^{111}\text{In-Cy5}_{0.5}\text{CD}_9\text{PIBMA}_{39}$ was administered two hours after local deposition of ^{99m}Tc -MAA-Ad in mice. Dual-isotope SPECT imaging and quantitative biodistribution studies were performed at 2 and until 44 h post intravenous host vector administration.

Results

The individual vectors portrayed less than 5% dissociation of the radioisotope over the course of 20 h. Dissociation of $[\text{MAA-Ad-}^{111}\text{In-Cy5}_{0.5}\text{CD}_9\text{PIBMA}_{39}]$ complexes remained within a 10–20% range after incubation in serum. *In vivo* dual-isotope SPECT imaging of host-guest interactions revealed co-localization of the tracer components. Quantitative assessment of the biodistribution revealed that the hepatic accumulation of the host vector nearly doubled between 2 h and 44 h post-injection (from 14.9 ± 6.1 %ID/g to 26.2 ± 2.1 %ID/g).

Conclusions

Assessment of intra-hepatic host-guest complexation was successfully achieved using dual isotope multiplexing, underlining the complex stability that was found *in situ* (up to 44 h in serum). Overall, the results obtained in this study highlight the potential of supramolecular chemistry as a versatile platform that could advance the field of nanomedicine.

INTRODUCTION

Hepatocellular carcinoma (HCC) and liver metastases of colorectal cancer (mCRC) are the third most common cause of cancer-related deaths worldwide.^{1,2} With currently 1.12 million deaths worldwide per year, both the incidence of these cancer types and their impact on health expenditure is increasing. Surgical excision is considered the first-line therapy but cannot be applied in grade 3–5 staged HCC. The substantial portion of inoperable patients that present metastatic liver tumors are therefore in need of alternative treatment strategies.^{3–5} One relatively novel treatment option that has presented potential to effectively manage these hepatic tumors is radio- or chemo-embolization⁶; of these two radioembolization is the most frequently applied. In HCC patients this embolization strategy has proven to be beneficial to survival in patients with HCC.⁷

Radioembolization is performed using a two-step interventional radiological theranostic procedure. In this procedure Single Positron Emission Computed Tomography (SPECT) imaging of macro-aggregated albumin (scout scan delivered by a CT guided catheter; ^{99m}Tc-MAA; d = 10–40 μm) is used to explore the potential of selective internal radiotherapy (i.e., radioembolization). When correct localization of the ^{99m}Tc-MAA is visualized, therapeutic β-emitting microparticles (d = 15–25 μm)⁸ containing ⁹⁰Y (SIR-Spheres®, Sirtex; Therasphere, BTG®) or ¹⁶⁶Ho (QuiremSpheres; Quirem Medical) are injected two weeks later via the same positioned catheter in the *a. hepatica*.⁹ The overlap in size and retention properties between the albumin macroaggregates and the microparticles has been sufficient for the clinical guidelines to define a ^{99m}Tc-MAA scout scan as a standard requirement to predict accurate delivery of therapeutic microspheres during a second intervention. Despite this inclusion in the guidelines, a mismatch between the scout scan and therapy delivery which can lead to adverse side effects and suboptimal dose delivery⁶ is seen in 30% of the cases.^{10–12} This indication signifies a need for innovative solutions that help refine the correlation between the two interventions (i.e., the scout scan and therapeutic delivery). Another drawback is the delay (≈ 14 days) between the execution of the scout scan and the therapeutic intervention that mainly occurs as result of the production/delivery time of the β-emitting microspheres.⁹

While some groups have proposed to use low-dose application of therapeutic microspheres during scout scans,¹³ we have previously explored an alternative route based on the use of a pre-targeting strategy. In this latter approach, the agent used to create a diagnostic scout scan provides the target for a secondary agent containing the therapeutic component. As proof of concept we explored cyclodextrin (CD)-based host and adamantane

vector.¹⁶ To evaluate the integrity of the individual compounds and the host-guest complexes formed, *in vitro* and *in vivo* stability studies were related to *in vivo* SPECT imaging and quantitative biodistribution patterns of both components. These longitudinal assessments were then used to determine the chemical refinements that are required to contemplate translation of the technology into the clinic.

Materials and Methods

General analytical procedures and information on the materials used are provided in the Supporting Information (SI).

Synthesis and analysis

Synthesis and characterization of both adamantane-tetrafluorophenol (Ad-TFP) and β -cyclodextrin-poly(isobutylene-alt-maleic-anhydride) (Cy_{5,0.5}CD₉PIBMA₃₉, ~18.7 kDa, diameter, ~11.7 nm) were carried out as recently described in.^{14, 15}

Radiolabeling of host vector MAA(-Ad) with technetium-99m and stability testing

Labeling of macro-aggregated albumin (MAA) with technetium (^{99m}Tc-MAA) and functionalization with Ad-TFP was carried out as described previously.¹⁵ The stability of the ^{99m}Tc-chelation was determined in fetal calf serum (FCS, Life Technologies Inc. CA) after 2, 4, and 20 h. The release of radioactivity was determined after centrifugation and two washing steps with PBS (3 min, 1,200xg) as described previously.¹⁵

Labeling of Cy_{5,0.5}CD₉PIBMA₃₉ with indium-111 (¹¹¹In-Cy_{5,0.5}CD₉PIBMA₃₉) and stability testing

The host-vector, Cy_{5,0.5}CD₉PIBMA₃₉, which contains an abundance of freely available -COOH moieties, was radiolabeled with indium-111. To 10 μ L of Cy_{5,0.5}CD₉PIBMA₃₉ (1 mg/mL PBS) was added 40 mL of 0.25 M ammonium acetate (pH 5) and 25-150 mL of an acidic solution of ¹¹¹InCl₃ (370 MBq/mL, Mallinckrodt Medical, Petten, The Netherlands). This mixture was gently shaken in the dark for 1 h at 37 °C. Thereafter, the pH was adjusted to 7.5 in PBS. The radiochemical purity of ¹¹¹In-Cy_{5,0.5}CD₉PIBMA₃₉ was determined at 1 and 20 h by instant thin layer chromatography (ITLC) on 1x7 cm ITLC-SG paper strips (Agilent Technologies, USA) with 0.25 M ammonium acetate (pH 5) as mobile phase.

The serum stability of the ^{99m}Tc-chelation was determined in fetal calf serum (FCS, Life Technologies Inc. CA). After 24 h the release of radioactivity was determined with centrifugation and washing steps as described above. To determine the stability in FCS,

$^{111}\text{In-Cy5}_{0.5}\text{CD}_9\text{PIBMA}_{39}$ was diluted in FCS (2.5 $\mu\text{g}/\text{mL}$) and shaken in a water bath at 37 °C for 20 h. After 2, 4, and 20 h samples of 0.1 mL were taken and the release of radioactivity was assessed by ITLC. For comparison, a similar set-up was performed for $^{111}\text{In-Cy5}_{0.5}\text{CD}_9\text{PIBMA}_{39}$.¹⁵

***In vitro* host-guest interactions and complex stability**

In line with previous studies,¹⁵ *in vitro* evidence for the host-guest complex formation between MAA-Ad and $^{111}\text{In-Cy5}_{0.5}\text{CD}_9\text{PIBMA}_{39}$ was provided by comparing the $^{111}\text{In-Cy5}_{0.5}\text{CD}_9\text{PIBMA}_{39}$ binding to MAA-Ad and non-functionalized MAA (control). Mixtures of 0.1 mL containing either MAA-Ad or MAA (0.1 mg/mL) with 0.1 mL $^{111}\text{In-Cy5}_{0.5}\text{CD}_9\text{PIBMA}_{39}$ (10 $\mu\text{g}/\text{mL}$, 1 MBq) were prepared in 0.8 mL PBS and the solutions were incubated for 1 h in a shaking water bath at 37 °C. After 2 rounds of spinning and washing with PBS for 5 min at 1,500 x g, the decay corrected radioactivity of the pellet and supernatant was measured in a dose-calibrator. Following correction for background activity, the host-guest interaction was expressed as the percentage of the total amount of radioactivity (% binding).

For stability measurements, either 0.1 mL MAA-Ad (0.1 mg/mL) with 0.1 mL $^{111}\text{In-Cy5}_{0.5}\text{CD}_9\text{PIBMA}_{39}$ (10 $\mu\text{g}/\text{mL}$, 1 MBq) or 0.1 mL $^{99\text{m}}\text{Tc-MAA-Ad}$ (0.1 mg/mL, 1 MBq) with 0.1 mL $\text{Cy5}_{0.5}\text{CD}_9\text{PIBMA}_{39}$ (10 $\mu\text{g}/\text{mL}$) were prepared as described above and after removal of non-complexed materials the complex was diluted in either 0.8 mL PBS or FCS and incubated for 44 h in a shaking water bath at 37 °C. Following incubation durations of 2, 20, and 44 h, 0.1 mL samples were diluted in 1 mL of PBS and centrifuged for 5 min at 1,500 x g. The decay corrected radioactivity of both the pellet and supernatant was measured in a dose-calibrator. Hereby, the radioactivity of the pellet represented association of $\text{Cy5}_{0.5}\text{CD}_9\text{PIBMA}_{39}$ to MAA-Ad (expressed as % of binding).

IMAGING EXPERIMENTS

Animals

In vivo studies were performed using 2–4-month-old Swiss mice (20–35 g, Crl:OF1 strain, Charles River Laboratories, USA). All animal studies were approved by the institutional Animal Ethics Committee (DEC permit 12160) of the Leiden University Medical Center. Mice were kept under specific pathogen-free conditions in the animal housing facility of the LUMC. Food and water were provided *ad libitum*.

Animal model

An embolization setup of the liver was performed according to previously described procedures.^{15,17} In brief, ^{99m}Tc-MAA-Ad (0.1 mg/mL, 2-5 MBq, n=6) was injected into the spleen of the mice (embolization step). Two h after embolization, a second injection with ¹¹¹In-Cy5_{0.5}CD₉PIBMA₃₉ (1 µg, 10 MBq) was administered I.V.. At 2, 12, 20, or 44 h the animals were imaged using SPECT and fluorescence imaging and quantified with biodistribution studies (see SPECT and fluorescence imaging protocols and biodistribution studies described below). Non-functionalized ^{99m}Tc-MAA (0.1 mg/mL, 2-5 MBq, n=6), or mere PBS (n=3) served as controls.

General SPECT imaging

SPECT imaging was performed as previously described.¹⁵ In brief, mice were placed and fixed onto a dedicated positioning bed of a three-headed U-SPECT-2 (MILabs, Utrecht, the Netherlands) at various intervals after injection of the host vector, while being under continuous 1-2% isoflurane anesthesia.¹⁸ Radioactivity counts (range 0-600 keV) from total body scans were acquired for 30 min. For reconstruction from list mode data, the photo peak energy window was centered at 140 keV (for technetium-99m) or 240 keV (for indium-111) with a window width of 20%. Longitudinal differences in ¹¹¹In accumulation in mice were quantified by calculating radioactivity counts in regions of interest (ROI's). For this purpose, on the reconstructed images, using AMIDE's Medical Image Data Examiner (<http://amide.sourceforge.net>) ROI's were drawn over various tissues (including bone and joints as these were not assessed with routine biodistribution studies) allowing to determine radioactive counts in various tissues over time in a single mouse. ROI's drawn over the jugular veins were taken as a representative for the radioactivity in blood values. After imaging, mice were euthanized and the organs were removed and weighed to determine the percentage of injected dose per gram tissue (%ID/g). Blood samples obtained at various intervals of sacrifice, were used to determine the clearance from the blood fraction (expressed as the pharmacological half-life $t_{1/2}$) was calculated using GraphPad Prism version 5.01 for Windows (GraphPad Software, San Diego CA, USA).

Fluorescence imaging protocol

Dual-labeled Cy5_{0.5}CD₉PIBMA₃₉ was also equipped with a Cy5 fluorophore to perform confocal microscopy as described previously,^{14,15} and in this study allows to perform macroscopic and eventually microscopic evaluation of the fluorescent signal of Cy5_{0.5}CD₉PIBMA₃₉ in excised tissues from mice using a preclinical IVIS Spectrum imaging

system (Caliper Life Science, Hopkinton, MA). Images of the Cy5-dye were acquired following excitation at 640 nm, and light was collected > 680 nm (acquisition time 5 s). Quantitative analysis of the fluorescence in the tissues (photons/sec/cm²) was performed using the Living Image software from xenogeny v 3.2 (Caliper LS) at equal image adjustment settings.

Statistical analysis

All data are presented as mean value (\pm SD) of 3–6 independent measurements. Statistical analysis for differences between groups in the animal studies were performed by with Student's two-tailed independent samples T-test. Significance was assigned for p -values < 0.05. All analyses and calculations were performed using Microsoft® Office Excel 2010 and GraphPad Prism version 5.01 for Windows (GraphPad Software, San Diego, CA, USA).

RESULTS

Radiolabeling, functionalization, and stability of the vectors

Radiolabeling of guest vector with technetium-99m for 1 h at 37 °C yielded $92.8 \pm 3.8\%$ binding of the total added radioactivity. After incubating ^{99m}Tc-MAA in FCS at 37 °C for 20 h the release of radioactivity was shown to be less than 5%. Labeling of ¹¹¹In to Cy5_{0.5}CD₉PIBMA₃₉ for 1 h at 37 °C yielded $95.6 \pm 3.6\%$ of binding of the total added radioactivity determined by instant thin layer chromatography (ITLC). To determine the chelation stability, the host vector was incubated in FCS at 37 °C for 20 h. As depicted in Figure 1A the amount of ¹¹¹In-activity dissociating from the host after incubating in serum at 37 °C for 20 h was about 5% which indicates that the labeling was of the host with indium-111 was robust.

***In vitro* host-guest interactions**

Host-guest supramolecular interactions *in vitro* increased complexation of the ¹¹¹In-Cy5_{0.5}CD₉PIBMA₃₉ to MAA-Ad by nearly two-fold as compared to what was achieved with non-Ad-functionalized MAA ($53.8 \pm 4.3\%$ vs $29.4 \pm 5.1\%$ respectively; $p < 0.001$, $n=8$; Figure 1B). This indicates that host-guest interactions influence the complex formation. After 44 h incubation in either PBS or FCS, complex dissociation was found to be in the 10–20% range (see Figure 1C).

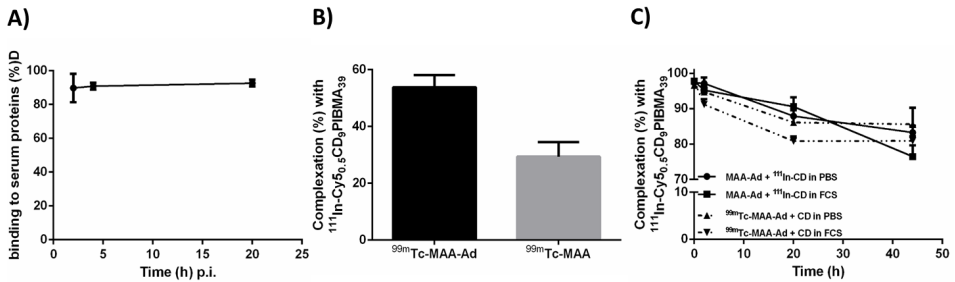


Figure 1. A) Serum binding of $^{111}\text{In-Cy5-CD}_9\text{-PIBMA}_{39}$ over 20 h at 37 °C. **B)** *In vitro* host-guest complexation between guest vectors (MAA-Ad or MAA) and the host-vector ($^{111}\text{In-Cy5}_{0.5}\text{CD}_9\text{PIBMA}_{39}$) after 1 h at 37 °C. Data are expressed as the mean \pm SD of the percentage of binding. **C)** *In vitro* stability determined at 37 °C of the host-guest complexation between guest vector MAA-Ad with host vector $^{111}\text{In-Cy5}_{0.5}\text{CD}_9\text{PIBMA}_{39}$ in PBS or FCS (straight lines) and $^{99\text{m}}\text{Tc-MAA-Ad}$ with $^{111}\text{In-Cy5}_{0.5}\text{CD}_9\text{PIBMA}_{39}$ in PBS or FCS (interrupted lines). Values are expressed as the % of radioactivity associated with the washed pellet.

***In vivo* host-guest complex formation**

To further validate the use of a supramolecular pre-targeting concepts during liver radioembolization, a non-tumor bearing animal model was used. The embolization setup in the liver was performed according to previously described procedures.^{15,17} The most important reason for choosing this approach is that hepatic catheterization in mice is invasive and would have resulted loss of many mice because of heavy bleedings. These bleeding would, in turn, have resulted in radioactive contaminations.

Dual-isotope SPECT imaging facilitated *in vivo* monitoring of host-guest interactions between $^{111}\text{In-Cy5}_{0.5}\text{CD}_9\text{PIBMA}_{39}$ and $^{99\text{m}}\text{Tc-MAA-Ad}$. The 6 h half-life of $^{99\text{m}}\text{Tc}$ meant its distribution could only be reliably monitored up to 20 h p.i. by means of SPECT imaging (Figure 2A). Biodistribution studies displayed residual $^{99\text{m}}\text{Tc-MAA-Ad}$ activity in the spleen (injection site; amounting to $80.4 \pm 23.2\%$ ID/g, $64.2 \pm 5.6\%$ ID/g, and $57.9 \pm 8.4\%$ ID/g at 2, 12, and 20 h p.i. respectively) and demonstrated prolonged diffusion of the radioactive signal from the spleen to the liver (amounting to $13.2 \pm 2.2\%$ ID/g, $36.4 \pm 5.3\%$ ID/g, and $43.0 \pm 20.2\%$ ID/g at 2, 12, and 20 h p.i., respectively; Figure S1).

Host-guest complexation between $^{111}\text{In-Cy5}_{0.5}\text{CD}_9\text{PIBMA}_{39}$ and $^{99\text{m}}\text{Tc-MAA-Ad}$ was monitored *in vivo* by dual-isotope SPECT imaging. Figure 2B shows the distribution of the host vector in mice pretargeted with guest vector at 2, 12, 20 or 44 h p.i. of the host vector SPECT imaging of ^{111}In displayed the biodistribution of the host vector. As a result of the 2.8 d half-life of ^{111}In , the time-related uptake of the host vector in the liver of mice could

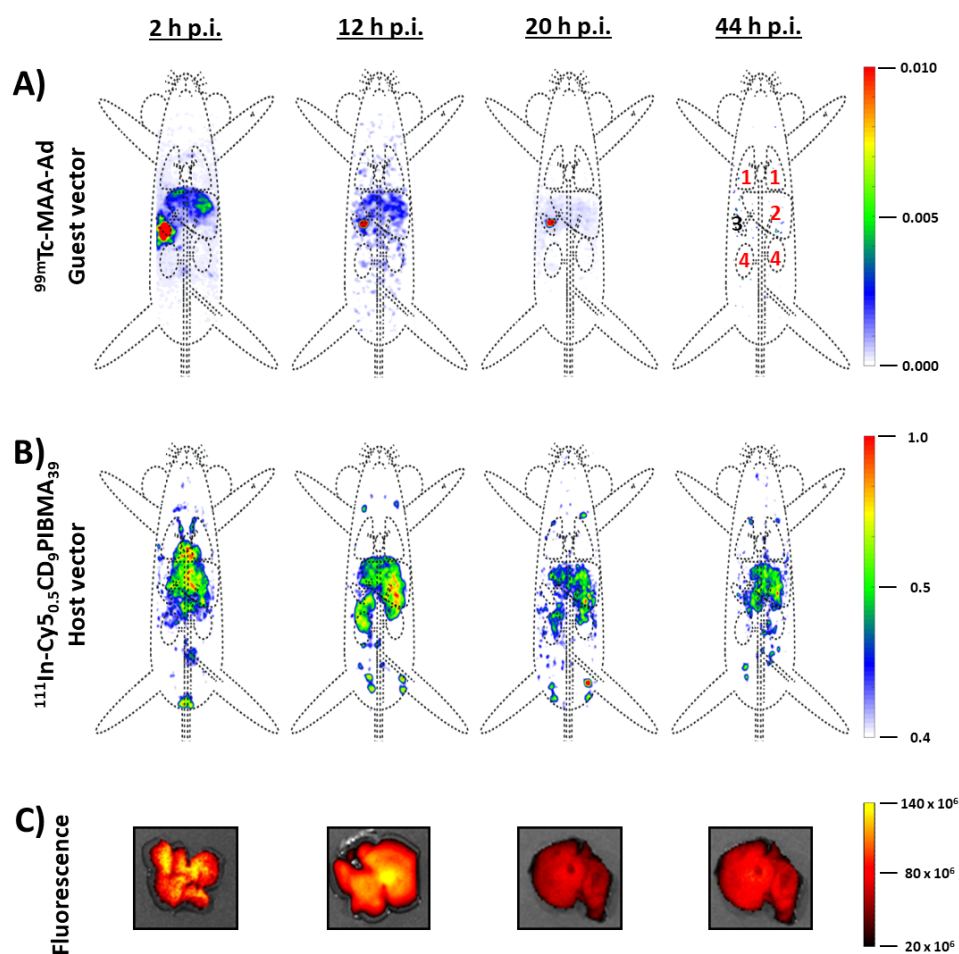


Figure 2. Time-related (2, 12, 20 and 44 h p.i.) dual-isotope SPECT biodistribution of **A)** intrasplenic administration of guest-vector ^{99m}Tc -MAA-Ad and **B)** Intravenous administered host-vector ^{111}In -Cy $_{0.5}$ CD $_9$ PIBMA $_{39}$. Organs are marked as **(1)** lungs, **(2)** liver, **(3)** spleen, and **(4)** kidneys. The scale bars indicate the intensity of radioactivity expressed as arbitrary units. p.i. = post-injection.

be studied up to 44 h p.i. Longitudinal differences in ^{111}In accumulation were quantified either by calculating radioactivity counts in ROI's (Figure 4A–F) or as quantitative biodistribution studies (see Figure 5A & Table S1). These analyses revealed that at 20 h p.i. the hepatic uptake of the host vector was at its maximum (approximately 27 %ID/g). The observed intestinal uptake of ^{111}In -isotopes (Table S2) is indicative for hepatic uptake

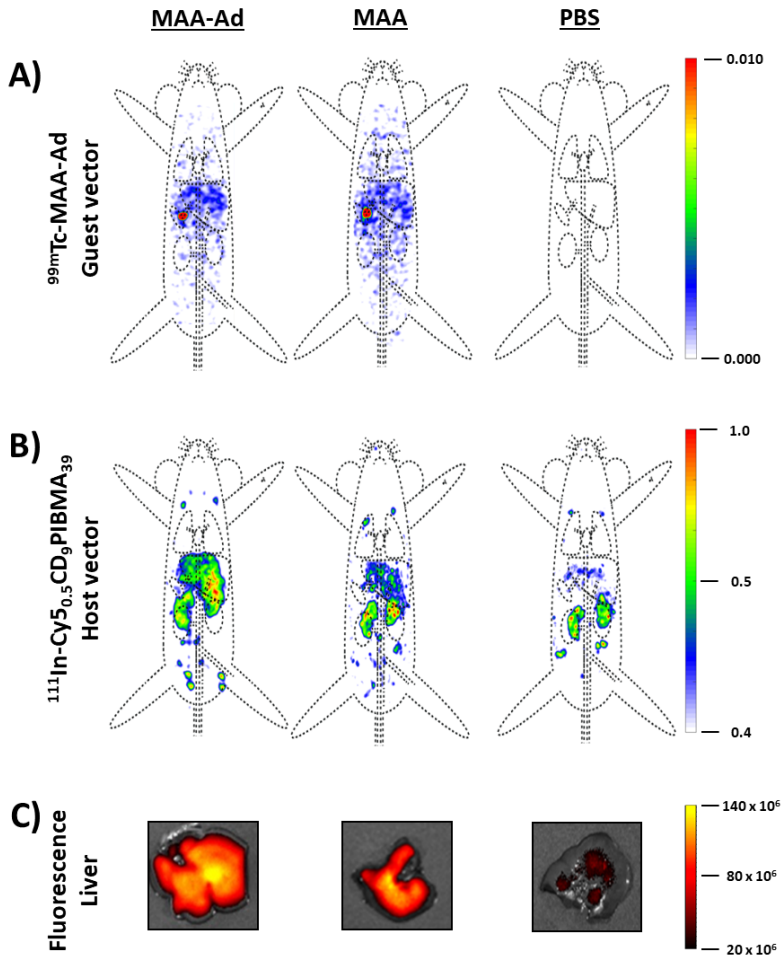


Figure 3. Dual-isotope SPECT biodistribution 12 h p.i. of **A)** mice pre-targeted with intrasplenic administration of guest vector ^{99m}Tc -MAA-Ad. Mice, pre-targeted with either non-functionalized ^{99m}Tc -MAA or PBS are used for comparison. Organs are marked as in Figure 2. **B)** Bio-distribution of host vector ^{111}In -Cy $_{5.0.5}$ CD $_9$ PIBMA $_{39}$ after intravenous administration. **C)** Uptake of the host vector ^{111}In -Cy $_{5.0.5}$ CD $_9$ PIBMA $_{39}$ in the liver determined by *ex-vivo* fluorescence imaging at equal settings. The scale bar indicates the intensity of fluorescence expresses as photons/sec/cm 2 .

followed by intra-intestinal secretion. From 2 h onwards we observed small amounts of ^{111}In accumulation in the shoulder joints, knee joints, pelvis, kidney, and diffuse uptake in bone (Figure 2B, Figure 3B, Figure 4D), but bone uptake remained unchanged over time (Figure 2A, B, Figure 4D). Given the concurrence with known reservoirs for free $^{111}\text{In}^{3+}$,¹⁹⁻²¹

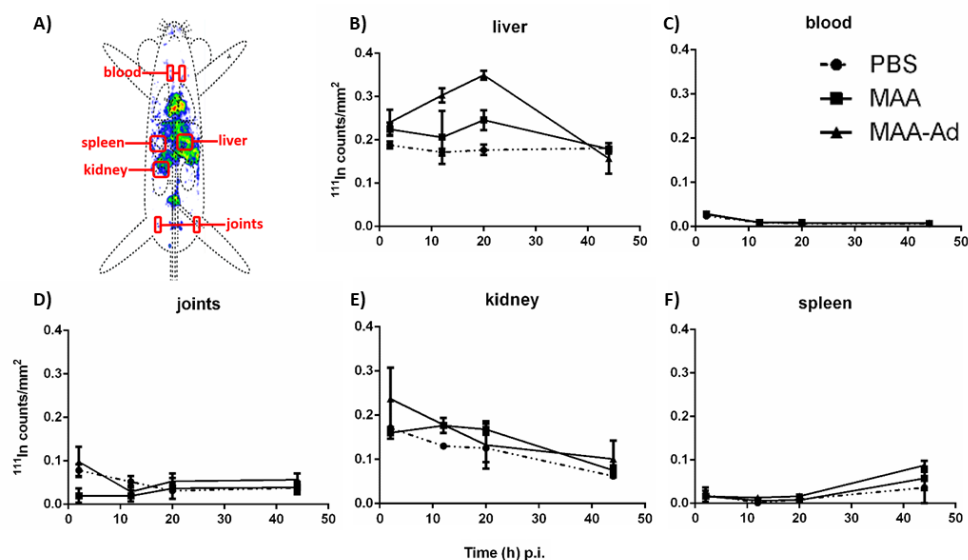


Figure 4. Time-dependent uptake of ^{111}In -Cy $_{5,0.5}$ -CD $_9$ -PIBMA $_{39}$ in various tissues determined from **A)** radioactivity calculations in ROI's. Data are expressed as the ^{111}In radioactivity counts per mm 3 on the scintigrams in regions of interest (ROI's) drawn over **B)** liver, **C)** blood, **D)** joints, **E)** kidney, and **F)** spleen.

the isotope is most likely dissociated from the carboxylic acid moieties on the polymer backbone. Our results indicate that both methods, either by ROI's or biodistribution assays, provide an accurate representation of the accumulation of the host vector in various tissues in mice. Lung shunting, an essential property to prevent side effects due to off-target delivery,^{2,11} was not observed at any time point.

Liver uptake was increased by nearly 3-fold in mice treated with the functionalized pre-targeting vector ($p < 0.01$) as compared to the liver uptake of the host vector in control mice injected with $^{99\text{m}}\text{Tc}$ -MAA (10.8 ± 4.7 %ID) or PBS (8.6 ± 3.1 %ID; Figure 3B & Table S1, Figure 4B). Despite the presence of $^{99\text{m}}\text{Tc}$ -MAA(-Ad) signal in the spleen (see Figure 3A), accumulation of host vector in this organ was equal to that in PBS controls (Figure 4B & Table S1). Whether the hepatic uptake of the host vector in the animals that received $^{99\text{m}}\text{Tc}$ -MAA depended on non-specific interaction with MAA (as was measured *in vitro* Figure 1B) or because of the clogging of the microvasculature by MAA particles was undeterminable.

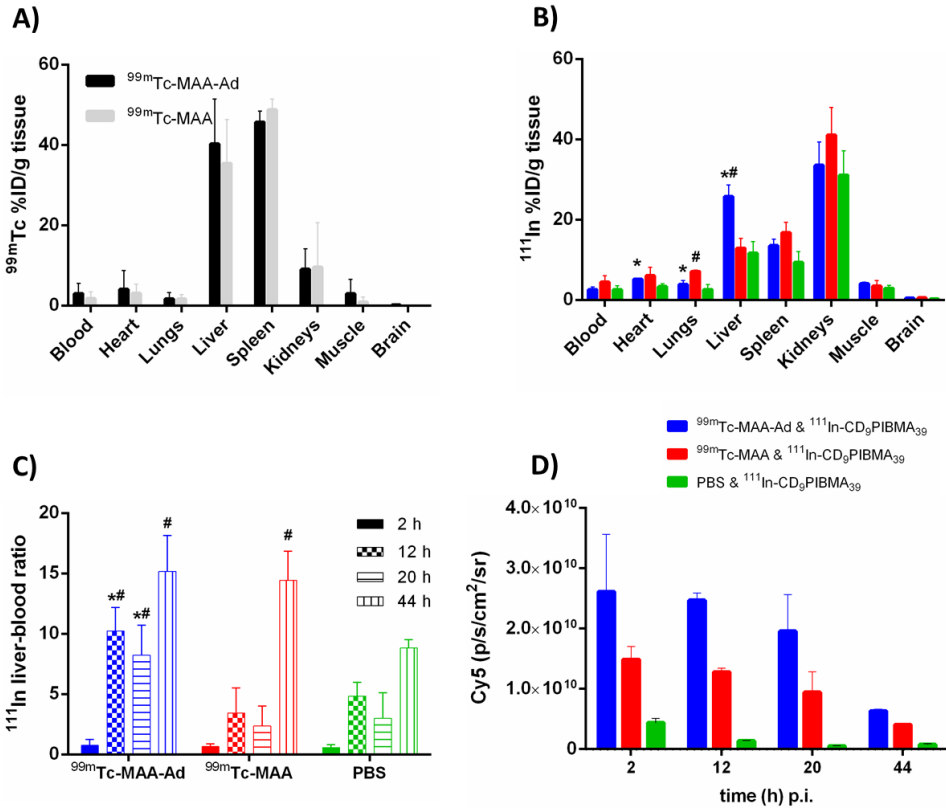


Figure 5. **A)** The bio-distribution of guest vectors ^{99m}Tc -MAA-Ad and ^{99m}Tc -MAA at various intervals after local administration. Data (expressed as the mean \pm SD of the percentage of the injected dose per gram tissue (%ID/g) of 3 observations) were calculated based on the radioactive counts measured in indicated tissues at 12, and 20 h post-injection. **B)** Biodistribution of intravenous administered ^{111}In -Cy $_{5.0}$ CD $_9$ PIBMA $_{39}$ (host vector) 12 h after hepatic pre-targeting with guest vectors MAA-Ad (blue bars), MAA (red bars) or as control PBS (green bars). **C)** Dynamic hepatic uptake of intravenous administered host vector ^{111}In -Cy $_{5.0}$ CD $_9$ PIBMA $_{39}$. Data are expressed as the mean \pm SD ratios of the %ID/g in liver and blood measured at 2, 12, 20, and 44 h post-injection of the host vector. For all pre-targeting settings at 44 h p.i. liver-to-blood ratios for ^{111}In -Cy $_{5.0}$ CD $_9$ PIBMA $_{39}$ are increased compared to the earlier intervals which is indicative for clearance of proteolytic or metabolic products. **D)** Ex-vivo fluorescence imaging analysis of the biodistribution of ^{111}In -Cy $_{5.0}$ CD $_9$ PIBMA $_{39}$ in excised livers of mice pre-targeted with ^{99m}Tc -MAA-Ad, ^{99m}Tc -MAA, or PBS at various intervals until 44 h p.i. The fluorescence signal is determined from regions of interest (ROI's) drawn over the liver. Data are expressed as the average radiance p/s/cm 2 /sr after correction for background activity. * = $p < 0.01$ compared to ^{99m}Tc -MAA, # = $p < 0.01$ compared to PBS.

Another interesting observation is the shorter blood half-life ($t_{1/2} = 192$ min) calculated for the host vector in mice pre-targeted with guest vector ^{99m}Tc -MAA-Ad compared to the half-life of the host vector in mice pretargeted with control guest vector ^{99m}Tc -MAA ($t_{1/2} = 306$ min) or PBS ($t_{1/2} = 318$ min) (Table S2). The uptake of ^{111}In activity in other tissues, e.g., blood, heart, lungs, muscle, and brains showed a decrease in uptake of ^{111}In radioactivity over time which was comparable between the two guest vectors or PBS (Table S1), most likely as a result of the clearance of ^{111}In -Cy $_{5.5}$ CD $_9$ PIBMA $_{39}$ from these tissues. At all intervals liver-to-blood ratios for mice pre-targeted with ^{99m}Tc -MAA-Ad were highest whereby the liver-to-blood ratio peaked at 44 h p.i.

Fluorescence imaging

Ex vivo fluorescence imaging analysis of the biodistribution of the host vector in various excised tissues of mice pretargeted with guest vectors ^{99m}Tc -MAA-Ad and ^{99m}Tc -MAA revealed an intense fluorescence signal in the liver (Figure 3C & Figure 5D) at all time points after administration of the host (2.0 – 2.6×10^{10} p/s/cm 2 /sr) which was highest for ^{99m}Tc -MAA-Ad compared to those for MAA (0.9 – 1.5×10^{10} p/s/cm 2 /sr) or PBS (0.06 – 0.4×10^{10} p/s/cm 2 /sr) which follows the trend as observed for radioactivity with ^{111}In -Cy $_{5.5}$ CD $_9$ PIBMA $_{39}$. At 44 h p.i. all values dropped below 0.6×10^{10} p/s/cm 2 /sr.

DISCUSSION

In this study we demonstrated that supramolecular interactions can form stable host-guest complexes between the host vector ^{111}In -Cy $_{5.5}$ CD $_9$ PIBMA $_{39}$ and guest vector ^{99m}Tc -MAA-Ad *in vitro* and *in vivo*. The stability of these complexes over longer time periods strengthens the case for supramolecular pre-targeting strategies for radioembolization. Corroborating our previous results,¹⁵ we did not observe lung shunting, an essential property to prevent side effects due to off-target delivery.^{2,11} Since complex formation could be realized up until 20 h, the technology can accommodate single-session procedures whereby the host vector therapy is administered within hours after the scout scan (MAA-Ad; guest vector). In current clinical practice these procedures are performed several weeks apart.²² A single-session procedure would be more patient-friendly as after the correct administration of the scout vector a therapeutic vector can be directly administered via the same catheter.²³ In addition to decreasing the invasiveness of the embolization procedure, cost reduction can also be achieved, as the secondary host vectors do not demand functionalization with

relatively expensive (e.g., ^{90}Y or ^{166}Ho) isotopes, but could also act as carrier for cheaper therapeutical isotopes such as rhenium-188 or lutetium-177.²⁴ Uniquely for our approach is that isotope labelling could be converted into kit chemistry.

From SPECT images (Figure 2A, B, Figure 3A, B), biodistribution data (Figure 4, 5, Table S1), and fluorescence imaging (Figure 3C, Figure 5D) it may be concluded that, while initially predominantly present in the blood, $^{111}\text{In-Cy5}_{0.5}\text{CD}_9\text{PIBMA}_{39}$ actively co-localizes with the MAA-Ad guest vector in the liver, resulting in increased uptake up to 20 h p.i. In addition to this conclusion, the 12 h timepoint gave the most optimal liver-to-blood ratios; Figure 2–4, Table S1). Clearly, the complex formation in the presence of MAA-Ad is unaffected by the strong serum interactions recorded for $^{111}\text{In-Cy5}_{0.5}\text{CD}_9\text{PIBMA}_{39}$ (approximately 90%; Figure S1).

It was found that unbound host vector was excreted via both renal and hepatic clearance; most likely the latter occurred *via* the reticuloendothelial system.²⁵ The hepatic clearance complicates accurate performance assessments of hepatic and spleen signals at the 44 h time point. Ideally, future versions of the host vector are synthetically refined so that uptake in radiation-sensitive background organs such as the kidneys is minimized. This development may be achieved by dose optimization for the host vector or fine-tuning the polymer's functional groups²⁶; these optimizations can possibly help to control the pharmacokinetics including the serum binding properties. In drug efficacy studies, it is often considered critical to account for plasma protein binding as this relates to the availability of the free drug, its half-life, and its subsequent renal elimination.²⁷ The lack of pulmonary shunting suggests $^{99\text{m}}\text{Tc-MAA-Ad}$ particles remained confined in the liver and are not released into the vasculature (Figure S1). Proteolytic breakdown of $^{99\text{m}}\text{Tc-MAA-Ad}$ as reported for pulmonary and hepatic injected $^{99\text{m}}\text{Tc-MAA}$ ²⁸ was not observed in our experimental setup; no accumulation of unconjugated $^{99\text{m}}\text{Tc}$ -activity was observed in typical reservoir tissues, e.g., thyroid, salivary glands and stomach.¹⁹ This apparent increase in both MAA-Ad and MAA stability remains speculative, but we hypothesize that it could be attributed to a different proteolytic breakdown pathway of aggregated human albumin particles in mice.

We observed long-term complex formation, which was affected by only two small factors of dissociation. Firstly, dissociation of $^{111}\text{In}^{3+}$ from the host vector occurred in the initial phase after intravenous injection, which was in line with the 5% dissociation observed *in vitro*. The use of dedicated chelators that support stable chelation of the radioisotope could prevent this effect.²⁹ Secondly, *in vitro* for $[^{111}\text{In-Cy5}_{0.5}\text{CD}_9\text{PIBMA}_{39}\text{-}^{99\text{m}}\text{Tc-MAA-Ad}]$ a 20% complex dissociation was observed over a 44 h timespan, which was confirmed *in*

vivo with the biodistribution assays. Indeed, a slow rate of excretion of about 20%/g for $^{111}\text{In-Cy}_{0.5}\text{CD}_9\text{PIBMA}_{39}$ was observed in this study. Again, future synthetic refinements could further address the stability by reducing the dissociation of the host vector and by improving the chelation of the radioisotope.

While serum–albumin binding is widely explored, clinical albumin-based nanodevices are more scarce.³⁰ Some examples are drug delivery of therapeutic agents with targeted albumin nanoparticles,³¹ $^{99\text{m}}\text{Tc}$ -labeled albumin colloids for the visualization of the lymphatic vessels,³² and surgical sentinel node detection with ICG- $^{99\text{m}}\text{Tc}$ -nanocolloid.³³ With the presented radioembolization strategy we hope to promote the usage of biodegradable particles for nanomedicine.³⁴ Alternatively, the employed pre-targeting concept could be equally effective on different, *e.g.*, more spherical synthetic microparticles such as gold particles or quantum dots.³⁵⁻³⁶

A debate with regard to radioembolization technologies on whether or not the agents should be classified as medical technology or drugs is ongoing. Despite being chemical in nature and the fact that these agents administer a radiation dose to a patient even when used incorrectly, commercial microspheres are considered a medical device. Although the practical steps during the application are similar and the components don't actively interact with the body's metabolic or immune system (by relying on supramolecular interactions) may mean the proposed technology could be considered as a drug by the designated authorities. In that case it would affect the cost of translation and the quality standards that have to be met. The composition of the microparticles used as pre-targeting platform could potentially influence this selection.

CONCLUSIONS

The reported dual-isotope multiplexing and fluorescence imaging data further underlines the potential of using multivalent host–guest interactions between Ad and CD on albumin-based nanodevices *in vivo*. With that, a tool has been created that could help address unmet clinical needs in the field of radioembolization.

Acknowledgements

We thank M.N. van Oosterom for his assistance with the reconstruction of the SPECT images. The research leading to these results was funded with grants from: the European Research Council (ERC) under the European Union's Seventh Framework Program

FP7/2007-2013 (grant agreement number 2012-306890), from the Netherlands Organization for Scientific Research (VIDI-grant - STW BGT11272) and the 2015-2016 Postdoctoral Molecular Imaging Scholar Program Grant granted by the Society of Nuclear Medicine and Molecular Imaging (SNMMI, Eurostars project E! 11079 and the Education and Research Foundation (ERF) for Nuclear Medicine and Molecular Imaging.

REFERENCES

1. A. Forner; J. M. Llovet; J. Bruix, Hepatocellular carcinoma. *The Lancet* **2012**, 379 (9822), 1245-1255.
2. F. E. Boas; L. Bodej; C. T. Sofocleous, Radioembolization of colorectal liver metastases: indications, technique, and outcomes. *J Nucl Med* **2017**, 58 (Supplement 2), 1045-1115.
3. G. A. van Hazel; V. Heinemann; N. K. Sharma, et al., SIRFLOX: randomized phase III trial comparing first-line mFOLFOX6 (plus or minus Bevacizumab) versus mFOLFOX6 (plus or minus Bevacizumab) plus selective internal radiation therapy in patients with metastatic colorectal cancer. *J Clin Oncol* **2016**, 34 (15), 1723-31.
4. H. S. Wasan; P. Gibbs; N. K. Sharma, et al., First-line selective internal radiotherapy plus chemotherapy versus chemotherapy alone in patients with liver metastases from colorectal cancer (FOXFIRE, SIRFLOX, and FOXFIRE-Global): a combined analysis of three multicentre, randomised, phase 3 trials. *Lancet Oncol* **2017**, 18 (9), 1159-1171.
5. D. Janevska; V. Chaloska-Ivanova; V. Janevski, Hepatocellular carcinoma: risk factors, diagnosis and treatment. *Open Access Maced J Med Sci* **2015**, 3 (4), 732-736.
6. R. Duran; J. Chapiro; R. E. Scherthaner, et al., Systematic review of catheter-based intra-arterial therapies in hepatocellular carcinoma: state of the art and future directions. *Br J Radiol* **2015**, 88 (1052), 20140564.
7. B. Sangro; L. Carpanese; R. Cianni, et al., Survival after yttrium-90 resin microsphere radioembolization of hepatocellular carcinoma across Barcelona clinic liver cancer stages: A European evaluation. *Hepatology* **2011**, 54 (3), 868-878.
8. R. Salem; R. J. Lewandowski; V. L. Gates, et al., Research reporting standards for radioembolization of hepatic malignancies. *J Vasc Intervent Radiol* **2011**, 22 (3), 265-278.
9. R. Hickey; R. J. Lewandowski; T. Prudhomme, et al., 90Y radioembolization of colorectal hepatic metastases using glass microspheres: safety and survival outcomes from a 531-patient multicenter study. *J Nucl Med* **2016**, 57 (5), 665-671.
10. L. Uliel, H.D. Royal, M.D. Darcy, et al., From the angio suite to the y-camera: Vascular mapping and 99mTc-MAA hepatic perfusion imaging before liver radioembolization - A comprehensive pictorial review, *J Nucl Med* **2012** 53 (11) 1736-1747..
11. A. Riaz, R. Awais, R. Salem, Side effects of Yttrium-90 radioembolization, *Front Oncol* **2014**, 4 (198) 1-11.
12. M. Xing, S. Lahti, N. Kokabi, et al., 90Y Radioembolization lung shunt fraction in primary and metastatic liver cancer as a biomarker for survival, *Clin Nucl Med* **2016**, 41 (1) 21-27.

13. E. Garin, Y. Rolland, S. Laffont, et al., Clinical impact of (99m)Tc-MAA SPECT/CT-based dosimetry in the radioembolization of liver malignancies with (90)Y-loaded microspheres, *Eur J Nucl Med Mol I* **2016**, *43* (3) 559-75.
14. M. T. Rood; S. J. Spa; M. M. Welling, et al., Obtaining control of cell surface functionalizations via pre-targeting and supramolecular host guest interactions. *Sci Rep* **2017**, *7*, 39908.
15. S. J. Spa; M. M. Welling; M. N. van Oosterom, et al., A Supramolecular approach for liver radioembolization. *Theranostics* **2018**, *8* (9), 2377-2386.
16. M. Palmowski; A. Goedicke; A. Vogg, et al., Simultaneous dual-isotope SPECT/CT with ^{99m}Tc- and ¹¹¹In-labelled albumin microspheres in treatment planning for SIRT. *Eur Radiol* **2013**, *23* (11), 3062-3070.
17. H. Kasuya; D. K. Kuruppu; J. M. Donahue, et al., Mouse models of subcutaneous spleen reservoir for multiple portal venous injections to treat liver malignancies. *Cancer. Res.* **2005**, *65* (9), 3823-7.
18. M. M. Welling; A. Bunschoten; J. Kuil, et al., Development of a hybrid tracer for SPECT and optical imaging of bacterial infections. *Bioconjug Chem* **2015**, *26* (5), 839-849.
19. *Limits for intakes of radionuclides by workers*. Pergamon Press: Oxford, 1980; Vol. 4.
20. F. P. Castronovo, Jr.; H. N. Wagner, Jr., Comparative toxicity and pharmacodynamics of ionic indium chloride and hydrated indium oxide. *J Nucl Med* **1973**, *14* (9), 677-82.
21. E. H. Gilbert; J. D. Earle; E. Glatstein, et al., ¹¹¹indium bone marrow scintigraphy as an aid in selecting marrow biopsy sites for the evaluation of marrow elements in patients with lymphoma. *Cancer* **1976**, *38* (4), 1560-1567.
22. L. Sancho, M. Rodriguez-Fraile, J.I. Bilbao, et al., Is a technetium-99m macroaggregated albumin scan essential in the workup for selective internal radiation therapy with yttrium-90? An analysis of 532 patients, *J Vasc Intervent Radiol* **2017**, *28* (11) 1536-1542.
23. N. Rostambeigi, A.S. Dekarske, E.E. Austin, et al., Cost effectiveness of radioembolization compared with conventional transarterial chemoembolization for treatment of hepatocellular carcinoma, *J Vasc Intervent Radiol* **2014**, *25* (7) 1075-1084.
24. M.A. Lyra, A. Georgantzoglou, S. Kordolaimi, et al., Radioisotopes Production and Dosimetry, Nuclear Medicine Therapy, *Hellenic Association of Medical Physicists*, Athens, Greece, **2011**.
25. R. Lang; X. Jun-Hua; C. Bo, et al., Synthetic nanoparticles camouflaged with biomimetic erythrocyte membranes for reduced reticuloendothelial system uptake. *Nanotechnol* **2016**, *27* (8), 085106.

26. F. Alexis; E. Pridgen; L. K. Molnar, et al., Factors affecting the clearance and biodistribution of polymeric nanoparticles. *Mol Pharm* **2008**, *5* (4), 505-515.
27. D. A. J. Bow; J. L. Perry; J. D. Simon, et al., The impact of plasma protein binding on the renal transport of organic anions. *J Pharmacol Exp Ther* **2006**, *316* (1), 349-355.
28. O.S. Grosser, J. Ruf, D. Kupitz, et al., Pharmacokinetics of 99mTc-MAA- and 99mTc-HSA-Microspheres Used in Preradioembolization Dosimetry: Influence on the Liver-Lung Shunt, *J Nucl Med*, **2016**, *57* (6) 925-927.
29. R. Schibli; A. P. Schubiger, Current use and future potential of organometallic radiopharmaceuticals. *Eur J Nucl Med Mol Imag* **2002**, *29* (11), 1529-1542.
30. A. Loureiro; N. G. Azoia; A. C. Gomes, et al., Albumin-based nanodevices as drug carriers. *Curr Pharm Des* **2016**, *22* (10), 1371-90.
31. H. Kouchakzadeh; M. S. Safavi; S. A. Shojaosadati, Efficient delivery of therapeutic agents by using targeted albumin nanoparticles. *Adv Protein Chem Struct Biol* **2015**, *98*, 121-43.
32. N. S. Van den Berg; T. Buckle; G. I. Kleinjan, et al., Hybrid tracers for sentinel node biopsy. *Q J Nucl Med Mol Imaging* **2014**, *58* (2), 193-206.
33. G. H. Kleinjan; E. van Werkhoven; N. S. van den Berg, et al., The best of both worlds: a hybrid approach for optimal pre- and intraoperative identification of sentinel lymph nodes. *Eur J Nucl Med Mol Imaging* **2018**.
34. M. Jamre; M. Shamsaei; M. Erfani, et al., Preparation and evaluation of ¹⁸⁸Re sulfide colloidal nanoparticles loaded biodegradable poly (L-lactic acid) microspheres for radioembolization therapy. *J Labelled Comp Radiopharm* **2018**.
35. M.-C. Daniel; D. Astruc, Gold nanoparticles: assembly, supramolecular chemistry, quantum-size-related properties, and applications toward biology, catalysis, and nanotechnology. *Chem Rev* **2004**, *104* (1), 293-346.
36. Y. Liu; H. Wang; Y. Chen, et al., Supramolecular aggregates constructed from gold nanoparticles and I-Try-CD polypseudorotaxanes as captors for fullerenes. *J Am Chem Soc* **2005**, *127* (2), 657-666.





SUPPORTING INFORMATION CHAPTER 4

***In vivo* stability of supramolecular host-guest complexes monitored by dual- isotope multiplexing in a pre-targeting model of experimental liver radioembolization**

EXPERIMENTAL PROCEDURES

General

All chemicals were obtained from commercial sources and used without further purification. Solvents were obtained from Actua-All Chemicals (Oss, The Netherlands) in HPLC grade and used without further purification. The reactions were monitored by thin layer chromatography (TLC) and/or mass spectrometry using a Bruker microflex™ LRF MALDI-TOF. HPLC was performed on a Waters (Etten-Leur, The Netherlands) HPLC system using a 1525EF pump and a 2489 UV/VIS detector. For preparative HPLC a Dr. Maisch GmbH (Ammerbuch, Germany) Reprosil-Pur 120 C18-AQ 10 μm (250 \times 20 mm) column was used (12 mL/min). For semi-preparative HPLC a Dr. Maisch GmbH Reprosil-Pur C18-AQ 10 μm (250 \times 10 mm) column was used (5 mL/min). For analytical HPLC a Dr. Maisch GmbH Reprosil-Pur C18-AQ 5 μm (250 \times 4.6 mm) column was used applying a gradient of 0.1% TFA in $\text{H}_2\text{O}/\text{CH}_3\text{CN}$ 95:5 to 0.1% TFA in $\text{H}_2\text{O}/\text{CH}_3\text{CN}$ 5:95 in 20 min (1 mL/min). NMR spectra were taken using a Bruker DPX-300 spectrometer (300 MHz ^1H NMR, 75 MHz ^{13}C NMR) and chemical shifts (δ) are reported relative to TMS ($\delta = 0$) and/or referenced to the solvent in which they were measured.

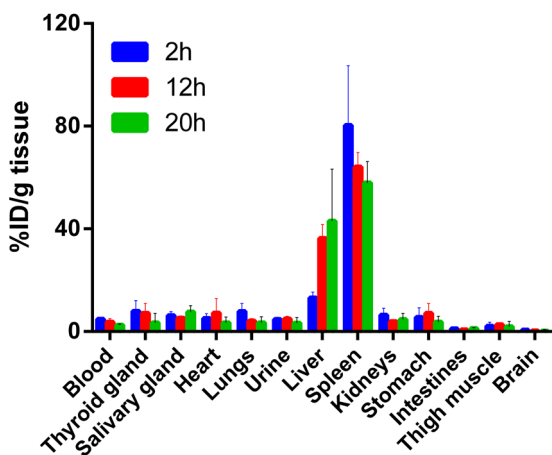


Figure S1. Quantified biodistribution of pre-targeting of the liver with locally administered primary vector (guest) $^{99\text{m}}\text{Tc}$ -MAA-Ad at various intervals. Data (expressed as the mean \pm SD of the percentage of the injected dose per gram tissue (%ID/g) of 3 observations) were calculated based on the radioactive counts measured in indicated tissues at 2, 12, and 20 h post-injection. Values of $^{99\text{m}}\text{Tc}$ -activity calculated at 44 h p.i. were deemed unreliable as the radioactivity counts were very low.

Table S1. The biodistribution of intravenously administered secondary vector (host) $^{111}\text{In-Cy5}_{0.5}\text{CD}_9\text{PIBMA}_{39}$ (host molecule) after hepatic pre-targeting with guest molecules: $^{99\text{m}}\text{Tc-MAA-Ad}$, $^{99\text{m}}\text{Tc-MAA}$, or PBS. Data (expressed as the mean \pm SD of the percentage of the injected dose per gram tissue (%ID/g) of 3-6 observations) were calculated based on the radioactive counts measured in various tissues at 2, 12, 20, and 44 h post-injection of the radioactive tracer. The significance of difference ($p < 0.01$) is indicated with * compared to = $^{99\text{m}}\text{Tc-MAA}$ (control), or † compared to PBS ($^{111}\text{In-Cy5}_{0.5}\text{CD}_9\text{PIBMA}_{39}$ reference distribution) according to Student's T-test.

| Tissue | Time h p.i. | Guest: $^{111}\text{In-Cy5}_{0.5}\text{CD}_9\text{PIBMA}_{39}$ | | |
|----------------|----------------|--|------------------------------|-----------------|
| | | $^{99\text{m}}\text{Tc-MAA-Ad}$ | $^{99\text{m}}\text{Tc-MAA}$ | PBS |
| Blood | 2 | 22.5 \pm 6.4 [‡] | 18.1 \pm 2.9 [‡] | 13.7 \pm 1.9 |
| | 12 | 2.6 \pm 0.6 | 4.4 \pm 1.7 | 2.5 \pm 1.0 |
| | 20 | 3.5 \pm 0.8 | 3.8 \pm 0.7 | 3.1 \pm 1.3 |
| | 44 | 1.8 \pm 0.2 | 1.6 \pm 0.1 | 1.8 \pm 0.3 |
| Heart | 2 | 10.2 \pm 4.1 ^{*†} | 8.0 \pm 1.3 | 7.2 \pm 1.5 |
| | 12 | 5.2 \pm 0.2 [‡] | 6.0 \pm 2.1 | 3.4 \pm 0.6 |
| | 20 | 4.1 \pm 0.3 [*] | 5.0 \pm 0.9 | 3.9 \pm 1.8 |
| | 44 | 8.3 \pm 2.4 [‡] | 6.2 \pm 0.6 [‡] | 4.5 \pm 0.1 |
| Lungs | 2 | 10.2 \pm 2.5 ^{*†} | 7.6 \pm 1.3 | 8.9 \pm 1.4 |
| | 12 | 3.9 \pm 1.0 [*] | 7.1 \pm 0.4 [‡] | 2.6 \pm 1.3 |
| | 20 | 4.2 \pm 0.5 [*] | 5.3 \pm 0.9 | 4.6 \pm 1.8 |
| | 44 | 7.3 \pm 1.1 [*] | 5.5 \pm 1.3 | 7.6 \pm 1.0 |
| Liver | 2 | 14.9 \pm 6.1 [‡] | 11.4 \pm 2.7 [‡] | 7.6 \pm 2.3 |
| | 12 | 25.8 \pm 2.9 ^{*†} | 12.9 \pm 2.5 | 11.7 \pm 2.9 |
| | 20 | 27.0 \pm 1.3 ^{*†} | 10.8 \pm 4.7 | 8.6 \pm 3.1 |
| | 44 | 26.2 \pm 2.1 ^{*†} | 22.7 \pm 2.3 [‡] | 15.7 \pm 2.8 |
| Spleen | 2 | 9.7 \pm 3.4 [‡] | 7.1 \pm 0.8 [‡] | 5.5 \pm 1.4 |
| | 12 | 13.5 \pm 1.6 | 16.7 \pm 2.6 | 9.4 \pm 2.7 |
| | 20 | 11.8 \pm 1.5 [‡] | 9.4 \pm 0.5 | 10.2 \pm 2.7 |
| | 44 | 17.9 \pm 5.0 ^{*†} | 13.0 \pm 3.1 | 11.3 \pm 0.7 |
| Kidneys | 2 | 20.9 \pm 7.0 ^{*†} | 10.0 \pm 1.9 [‡] | 13.0 \pm 2.3 |
| | 12 | 33.5 \pm 5.8 | 41.1 \pm 6.8 | 31.8 \pm 6.1 |
| | 20 | 29.7 \pm 5.3 | 29.2 \pm 5.8 | 33.3 \pm 12.2 |
| | 44 | 29.6 \pm 3.6 | 29.7 \pm 3.3 [‡] | 26.0 \pm 3.6 |
| Muscle | 2 | 4.0 \pm 1.9 ^{*†} | 2.0 \pm 0.4 | 2.2 \pm 0.4 |
| | 12 | 4.0 \pm 0.4 | 3.5 \pm 1.4 | 2.9 \pm 0.7 |
| | 20 | 2.2 \pm 0.6 [*] | 3.4 \pm 0.9 | 2.6 \pm 0.6 |
| | 44 | 3.9 \pm 0.4 ^{*†} | 3.4 \pm 0.3 [‡] | 3.6 \pm 0.3 |
| Brain | 2 | 0.6 \pm 0.2 ^{*†} | 0.4 \pm 0.1 | 0.4 \pm 0.1 |
| | 12 | 0.4 \pm 0.1 [‡] | 0.5 \pm 0.2 | 0.3 \pm 0.1 |
| | 20 | 0.3 \pm 0.1 | 0.5 \pm 0.2 | 0.3 \pm 0.2 |
| | 44 | 0.5 \pm 0.02 [‡] | 0.5 \pm 0.04 [‡] | 0.4 \pm 0.02 |

Table S2. The uptake of intravenously administered secondary vector (host) $^{111}\text{In-Cy5}_{0.5}\text{CD}_9\text{PIBMA}_{39}$ in scavenging tissues, excretion rate and clearance. Data (expressed as the mean \pm SD of the percentage of the injected dose per gram tissue (%ID/g) of 3-6 observations) were calculated based on the radioactive counts measured in various tissues at 2, 12, 20, and 44 h post-injection of the radioactive tracer. The significance of difference ($p < 0.01$) is indicated with *compared to = $^{99\text{m}}\text{Tc-MAA}$ (control), or † compared to PBS (reference distribution) according to Student's T-test.

| Tissue | Time | Guest | | |
|-----------------|---------------------------|---------------------------------|------------------------------|----------------|
| | h p.i. | $^{99\text{m}}\text{Tc-MAA-Ad}$ | $^{99\text{m}}\text{Tc-MAA}$ | PBS |
| Urine & bladder | 2 | 5.9 \pm 0.8 | 6.2 \pm 0.9 | 7.5 \pm 1.5 |
| | 12 | 4.8 \pm 1.7 | 4.3 \pm 2.4 | 3.2 \pm 0.6 |
| | 20 | 3.6 \pm 0.9 [†] | 4.7 \pm 1.8 [†] | 2.5 \pm 0.6 |
| | 44 | 4.9 \pm 0.7* | 4.0 \pm 0.7 | 5.6 \pm 0.3 |
| Thyroid gland | 2 | 8.0 \pm 2.9* [†] | 6.8 \pm 1.7 | 5.8 \pm 0.7 |
| | 12 | 8.2 \pm 2.4 | 5.1 \pm 5.2 | 5.3 \pm 2.1 |
| | 20 | 6.2 \pm 1.1 | 5.7 \pm 2.1 | 5.8 \pm 1.7 |
| | 44 | 6.0 \pm 2.3 | 4.5 \pm 2.2 | 5.8 \pm 1.6 |
| Salivary gland | 2 | 5.8 \pm 2.1* [†] | 4.3 \pm 0.8 | 4.5 \pm 0.8 |
| | 12 | 6.5 \pm 1.3 [†] | 7.6 \pm 1.9 | 5.2 \pm 1.1 |
| | 20 | 7.4 \pm 0.7 [†] | 7.5 \pm 1.8 | 5.7 \pm 1.5 |
| | 44 | 11.2 \pm 0.4 | 11.3 \pm 0.7 | 11.2 \pm 4.6 |
| Stomach | 2 | 2.2 \pm 0.9 [†] | 1.9 \pm 0.6 | 1.7 \pm 0.6 |
| | 12 | 2.3 \pm 0.7 | 1.5 \pm 0.7 | 1.2 \pm 0.9 |
| | 20 | 2.0 \pm 1.0* [†] | 1.2 \pm 0.8 | 0.9 \pm 1.1 |
| | 44 | 5.6 \pm 0.5 [†] | 4.5 \pm 0.8 [†] | 6.7 \pm 0.5 |
| Intestines | 2 | 5.1 \pm 2.4* [†] | 3.2 \pm 0.5 | 2.7 \pm 0.6 |
| | 12 | 5.0 \pm 2.8 | 8.1 \pm 3.6 | 3.6 \pm 1.5 |
| | 20 | 5.9 \pm 0.7 | 8.4 \pm 2.9 | 4.6 \pm 3.0 |
| | 44 | 11.0 \pm 1.8 [†] | 7.7 \pm 2.6 | 8.2 \pm 0.5 |
| Excretion (%ID) | 2 | 4.5 \pm 2.7 | 4.2 \pm 6.1 | 3.6 \pm 0.7 |
| | 12 | 11.1 \pm 9.5 [†] | 15.3 \pm 9.3 | 21.0 \pm 1.7 |
| | 20 | 14.3 \pm 1.7* | 8.5 \pm 4.6 | 11.7 \pm 3.6 |
| | 44 | 17.7 \pm 2.4 | 18.8 \pm 1.2 | 22.8 \pm 5.0 |
| Clearance | half-life $t_{1/2}$ (min) | | | |
| | 192 | 306 | 318 | |
| | (R ² 0.864) | (R ² 0.980) | (R ² 0.943) | |

Table S3. Dynamic hepatic uptake of intravenously administered secondary vector (host) $^{111}\text{In-Cy5}_{0.5}\text{CD}_9\text{PIBMA}_{39}$. Data (expressed as the mean \pm SD liver-to-blood ratios calculated between the percentages of the injected dose per gram tissue (%ID/g) of liver and blood (of 3-6 observations) based on the radioactive counts measured in these tissues at 2, 12, 20, and 44 h post-injection of secondary vector $^{111}\text{In-Cy5}_{0.5}\text{CD}_9\text{PIBMA}_{39}$ after hepatic pre-targeting. The significance of difference ($p < 0.01$) is indicated with * compared to $^{99\text{m}}\text{Tc-MAA}$ (control), or † compared to PBS (reference distribution) according to Student's T-test.

| Ratio | Time | Guest | | |
|----------------|--------|---------------------------------|------------------------------|---------------|
| | h p.i. | $^{99\text{m}}\text{Tc-MAA-Ad}$ | $^{99\text{m}}\text{Tc-MAA}$ | PBS |
| Liver-to-blood | 2 | 0.8 \pm 0.5 | 0.7 \pm 0.2 | 0.6 \pm 0.2 |
| | 12 | 10.2 \pm 2.0* | 3.4 \pm 2.1 | 4.9 \pm 1.1 |
| | 20 | 8.2 \pm 2.5† | 2.4 \pm 1.6 | 3.0 \pm 2.1 |
| | 44 | 15.2 \pm 3.0† | 14.4 \pm 2.4† | 8.8 \pm 0.7 |



Adapted from: Spa SJ, Bunschoten A, Rood MTM, Peters RJB, Koster AJ, van Leeuwen FWB.

Eur. J. In. Org. 2015;2015:4603-4610



CHAPTER **5**

**Orthogonal Functionalization of Ferritin
via Supramolecular Re-Assembly**

ABSTRACT

To investigate if the degree of functionalization of ferritin could be controlled using a supramolecular self-assembly process, two photophysical separable batches of ferritin were created by functionalizing ferritin capsids with either Cy3- or Cy5-dye (loading rate of about 50%). After dis-assembly, Cy3-, Cy5- as well as non-functionalized ferritin subunits were mixed in variable ratios. Photophysical measurements revealed that the ratio in which the subunits were mixed was indeed indicative for the ratios in which the functionalized subunits were observed in the re-assembled capsids. During re-assembly, however, a slight preference for the inclusion of non-functionalized subunits was observed, indicating that the reactivity decreased following functionalization. The iron biomineralization properties of ferritin were retained by the multi-functionalized capsids as Fe^{II} diffused rapidly inside, making it visible by transmission electron microscopy (TEM). These combined data indicate that it is possible to functionalize ferritin in an orthogonal manner using the supramolecular interaction between ferritin subunits.

INTRODUCTION

In nature, supramolecular protein assemblies can provide functional structures, which in fact can be seen as natural (bio-)nanoparticles. Examples are: viral capsids,^{1,2} bacteriophages,³ and ferritin.⁴ While the first two are disease related, the latter is responsible for a critical component in life, namely the iron metabolism of cells.^{5,6} Through chemical manipulation, however, ferritin can also be applied for other purposes. Promising ferritin based drug carriers, for example for photodynamic therapy,^{4,7} have been developed by replacing the iron core with (small) drug molecules.⁸⁻¹⁰ The relatively large surface area of ferritin also allows for a high loading capacity of fluorescent dyes and/or targeting ligands.¹¹⁻¹³ However, among the many ferritin derivatives developed, the MRI contrast agents seem to be the most promising.^{11,14} These agents, although functionalized, retain the natural iron mineralization property of ferritin. After mineralization, iron is present in the 8 nm cavity of ferritin capsids as ferrihydrite, and provides contrast on MRI.¹⁵⁻¹⁷

Large non-covalent natural complexes such as DNA helices, viruses and organelles, assemble into complex structures in an controlled manner.^{18,19} By copying from nature, the control on the composition in polymer cross-linking was improved via orthogonal multi-site self-assembly, obtaining polymers with tunable functionality.²⁰⁻²² In a similar approach, orthogonally functionalized nanofibers were created by the multicomponent co-assembly of integrin binding ligands Gly-Arg-Gly-Asp-Ser (GRGDS), Pro-His-Ser-Arg-Asn (PHSRN), and fluorophore functionalized building blocks.²³ Furthermore, it has been shown that dual functionality on spherical protein capsids, like cowpea chlorotic mottle virus, could be obtained by re-assembly of two differently functionalized protein subunits.²⁴⁻²⁶

The surface of (bio-)nanoparticles, like ferritin, can be modified by conventional conjugation procedures targeting the amino acids such as lysine.^{2,27} Although a substantial collection of bio-conjugation techniques are available, controlled introduction of multiple functionalities via this route remains challenging.²⁸ We reasoned that an orthogonal functionalization approach via consecutive dis- and re-assembly could provide the opportunity to control the degree of (multi)functionality on ferritin scaffolds. Ferritin, a bio-nanoparticle consisting of 24 identical protein subunits each 20 kDa in weight on average,²⁹ can be dis- and re-assembled by alteration of the pH.^{30,31} To investigate if three different types of subunits could be introduced controllably via supramolecular re-assembly, we functionalized (apo)ferritin with either Cy3 or Cy5, while retaining some non-functionalized subunits (Figure 1, A). Different subunits were then mixed in three

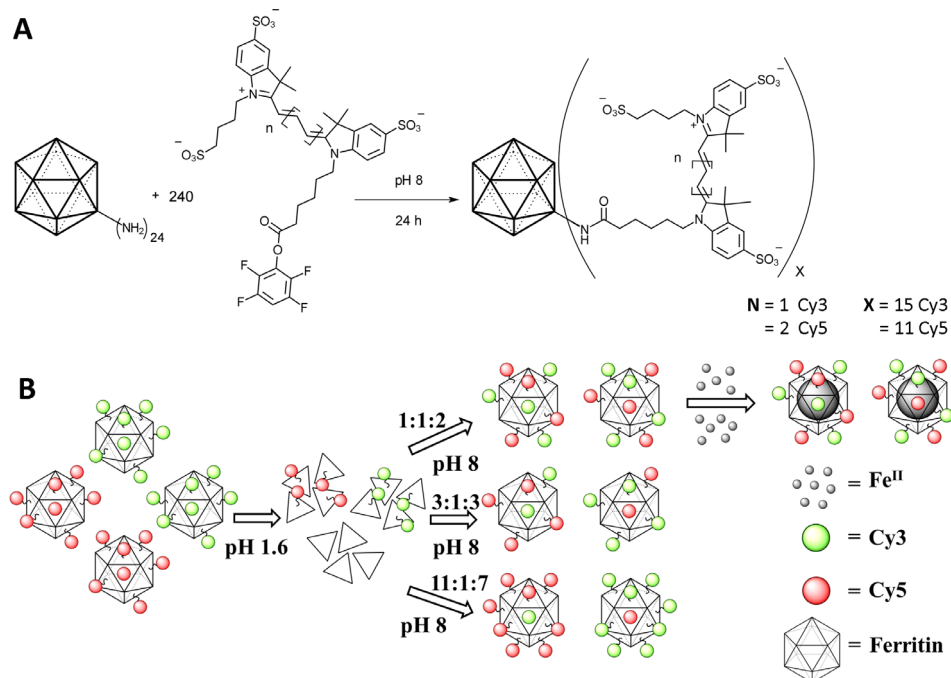


Figure 1. **A**) Functionalization of ferritin with a Cy3 or Cy5 dye, 10 eq. to ferritin subunit, in phosphate buffer pH 8. **B**) Orthogonal functionalization of ferritin with Cy3 (green) and Cy5 (red). Cy3-, Cy5-, and non-functionalized subunits are added together in the indicated ratio, following re-assembly at pH 8. After re-assembly functionalized capsids are mixed with Fe^{II} (grey) to obtain iron loaded ferritin capsids.

different ratios (Figure 1, B) and after re-assembly we evaluated how the ratio of these statistical mixtures influenced the functionalization of newly formed capsids. The photophysical interaction between the two dyes enabled accurate analysis of the orthogonal functionalization. After re-assembly, the multi functionalized ferritin capsids were exposed to Fe^{II} -ions to evaluate if they retained their intrinsic iron biomineralization properties (Figure 1, B).

EXPERIMENTAL

General

Solvents and chemicals were obtained from Actua-All (Oss, The Netherlands) and Sigma Aldrich (Zwijndrecht, The Netherlands), were used without further purifications. The

apoferritin from equine spleen was obtained from Sigma Aldrich and was stored in aliquots (50 μL , 37 $\mu\text{g}/\mu\text{L}$ in PBS) at 4 $^{\circ}\text{C}$. Short before the experiments, sufficient aliquots of apoferritin were washed 3 times with phosphate buffered saline (PBS) over a 100 kDa to re-move free subunits and small contaminants. Other ferritin fil-trations were also performed with Amicon Ultra-0.5 mL Centrifugal Filters from Merck Millipore (Amsterdam, The Netherlands). Ferritin concentrations were determined by absorption measurements (280 nm, ϵ -subunits = 14565 $\text{L mol}^{-1} \text{cm}^{-1}$) with a Nanodrop ND-1000 spectrophotometer from thermo scientific (Landsmeer, The Netherlands), just as the other UV/Vis absorption measurements. SEC was performed on an Aktatm Pure 25 instrument from GE Healthcare (Eindhoven, The Netherlands), if sample collection was required the corresponding fraction collector F9-R was de-ployed. The size exclusion column was a superdex 200 (GE Healthcare), and SEC was performed with 600 μL injection volume with PBS as eluent. The PBS was obtained from B. Braun (Oss, The Netherlands) in sterile and oxygen free conditions and was applied without further treatment. The fluorescence measurements were performed on a LS55 fluorescence spectrometer from Perkin-Elmer (Groningen, The Netherlands). NMR spectra were measured on Bruker DPX 300 Hz (Leiderdorp, The Netherlands). Mass spectra were measured on a Bruker microflex MALDI-TOF. TEM imaging was performed on a FEI Tecnai 12 BioTwin 120 kV TEM (Eindhoven, The Netherlands). ICP-MS measurements were performed on a Thermo Finnigan Element 2 equipped with an autosampler and a conical glass concentric from thermo scientific (Landsmeer, The Netherlands). For HPLC analysis and purifications a Waters HPLC system (Etten-Leur, The Netherlands) consisting of HPLC 1525 Pump and 2489 UV/Vis detector using a Reprosil-Pur 120 C18-AQ 10 μm column (250 \times 20 mm) for purification and a Reprosil-Pur C18-AQ 5 μm column (250 \times 4.6 mm) for analysis, from Dr. Maisch (Ammerbuch, Deutschland).

Synthesis of $\text{Cy5}(\text{SO}_3)_2\text{-SO}_3\text{-CO}_2\text{H}$ and $\text{Cy3}(\text{SO}_3)_2\text{-SO}_3\text{-CO}_2\text{H}$

Both $\text{Cy5} [\text{Cy5}(\text{SO}_3)_2\text{-SO}_3\text{-CO}_2\text{H}]$ and $\text{Cy3} [\text{Cy3}(\text{SO}_3)_2\text{-SO}_3\text{-CO}_2\text{H}]$ were synthesized according to literature procedure.³²

Synthesis of Cy5-TFP (Figure 1, A)

$\text{Cy5}(\text{SO}_3)_2\text{-SO}_3\text{-CO}_2\text{H}$ (190 mg, 0.25 mmol) was dissolved in DMF (10 mL). To this DCC (77 mg, 0.37 mmol) and TFP (125 mg, 0.75 mmol) was added and the reaction was stirred overnight at room temp. The next day another equivalent of DCC and TFP were added, together with *N,N*-diisopropylethylamine (DIPEA, 124 μL , 0.75 mmol). The day here-after, the reaction mixture was added to 250 mL of EtOAc and a blue precipitate was isolated.

The crude product was first purified by silica column chromatography (40% MeOH in EtOAc) and further purified by reversed phase HPLC with a gradient from 5% MeCN to 95% MeCN in H₂O (containing 0.1% TFA) in 100 min. Pure fractions were pooled and lyophilized, which yielded 55 mg (24%) of pure product. ¹H NMR [300 MHz, (CD₃)₂SO, 25 °C]: δ = 8.35 (t, J = 13.1 Hz, 2 H, CH of bridge), 7.93 (m, 1 H, CH of TFP), 7.80 (s, 2 H, Ar-H), 7.62 (d, J = 8.2 Hz, 2 H, Ar-H), 7.33 (dd, J = 16.6, 8.3 Hz, 2 H, Ar-H), 6.58 (m, 1 H, CH of bridge), 6.36 (m, 2 H, CH of bridge), 4.07 (m, 4 H, N-CH₂), 2.79 (t, J = 7.1 Hz, 2 H, CH₂COOC), 2.55 (m, 2 H, CH₂-SO₃), 1.97–0.93 [m, 22 H, 5CH₂ with s at 1.68 for C-(CH₃)₂] ppm. ¹³C NMR [75 MHz, (CD₃)₂SO, 25 °C]: δ = 174.33, 169.51, 154.36, 154.06, 145.28, 145.13, 142.03, 141.89, 140.57, 140.48, 126.04, 119.89, 110.30, 110.06, 104.44, 103.69, 103.35, 101.27, 95.37, 54.93, 50.58, 49.46, 48.91, 33.46, 27.07, 26.66, 25.84, 25.61, 24.20, 22.37 ppm. MS (MALDI-TOF): [M]⁺ calculated for C₄₁H₄₅F₄N₂O₁₁S₃⁺: 913.2, found 913.6 ppm.

Synthesis of Cy3-TFP (Figure 1, A)

Cy3(SO₃)₂-SO₃ (111 mg, 0.15 mmol) was dissolved in DMF (10 mL). To this DCC (62 mg, 0.30 mmol), tetrafluorophenol (TFP, 100 mg, 0.60 mmol), and DIPEA (100 μL, 0.6 mmol) was added and the reaction was stirred overnight at RT. The next day another equivalent of DCC, two equivalents of TFP and 2 equiv. of DIPEA were added and reacted over weekend. The reaction was concentrated in vacuo and purified by silica column chromatography (40% MeOH in EtOAc). The resulting product was lyophilized, which yielded 44 mg (31%) of pure product. ¹H NMR [300 MHz, (CD₃)₂SO, 25 °C]: δ = 8.36 (t, J = 13.4 Hz, 1 H, CH of bridge), 7.92 (m, 1 H, CH of TFP), 7.79 (s, 2 H, Ar-H), 7.66 (d, J = 8.2 Hz, 2 H, Ar-H), 7.42 (dd, J = 14.2, 8.4 Hz, 2 H, Ar-H), 6.57 (dd, J = 13.4, 3.2 Hz, 2 H, CH of bridge), 4.13 (m, 4 H, N-CH₂), 2.82 (t, J = 7.1 Hz, 2 H, CH₂COOC), 2.51 (m, 2 H, CH₂-SO₃), 1.87–0.94 [m, 22 H, 5CH₂ with s at 1.70 for C-(CH₃)₂] ppm. ¹³C NMR [75 MHz, (CD₃)₂SO, 25 °C]: δ = 174.14, 169.58, 149.94, 145.78, 145.73, 141.87, 141.75, 140.10, 126.24, 119.86, 119.82, 110.86, 110.67, 104.75, 104.43, 104.12, 103.10, 50.67, 48.91, 43.90, 43.77, 32.35, 27.42, 26.71, 26.04, 25.29, 24.04, 22.54 ppm. MS (MALDI-TOF): [M]⁺ calculated for C₃₉H₄₃F₄N₂O₁₁S₃⁺: 887.2, found 887.8.

Ferritin Functionalization with Cy3 or Cy5

Filtered apoferritin (5 mg, 245 pmol) in PBS (300 μL) was mixed with phosphate buffer (300 μL, pH 8, 0.1 M) and subsequently a solution of Cy5-TFP (2 mg, 2.19 μmol) or Cy3-TFP (2 mg, 2.25 μmol) in DMSO (10 μL) was added. After one night stirring at RT the ferritin capsids were washed by sequential filtering over 100 kD Amicon filters until the filtrate was no longer blue. By absorption measurements the concentration of Cy3 ($\epsilon = 150 \cdot 10^3$

L mol⁻¹ cm⁻¹) or Cy5 ($\epsilon = 250 \cdot 10^3$ L mol⁻¹ cm⁻¹) and ferritin subunits ($\epsilon = 14.6 \cdot 10^3$ L mol⁻¹ cm⁻¹) was determined. The reaction was performed three times with the same batch of apoferritin to obtain a final labelling ratio of 0.65 Cy3/subunit and 0.47 Cy5/subunit, corresponding with 15 Cy3/ferritin and 11 Cy5/ferritin respectively.

Dis-Assembly and Re-Assembly of Ferritin

Method 1: Conventional method at room temp and *Method 2:* Conventional method at 37 °C. To apoferritin (50 μ L, 1.85 mg) in H₂O (3 mL), HCl solution (195 μ L, pH 0.3, 0.5 M) was added to obtain a pH of 1.6. After 15 min of stirring at RT an aliquot (200 μ L) was taken and diluted to 600 μ L for SEC analysis. Simultaneously, NaOH solution (205 μ L, pH 13.7, 0.5 M) was added drop wise to the reaction mixture returning it slowly to physiological pH. Subsequently, the reaction was stirred for at least 24 h at RT (method 1) or 37 °C (method 2). Re-assembled capsids were obtained with 14 \pm 13% yield (method 1) and 15 \pm 11% yield (method 2).

Method 3: Change of pH by buffer replacement via filtration.

Washed apoferritin (20 μ L, 0.36 mg) was added to HCl-KCl buffer (200 μ L, pH 1.6, 0.1 M, 0.05 % w/w Tween 20), resulting in a concentration of 1.6 mg/mL ferritin. The reaction mixture was shaken at RT for 15 min and the volume was subsequently reduced to 100 μ L by filtration through 10 kDa Amicon filter. Sodium phosphate buffer (400 μ L, pH 8.6, 0.1 M, 0.05 % w/w Tween 20) was added, followed again by reducing the volume to 100 μ L. This was repeated three times, thereby replacing the HCl-KCl buffer step by step. The reaction mixture was recovered from the filter and supplemented with sodium phosphate buffer (500 μ L, pH 8.6, 0.1 M, 0.05 % w/w Tween 20) obtaining a final pH of 8.6. The resulting ferritin solution (600 μ L, 0.62 mg/mL, pH 8.6) was shaken at 37 °C for at least 24 h. Re-assembled capsids were obtained with 14 \pm 9% yield.

Method 4: Change of pH by adding a basic buffer to an acidic solution.

Washed apoferritin (20 μ L, 0.36 mg) was added to HCl-KCl buffer (200 μ L, pH 1.6, 0.03 M, 0.05 % w/w Tween 20), resulting in a concentration of 1.6 mg/mL ferritin. The reaction mixture was shaken at room temperature for 15 min and subsequently, sodium phosphate buffer (400 μ L, pH 8.6, 0.05 M, 0.05 % w/w Tween 20) was added, bringing the pH towards 8. The resulting ferritin solution (600 μ L, 0.62 mg/mL, pH 8) was shaken at 37 °C for at least 24 h. Re-assembled capsids were obtained with 25 \pm 5% yield.

Orthogonal Functionalization of Ferritin with Cy-Dye According to Method 4

Cy3-ferritin subunits, Cy5-ferritin subunits and unmodified ferritin subunits were varied in the ratios of 4.5:4.5:13 (experiment A), 10.7:3.5:9.8 (experiment B), and 13.8:1.3:12.7 (experiment C) on average. Experiment A was performed twice, B was performed three times and C was performed five times. For each experiment a separate stock solution of dis-assembled Cy3- and Cy5-ferritin capsids was prepared. First, the necessary quantities of Cy3- and Cy5-ferritin capsids for each reaction were calculated via:

$$Cy3 = \frac{0.66 \cdot 10^{-9}}{\left(\frac{0.65}{0.47N} + 1\right)} \quad Cy5 = \frac{0.66 \cdot 10^{-9}}{\left(\frac{0.47N}{0.65} + 1\right)}$$

with $Cy3$ or $Cy5$ = mol Cy3- or Cy5 functionalized ferritin capsids, N = the ratio of Cy3-subunit/Cy5-subunits aimed at, $0.66 \cdot 10^{-9}$ the total quantity (mol) of ferritin capsids in each separate reaction, and 0.65 or 0.47 being the labelling yields of the Cy-dye functionalized ferritin. Secondly, the quantities of Cy3-ferritin capsids (0.56 nm, 1.36 nm, 2.96 nm) and Cy5-ferritin capsids (0.77 nmol, 0.63 nmol, or 0.37 nmol), calculated for two or more experiments of A, B, or C, were dissolved in separate solutions of HCl-KCl buffer (200 μ L, 300 μ L or 500 μ L, respectively), resulting in the stock solutions consisting of Cy3- and non-functionalized subunits, or Cy5- and non-functionalized subunits. For each re-assembly reaction, aliquots (100 μ L) of the appropriate stock solutions were mixed together (1:1, 200 μ L final volume) to obtain mixtures of dis-assembled Cy3-, Cy5- and non-functionalized ferritin subunits in the ratios aimed at. Then, the sodium phosphate buffer (400 μ L) was added and the reaction shaken for 24 h at 37 °C. Both reactions of experiment A were pooled and concentrated to 600 μ L using a 100 kDa Amicon filter. The concentrated sample was purified by SEC and the fractions from 10 to 12 mL and from 13 to 15.5 mL elution volume (0.5 mL/fraction) collected. The same was done for experiment B and C. The obtained re-assembled ferritin capsids were further analysed by TEM, absorption and fluorescence spectroscopy (Figures 2 and 3). The orthogonally functionalized ferritin capsids were obtained with approximately $17 \pm 2\%$ yield in all three reactions.

Yield Calculations of Re-Assembly

The yield of the re-assembly method was computed from the SEC data. The total area under the SEC curve was equated to 100%, hereby the sum of area underneath the peak of interest is the yield of the corresponding construct. To determine the percentage of the re-assembled ferritin capsids in the sample, the area under the peak at retention volumes 13–15.5 mL (re-assembled capsids) were used (Figure 2, B).

Iron Incorporation

The incorporation of iron was performed following a literature procedure with small modifications.³³ In short, apoferritin (non-functionalized, Cy3-functionalized, and Cy3-, Cy5 functionalized by re-assembly) was dissolved in tris buffer (pH 8, 50 mM Tris-HCl, 100 mM NaCl, 10 mM MgCl₂) to obtain a 0.5 μM ferritin capsid concentration. Subsequently 1000 X excess to ferritin capsids of (NH₄)₂Fe(SO₄)₂ dissolved in degassed Milli-Q (< 0.6 mg/mL), was slowly added in 10 steps. After 30 min standing exposed to air, the capsids were washed 3 times with demi water over a 100 kDa Amicon filter and subsequently collected in tris-buffer (100 μL final volume).

TEM Protocol

For TEM imaging 5 μL PBS containing approximately 2.5·10¹⁴ ferritin capsids was incubated on carbon and formvar coated copper EM grids for 1 min, and subsequently the sample was stained with one drop of uranyl acetate 2% for 10 seconds. After each step the remaining solvent was removed by blotting.

ICP-MS Protocol

An analytical sample was digested in a per-fluoroalkoxy (PFA) microwave digestion tube to which 10 mL of nitric acid (70 % HNO₃) were added. All samples were digested in a MARS microwave system for 50 min. The temperature program was as follows: at 1200 W power from 20 to 150 °C in 15 min, then to 180 °C in 15 min, and finally constant at 180 °C for 20 min. Following digestion and cooling to room temperature the digest was diluted and analyzed with a Thermo Finnigan Element 2 equipped with an auto sampler and a conical glass concentric nebulizer, and operated at an RF power of 1000 W. The argon gas flows were at the following settings; plasma, 15 L/min; nebulizer, 1.1 L/min; auxiliary, 1.2 L/min. The sample flow rate to the nebulizer was set at 0.5 mL/min. To minimize polyatomic interferences from ³⁶Ar¹⁶O, the instrument was operated in medium resolution mode and iron was measured at m/z 55.85.

RESULTS AND DISCUSSION

Re-Assembly of Ferritin Capsids

The heteropolymeric apoferritin from equine spleen was selected for the investigation, since it is one of the commonly applied and more investigated ferritin platforms.^{31, 34-37}

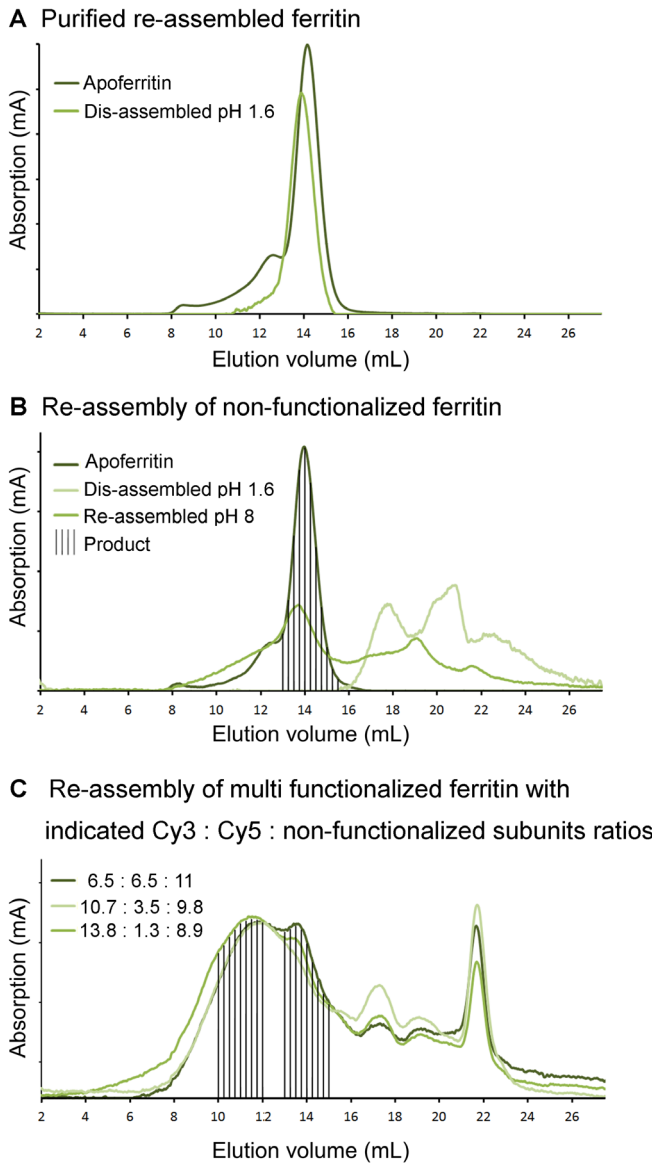


Figure 2. Size exclusion chromatography curves **A)** Ferritin capsids before re-assembly and after dis- and re-assembly following purification. **B)** SEC curves of apoferritin, dis-assembled subunits (pH 1.6), and after re-assembly (pH 8). The fraction containing correctly sized capsids is highlighted. **C)** Crude reaction sample after orthogonal functionalization of ferritin via re-assembly, with indicated ratios of Cy3: Cy5 : non-functionalized subunits ratios. Fraction containing aggregates (10–12 mL) and correctly formed capsids (13–15.5 mL) are highlighted. The corresponding TEM images revealing the composition of the SEC fractions are given in Figure 3 (D and C), respectively.

However, in our hands the literature procedure for the re-assembly of ferritin capsids^{30,31} proved to be cumbersome and gave a low reproducibility. To improve the reproducibility and ease of the assembly process, we set-up an alternative re-assembly protocol. From four methods tested (see Experimental section), the one by which we achieved the best pH control and smallest yield variation was considered best (method 4). In this method dis-assembly was realized by dissolving ferritin in a hydrochloric acid solution of pH 1.6. Subsequent re-assembly was accomplished by adding a weak phosphate buffer of pH 8.6 (twice the volume of the acidic solution). The resulting basic solution had to be shaken for two days (37 °C) to reach equilibrium.

Re-assembled ferritin capsids were analysed and purified by size exclusion chromatography (SEC). The peaks corresponding to the parental ferritin capsids and (purified) re-assembled ferritin capsids both eluted from the column after the same amount of elution volume (Figure 2, A), indicating both compounds were identical in size. For further confirmation both structures were analysed by transmission electron microscopy (TEM). The parental ferritin capsids could be imaged as circular structures of 12.1 X 0.7 nm in diameter using negative staining (Figure 3, A). These observations confirm previous reports.³⁸ After re-assembly and purification the TEM images revealed comparable circular structures with a diameter of 12.6 X 0.7 nm, indicating the re-assembly method was successful (Figure 3, B–C).

In the literature, re-assembly of ferritin is referred to as a simple and robust method;^{36,39} the yield of this reaction is seldom mentioned and successful re-assembly is often not verified. However, there are reports of low yielding ferritin re-assemblies.⁴⁰⁻⁴¹ We also obtained a relatively low re-assembly yield for non-functionalized ferritin (25 ± 5%). It is proposed that subunits re-assemble through the formation of (stable) dimers, trimers and dodecamers.⁴² Hereby, the reaction steps; $24M_1 \leftrightarrow 8M_2 + 8M_1 \leftrightarrow 8M_3 \leftrightarrow 4M_6 \leftrightarrow 2M_{12} \leftrightarrow 1M_{24}$ are proposed (with M_1 referring to a single subunit).⁴⁰⁻⁴² Formation of other intermediate assemblies is thought to result in so-called “dead-end structures”,²⁹ such as the rod-like structures with random dimensions that we found as side products (Figure 3, D). According to Kim et al. these structures may originate from the trimer intermediate.⁴¹

After investigating the structure of ferritin capsids by small-angle X-ray scattering (SAXS), Kim et al.⁴¹ concluded that re-assembly of ferritin is only pseudo reversible over a pH range of 2.66 to 10, and that a pH < 2 is necessary for complete dissociation. The same group also stated that from pH < 2 intact ferritin capsids could never be fully recovered; one or two subunits would always be missing after re-assembly. We, however, have not found any indications suggesting the re-assembled capsids miss a subunit. In fact TEM analysis

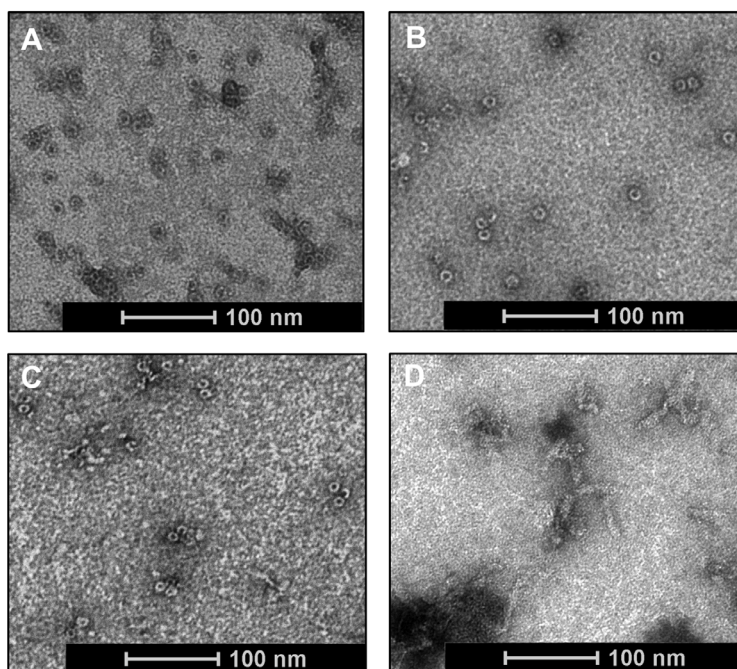


Figure 3. TEM images of ferritin capsids, stained with uranyl acetate. **A)** Parental ferritin capsids. **B)** Re-assembled ferritin capsids. **C)** SEC fraction containing re-assembled multi functionalized ferritin capsids. **D)** SEC fraction containing aggregates.

indicated closed-ring structures. This said we also lack proof that the re-assembled capsids comprise of 24 subunits.

Conjugation of Cy3 or Cy5 to Ferritin

To create two chemically similar but photophysically separable batches of ferritin capsids, one batch of ferritin was functionalized with Cy3- and another with Cy5-dye (Figure 1, A). For efficient conjugation the Cy-dyes were activated as tetrafluorophenol (TFP) esters. The TFP ester proved to be less prone to hydrolysis than the more generally applied N-hydroxylsuccinimide (NHS) ester and as a result higher labelling yields were obtained compared to NHS activated Cy-dyes (data not shown). After functionalization, labelling yields of 15 (62.5 %) Cy3 or 11 (45.8 %) Cy5 dyes on each ferritin capsid were obtained. The labelling yields were derived from the ratio between the subunit- and Cy-dye concentration, calculated from the absorption spectra measured at 280 nm (Cy3) and 550 nm (Cy3) or 650 nm (Cy5).

Table 1. Ratios of Cy3-, Cy5- and non-functionalized subunits.

| Dis-assembled subunits Cy3 : Cy5 : non-functionalized | Re-assembled capsids Cy3 : Cy5 : non-functionalized |
|--|--|
| 6.5 : 6.5 : 11 | 4.4 : 4.1 : 15.5 |
| 10.7 : 3.5 : 9.8 | 8.1 : 3.4 : 12.5 |
| 13.8 : 1.3 : 8.9 | 9.0 : 1.3 : 13.7 |
| 0.0 : 11.3 : 12.7 | 0.0 : 9.8 : 14.2 |
| 15.6 : 0.0 : 8.4 | 14 : 0.0 : 10.0 |

Orthogonal Functionalization with Cy3 and Cy5 by Supramolecular Re-Assembly

To investigate if the degree of functionalization could be controlled using supramolecular self-assembly processes, the two separately functionalized batches of ferritin were disassembled and mixed. By mixing Cy3-functionalized, Cy5-functionalized and non-functionalized subunits at pH 1.6 in variable ratio's following re-assembly at pH 8 (Table 1), we evaluated how the ratio of this mixture influenced the orthogonal functionalization of newly formed capsids. To obtain the desired Cy-dye functionalized sub-units ratios (Table 1), the number of Cy3-functionalized subunits was increased, while the number of Cy5-function-alized subunits was decreased; Cy5 was detectable at a lower concentration range than Cy3, and therefore more suitable for use at lower quantities (Figure 4, A).

Different to what we observed after the re-assembly of non-functionalized ferritin subunits, re-assembly using differently functionalized subunits merely yielded a small (shoulder) peak of product, while the peak belonging to the aggregates increased substantially (Figure 2, C). Although less pronounced, an increase in aggregate formation was also observed after the individual re-assembly of Cy3- or Cy5-functionalized ferritin capsids (data not shown). TEM analysis revealed that correctly formed capsids were still the main content in the 13–15.5 mL elution volume fractions (Figure 3, C) and the same analysis indicated that these samples contained $\leq 10\%$ pollution of larger constructs. The samples at elution volume 10–12 mL consisted of larger aggregates of which some adopted a rod like conformation with 5 X 40 nm dimensions (Figure 3, D).

The degree of functionalization was derived from the absorption spectra (Figure 4, A), assuming the re-assembled capsids were build up from 24 subunits. Ratio's calculated for capsids consisting of 23 subunits did not result in significant different values (less than 1 % variation). Table 1 reveals that the ratios in which Cy3-functionalized, Cy5-functionalized, and non-functionalized subunits were mixed was indicative for the ratios in which they were observed on the re-assembled ferritin capsids. However, we did observe small

deviations between the Cy3- and Cy5-ratios when adding the variable subunits in the maximum ratio of 13.8:1.3:8.9. When differently functionalized subunits were mixed, in all cases the relative ratio of non-functionalized subunits increased slightly. This trend was less pronounced when the re-assembly was performed with only one type of Cy-dye functionalized subunit.

Although our experiments indicate that the envisioned orthogonal functionalization with three functionalities via ferritin self-assembly is feasible, the presence of relatively small Cy-dyes on a protein subunit already seems to negatively influence the delicate re-assembly process (Figure 2, C). Moreover, the supramolecular re-assembly process of non-functionalized ferritin subunits seems to have a higher reactivity. These features combined indicate that assembly of functionalized subunits will more often result in “dead end structures”. Given these observations, it is not likely this statistical re-assembly approach of heteropolymeric apoferritin of equine spleen can be translated towards the introduction of larger substituents such as targeting peptides. For such substituents, a solution may lie in the initial use of small bi-functional linkers. These substituents can be used to introduce new reactive groups such as (protected) thiols or azides,^{43,44} which can be selectively functionalized after the re-assembly process.⁴⁵

Changing towards a more simplified re-assembly platform could also have a positive effect on the results. The Ferritin family has other members beside the mammalian equine spleen ferritin, such as the DNA-binding proteins from starved cells (Dps), or homopolymeric bacteria ferritins (Bfr).²⁹ While the mammalian ferritin is built up from heavy (H) and light (L) subunits (24 in total), Dps only consist of 12 such subunits,²⁵ and homopolymeric Bfr is only built up from H subunits (24 in total).^{29,46} These latter two ferritin types are less complex in their structure, and thereby may provide a re-assembly process that is more suitable for functionalization.

To validate if Cy3- and Cy5-functionalized subunits were in fact combined on the same capsids, their photophysical interactions were analysed. If Cy3 and Cy5 are on the same molecule, and in close proximity to each other (< 10 nm), Förster Resonance Energy Transfer (FRET) should occur from Cy3 to Cy5.⁴⁷ Since ferritins surface area is 452 nm² ($4\pi r^2$, with $r = 6$ nm) and there are 10 ± 2 dyes on average after orthogonal functionalization, each dye has 45.2 nm² circle space (assuming they are equally spaced); this results in an r_{dye} of 3.8 nm. This distance should be sufficient to allow for FRET. Indeed Cy3 excitation at 525 nm resulted in two peaks corresponding to Cy3- (570 nm) and Cy5-emission (670 nm). The intensity of the FRET emission decreased with decreasing Cy3: Cy5 ratio (Figure 4, B). Even with Cy5 quantities as low as one Cy5 per ferritin capsid (Cy3: Cy5: non-functionalized = 9.0:1.3:13.7) FRET could still be observed (Figure 4, B).

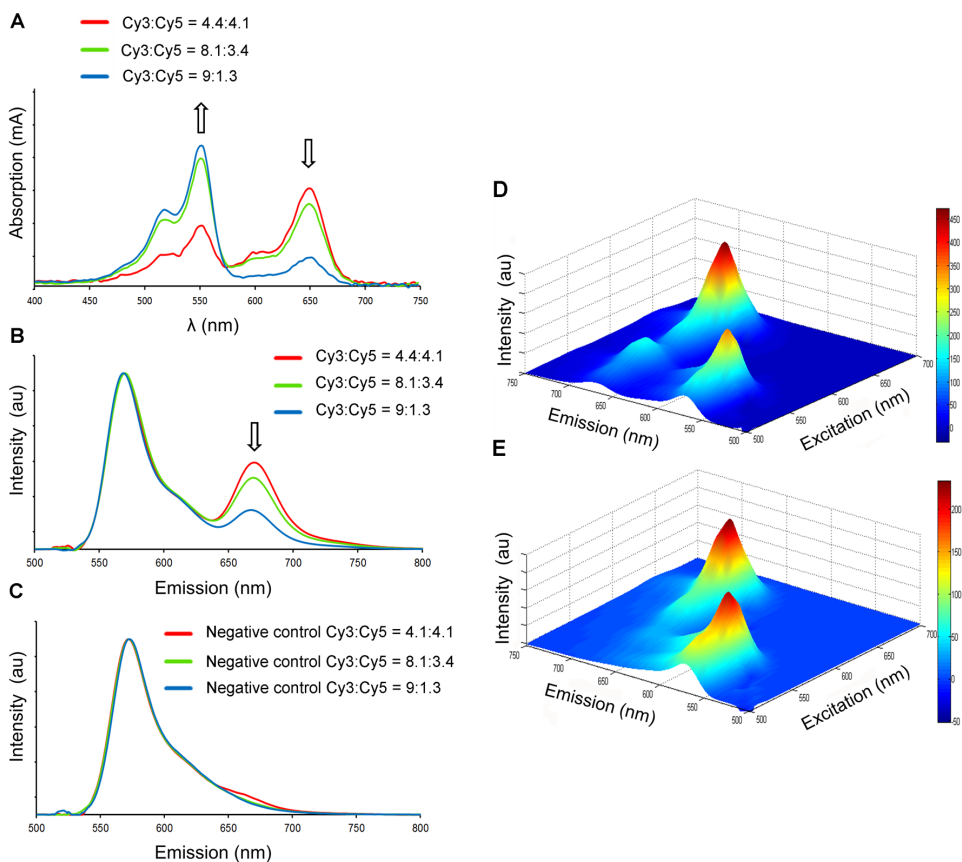


Figure 4. Photophysical measurements of orthogonal functionalized ferritin. **A**) Absorption measurements normalized on ferritin content, arrows indicate the increasing and decreasing signal of Cy3 and Cy5 upon increasing Cy3: Cy5 ratio. **B**) Normalized fluorescence emission spectra after excitation at 525 nm. With increasing Cy3: Cy5 ratio, the FRET signal decreases with the amount of Cy5 dyes. **C**) Control for FRET measurements shown in B; samples contain mixtures of separate Cy3- and Cy5-functionalized ferritin capsids at similar Cy-dye concentrations as the corresponding re-assembled capsids. **D**) 3D fluorescence emission spectrum showing FRET of Cy3: Cy5: non-functionalized = 6.5: 6.5: 11 functionalized ferritin, excited from 525 to 700 nm. **E**) Control for FRET measurement shown in C; mixture of separate Cy3- and Cy5-functionalized ferritin capsids at similar concentrations as the Cy3: Cy5: non-functionalized = 4.4: 4.1: 15.5 re-assembled capsids.

To confirm the (FRET) origin of the observed Cy5 emission, mixtures of separate Cy3- and Cy5-functionalized ferritin capsids were measured with similar Cy3 and Cy5 concentrations as the corresponding re-assembled capsids. Other than in the dual-

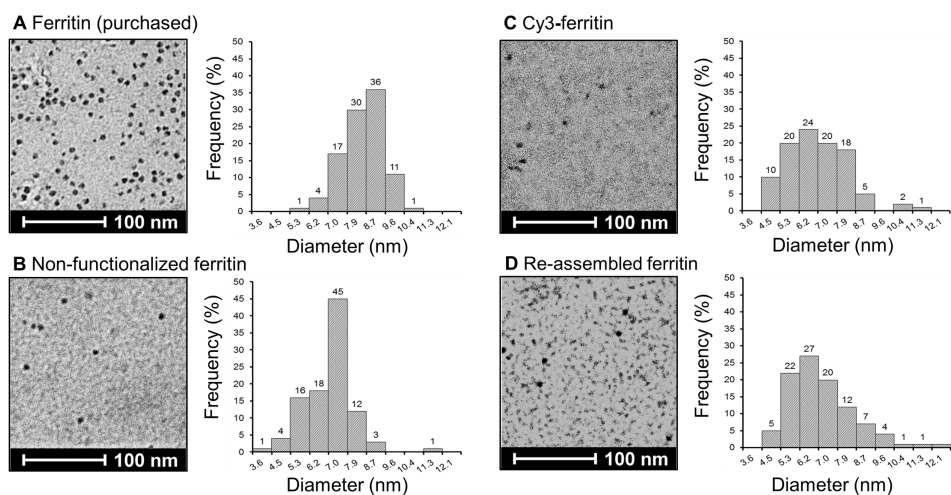


Figure 5. TEM analysis of FeII biomineralization with corresponding size histograms of purchased ferritin containing iron and ferritin samples treated with 1000 molar Fe excess to ferritin capsids. **A)** Commercially purchased ferritin, **B)** Non-functionalized ferritin, **C)** Cy3-functionalized ferritin, and **D)** re-assembled multi functionalized ferritin.

functionalized capsids, in these control samples FRET interactions (Cy5 emission peak after Cy3 excitation) could not be observed (Figure 4, C). To further visualize the FRET effect a 3D plot (Figure 4, D) of the excitation and emission spectrum Cy3: Cy5: non-functionalized = 4.4:4.1:15.5 was measured together with its negative control (Figure 4, E). The conclusion that Cy3 and Cy5 are indeed located on the same capsid after re-assembly was also underlined by additional SEC measurements (Supporting Information).

Iron Biomineralization by Multi Functionalized Ferritin

The biomineralization properties of ferritin results in the Fe^{II} nucleation into a ferrimagnetic iron core.⁴⁸⁻⁵⁰ To validate if orthogonally functionalized ferritin capsids are still capable of iron mineralization, they were dissolved in an iron-ion rich solution and analysed using TEM. The same was done with non-functionalized (apo) ferritin and Cy3-functionalized ferritin. The obtained images were compared to commercially purchased iron bearing ferritin (Figure 5, A). The iron cores are visible in each image (Figure 5) as dark dots, with an average diameter of: 7.8 ± 0.9 nm for purchased ferritin, 6.2 ± 1.0 nm for non-functionalized ferritin, 6.1 ± 1.4 nm for Cy3-functionalized ferritin, and 6.3 ± 1.5 nm for re-assembled Cy3-, Cy5-functionalized ferritin. The loading method for iron, resulted in

Table 2. ICP-MS results of indicated ferritin samples.

| Sample | Ferritin $\mu\text{Mol/L}^{\text{a}}$ | Fe mmol/L^{b} | Fe / Ferritin % $^{\text{c}}$ |
|-----------------------------|---------------------------------------|-------------------------------|-------------------------------|
| Ferritin (purchased) | 14.7 | 3.6 | 100 |
| Non-functionalized ferritin | 13 | 1.5 | 48.4 |
| Cy3-ferritin | 9.1 | 0.7 | 29.7 |
| Re-assembled ferritin | 1.9 | 0.2 | 50.0 |

[a] Determined by absorption measurements. [b] Determined by ICP-MS measurements. [c] Iron loading percentage relative to purchased ferritin.

approximately 2 nm smaller sized iron cores compared to the purchased ferritin, with a slightly larger spread in size for the functionalized ferritin capsids (Figure 5, C and D).

According ICP-MS the biomineralisation properties of ferritin are retained by the re-assembled Cy3-, Cy5-functionalized ferritin capsids and seem as efficient as for the non-functionalized ferritin (Table 2). Only the Cy3-functionalized ferritin yielded slightly lower percentage of Fe^{III} particles per capsid. Apparently, the higher quantity of Cy-dyes conjugated to the capsid, 16 instead of 8.5 as for the re-assembled ferritin, reduced the inwards diffusion of iron. That the biomineralization of iron inside the re-assembled Cy3-, Cy5-functionalized ferritin capsids was as efficient as for non-functionalized ferritin capsids was further confirmed by fluorescence measurements (Supporting Information); by increasing iron concentration within the capsids the fluorescence quenching of the proteins (mainly tyrosine) is quenched.⁵¹⁻⁵³

In theory, the re-assembled ferritin capsids might be one subunit short, as discussed above.⁴¹ If this occurs, however, it does not seem to influence the iron-mineralization process. As a result, the described orthogonal functionalization technique seems compatible with iron loading and could be an additional tool in the future development of MRI contrast agents.

CONCLUSIONS

With these studies we have shown that ferritin can act as supramolecular basis for the controlled generation of orthogonally functionalized ferritin bio-nanoparticles that may find an application in e.g. MRI imaging. This said attaching relatively small dye substituents on the protein subunits already had a negative influence on the self-assembly process.

Acknowledgments

The research leading to these results has received funding from the European Research Council (ERC) under the European Union's Seventh Framework Programme FP7/2007-2013 (grant agreement number 2012-306890), from the NWO nano-Grant (STW 11435), and from the Netherlands Organisation for Scientific Research (NWO) (STW BGT 11272).

REFERENCES

1. N. F. Steinmetz; D. J. Evans, Utilisation of plant viruses in bionanotechnology. *Org. Biomol. Chem.* **2007**, *5* (18), 2891-2902.
2. L. A. Lee; H. G. Nguyen; Q. Wang, Altering the landscape of viruses and bionanoparticles. *Org. Biomol. Chem.* **2011**, *9* (18), 6189-6195.
3. M. G. Mateu, Assembly, stability and dynamics of virus capsids. *Arch. Biochem. Biophys.* **2013**, *531* (1-2), 65-79.
4. Z. Heger; S. Skalickova; O. Zitka, et al., Apoferritin applications in nanomedicine. *Nanomedicine* **2014**, *9*, 2233-2245.
5. H. N. Munro; M. C. Lincer, Physiological Reviews. *Am. Phys. Soc.* **1978**, *58* (2), 317 - 396.
6. N. J. Sanghamitra; T. Ueno, Expanding coordination chemistry from protein to protein assembly. *Chem. Commun.* **2013**, *49*, 4114-4126.
7. Z. Zhen; W. Tang; Y.-j. Chuang, et al., Tumor Vasculature Targeted Photodynamic Therapy for Enhanced Delivery of Nanoparticles. *ACS Nano* **2014**, (6), 6004-6013.
8. Q. A. Pankhurst; C. J.; S. K. Jones, et al., Applications of magnetic nanoparticles in biomedicine. *J. Phys. D: Appl. Phys.* **2003**, *36*, R167-R181.
9. J. F. Hainfield, Uranium-loaded apoferritin with antibodies attached: Molecular design for uranium neutron-capture Therapy. *Med. Sci.* **1992**, *89*, 11064-11068.
10. Z. Yang; X. Wang; H. Diao, et al., Encapsulation of platinum anticancer drugs by apoferritin. *Chem. Commun. (Camb)* **2007**, *33* (33), 3453-3455.
11. M. Uchida; M. L. Flenniken; M. Allen, et al., Targeting of Cancer Cells with ferrimagnetic Ferritin Cage Nanoparticles. *J. Am. Chem. Soc.* **2006**, *128*, 16626-16633.
12. C. Cao; X. Wang; Y. Cai, et al., Targeted in vivo imaging of microscopic tumors with ferritin-based nanoprobes across biological barriers. *Adv. Mater.* **2014**, *26* (16), 2566-2571.
13. K. Fan; C. Cao; Y. Pan, et al., Magnetoferritin nanoparticles for targeting and visualizing tumour tissues. *Nat. Nanotechnol.* **2012**, *7* (7), 459-464.
14. Z. Zhen; W. Tang; T. Todd, et al., Ferritins as nanoplatforms for imaging and drug delivery. *Expert. Opin. Drug. Deliv.* **2014**, *11* (12), 1913-1922.
15. D. Resnick, Modeling of the magnetic behavior of $\gamma\text{-Fe}_2\text{O}_3$ nanoparticles mineralized in ferritin. *J. Appl. Phys.* **2004**, *95* (11), 7127.
16. E. Valero; S. Fiorini; S. Tambalo, et al., In vivo long-term magnetic resonance imaging activity of ferritin-based magnetic nanoparticles versus a standard contrast agent. *J. Med. Chem.* **2014**, *57* (13), 5686-5692.

17. B. Cohen; H. Dafni; G. Meir, et al., Ferritin as an endogenous MRI reporter for noninvasive imaging of gene expression in C6 glioma tumors. *Neoplasia* **2005**, *7* (2), 109-117.
18. W. F. Rurup; J. Snijder; M. S. T. Koay, et al., Self-sorting of foreign proteins in a bacterial nanocompartment. *J. Am. Chem. Soc.* **2014**, *136* (10), 3828-3832.
19. H. Zope; F. Versluis; A. Ordas, et al., Om votrp amd om vivo supramolecular modification of biomembranes using a lipidated coiled-coil motif. *Angew. Chem. Int. Ed.* **2013**, (52), 14247-14251.
20. J. M. Pollino; K. P. Nair; L. P. Stubbs, et al., Cross-linked and functionalized 'universal polymer backbones' via simple, rapid, and orthogonal multi-site self-assembly. *Tetrahedron* **2004**, *60* (34), 7205-7215.
21. L. Brunsveld; B. J. B. Folmer; E. W. Meijer, et al., Supramolecular Polymers. *Chem. Rev.* **2001**, *101*, 4071-4097.
22. X. Yan; S. Li; J. B. Pollock, et al., Supramolecular polymers with tunable topologies via hierarchical coordination-driven self-assembly and hydrogen bonding interfaces. *Proc. Natl. Acad. Sci. U S A* **2013**, *110* (39), 15585-15590.
23. P. Besenius; Y. Goedegebure; M. Driesse, et al., Peptide functionalised discotic amphiphiles and their self-assembly into supramolecular nanofibres. *Soft matter* **2011**, (7), 7980-7983.
24. X. Lin; J. Xie; L. Zhu, et al., Hybrid ferritin nanoparticles as activatable probes for tumor imaging. *Angew. Chem. Int. Ed.* **2011**, (7), 1569-1572.
25. S. Kang; L. M. Oltrogge; C. C. Broomell, et al., Controlled Assembly of Bifunctional Chimeric PRotein Cages and Composition Analysis Using Noncovalent Mass Spectrometry. *J. Am. Chem. Soc.* **2008**, *130*, 16527-16529.
26. E. Gillitzer; P. Suci; M. Young, et al., Controlled ligand display on a symmetrical protein-cage architecture through mixed assembly. *Small* **2006**, (8), 962-966.
27. M. T. Smith; A. K. Hawes; B. C. Bundy, Reengineering viruses and virus-like particles through chemical functionalization strategies. *Curr. Opin. Biotechnol.* **2013**, *24* (4), 620-626.
28. N. Stephanopoulos; M. B. Francis, Choosing an effective protein bioconjugation strategy. *Nat. Chem. Biol.* **2011**, *7* (12), 876-884.
29. Y. Zhang; B. P. Orner, Self-assembly in the ferritin nano-cage protein superfamily. *Int. J. Mol. Sci.* **2011**, *12* (8), 5406-5421.
30. S. Aime; L. Frullano; S. G. Crich, Compartmentalization of a Gadolinium Complex in the Apoferritin Cavity: A Route To Obtain High Relaxivity Contrast Agents for Magnetic

- Resonance Imaging. *Angew. Chem. Int. Ed.* **2002**, *41*, 1017-1019.
31. J. C. Cutrin; S. G. Crich; D. Burghlelea, et al., Curcumin/Gd loaded apoferritin: a novel "theranostic" agent to prevent hepatocellular damage in toxic induced acute hepatitis. *Mol. Pharm.* **2013**, *10* (5), 2079-2085.
 32. L. Wang; J. Fan; X. Qiao, et al., Novel asymmetric Cy5 dyes: Synthesis, photostabilities and high sensitivity in protein fluorescence labeling. *J. Photochem. Photobiol. A: Chem.* **2010**, *210* (2-3), 168-172.
 33. S. stefanini; S. Cavallo; B. Montagnini, et al., Incorporation of iron by the unusual dodecameric ferritin from *Listeria innocua*. *Biochem. J.* **1999**, *338*, 71-75.
 34. S. G. Crich; B. Bussolati; L. Tei, et al., Magnetic resonance visualization of tumor angiogenesis by targeting neural cell adhesion molecules with the highly sensitive gadolinium-loaded apoferritin probe. *Cancer Res.* **2006**, *66* (18), 9196-9201.
 35. Silvio Aime; Luca Frullano; S. G. Crich, Compartmentalization of a Gadolinium Complex in the Apoferritin Cavity: A Route To Obtain High Relaxivity Contrast Agents for Magnetic Resonance Imaging**. *Angew. Chem. Int. Ed.* **2002**, *41*, 1017 - 1019.
 36. B. Webb; J. Frame; Z. Zhao, et al., Molecular Entrapment of Small Molecules within the Interior of Horse Spleen Ferritin. *Arch. Biochem. Biophys.* **1994**, *309*, 178-183.
 37. M. T. Klem; D. a. Resnick; K. Gilmore, et al., Synthetic control over magnetic moment and exchange bias in all-oxide materials encapsulated within a spherical protein cage. *J. Am. Chem. Soc.* **2007**, *129* (1), 197-201
 38. E. C. Theil, Ferritin: Structure, gene, regulation, and cellular function in animals, plants, and microorganisms. *Ann. Rev. Biochem.* **1987**, *56*, 289-315.
 39. C. Bernacchioni; V. Ghini; C. Pozzi, et al., Loop electrostatics modulates the intersubunit interactions in ferritin. *ACS Chem. Biol.* **2014**, *9* (11), 2517-2525.
 40. D. J. Huard; K. M. Kane; F. A. Tezcan, Re-engineering protein interfaces yields copper-inducible ferritin cage assembly. *Nat. Chem. Biol.* **2013**, *9* (3), 169-176.
 41. M. Kim; Y. Rho; K. S. Jin, et al., pH-dependent structures of ferritin and apoferritin in solution: disassembly and reassembly. *Biomacromolecules* **2011**, *12* (5), 1629-1640.
 42. M. Gerl; R. Jaenicke, Mechanism of the self-assembly of apoferritin from horse spleen. *Eur. Biophys. J.* **1978**, *15*, 103-109.
 43. Q. Zeng; T. Li; B. Cash, et al., Chemoselective derivatization of a bionanoparticle by click reaction and ATRP reaction. *Chem. Commun. (Camb)* **2007**, *14* (14), 1453-1555.
 44. N. F. Steinmetz; D. J. Evans; G. P. Lomonossoff, Chemical introduction of reactive thiols into a viral nanoscaffold: a method that avoids virus aggregation. *Chembiochem : a European journal of chemical biology* **2007**, *8* (10), 1131-1136.

45. L. I. Willems; H. S. Overkleeft; S. I. Kasteren, Current Developments in Activity-Based Protein Profiling. *Bioconjugate Chem.* **2014**, (25), 1181-1191.
46. M. Liang; K. Fan; M. Zhou, et al., H-ferritin-nanocaged doxorubicin nanoparticles specifically target and kill tumors with a single-dose injection. *Proceedings of the National Academy of Sciences of the United States of America* **2014**, 111 (41), 14900-14905
47. S. Lee; J. Lee; S. Hohng, Single-Molecule Three-Color FRET with Both Negligible Spectral Overlap and Long Observation Time. *PLoS ONE* **2010**, 5 (8), 12270-12279.
48. M. T. Klem; M. Young; T. Douglas, Biomimetic magnetic nanoparticles. *Mater. Today* **2005**, 8 (9), 28-37.
49. N. Chasteen; P. Harrison, Mineralization in ferritin: an efficient means of iron storage. *J. Struct. Biol.* **1999**, 126, 182-194.
50. M. Allen; D. Willits; J. Mosolf, et al., Protein Cage Constrained Synthesis of Ferrimagnetic Iron Oxide Nanoparticles. *Adv. Mater.* **2002**, 14, 1562-1565.
51. A. B. T. Ghisaidoobe; S. J. Chung, Intrinsic Tryptophan Fluorescence in the Detection and Analysis of Proteins: A Focus on Forster Resonance Energy Transfer Techniques. *Int. J. Mol. Sci.* **2014**, 15 (15), 22518-22538.
52. F. Bou-Abdallah; P. Santambrogio; S. Levi, et al., Unique iron binding and oxidation properties of human mitochondrial ferritin: a comparative analysis with Human H-chain ferritin. *J. Mol. Biol.* **2005**, 347 (3), 543-554.
53. K. Orino; T. Miura; S. Muto, et al., Sequence analysis of canine and equine ferritin H and L subunit cDNAs. *DNA Sequence* **2005**, 16 (1), 58-64.





SUPPORTING INFORMATION CHAPTER 5

**Orthogonal Functionalization of Ferritin
via Supramolecular Re-Assembly**

RESULTS

SEC of multi functionalized re-assembled ferritin

To support the conclusion from the FRET results that Cy3- and Cy5-modified subunits are located on the same ferritin capsid after re-assembly, additional SEC measurements were performed. In these experiments, UV absorbance at 550 nm and 650 nm was measured, to detect the Cy3- and Cy5-dyes conjugated to the capsids (Figure S1). As negative control for the duo-functionalized ferritin capsids, a mixture of separately functionalized Cy3- and Cy5-ferritin was prepared with the same Cy3 and Cy5 concentration as the re-assembled sample with ratio Cy3: Cy5: non-functionalized = 4.4 : 4.1 : 15.5. Although less conclusive than the FRET data, a difference in the SEC graph between the two samples is visible. For the duo-functionalized ferritin capsids, the Cy3 and Cy5 absorbance signal elute exactly at the same time and form one peak. In contrast, the sample containing the mixture of Cy3- and Cy5-ferritin capsids shows a Cy5 absorbance peak that is slightly shifted in comparison with the Cy3 absorbance peak, resulting in two distinguishable elution peaks. Although this data is not conclusive on its own, together with the FRET data it does support the conclusion that after re-assembly the Cy3- and Cy5-subunits are located within the same ferritin capsid.

Fluorescence of the variable functionalized ferritin capsids

When apoferritin is excited at 270 nm, the proteins emit light between 300 and 400 nm with a maximum at 310 nm (Figure S2), this fluorescence originates from the tyrosine and tryptophan amino acids.¹ With increasing iron concentration within the ferritin capsids the fluorescence of the proteins (mainly tyrosine)¹⁻² is quenched. Thereby the amount of quenching is an indication of the number of iron inside.

The decrease in fluorescent signal with increasing Fe^{III} / capsid is depicted in Figure S2A, where the emission spectra of apoferritin and apoferritin treated with 400-, 600-, 800- and 1000 molar excess of iron to ferritin capsids are plotted. Figure S2B shows the fluorescent signal of apoferritin, purchased ferritin containing iron, non-functionalized ferritin, ferritin-Cy3 and re-assembled ferritin of which the latter three were also treated with 1000 molar excess of iron.

The data shows that Cy3-functionalized ferritin contains the least amount of iron and that purchased ferritin contains the most, since its fluorescence signal at 340 nm (tryptophan) is also lowered compared to non-functionalized ferritin. The re-assembled ferritin and non-functionalized contain comparable amounts, with non-functionalized ferritin containing slightly more according to the 340 nm peak.

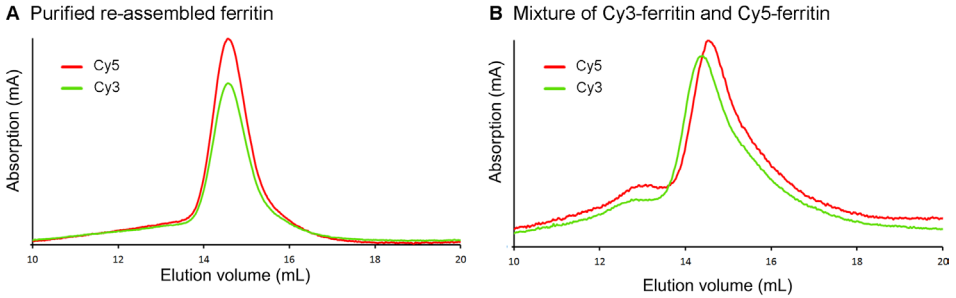


Figure S1. SEC of Cy3-, and Cy5-functionalized ferritin (**A**) and a mixture of separately functionalized Cy3-ferritin and Cy5-ferritin (**B**). With red: the absorption signal of Cy5 (650 nm) and green: the absorption signal of Cy3 (550 nm) of the corresponding sample, both absorbance signals were measured simultaneously.

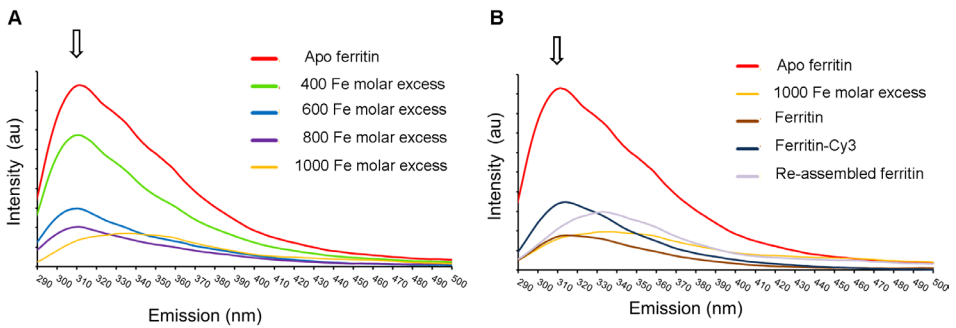


Figure S2. Emission spectra of ferritin capsids after excitation at 270 nm with ferritin capsids concentration set at 0.05 absorbance. **A**) Ferritin capsids treated with increasing molar excess of iron to ferritin capsid. **B**) Non-functionalized, Cy3-functionalized and re-assembled ferritin after treatment with 1000 molar excess of iron to ferritin capsids, purchased ferritin and apoferritin are shown for comparison.

REFERENCES

1. A. B. T. Ghisaidoobe; S. J. Chung, Intrinsic Tryptophan FLuorescence in the Detection and Analysis of Proteins: A Focus on Forster Resonance Energy Transfer Techniques. *Int. J. Mol. Sci.* **2014**, *15* (15), 22518-22538.
2. K. Orino; T. Miura; S. Muto, et al., Sequence analysis of canine and equine ferritin H and L subunit cDNAs. *DNA Sequence* **2005**, *16* (1), 58-64.





Adapted from: Spa SJ, Hensbergen AW, van der Wal S, Kuil J, van Leeuwen FWB.
Dyes and Pigments 2018;152:19-28

and

Spa SJ, Hensbergen AW, van der Wal S, Kuil J, van Leeuwen FWB.
Data Brief 2019;22:50-55



CHAPTER 6

**The influence of systematic structure alterations
on the photophysical properties and conjugation
characteristics of asymmetric cyanine 5 dyes**

ABSTRACT

The light spectrum above 650 nm allows for good tissue penetration depths, therefore far-red and near-infrared fluorescent dyes are popular fluorophores applied in (bio)medical diagnostics, including image-guided surgery. Unfortunately, near-infrared fluorescent dyes often suffer from instability and limited brightness, two important features that, together with the labelling efficiency (e.g., non- one- or di-conjugated products) and serum-dye interactions are key elements that drive in vivo characteristics. Due to the fact that stability and brightness of far-red fluorophores are often superior over near-infrared dyes, interest in the use of dyes such as Cy5 is increasing. As there are clear indications that the chemical structure of a dye influences the (photo)physical properties, these properties of ten structural variants of asymmetrical Cy5-(R₁)R₂-(R₃)COOH (R representing the varied substituents) dyes were extensively studied. While stacking in solution was not induced in most of the Cy5 far-red dyes, multimers and stacking characteristics were observed in protein conjugates. Although all dye variants were shown to be stable towards photobleaching, clear differences in brightness and serum interactions were found. Combined, these findings indicate that there is a direct relation between chemical substituents and the properties of Cy5 dyes, and that this feature should be considered when using fluorescent dyes in future tracer development.

INTRODUCTION

Fluorescent dye-based guidance during surgical interventions is being recognised as an improvement in the accuracy of clinical care.¹⁻³ In clinical trials, fluorescence imaging has been used as a sole modality or in a bimodal/hybrid form, wherein it extends the field of nuclear medicine.⁴ While fluorescence emissions across the light spectrum have been used for image-guided surgery,² emphasis lies on the use of dyes emitting in the far-red (650 nm < λ_{em} < 750 nm) or near-infrared (NIR; $\lambda_{em} \geq 750$ nm) region.⁵ This theoretical preference can be attributed to the enhanced penetration depths and limited autofluorescence at these wavelengths.

Unfortunately, the dye chemistry, stability and/or photophysical properties of near-infrared dyes are limited compared to dyes emitting at lower wavelengths. For example, the most commonly applied near-infrared dye indocyanine green (**ICG**) is prone to stack/aggregate from aqueous solutions and has a low quantum yield ($Q_F = 0.3\%$ in H₂O).⁶ More experimental dyes such as IRdye 800CW also have a low quantum yield ($Q_F = 3.4\%$ in H₂O)⁷ and have been shown to be chemically unstable with respect to endogenous nucleophiles.⁸ These limitations have boosted the interest in far-red dyes. For instance, methylene blue (**MB**), a clinically applied dye with a weak far-red fluorescence emission ($Q_F = 3\%$ in H₂O) has been applied in humans to image ureters,⁹ parathyroid glands,¹⁰ and bile ducts,¹¹ despite the FDA warning against its use.¹² As an alternative, the Cyanine 5 (Cy5) family provides relatively bright ($\sim 3 \cdot 10^4 \text{ M}^{-1} \text{ cm}^{-1}$; $Q_F \approx 20\%$ in H₂O)¹³ far-red fluorophores and encompasses many structural variations. A prime example of a Cy5-based imaging agent in clinical use is found in GE-137 (now EM-137), a Cy5 labelled c-Met-targeting peptide that was effectively used for identification of colorectal polyps in humans.¹⁴ Furthermore, the Cy5-containing nanoparticles ¹²⁴I-cRGDY-PEG-C have been used to target metastatic melanoma.¹⁵

To convert Cy5-dyes into imaging agents of value for fluorescence guided surgery, these dyes have to be conjugated to targeting vectors. When a targeting vector has multiple conjugation sites, e.g. a protein, labelling may not be straightforward. A ratio of one dye per targeting vector is generally aimed at, but the final product often consists of, e.g., a mixture of none-, one-, di-, and/or tri-dye-conjugated imaging agents. In case multiple dyes are located on a single targeting vector, the occurrence of dye-stacking or Förster Resonance Energy Transfer (FRET) between the dyes can cause luminescence quenching, a feature that reduces the brightness of the imaging agent.⁸

Conjugation of imaging labels, and especially an excess thereof, may also negatively influence the binding specificity and pharmacokinetics of a targeting vector. Dependent

on the size of the targeting vector, the scale of these effects varies,¹⁶ being most prominent when relatively small peptides are used.^{14,17} Nevertheless, this effect is also reported for larger proteins such as mAb conjugates.¹⁸ When dyes express an affinity for serum proteins such as human serum albumin, e.g., **ICG** and $\text{Cy5-(Ar)SO}_3\text{-(Ar)SO}_3$,¹⁹⁻²¹ this may further effect the tracer pharmacokinetics.

In order to determine the influence of the structure of a fluorescent dye on its utility as an imaging label, ten Cy5 analogues were synthesised and compared with the reference compound **MB**. By alternating the aromatic (R_1 and R_3) and alkyl substituents (R_2), molecular variations on $\text{Cy5-(R}_1\text{)R}_2\text{-(R}_3\text{)COOH}$ were systematically evaluated for their photophysical properties, chemical- and photo-stability, serum protein interaction, dye-dye stacking tendencies, and conjugation efficiency (Figure 1).

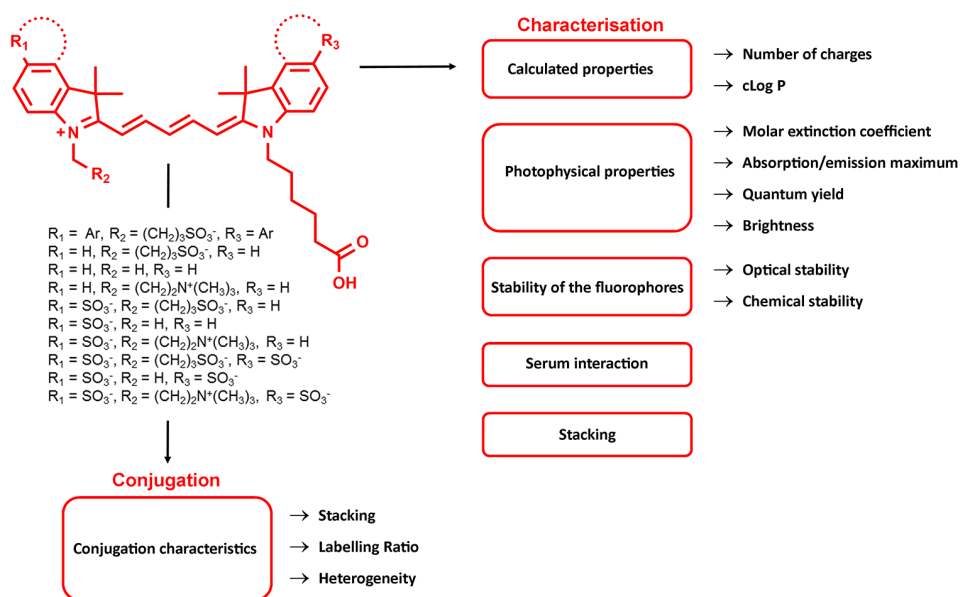


Figure 1. Overview of the subjects and fluorophore properties investigated and discussed throughout the article.

EXPERIMENTAL

General

For the synthesis of the fluorophores (Compound **1–21**), the electron density modelling, cLog P calculations, and information on the materials used, please refer to the Supporting information (SI).

Ubiquitin labelling (compound 22–30)

Stock solutions of the NHS-activated fluorophores (**12–21**, see SI) were prepared in DMSO and the percentage of activated dye was determined by HPLC (see also SI 'NHS activation'). Subsequently, Ubiquitin (16 nmol) was dissolved in 500 μL of phosphate buffer (0.1 M, pH 8.4; 2.67 g HNa_2PO_4 + 0.14 g H_2NaPO_4 in 200 μL H_2O). Appropriate amounts of the fluorophore stock solution were added, ensuring that each sample contained 3 equivalents activated dye (50 nmol, 100 μM final concentration) and that the DMSO content in the final solution was < 10%. The mixtures were shaken at room temperature for 6.5 h and the labelled Ubiquitin was washed with PBS by filtration over a 3 K Amicon® filter subsequently. When the filtrate was no longer blue, the residue was collected in 100 μL PBS. Dye–Ubiquitin conjugates were analysed by mass spectrometry (MALDI-TOF) and absorption measurements (NanoDrop). To determine the average labelling ratio, the dye concentration was calculated from absorption measurements in DMSO around 650 nm (Table 1) and the obtained values were then divided by the known protein concentration (0.16 mM). For compound 30 significant precipitation was observed after the reaction, therefore the protein content in this sample also was determined by absorption ($\epsilon_{280} = 1490 \text{ M}^{-1} \text{ cm}^{-1}$; calculated from the amino acid sequence).²² Since Cy5 also shows absorbance at this wavelength, a correction was made by measuring the absorbance of free dye at this concentration and subtracting it from the absorbance value measure for the dye-containing Ubiquitin.

Photophysical properties

Molar extinction coefficient (ϵ) of compound 1–11

To obtain a 4mM stock solution of **MB (1)**, 3.2 mg Methylene blue hydrate (Fisher Scientific) was dissolved in 4mM ethylene carbonate in DMSO-d_6 (1500 μL) and the exact concentration was determined by NMR using ethylene carbonate as internal standard.⁸ To allow for absorption measurements, the 4 mM stock solutions of the dyes in DMSO-d_6 (**1–11**, for details, see SI) were diluted to 100 μM in DMSO, H_2O or PBS.

From the 100 μM concentration, 50 μM and 5 μM concentrations were made from which further two-fold dilution in the same medium followed to obtain a final concentration range of 100, 50, 25, 12.5, 5, 2.5, 1.2, 0.6, and 0.3 μM , respectively. Absorption spectra were measured using 1 mL disposable plastic cuvettes ($l = 1$ cm; Brand, Germany) for concentrations ≤ 5 μM , quartz cuvettes ($l = 0.1$ cm; Hellma standard cell, Macro) for 12, 25, and 50 μM concentrations, and two glass microscopy slides held together with a 0.14 mm thick PET plastic spacer for the 100 μM concentration to keep the signal below 1.5 AU. Optical density was measured 10 min after preparation and the plotted absorbance was normalised for cuvette path length and concentration. The ϵ was then determined by applying a linear regression coefficient.

Absorbance spectra of the labelled Ubiquitin (22–30)

The Ubiquitin solutions collected after synthesis (for synthesis procedures see SI) were diluted 100 \times in PBS and the absorbance spectra were measured using NanoDrop. Subsequently, the obtained spectra were normalised for dye concentration.

Quantum yield and emission maximum determination of compound 1–11 and 22–30

Fluorescence spectra were measured at $\lambda_{\text{ex}} = 606$ nm for compounds **3–11** and the Ubiquitin conjugates **22–30**, and $\lambda_{\text{ex}} = 620$ nm for **1–2**, using 1 cm disposable plastic 4.5 mL cuvettes (Kartell, Germany). 3 mL of 0.5 μM dye was prepared in PBS (1–11, 22–30) by first preparing 100 μM solutions in PBS from the DMSO- d_6 dye stock (2–9 and MB solutions) or from dilutions of the Ubiquitin conjugates (**22–30**) (see SI for synthesis). To determine the quantum yield, the absorbance at $\lambda = 606$ (compounds **3–11** and **22–30**) or $\lambda = 620$ nm (compound **1–2**) of 0.5 μM and 0.25 μM were measured and correlated with the integrated fluorescent emission. The regression coefficient of the resulting plot for the unknown dyes was then compared to the regression coefficient of Cy5-(SO₃)COOH-(SO₃)COOH (Figure 2), which has a known quantum yield ($Q_f = 27\%$).¹³

Stability

Chemical stability of compound 1–11 towards glutathione

Solutions of 0.25 mM dye (from DMSO- d_6 NMR solutions) and 0.5 mM glutathione in 4-(2-hydroxyethyl)-1-piperazine-ethanesulfonic acid buffer (HEPES, 0.1 M, pH 7.4) were freshly made. Prior to the addition of glutathione to the HEPES buffer, nitrogen was bubbled through the HEPES buffer to remove oxygen and reduce the rate of disulfide formation of glutathione. The solutions were immediately put into the sample manager

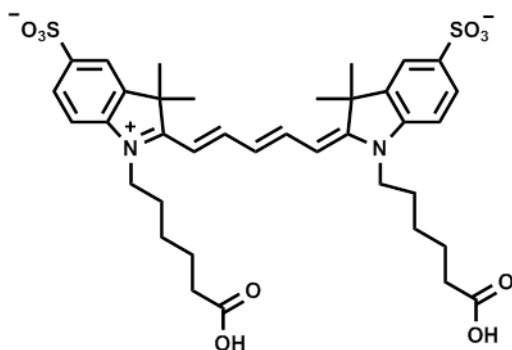


Figure 2. Chemical structure of the reference compound applied for the quantum yield determination; Cy5-(SO₃)COOH-(SO₃)COOH.

(37 °C) of a Waters Acquity UPLC-MS system equipped with an Acquity UPLC photodiode array detector, an SQ Detector mass spectrometer and a Waters BEH C18 130 Å 1.7 μm (100 × 2.1 mm) column (flow rate: 0.5 mL/min). Analysis was performed every 30 min using a gradient of 0.05% TFA in H₂O/0.04% TFA in CH₃CN 95:5 to 0.05% TFA in H₂O/0.04% TFA in CH₃CN 5:95 in 5.44 min. The stability of the dyes was calculated relative to the integration of the chromatogram at t = 0 h.

Optical stability of compound 1–11

For the optical stability measurements, a prototype Karl Storz camera setup (KARL STORZ Endoskope GmbH & Co. KG, Tuttlingen, Germany) was applied. This camera setup included an IMAGE1 S H3-Z FI Three-Chip FULL HD camera head equipped with a 0° laparoscope in combination with an IMAGE 1 S CONNECT module, an IMAGE 1 S H3- LINK module and a Cy5-modified D-light C light source (590–680 nm emission). A standard eyepiece adapter containing a filter that passes through light between 640 and 720 nm (Cat no. 20100034; KARL STORZ Endoskope GmbH & Co. KG) was placed between the camera and the laparoscope to image the Cy5 fluorescence. From the DMSO-d₆ dye stock solutions (see synthesis in SI) 100 μM solutions in PBS were prepared. Subsequently, from the 100 μM solutions, 3.0 mL of 1 μM solutions were prepared in 4.5 mL disposable cuvettes (Kartell, Germany). The cuvettes were placed in front of the prototype Karl Storz camera and illuminated at maximum intensity for 30 min. At five-minute intervals the fluorescence was measured with λ_{ex} = 602 nm. The reduction in fluorescence intensity was plotted and normalised relative to the fluorescence intensity obtained at t = 0 min.

Serum protein interaction

Serum protein binding was assayed using the single-use Rapid Equilibrium Dialysis (RED) plate kit with an 8 kD MWCO (Pierce, Thermo Scientific). Serum (300 μL , fetal bovine serum, heat inactivated) was placed into the dialysis chamber and phosphate buffer (500 μL , 100 mM phosphate and 150 mM NaCl, pH = 7.2) was placed into the reservoir chamber. The dyes were added from a DMSO stock (100 μM , 3 μL) to the dialysis chamber ($n = 2$) and in duplicate samples ($n = 2$) to the reservoir chamber. The plate was subsequently closed using sealing tape and incubated at room temperature on a rocking shaker for 18 h, after which 100 μL aliquots were withdrawn from both chambers for each dye. 100 μL phosphate buffer was then added to the aliquots containing serum, and 100 μL serum was added to the aliquots containing phosphate buffer. All aliquots were transferred to a white 96-well plate (Greiner Lumitrac 600) and fluorescence was quantified at $\lambda_{\text{ex}} = 620 \text{ nm}$ using a PerkinElmer LS 55 fluorometer (equipped with a red-sensitive detector and a plate-reader attachment). Serum protein binding percentages were calculated using the manufacturer's protocol (eq. (1)):

$$\%_{\text{bound}} = \left(100 - \frac{[\text{buffer chamber}]}{[\text{serum chamber}]} \right) \cdot 100 \quad \text{eq. (1)}$$

Stacking behaviour of compound 1–11 in different solvents

To determine the stacking behaviour of the dyes (**1–11**) in DMSO, H_2O or PBS, the same dilutions and absorbance measurements were performed as described for measuring the molar extinction coefficient ("*Molar extinction coefficient (ϵ) of compound 1–11*").

RESULTS AND DISCUSSION

Chemical properties

The number of charges, and calculated Log P (cLog P) values of the investigated fluorophores are given in Figure 3. Overall, the calculated net charge decreased with increasing number of sulfonate moieties on the aromatic ring, which also resulted in decreasing cLog P values. The highest cLog P value was, as expected, calculated for compound **2** due to the presence of additional benzene rings. The lowest cLog P value was found for compound **11**, as a result of the high total number of charges (5). The cLog P value of **MB (1)** was most similar to the cLog P value calculated for compound **6**.

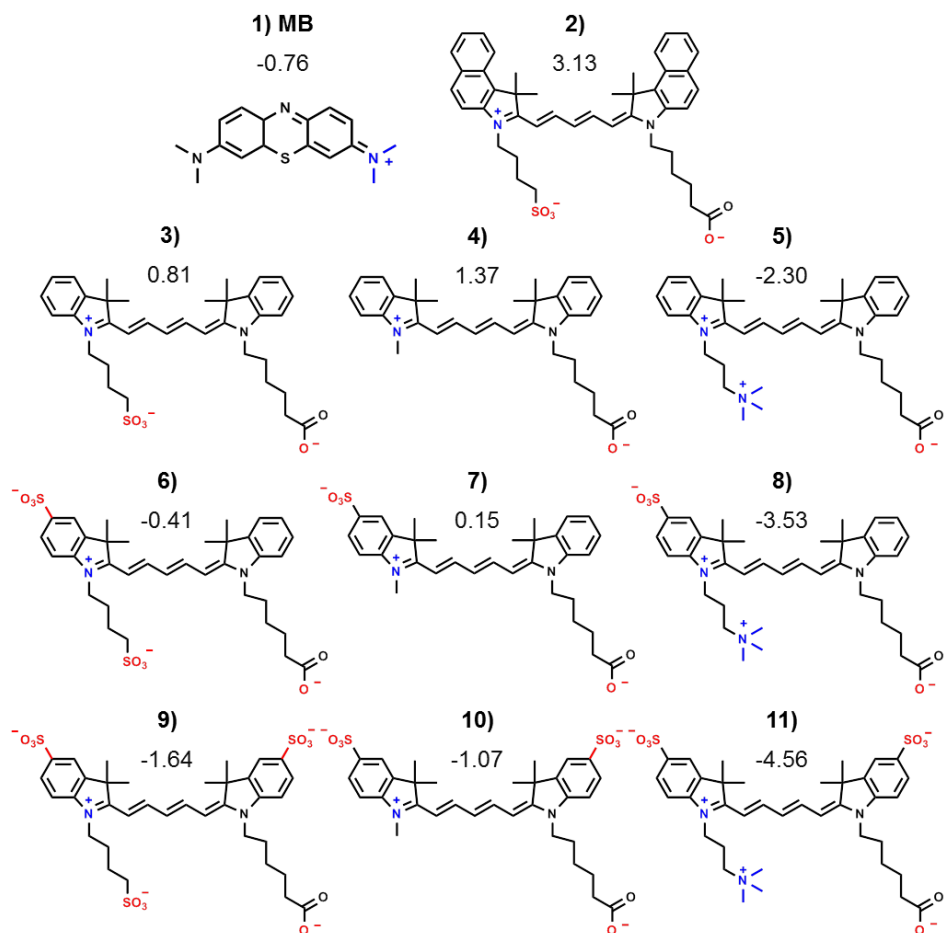


Figure 3. The cLog P values for compounds **1-11**. In the compound structures the positively charged groups are indicated in blue and negatively charged groups are indicated in red.

Photophysical properties

The molar extinction coefficient (ϵ) was calculated via the regression coefficient between the concentration and the absorbance determined from a linear concentration range between 0.3 and 5 μM in DMSO, H_2O , and PBS. In DMSO, except for compounds **2, 4** ($\epsilon \approx 185.000 \text{ M}^{-1} \text{ cm}^{-1}$) and **MB (1)** ($\epsilon = 84.000 \text{ M}^{-1} \text{ cm}^{-1}$), all dyes had $\epsilon > 200.000 \text{ M}^{-1} \text{ cm}^{-1}$. The ϵ determined for **MB** in DMSO was in line with the literature, which reported values between 70.000 and 95.000 $\text{M}^{-1} \text{ cm}^{-1}$.^{23,24} For compounds **3-8** the ϵ decreased with about

25% when changing the solvent from DMSO to H₂O or PBS. A more substantial decrease (37%) was observed for the more lipophilic compound **2**. Remarkably, for the more soluble compounds with two aromatic sulfonates (**9–11**) the change in solvent resulted in a 10% increase in the ϵ and gave extinction coefficients of 242.000, 220.000 and 231.000 M⁻¹cm⁻¹ in PBS respectively (Table 1).

The absorption/emission maxima of the Cy5 fluorophores (**2–11**) observed in DMSO had Stokes shifts of about 20 nm (Table 1) while **MB (1)** had a Stokes shift of 16 nm. Changing the solvent from DMSO towards H₂O or PBS caused a hypsochromic shift in the absorption/ emission maximum of 10 nm for **2–11** and only a minor shift (5 nm) for **MB**. Comparison of the absorption/emission maxima (Table 1) with the structure of the dyes (Fig. 3), revealed that all compounds with a sulfonate on both aromatic rings (**9–11**) displayed a slight bathochromic shift of around 5 nm in their maxima. This bathochromic shift has also been reported for other fluorophores in the Cy5 family.²⁵ This effect was, however, not observed when no or just one aromatic sulfonate was present at this location (e.g., **9** vs **3** and **6**, Table 1).

In practice, the environment of the fluorophores will be aqueous, hence the quantum yield measurements were performed in PBS and related to that of Cy5-(SO₃)COOH-(SO₃)COOH ($\Phi_f = 27\%$).¹³ In line with the above-presented molar extinction coefficients, the quantum yields of compounds **9**, **10**, and **11** were also the highest (23%) from the series; the other Cy5-dye derivatives displayed quantum yields around 13% or lower (Table 1). In contrast, **MB** yielded a quantum yield of merely 3%. It is interesting to note that the quantum yields did not alter significantly upon changing the alkyl substituent (e.g., **3** vs **4** vs **5**, Table 1), or changing the number of aromatic sulfonates from 0 to **1** (e.g., **3** vs **6**). As Fisher et al. suggested,²⁶ a clear trend between the structure of dyes and the quantum yield seems to be missing.

Although emphasis is generally placed on the molar extinction coefficient or quantum yield individually, the combination of both properties, i.e., the brightness (quantum yield x molar extinction coefficient),²⁷ often gives more insight in the optical capability of the fluorophores. This difference also becomes apparent from Figure 4, where all 11 fluorophores are imaged by a prototype Karl Storz camera setup ($\lambda_{ex} = 590\text{--}680$ nm, data collection between 640 and 750 nm). For proper in vivo visualisation, a signal-to-background ratio (e.g., tumour-to-muscle) of at least 2 is required.²⁸ On the basis of the signal-to-background ratio calculated from Figure 4, one can deduct that a brightness $> 1 \cdot 10^4$ M⁻¹cm⁻¹ is required to achieve a signal-to-background ratio > 2 . With a brightness of $3 \cdot 10^3$ M⁻¹cm⁻¹ and a signal-to-background ratio of 1.6, **MB** fluorescence was considered too

Table 1. Photophysical properties of compound **1–11**, including the quantum yields of **22–30**. With ϵ for molar extinction coefficient, $\lambda_{ex}/\lambda_{em}$ for excitation/emission wavelength, Φ_F for quantum yield and n. a. for not applicable.

| Dye | ϵ in DMSO ^a (M ⁻¹ ·cm ⁻¹) | ϵ in water ^a (M ⁻¹ ·cm ⁻¹) | ϵ in PBS ^a (M ⁻¹ ·cm ⁻¹) | $\lambda_{ex}/\lambda_{em}$ in DMSO (Stokes shift; nm) | $\lambda_{ex}/\lambda_{em}$ in H ₂ O and PBS (Stokes shift; nm) | Φ_F in PBS ^b Non-conjugated | Φ_F in PBS ^b Conjugated (22–30) |
|--------------|---|---|--|---|---|--|--|
| MB(1) | 84 · 10 ³ | 77 · 10 ³ | 71 · 10 ³ | 670/686 (16) | 665/679 (14) | 3% | n.a. ^c |
| 2 | 181 · 10 ³ | 113 · 10 ³ | 112 · 10 ³ | 688/710 (22) | 678/695 (17) | 10% | n.a. ^c |
| 3 | 200 · 10 ³ | 199 · 10 ³ | 203 · 10 ³ | 655/671 (16) | 643/659 (16) | 14% | 5% |
| 4 | 188 · 10 ³ | 176 · 10 ³ | 174 · 10 ³ | 647/667 (20) | 640/656 (16) | 13% | 10% |
| 5 | 218 · 10 ³ | 193 · 10 ³ | 193 · 10 ³ | 658/677 (19) | 638/658 (20) | 13% | 12% |
| 6 | 228 · 10 ³ | 206 · 10 ³ | 206 · 10 ³ | 655/675 (20) | 643/660 (17) | 13% | 9% |
| 7 | 238 · 10 ³ | 176 · 10 ³ | 212 · 10 ³ | 653/672 (19) | 642/658 (16) | 13% | 3% |
| 8 | 200 · 10 ³ | 146 · 10 ³ | 149 · 10 ³ | 647/673 (26) | 637/657 (20) | 9% | 14% |
| 9 | 219 · 10 ³ | 245 · 10 ³ | 242 · 10 ³ | 660/679 (19) | 648/664 (16) | 22% | 21% |
| 10 | 204 · 10 ³ | 233 · 10 ³ | 220 · 10 ³ | 658/677 (19) | 646/662 (16) | 23% | 14% |
| 11 | 209 · 10 ³ | 223 · 10 ³ | 231 · 10 ³ | 659/677 (18) | 645/661 (16) | 23% | 20% |

^a Fresh dilutions from the DMSO stock were made and measured within 2 h.

^b Relative quantum yield, compared to Cy5-(SO₃)COOH-(SO₃)COOH ($\Phi_F = 27\%$) [13].

^c Labelling was not successful.

weak to be detected accurately (Figure 4B). Since fluorescence imaging of **MB** has already been used in clinical trials, this finding underlines the medical potential of the relatively bright Cy5 dyes.²⁹

Figure 4 indicates that the fluorophores with two aromatic sulfonates (**9–11**) possess the best optical properties. It is known that electron withdrawing groups, e.g., sulfonates, substituted on the aromatic ring, increase the brightness of such fluorophores.³⁰ Interestingly, despite their match in brightness, Spartan calculations revealed differences in the theoretical electron densities (Figure S2). Hence, in line with the report by Levitus et al.,³¹ the positive effect of aromatic sulfonates on the optical properties might not solely lie in the electrostatic withdrawing capacity. According to the combined data in Table 1 and Figure S2, the concept of reinforced conformational stability seems to offer a more probable explanation for the sulfonate induced increase in fluorescence brightness; cis–trans photoisomerisations of the central methine bridge influences the fluorescence brightness.³²

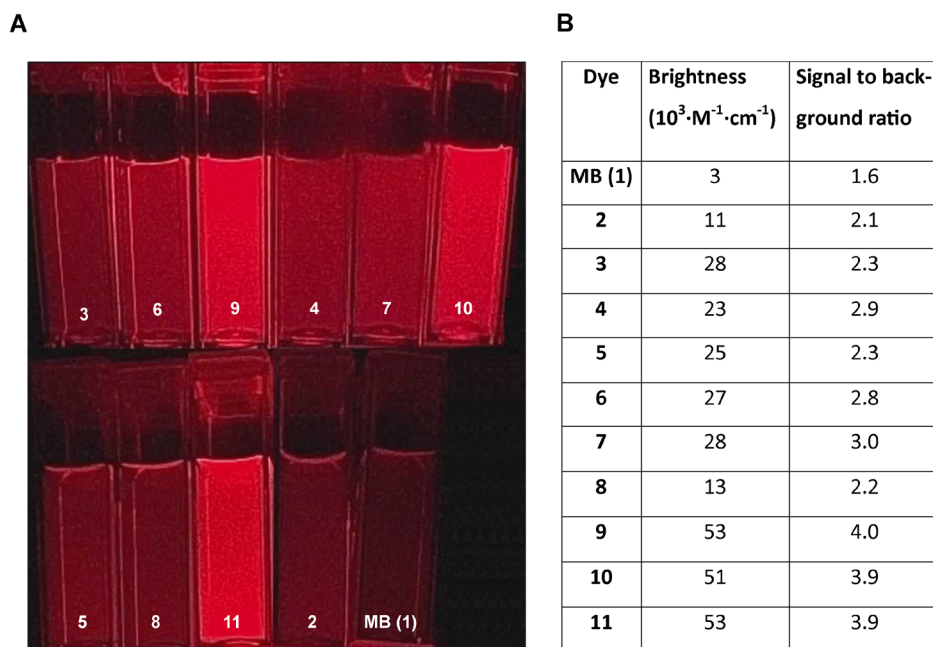


Figure 4. Brightness of the fluorophores in PBS (1 μM) measured by Storz camera (**A**) or calculated (**B**). From the image (**A**) the corresponding signal-to-background ratios were calculated (**B**). Overall, the fluorophores with two aromatic sulfonates (**9–11**) emit the brightest fluorescence, while **MB** is hardly visible at all (signal to background ratio < 2).

In the ground state, the main conformation of the Cy5 dyes is the trans-conformation.³¹ However, when excited, the methine bridge can rotate around its C–C bonds, twisting towards the cis-conformation.^{31,33} In the cis-conformation, the most probable route towards the ground state is via nonluminescent internal conversion due to the high overlap in the vibronic wave functions (Frank Condon factor).²⁵ It has been speculated that sulfonation of the aromatic rings increases the stability of the transconformation, thereby reducing the rate of cis–trans photoisomerisation^{31,33} and increasing the fluorescence brightness.

Stability of the fluorophores

As the fluorophores **2–11** were synthesised with a future use in image-guided surgery in mind, their optical stability was tested by exposure to a light source of a dedicated laparoscopic fluorescence camera ($\lambda_{\text{ex}} = 590\text{--}680 \text{ nm}$). With the exclusion of ambient light, fluorophore solutions of 1 μM in PBS were irradiated for a duration of 30 min, with an

assessment of their fluorescence intensity at five-minute intervals. For most compounds, more than 90% of fluorescent signal remained after 30 min, indicating good optical stability (Figure 5A). Only compound **2** showed 30% photobleaching. Although subtle, it is interesting to note that the fluorophores without sulfonates on the aromatic rings portrayed a slightly lower photostability (**3–5**; ~88% remaining fluorescence intensity) compared to the dyes with a sulfonated side chain (**6–11**; 95% remaining fluorescence intensity). This indicates that the substitution of sulfonates on the aromatic rings positively affects the optical stability of the fluorophores.

Earlier studies have underlined that it is also important that the dyes are chemically stable in an *in vivo* environment.^{8,34} To evaluate the chemical stability of the dyes towards endogenous nucleophiles, they were incubated for up to 6 h at 37 °C in a model buffer containing 0.5 mM glutathione.^{8,35} UPLC-MS was used to discriminate if any adducts were formed by reaction with the respective thiol. As apparent from Figure 5B, all fluorophores remained stable and fluorescent at the given conditions. This finding excludes the formation of unwanted products during *in vivo* administration, as was previously reported for the NIR dyes ZW800-1 and IRdye 800-CW.⁸

Serum protein interaction

Next to the stability of the fluorophores towards endogenous nucleophiles, the tendency of the dyes to non-covalently bind to serum proteins was also evaluated. Equilibrium dialysis against serum (18 h) revealed clear differences between the dyes (Figure 5C). Increasing the number of sulfonates on the aromatic ring induced an approximate 50% decrease in serum protein binding following each sulfonate introduced. Introducing a sulfonate on the side chain reduced the albumin interaction with about 30% compared to the neutral (Me-) substituted dyes. The quaternary-amine substituents reduced this even further. When these findings were related to the cLog P values, it appeared that there is a threshold value at cLog P = 0.8. For dyes portraying a cLog P above this value, i.e. lipophilic dyes, a serum protein binding tendency of > 50% was observed (compound **2**, **3** and **4**). When the cLog P value drops below 0.8, the influence of the lipophilicity seems to become less substantial and the number of charges on the compounds started to play a role, with the lowest percentage of binding found for compound **9** and **11** (< 10%; five total charges). Overall, both the aromatic substituents and alkyl substituents play a prominent role in the interaction with serum proteins.

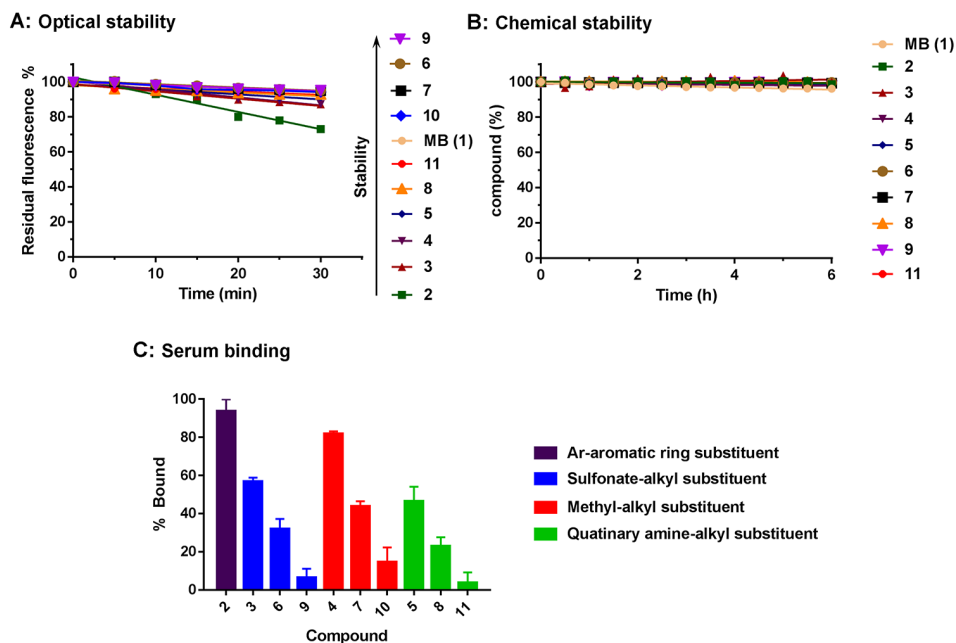


Figure 5. Optical and chemical stability of the fluorophores and their tendency to interact with serum proteins. **A)** Optical stability; the dyes were illuminated using the light source of a prototype Karl Storz camera setup ($\lambda_{\text{ex}} = 590\text{--}680\text{ nm}$). Reduction in fluorescence was measured up to 30 min with five-minute intervals. Dyes are given in order of decreasing stability in the legend (arrow). **B)** Chemical stability of the eleven dyes in 0.5 mM glutathione in HEPES (pH 7.4) at 37 °C as assayed overtime by UPLC-MS. **C)** Percentage of fluorophore bound to serum proteins after 18 h of dialysis with serum versus PBS. The fluorophores are grouped in colour by their alkyl substituents and within each group the dye with non-, one-, and two-sulfonates on the aromatic ring are given from left to right.

Stacking behaviour

Previously we found that the degree of dye stacking observed in the reaction mixture was predictive for the amount of stacking of the dyes on the obtained conjugation products.⁸ In general, the presence of multiple (stacked) dyes on the final product reduces the brightness and homogeneity of the sample. Therefore, the stacking-based aggregation rates of the 11 compounds investigated were determined in DMSO, PBS and H₂O at concentrations ranging from 0.3 to 100 μM . Compounds **3–11** did not aggregate in these solvents (Figure 6, and Figure S3) while **MB** and compound **2** did demonstrate distinct stacking in the aqueous media (Figure 6). Compound **2** showed aggregation at concentrations higher than 2.5 μM in PBS and H₂O. A comparable aggregation tendency

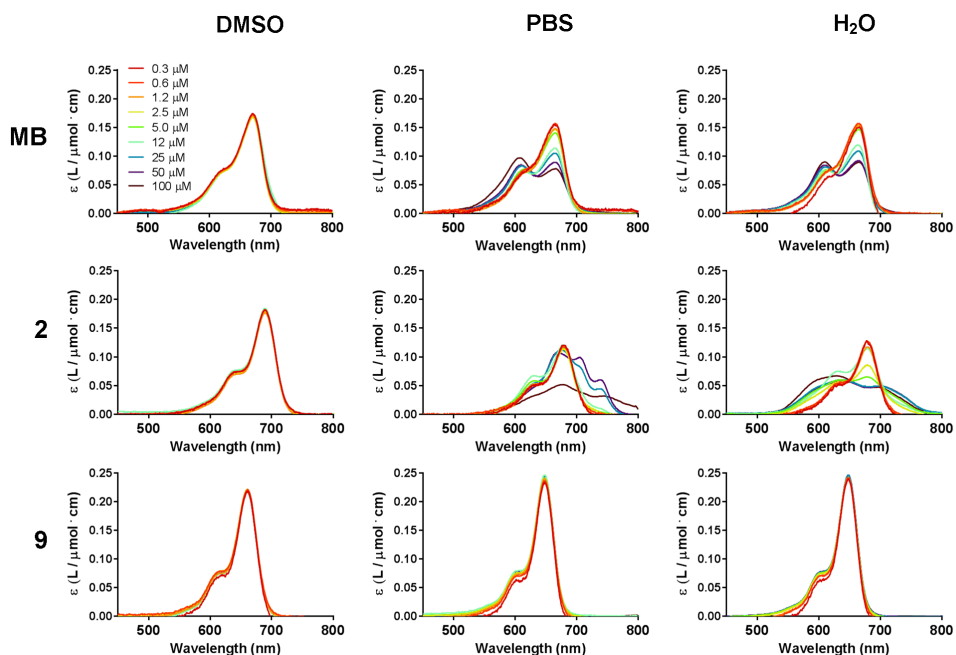
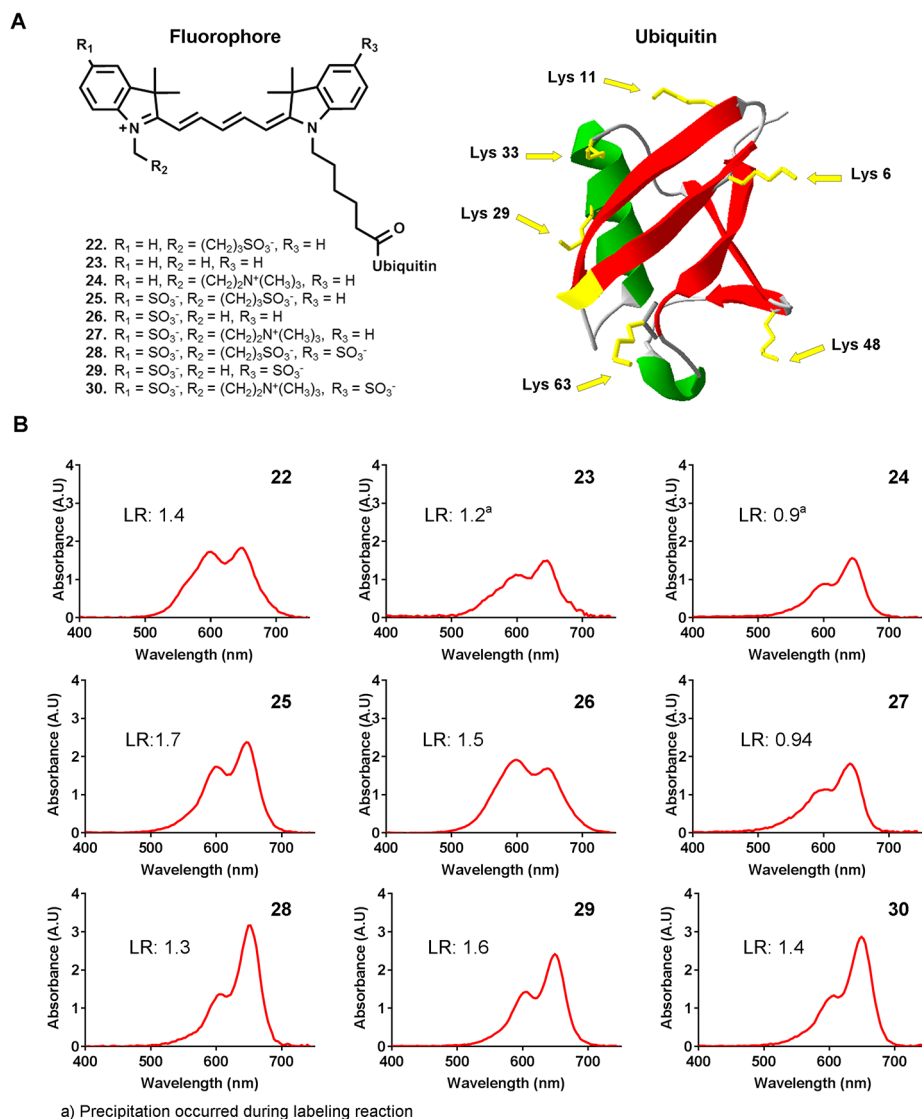


Figure 6. The stacking concentration dependency of **MB** and compound **2**, and **9** measured in DMSO, PBS and H₂O at concentrations ranging from 0.3 to 100 μM. Compound **9** is shown as model for compound **3–11** as they were all comparable. For detailed visualisation of each compound separately please see Figure S3.

was reported earlier for **ICG**.⁸ Based on this, the observed stacking at > 2.5 μM concentration in aqueous medium seems to be induced by the presence of the two additional aromatic rings. **MB** showed an even stronger dimeric stacking tendency than compound **2**, while the concentration dependency of this effect was comparable to that of compound **2** (Figure 6).²³

Conjugation

To investigate if the structure variations in the fluorophores have an influence on their conjugation characteristics, compounds **2–11** were activated (yielding compound **12–21**, see SI) and conjugated to the reference protein Ubiquitin. This small (~8.5 kDa),³⁶ well-known regulatory protein is present in almost every eukaryotic cell and contains 7 lysine residues of which 6 are solvent-exposed (Figure 7A) (evaluated from the PDB structure 5DK8). The low molecular weight of Ubiquitin makes it possible to study the labelling process via mass spectrometry (MS), which helps provide insight into the homogeneity



of the products obtained within a single sample. Relating these findings to the absorbance profiles of the same products allowed for the determination of relative labelling ratios.

The labelling with the fluorophore **2** was unsuccessful due to its low solubility at the required concentrations (100 μ M). Thus, the conjugation reactions yielded nine Ubiquitin

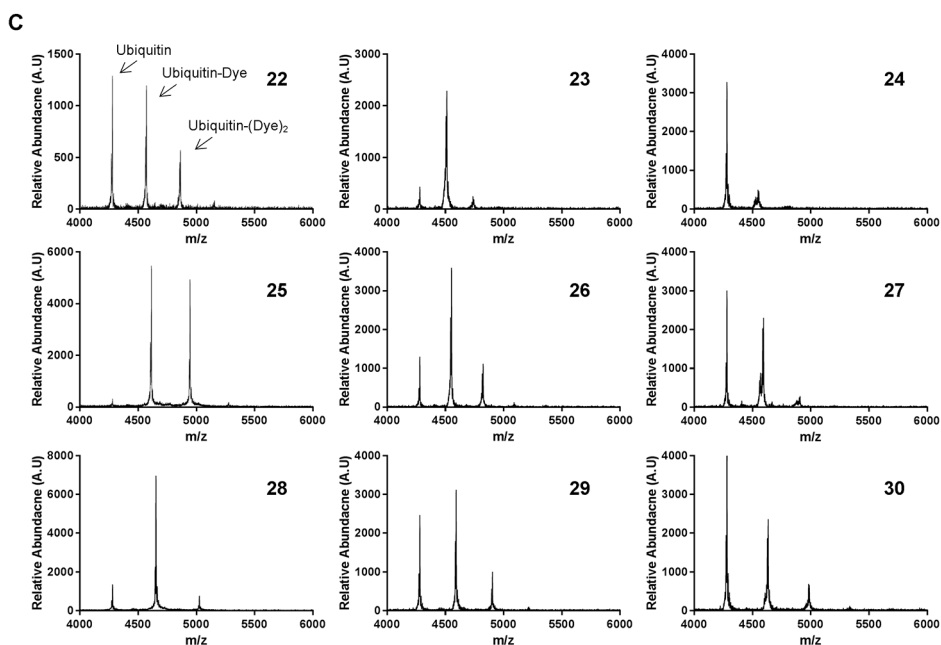


Figure 7. A) The Cy5 dyes conjugated to Ubiquitin. Within the structure of Ubiquitin the surface-exposed lysine groups and the N-terminus are indicated in yellow as probable binding sides for the fluorophores. The image was constructed from the PDB structure 5DK8. **B)** Absorption spectra of the dyes conjugated to Ubiquitin (**22–30**) measured in PBS, including the dye loading rates (LR). The fluorophores on construct **22**, **23**, **25**, **26**, and **29** are stacking as is indicated by the increase of the right shoulder peak. The spectra are normalised on dye concentration to underline the differences in the shape of the absorbances. **C)** Mass spectra of the conjugated Cy5-Ubiquitin compounds. The mass signals of M_2^+ are shown as these were the most intense, with $m/z = 4278$ non-conjugated Ubiquitin, $m/z \approx 4500$ mono-conjugated Ubiquitin and $m/z \approx 4800$ di-conjugated Ubiquitin.

constructs (**22–30**). While previously no stacking was observed at the concentrations used in the reaction mixture (Figure 6), absorption spectra of the conjugation products **22**, **23**, **25**, **26**, and **29** revealed stacking (Figure 7B). The presence of sulfonate groups on the aromatic ring decreased the stacking as did the presence of a quaternary amine on the side chain. When measured in DMSO, these stacking interactions were no longer present due to increased solvation of the dyes (Figure S4) and the dye loading rates could be accurately determined (Figure 7B; LR).⁸ The calculated loading rates were found to be comparable (around 1) with exception of compounds **25** (1.7) and **29** (1.6). However, except for being the only two dyes with a -2 net charge (Figure 3) there is no clear indication why these loading rates were higher than the others.

When looking at the mass spectra of the conjugated Cy5–Ubiquitin conjugates (**22–30**) it becomes evident that the samples are heterogeneously labelled and that this effect differs between dyes (Figure 7C). For the dyes with the sulfonated side chain (**22, 25, 28**), only the fluorophore with two aromatic sulfonates (**28**) labelled homogeneously. For the dyes containing the methyl side chain (**23, 26, 29**) however, lower number of sulfonates on the aromatic rings resulted in a more homogeneously labelled Ubiquitin (**23**). MS analysis of the compounds with a quaternary amine on the side chain (**24, 27, 30**) was more complex. The low ionisation of the mono or di-conjugated Ubiquitin resulted in a discrepancy between the information obtained by MS and what was calculated from the absorbance spectra. Nevertheless, it can be concluded that here also, the labelling was heterogeneous as multiple peaks were visible. Combining the absorbance and MS data, we demonstrated that while absorption spectra clearly indicate that the Cy5 dyes undergo a significant degree of stacking (in PBS Figure 7B, not in DMSO; Figure S4), the same samples only displayed a limited amount of di-conjugated Ubiquitin products (Figure 7C). Furthermore, no stacking was observed for the free form of these compounds at the same concentration (Figure 4 and, Figure S3). This suggests that the stacking observed is not the traditional dye–dye stacking, but comes from stacking interactions with, e.g. tyrosine, tryptophan, or phenylalanine amino acids within the protein. According to the crystal structure of Ubiquitin, there is at least one phenylalanine spatially nearby every solvent-exposed Lysine (determined from the PDB structure 5DK8). The stacking interaction with the surrounding amino acids is also to be noted by the quantum yield (Table 1). After conjugation to the protein, the quantum yield of most compounds decreased, and the degree of reduction correlated with the observed amount of stacking. Indeed, the diminishing quantum yield did also not depend on whether the Ubiquitin is homogeneously labelled (one peak on the MS data), thus underlining the fact that the observed stacking occurs between the dye and neighbouring amino acids.

When the investigated dyes were compared in a biodistribution study with RGD it was found that compound **7** yielded superior *in vivo* properties.¹⁷ Based on the chemical characteristics investigated herein however, compound **7** did not stand out, pointing out that chemical characteristics are only one aspect in the development of efficient fluorescent tracers for *in vivo* use. In the end, the Cy5 dye becomes but a component of a larger molecular structure, of which the overall characteristics drive the targeting behaviour and biodistribution.¹⁷ Given the apparent balance that has to be obtained between the chemical characteristics of the dye and a targeting vector, it seems to be inevitable that labelling of an individual targeting vector goes hand-in-hand with screening of different Cy5-dyes

structures, e.g. as presented in Figure 3. Nevertheless, in fluorescent tracer design we would like to suggest that only dyes are used that are: (photo)chemically stable, bright enough to obtain a signal-to-background ratio of at least 2 with the cameras intended for clinical use, show no stacking in solution, and ideally label proteins homogeneously.

CONCLUSION

In this study, the characteristic chemical and photophysical properties of ten systematically altered Cy5 derivatives and their Ubiquitin conjugates were methodically analysed. Next to these structure–activity relationships, the compatibility of the dyes with a clinical-grade fluorescence laparoscope was also presented. Overall, the influence of the aromatic- and alkyl substituents on the chemical- and photophysical properties of the ten Cy5 dyes has been documented more clearly, providing a solid basis for future tracer developments.

Acknowledgements

The research leading to these results has received funding from the European Research Council (ERC) under the European Union's Seventh Framework Program FP7/2007–2013 (Grant No. 2012-306890), a Netherlands Organization for Scientific Research STW-VIDI grant (Grant No. STW BGT11272). We thank KARL STORZ Endoskope GmbH & Co. KG for providing the prototype Cy5 light source. We also like to thank A.R.P.M. Valentijn for making his lab available and providing the Waters Acquity UPLC-MS system.

REFERENCES

- 1 Ferrari E, Gu C, Niranjana D, et al., Synthetic self-assembling clostridial chimera for modulation of sensory functions. *Bioconjugate Chem.* **2013**, *24*, 1750–1759.
- 2 van Leeuwen FWB, Hardwick JCH, van Erkel AR. Luminescence-based imaging approaches in the field of interventional molecular imaging. *Radiology.* **2015**, *276*, 12–29.
- 3 Byrne WL, Delille A, Kuo C, et al., Use of optical imaging to progress novel therapeutics to the clinic. *J Contr Release.* **2013**, *172*, 523–34.
- 4 van Leeuwen FWB, Valdés-Olmos R, Buckle T, et al., Hybrid surgical guidance based on the integration of radionuclear and optical technologies. *Br J Radiol.* **2016**, *89*, 20150797
- 5 Yuan L, Lin W, Zheng K, et al., Far-red to near infrared analyte-responsive fluorescent probes based on organic fluorophore platforms for fluorescence imaging. *Chem Soc Rev* **2013**, *42*, 622–661.
- 6 Benson R, Kues HA. Fluorescence properties of indocyanine Green as related to angiography. *Phys Med Biol.* **1978**, *23*, 159–163.
- 7 Azhdarina A, Wilganowski N, Robinson H, et al., Characterization of chemical, radiochemical and optical properties of a dual-labeled MMP-9 targeting peptide. *Bioorg Med Chem.* **2011**, *19*, 3769–3776.
- 8 van Der Wal S, Kuil J, Valentijn ARPM, et al., Synthesis and systematic evaluation of symmetric sulfonated centrally C-C bonded cyanine near-infrared dyes for protein labelling. *Dyes Pigments.* **2016**, *132*, 7–19.
- 9 Verbeek FPR, Van Der Vorst JR, Schaafsma BE, et al., Intraoperative near infrared fluorescence guided identification of the ureters using low dose methylene Blue : a first in human experience. *JURO.* **2013**, *190*, 574–579.
- 10 Hossam M, Askar SM. Minimally invasive, endoscopic assisted, parathyroidectomy (MIEAP) with intraoperative methylene blue (MB) identification. *Egypt J Ear, Nose, Throat Allied Sci.* **2012**, *13*, 25–30.
- 11 Sari YS, Tunali V, Tomaoglu K, et al., Can bile duct injuries be prevented? "A new technique in laparoscopic cholecystectomy". *BMC Surg.* **2005**, *4*, 4–7.
- 12 FDA. Serious CNS reactions possible when methylene blue is given to patients taking certain psychiatric medications. <https://www.fda.gov/Drugs/DrugSafety/ucm263190.htm>
- 13 Mujumdar RB, Ernst LA, Mujumdar SR, et al., Cyanine dye labelling reagents: sulfoindocyanine succinimidyl esters. *Bioconjugate Chem.* **1993**, *4*, 105–111.

- 14 Burggraaf J, Kamerling IMC, Gordon PB, et al., Technical Reports Detection of colorectal polyps in humans using an intravenously administered fluorescent peptide targeted against c-Met. *Nat Med.* **2015**, *21*, 955-967
- 15 Phillips E, Penate-Medina O, Zanzonico PB, et al., Clinical translation of an ultrasmall inorganic optical-PET imaging nanoparticle probe. *Nanomedicine*, **2014**, *6*, 1–9.
- 16 Kuil J, Buckle T, Oldenburg J, et al., Hybrid peptide dendrimers for imaging of chemokine receptor 4 (CXCR4) expression. *Mol Pharm.* **2011**, *8*, 2444–2453.
- 17 Bunschoten A, van Willigen DM, Buckle T, et al., Tailoring fluorescent dyes to optimize a hybrid RGD-tracer. *Bioconjugate Chem.* **2016**, *27*, 1253–1258.
- 18 Zhou Y, Kim Y, Milenic DE, et al., In vitro and in vivo analysis of indocyanine Green-Labeled panitumumab for optical imaging - a cautionary tale. *Bioconjugate Chem.* **2014**, *25*, 1801–1810.
- 19 Bunschoten A, Buckle T, Kuil J, et al., Targeted non-covalent self-assembled nanoparticles based on human serum albumin. *Biomaterials.* **2012**, *33*, 867–875.
- 20 Bunschoten A, Buckle T, Visser NL, et al., Multimodal interventional molecular imaging of tumor margins and distant metastases by targeting $\alpha\beta 3$ integrin. *Chem biochem.* **2012**, *13*, 1039–1045.
- 21 Buckle T, Van Leeuwen AC, Chin PTK. A self-assembled multimodal complex for combined pre- and intraoperative imaging. *Nanotechnology.* **2010**, *21*, 1–9.
- 22 Pace CN, Vajdos F, Fee L, Grimsley G, Gray T. How to measure and predict the molar absorption-coefficient of a protein. *Protein Sci.* **1995**, *4*, 2411–2423.
- 23 Bergmann K, O'Konski CT. A spectroscopic study of methylene blue monomer, dimer, and complexes with montmorillonite. *J Phys Chem.* **1963**, *67*, 2169–2177.
- 24 Morgounova E, Shao Q, Hackel BJ, et al., Photoacoustic lifetime contrast between methylene blue monomers and self-quenched dimers as a model for dual-labeled activatable probes. *J Biomed Optic.* **2013**, *18*, 56004.
- 25 Tredwell CJ, Keary CM. Picosecond time resolved fluorescence lifetimes of the polymethine and related dyes. *Chem Phys.* **1979**, *43*, 307–316.
- 26 Fisher NI, Hamer FM. A comparison of the absorption spectra of some typical symmetrical cyanine dyes. *Proc Roy Soc.* **1936**, 703–723.
- 27 Chin PTK, Welling MM, Meskers SCJ, et al., Optical imaging as an expansion of nuclear medicine: Cerenkov-based luminescence vs fluorescence-based luminescence. *Eur J Nucl Med Mol Imaging* **2013**, *40*, 1283–1291.
- 28 Buckle T, Chin PTK, van den Berg NS et al., Tumor bracketing and safety margin estimation using multimodal marker seeds: a proof of concept. *J Biomed Optic.* **2012**, *15*, 56021.

- 29 Yeung TM, Volpi D, Tullis IDC, et al., Identifying ureters in situ under fluorescence during laparoscopic and open colorectal surgery. *Ann Surg.* **2016**, *263*, e1–2.
- 30 Mader O, Reiner K, Egelhaaf HJ, et al., Structure property analysis of pentamethine indocyanine dyes: identification of a new dye for life science applications. *Bioconjugate Chem.* **2004**, *15*, 70–78.
- 31 Levitus M, Ranjit S. Cyanine dyes in biophysical research: the photophysics of polymethine fluorescent dyes in biomolecular environments. *Q Rev Biophys.* **2011**, *44*, 123–151.
- 32 Netzel TL, Nafisi K, Zhao M, et al., Base-content dependence of emission enhancements, quantum yields, and lifetimes for cyanine dyes bound to double-strand DNA: photophysical properties of monomeric and bichromophoric DNA. *Stains. J Phys Chem.* **1995**, *99*, 17936–17947.
- 33 Schobel U, Egelhaaf H, Frohlich D, et al., Mechanisms of fluorescence quenching in donor – acceptor labeled antibody – antigen conjugates. *J Fluoresc.* **2000**, *10*, 147–154.
- 34 Cilliers C, Nessler I, Christodolu N, et al., Tracking antibody distribution with near infrared fluorescent dyes: impact of dye structure and degree of labelling on plasma clearance. *Mol Pharm.* **2017**, *14*, 1623-1633.
- 35 da Costa CM, dos Santos RCC, et al., A simple automated procedure for thiol measurement in human serum samples. *J Bras Patol Med Lab.* **2006**, *42*, 345-350
- 36 Goldstein G, Scheid M, Hammerling U, et al., Isolation of a polypeptide that has lymphocyte- differentiating properties and is probably represented universally in living cells. *Proc Natl Acad Sci U S A.* **1975**, *72*, 11–15.





SUPPORTING INFORMATION CHAPTER 6

**The influence of systematic structure alterations
on the photophysical properties and conjugation
characteristics of asymmetric cyanine 5 dyes**

EXPERIMENTAL SECTION

Materials

Solvents and chemicals were obtained from commercial sources and were used without further purification. HPLC purification and analysis were performed on a Waters HPLC system consisting of an HPLC 1525EF pump and a 2489 UV/Vis detector. Applying a Dr. Maisch GmbH Reprosil-Pur 120 C18-AQ 10 μm column (250 x 20 mm) operating at a flow rate of 12 mL/min for purification, and a Dr. Maisch GmbH Reprosil-Pur X18-AQ 5 μm column (250 x 4.6 mm) operating at a flow rate of 1 mL/min for analysis, using a gradient of 0.1% TFA in H₂O/CH₃CN 95:5 to 0.1% TFA in H₂O/CH₃CN 5:95 in 60 minutes. Lyophilisation was performed with a Steris GT4 lyophiliser. Mass spectrometry was performed on a Bruker Microflex MALDI-TOF. NMR spectra were measured on a Bruker DPX 300 MHz NMR. Absorbance was measured with either the Ultrospec 3000 UV-Visible spectrophotometer (Pharmacia Biotech) or with a NanoDrop 2000 UV-vis spectrophotometer (Thermo Scientific). The fluorescence measurements were performed on a Perkin-Elmer LS-55 fluorescence spectrometer.

SYNTHESIS

The Cy-dye building blocks

All indole-based building blocks were synthesised as previously described,¹ except for the indole-based building blocks: Indole-(Ar)Sulfonate and Indole-(Ar)COOH, which were synthesised according an adjusted literature procedure² shortly described below. All indole-building blocks were used without further purifications.

Indole-(Ar)Sulfonate

1,1,2-trimethyl-1H-benz[e]indole (6.3 g, 30 mmol) and 1,4-butane sultone (4.6 mL, 45 mmol) were dissolved in dry toluene (30 mL) and refluxed for 48 h. After cooling down the reaction mixture was filtered and the residue was washed with acetone to obtain the crude product (5.4 g).

Indole-(Ar)COOH

1,1,2-trimethyl-1H-benz[e]indole (4.8 g, 23 mmol) and 6-bromohexanoic acid (7.8 g, 40 mmol) were dissolved in acetonitrile (25 mL) and stirred for 3 days at 75 °C. The reaction

mixture was cooled down and the formed precipitate was collected by filtration. Subsequently the residue was washed with acetonitrile to give the crude product (2.2 g).

Cy5.5-dye (compound 2)

Cy5-(Ar)Sulfonate-(Ar)COOH (**2**) was synthesised according an adjusted literature procedure.^{3,4} Indole-(Ar)Sulfonate (2.1 g, 6 mmol) and 3-anilinoacraldehyde anil hydrochloride (1.7 g, 6.6 mmol) were dissolved in AcOH:Ac₂O (20 mL, 1:1). The reaction was refluxed until completion, as was visible by a shift in the absorbance maxima (from 375 nm to 450 nm) measured by UV-Vis. After concentrating *in vacuo*, the intermediate was dissolved in water and lyophilised. The intermediate was then dissolved in Ac₂O:pyridine (20 mL, 1:1 v/v) together with Indole(Ar)-COOH (**2**) (1.9 g, 6 mmol). The reaction mixture was refluxed and followed by UV-vis, it was deemed completed when the absorbance maxima had shifted from 450 nm towards 680 nm. The reaction mixture was cooled and concentrated *in vacuo* and the crude product Cy5-(Ar)Sulfonate-(Ar)COOH was purified by silica column chromatography (2:1 MeCN:MeOH v/v) and after pooling the product-containing fractions a semi-pure product was obtained (3.6 g). A small portion (50 mg) was further purified by preparative HPLC, and the product-containing fractions were collected and lyophilised to give 34.9 mg of product. Theoretically, this would yield 2.7 g of total product (64 %).

MS (MALDI-TOF): [C₄₃H₄₉N₂O₅S]⁺ calcd. 705.3, found 705.7. ¹H NMR (300 MHz, DMSO-d₆): 8.45 (t, 2H, CH), 8.26 (d, 2H, Ar-H), 8.11 – 8.03 (m, 4H, Ar-H), 7.84 – 7.62 (m, 4H, Ar-H), 7.51 (m, 2H, Ar-H), 6.65 (s, 1H, CH), 6.41 (dd, 2H, CH), 4.24 (s, 4H, N-CH₂), 2.54 (d, 2H, CH₂-SO₃), 2.21 (m, 2H, CH₂-CO), 1.96 (s, 12H, C-(CH₃)₂), 1.90-1.72 (mm, 6H, 3CH₂), 1.57 (m, 2H, CH₂), 1.42 (m, 2H, CH₂).

Cy5-dyes (compounds 3-11)

All Cy5-dyes were synthesised as reported previously.¹

Fluorophores stock solution

To ensure all possible counterions of the fluorophores were either potassium or chloride, the dyes were dissolved in 1 M KCL in H₂O:Acetonitrile (1:1, v/v with added 0.1% TFA) after purification and run over a preparative HPLC. After lyophilisation of the product containing fractions, the dyes were dissolved again in 4 mM ethylene carbonate (internal standard for NMR) in DMSO-d₆ to afford a 4 mM stock solution. To obtain a 4 mM stock solution of **MB (1)**, 3.2 mg Methylene blue hydrate (Fisher Scientific) was dissolved in 4 mM ethylene carbonate in DMSO-d₆ (1500 μL). By use of the internal standard, the exact concentration

of each stock solution could be determined by NMR. [5] Before further use the stock solutions were stored at 4 °C.

NHS activation of the fluorophores (compound 12-21)

General

To a solution of Cy5-dye (**3-11**) or Cy5.5-dye (**2**) (1.0 eq.) in DMSO (500 μ L) were added dipyrrolidino(N-succinimidyl)oxy)carbenium hexafluorophosphate (HSPyU) (2.2 eq.) and 4-methylmorpholine (NMM) (5.0 eq.). This reaction mixture was stirred at RT until completion as monitored by MALDI-TOF and TLC. The crude material was diluted with a solution of H₂O and MeCN (0.1% TFA, max 10% MeCN) before purification by preparative HPLC. The product-containing fractions were combined and lyophilised subsequently. As the NHS-activated carboxylic acid can slowly decompose during the lyophilisation process, the percentage of activated dye was determined by analytical HPLC before use.

Cy5-(Ar)sulfonate-(Ar)COOSu (12)

MALDI-TOF: [M+H]⁺ calculated 803.0, found 803.0. t_R = 43.8 min

Percentage of activated dye: 80%

Cy5-sulfonate-COOSu (13)

MALDI-TOF: [M+H]⁺ calculated 702.9, found 703.1. t_R = 38.7 min

Percentage of activated dye: 96%

Cy5-methyl-COOSu (14)

MALDI-TOF: [M]⁺ calculated 580.7, found 580.8. t_R = 42.6 min

Percentage of activated dye: 56%

Cy5-QAmine-COOSu (15)

MALDI-TOF: [M-H]⁺ calculated 665.9, found 665.9. t_R = 37.2 min

Percentage activated dye: 65%

Cy5-(SO₃)sulfonate-COOSu (16)

To the reaction mixture was added HSPyU (2.6 eq.) instead of the initially reported amount. For purification two HPLC runs according above description were performed.

MALDI-TOF: [M+2H]⁺ calculated 782.9, found 783.1. t_R = 32.4 min

Percentage of activated dye: 82%

Cy5-(SO₃)methyl-COOSu (17)

MALDI-TOF: $[M+H]^+$ calculated 660.8, found 660.7. $t_R = 35.9$ min
 Percentage of activated dye: 67%

Cy5-(SO₃)QAmine-COOSu (18)

MALDI-TOF: $[M]^+$ calculated 746.0, found 746.1. $t_R = 33.4$ min
 Percentage activated dye: >99%

Cy5-(SO₃)sulfonate-(SO₃)COOSu (19)

MALDI-TOF: $[M+3H]^+$ calculated 863.0, found 863.1. $t_R = 25.6$ min
 Percentage of activated dye: 58%

Cy5-(SO₃)methyl-(SO₃)COOSu (20)

MALDI-TOF: $[M+2H]^+$ calculated 740.9, found 740.9. $t_R = 28.7$ min
 Percentage of activated dye: >95%

Cy5-(SO₃)QAmine-(SO₃)COOSu (21)

To the reaction mixture were added HSPyU (3.5 eq.) and NMM (8.1 eq.) instead of the initially reported amounts.

MALDI-TOF: $[M+H]^+$ calculated 826.0, found 826.3. $t_R = 26.6$ min
 Percentage of activated dye: 93%

Electron density modelling and clog P calculations

Electrostatic potential mapping of the dyes was performed using Spartan '16 (Wavefunction, Irvine USA) using semi-empirical model and the PM6 method in the gas phase on the methylamide form of the fluorophores. The cLog P was calculated using molinspiration.¹

RESULTS

Design and Synthesis of the fluorophores

The pentamethine cyanine based fluorophores investigated in this work are shown in Figure S1. Their synthesis was reported earlier. In brief, this was accomplished by conjugation of the first indolenine, sulfo-indolenine or benzindolenine with a polymethine chain, obtaining hemicyanine intermediates with either the sulfonate-, methyl-, or quaternary amine substituents on the side chain (Figure S1). Subsequently, the hemicyanine

intermediate was linked with a second indolenine, sulfo-indolenine or benzindolenine, substituted with a carboxylic acid-alkyl group for further labelling.^{1,3,6} To obtain the specific indolenine compounds, the nitrogen on the commercially available indolenine, sulfo-indolenine or benzindolenine were alkylated with either, 1,4-butane sultone, methyl iodide or 6-bromohexanoic acid.^{3,7}

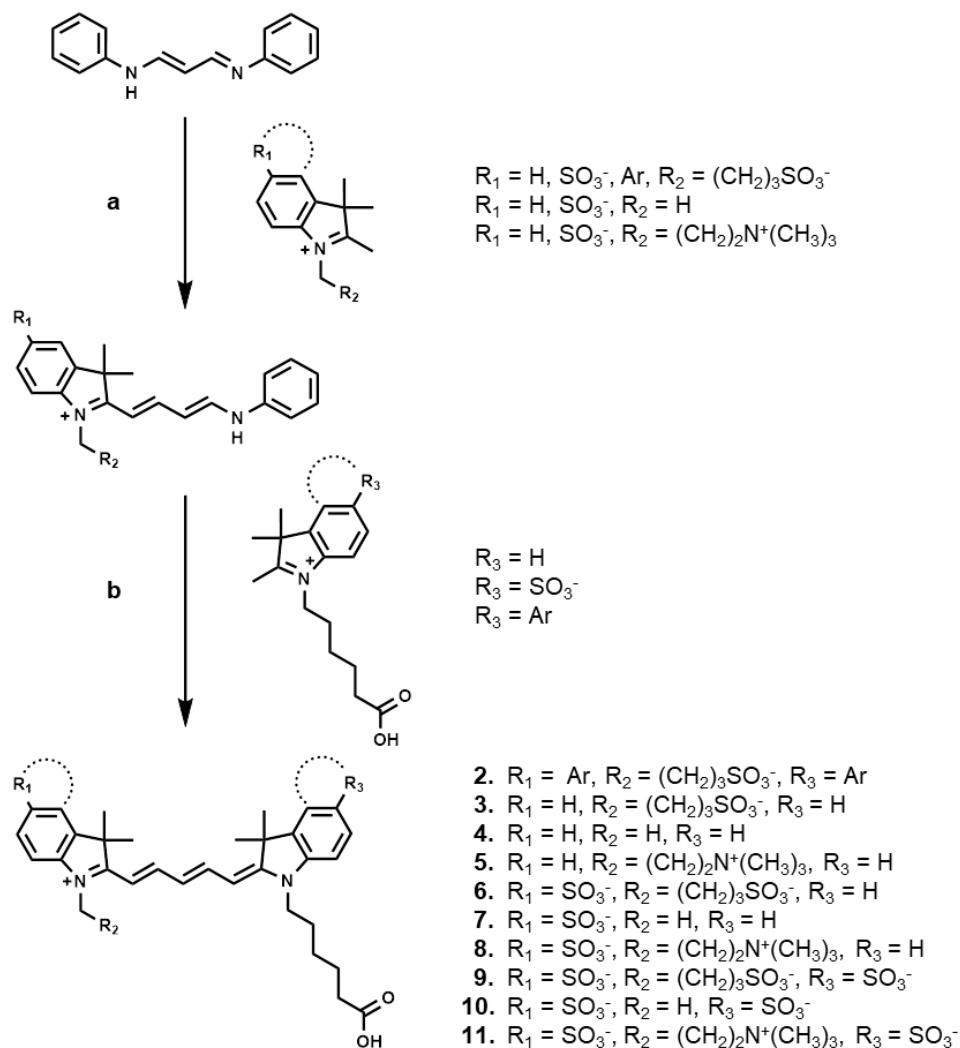


Figure S1. Synthesis of compound **2-11** according previously reported procedures: compound **2**,³ compound **3-11**.¹ Legend: a) $\text{Ac}_2\text{O}/\text{AcOH}$ 1:1, reflux, b) $\text{Ac}_2\text{O}/\text{Pyridine}$ 1:1, reflux.

Electrostatic density and conformation of the compounds

To obtain more insight into the structural differences between the fluorophores, their most stable conformation (lowest potential energy) and electron distribution were estimated using Spartan modelling software (See SI 1.3). Calculations were performed on the dyes including their counterions Cl⁻ or K⁺ (see SI; synthesis) to allow for comparison at neutral overall charges. Although the K⁺ ion is not included in the electron density cloud calculated by Spartan (Figure S2), its electrostatic effect on the sulfonate was included.

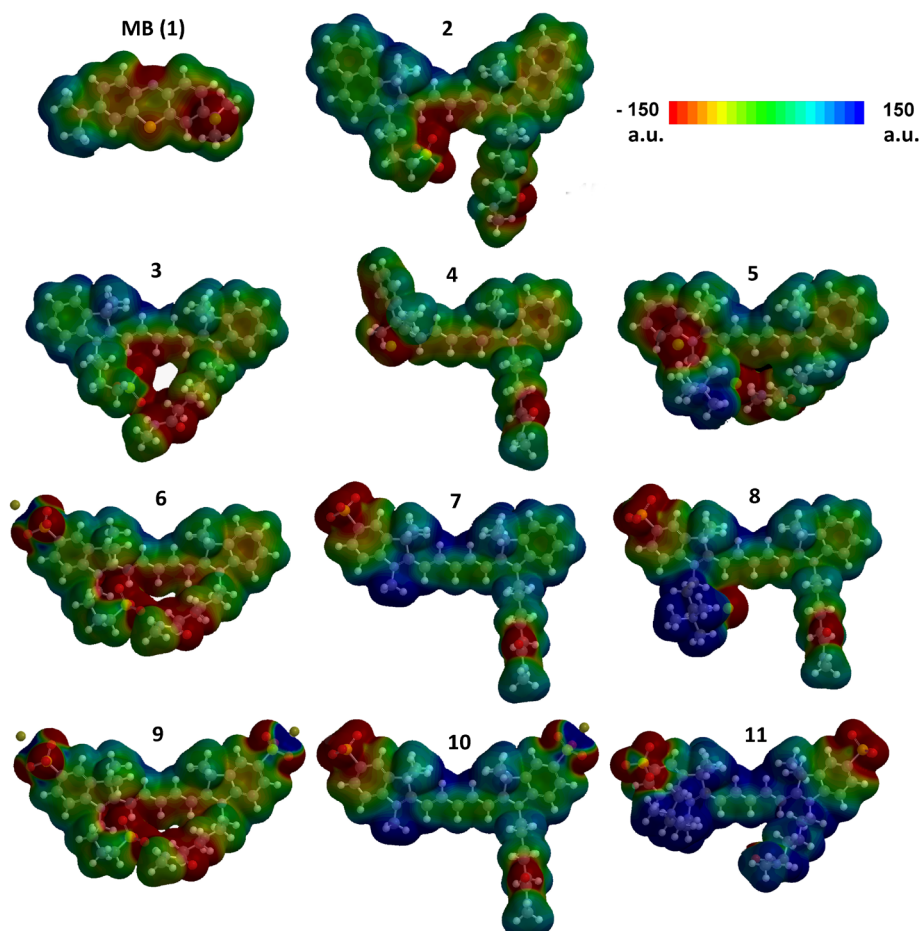


Figure S2. Electrostatic densities of compound **1-11**, overlaid over ball-and-stick models representing the theoretical most favoured conformation (lowest electron potential). The electron densities on the molecules are visualized from red to blue, with red representing the electron rich regions and blue the electron poor regions of the molecules.

Stacking of compound 3-11 in different solvents

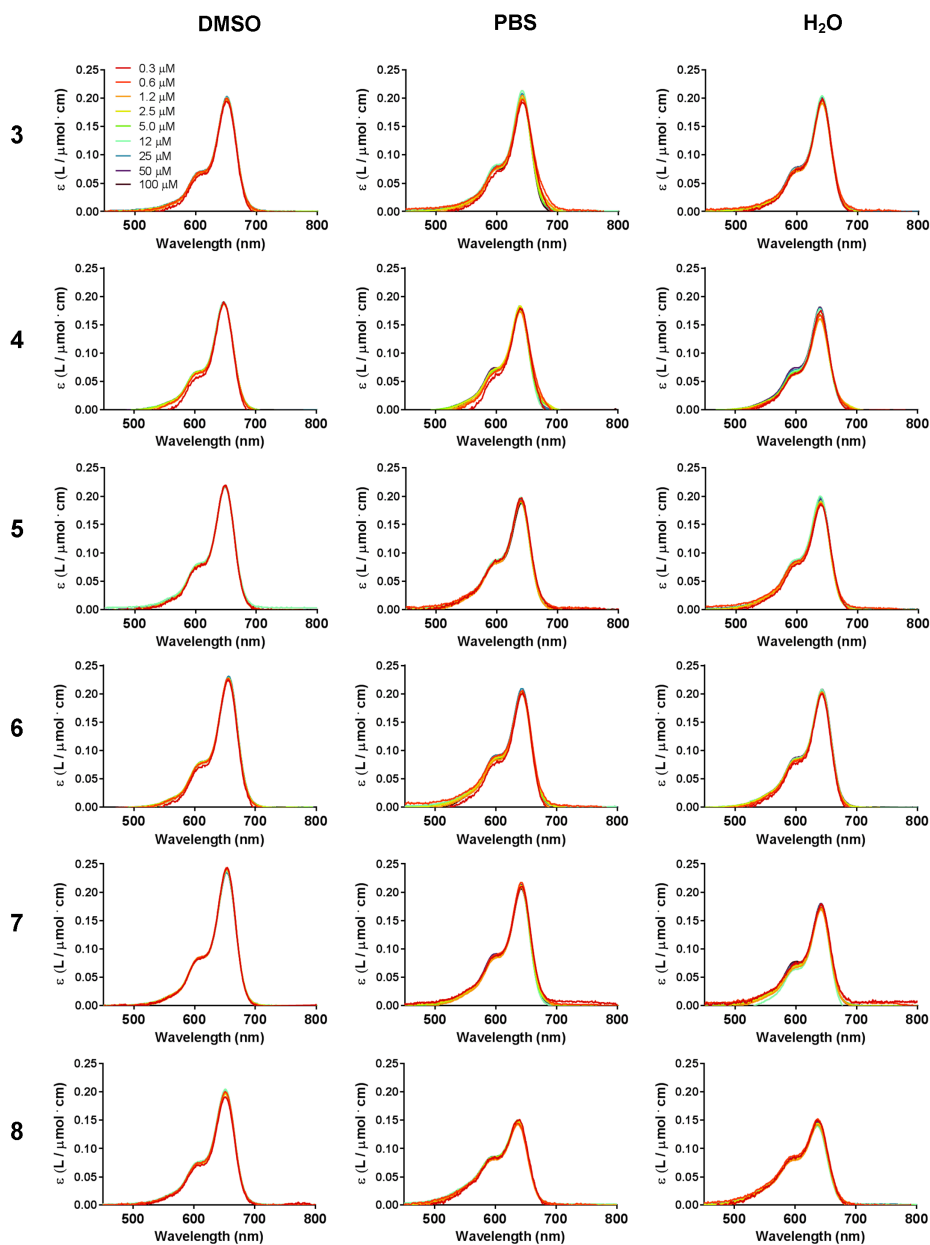


Figure S3. Stacking behaviour of compounds 3-11 in DMSO, PBS and H₂O measured at concentrations ranging from 0.3 – 100 μM

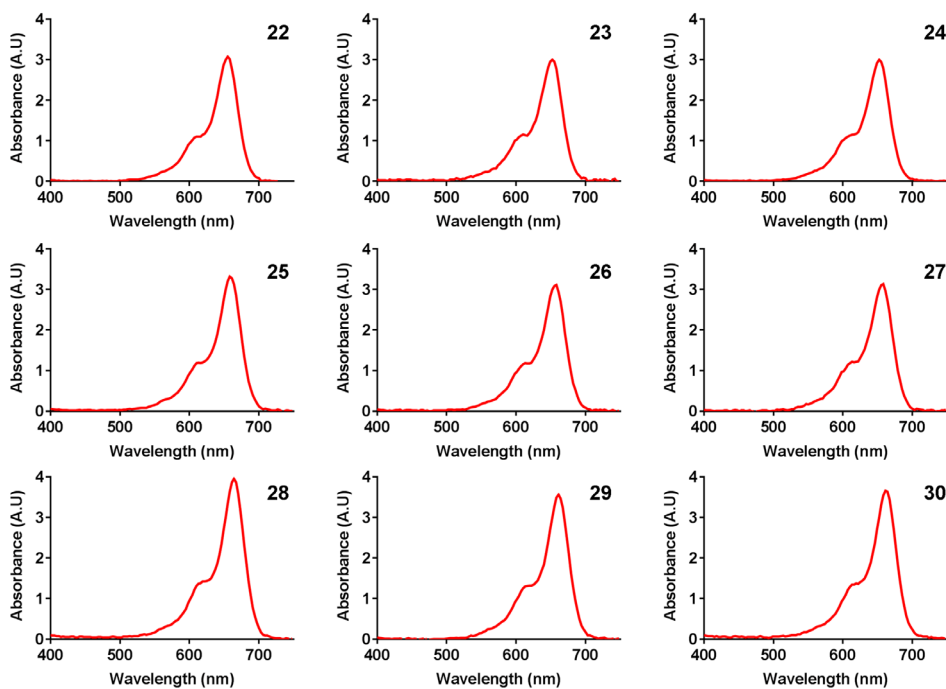


Figure S4. Absorption spectra of the fluorophores conjugated to Ubiquitin (**22–30**), measured in DMSO and normalised on dye concentration.

REFERENCES

- 1 Bunschoten A, van Willigen DM, Buckle T, et al., Tailoring Fluorescent Dyes To Optimize a Hybrid RGD-Tracer. *Bioconjug Chem.* **2016**, *27*, 1253–1258.
- 2 Mujumdar SR, Mujumdar RB, Grant CM, et al., Cyanine-labeling reagents: sulfobenzindocyanine succinimidyl esters. *Bioconjug Chem* **1996**, *7*, 356–362.
- 3 Mujumdar RB, Ernst L a, Mujumdar SR, et al., Cyanine dye labeling reagents: sulfaindocyanine succinimidyl esters. *Bioconjug Chem* **1993**, *4*, 105–111.
- 4 Bouteiller C, Clav G, Bernardin A, et al., Novel water-soluble near-infrared cyanine dyes: Synthesis, spectral properties, and use in the preparation of internally quenched fluorescent probes. *Bioconjug Chem* **2007**, *18*, 1303–1317.
- 5 Van Der Wal S, Kuil J, Valentijn ARPM, et al., Synthesis and systematic evaluation of symmetric sulfonated centrally C-C bonded cyanine near-infrared dyes for protein labelling. *Dye Pigment.* **2016**, *132*, 7–19.
- 6 Shershov VE, Spitsyn M a., Kuznetsova VE, et al., Near-infrared heptamethine cyanine dyes. Synthesis, spectroscopic characterization, thermal properties and photostability. *Dye Pigment.* **2013**, *97*, 353–360.
- 7 Wang L, Fan J, Qiao X, et al., Novel asymmetric Cy5 dyes: Synthesis, photostabilities and high sensitivity in protein fluorescence labeling. *J Photochem Photobiol A Chem.* **2010**, *210*, 168–172.





CHAPTER **7**

Future perspective

Due to the high heterogeneity among human cancers, the therapeutic efficacy varies between individual patients. Personalized therapy, or precision medicine, has the potential to overcome this shortcoming. In order to realize such precision medicine, careful control is required on the local accumulation of drugs, either via targeting of disease related molecular pathways or via local therapy. Both have provided the foundations for synthetic developments in the rising field of molecular imaging. In this setting technologies rising from the field of nanotechnology, in particular supramolecular chemistry can be employed to meet today's clinical needs.

The advantage of using non-covalent supramolecular interactions over covalent bond formation is that multivalent interactions between relatively simple building blocks allow for the realization of complex systems under physiological conditions. A prime example of an endogenous supramolecular system is DNA. When supramolecular chemistry is applied during the development of molecular imaging strategies, synthesis of a library of building blocks followed by a stoichiometric mix-and-match strategy can tailor different needs. As such a generic chemical toolbox can hold building blocks that serve a different purpose and supramolecular systems support multiplexing with different and or complementing target-, imaging- and therapy-entities.

While clinical studies with ICG-^{99m}Tc-nanocolloid have already underlined the power of supramolecular imaging in the field of molecular imaging, this thesis provides evidence that employing more complex supramolecular systems may provide value also. For example, the targeting of receptors with vectors that were functionalized with a host- or guest-moiety can direct secondary agents with complementary guest- or host-moieties, respectively, to these receptors. Chapter 2 provides evidence that this pre-targeting strategy can successfully be used to direct functionalized polymers and even functionalized whole-body cells to CXCR4 receptors, little imagination is required to see how this approach can be widely implemented. For example, in the future cocktails of various receptor targeting groups could be used to realize a higher labelling density (read host-or guest-moiety density) and as such supports strong multivalent interactions with a complementary secondary entity. Uniquely, non-specific background stainings are not likely to reach the appropriate loading density, thereby decreasing the chance of nonspecific labelling during the second step. Applications of the above pre-targeting strategies reach beyond imaging and accommodate image-guided interventions via theranostic approaches. When applied during local therapy, like the local administration of host-or guest functionalized

nanoparticles, supramolecular pre-targeting concepts open the door for a range of alternative applications and synthetic variations. Chapters 3 and 4 demonstrate the first steps towards the application of the supramolecular concepts in hepatic radioembolization therapy. The success of these imaging studies indicates that it is worthwhile to extend these efforts towards the targeted delivery of therapeutic isotopes and/or drugs.

While the efforts presented in this thesis stressed the translational potential of the developed supramolecular strategies, they also underline the influence that synthetic modification have on the *in vitro* and *in vivo* behavior of chemical entities. Clearly in future designs a lot can be gained by optimizing these chemical aspects.



CHAPTER **8**

Summary

In this work the possibility of employing supramolecular interactions to solve theranostics challenges are discussed. Both the host-guest interaction between β -cyclodextrin (β -CD) and adamantane (Ad) and the self-assembly property of ferritin were investigated to make a step towards creating new chemical entities that can be applied in precision therapy.

Chapter 2 describes how supramolecular host-guest interactions could be combined with membrane-receptor (pre)targeting. The first (pre-targeting) step included the specific introduction of the Ac-TZ14011 peptide, functionalized with Ad (guest) moieties, to the cellular surfaces ($K_D = 56$ nM). In a second step, the fluorescent β -CD-polymer (Cy5_{0.5}CD₁₀PIBMA₃₉ or Cy3_{1.5}CD₇₂PIBMA₃₈₉; multivalent host) bound to the surface of CXCR4 cells ($d = 24$ μ m) via CD-Ad host-guest interactions. Key for these interactions proved to be the ability to form multivalent CD-Ad interactions. The reversible system even allowed for a third layer of functionalization with Ad-functionalized entities, as some β -CD groups of the CD-polymer were still available for further Ad-binding. In the case where the Ad-functionalized entity was another cell, cell-cell interactions could be induced. Combined, it was shown that the formation of multivalent host-guest interactions can even be formed in the chemical challenging *in vitro* environment and that these interactions can be utilized to specifically label cellular surfaces in a pre-targeting setup.

In **Chapter 3** the formation of (multivalent) host-guest interactions was further challenged in an *in vivo* setup. Here CD-Ad interactions were employed during hepatic radioembolization, where they helped to provide a binding interaction between MAA-Ad micro particles ($d = 18$ μ m, $\sim 10^8$ Ad/MAA; guest) and (^{99m}Tc)-Cy5_{0.5}CD₁₀PIBMA₃₉ polymers (MW ~ 18.8 kDa; multivalent host). Initially confirmed in solution by radioisotope-based binding experiments and confocal microscopy, the interaction between the two vectors was explored *in vivo*. Here the biodistribution of ^{99m}Tc -Cy5_{0.5}CD₁₀PIBMA₃₉ (host-vector) was clearly affected by pre-administered MAA-Ad (guest-vector); a ten-fold increase in ^{99m}Tc -Cy5_{0.5}CD₁₀PIBMA₃₉ accumulation was observed in either the liver or lungs following local or intravenous MAA-Ad deposition respectively, an effect that was significantly less when pre-targeting was performed with MAA alone (control). Not only did these experiments provide the basis for a new approach to radioembolization, they also underline the potential of using CD-Ad host guest interactions for pre-targeting applications in an *in vivo* environment.

In **chapter 4** the opportunity of circumventing a mismatch between diagnostic and therapeutic embolization procedures using multivalent host-guest interactions was further

explored via the use of dual-isotope imaging. Herein the pre-administered guest-vector; Ad functionalized MAA particles, were labeled with technetium-99m ($^{99m}\text{Tc-MAA-Ad}$) and the host-vector, $\text{Cy}_{5_{0.5}}\text{CD}_9\text{PIBMA}_{39}$, was labeled with indium-111 (yielding $^{111}\text{In-Cy}_{5_{0.5}}\text{CD}_9\text{PIBMA}_{39}$). [$\text{MAA-Ad-}^{111}\text{In-Cy}_{5_{0.5}}\text{CD}_9\text{PIBMA}_{39}$] complexes proved to be stable in serum and dissociation in both PBS and FCS was within the 10-20% range while only 5% release of radioactivity was seen for the individual components. The anatomical overlap of hepatic deposits of $^{99m}\text{Tc-MAA-Ad}$ and accumulation of intravenously administered $^{111}\text{In-Cy}_{5_{0.5}}\text{CD}_9\text{PIBMA}_{39}$ was confirmed by dual-isotope multiplexing. The $14.9 \pm 6.1\%$ ID/g of uptake of the host-vector at 2 h nearly doubled to $26.2 \pm 2.1\%$ ID/g at 44 h post administration. Also, *in vivo* co-localization of both vectors was stable and again hepatic uptake values were significantly higher compared to those of control mice. Overall, the results from this study demonstrate that multivalent host-guest complexes between CD and Ad remain stable up to 44 h post administration despite the harsh *in vivo* environment.

In **chapter 5** the multivalent supramolecular interactions were made use of in an alternative setting to multi-functionalize the bionanoparticle (apo)ferritin. Dis- and re-assembly of ferritin occurs through the destruction and formation of multivalent hydrogen bonds and van der Waals forces and it was discussed how these forces could aid in obtaining control over (multi)functionalization of bionanoparticles. The system was tested with Cy3- Cy5- and non-functionalized ferritin. By disrupting the hydrogen bonds ferritin was dis-assembled and protein subunits with different functionalization's were obtained. Subsequently the stoichiometry of the subunits present in the re-assembly mixture determined the ratio in which the different functionalized subunits were found back in the re-assembled (apo)ferritin, albeit with a slight preference for the inclusion of non-functionalized subunits. Furthermore, after re-assembly the multi-functionalized (apo) ferritin particles were still able to collect iron (Fe^{II}) for possible MRI applications.

Since fluorescence imaging is a key tool for the analysis of supramolecular interactions and at the same time supports fluorescence guided interventions, in **chapter 6** insight was obtained on the relation between the functionalities on the cyanine 5 (Cy5) core structure and the brightness of the fluorophores e.g. absorption coefficient and quantum yield. In terms of fluorescence (brightness and stability) all Cy5 fluorophores outperformed methylene blue and were photo-stable in combination with a laparoscopic Cy5 Storz camera (30 minute exposure). Extending the chromatic core with additional benzene rings reduced the brightness and induced strong non-covalent assembly with serum proteins

such as albumin. As the π -electron rich chromatic core of Cy5 is ideal for the formation of multimers through van der Waals- and hydrophobic forces, the π -stacking characteristics of the Cy5 far-red dyes were also described. While most Cy5 far-red dyes did not stack in solution, multimer and stacking characteristics were observed after conjugation to ubiquitin. Combined, the identified direct relation between chemical substituents and the properties of Cy5 dyes calls for consideration in the design of novel fluorescence tracers.

In the **Future perspective** it was discussed how supramolecular chemistry could be employed to create a chemical toolbox to meet the clinical need of personalized medicine.





CHAPTER 9

**Samenvatting
List of Publications
Curriculum Vitea
Dankwoord**

SAMENVATTING

In dit werk wordt de mogelijkheid besproken om supramoleculaire interacties toe te passen om theranostische uitdagingen op te lossen. Zowel de interactie tussen de β -cyclodextrine (β -CD) gastheer en de adamantaan (Ad) gast en de zelf-assemblage van ferritine werden onderzocht om een stap te maken naar het creëren van nieuwe chemische entiteiten die kunnen worden toegepast in precisetherapie.

Hoofdstuk 2 beschrijft hoe supramoleculaire interacties tussen gastheer en gast kunnen worden gecombineerd met membraan-receptor (pre)targeting. De eerste (pre-targeting) stap omvatte de specifieke introductie van het Ac-TZ14011-peptide, gefunctionaliseerd met Ad (gast) eenheden, aan de cellulaire oppervlakken ($KD = 56$ nM). In een tweede stap bond het fluorescente (β -CD-polymeer (Cy_{5,5}CD₁₀PIBMA₃₉ of Cy_{3,3}CD₇₂PIBMA₃₈₉; multivalente gastheer) aan het oppervlak van CXCR4-cellen ($d = 24$ μ m) via de interacties tussen β -CD en Ad. Het vermogen om multivalente CD-Ad interacties aan te gaan was de basis voor deze functionalisatie. Omdat enkele β -CD-groepen van het CD-polymeer nog steeds beschikbaar waren voor verdere Ad-binding, kon het omkeerbare systeem zelfs gebruikt worden om een derde laag van functionalisering met Ad eenheden aan te brengen. Wanneer de met Ad gefunctionaliseerde entiteit een andere cel was, konden cel-cel-interacties worden geïnduceerd. Alles tezamen genomen, werd er aangetoond dat multivalente interacties tussen gastheer en gast zelfs kunnen worden gevormd in de chemische uitdagende *in vitro* omgeving en dat deze interacties kunnen worden gebruikt om cellulaire oppervlakken specifiek te labelen in een pre-targeting procedures.

In **Hoofdstuk 3** werd de vorming van (multivalente) interacties tussen gastheer en gast verder uitgedaagd in een *in vivo* opstelling. Hier werden CD-Ad interacties ingezet voor hepatische radioembolizatie, waar ze hielpen om een binding te vormen tussen MAA-Ad-microdeeltjes ($d = 18$ μ m, $\sim 10^8$ Ad/MAA; gast) en (^{99m}Tc)-Cy_{5,5}CD₁₀PIBMA₃₉ polymeren (MW $\sim 18,8$ kDa; multivalente gastheer). Aanvankelijk bevestigd in oplossing via op radio-isotoop gebaseerde bindings-experimenten en confocale microscopie, werd de interactie tussen de twee vectoren vervolgens onderzocht *in vivo*. De biodistributie van ^{99m}Tc-Cy_{5,5}CD₁₀PIBMA₃₉ (gastheer-vector) werd duidelijk beïnvloed door de vooraf toegediende MAA-Ad (gast-vector); een tienvoudige toename in de accumulatie van ^{99m}Tc-Cy_{5,5}CD₁₀PIBMA₃₉ werd waargenomen in de lever na lokale MAA-Ad toediening in hetzelfde

orgaan, of in de longen na intraveneuze toediening van MAA-Ad. Een effect dat significant minder was toen pre-targeting werd uitgevoerd met MAA alleen (controle). Niet alleen leverden deze experimenten de basis voor een nieuwe benadering van radioembolizatie, ze onderstrepen ook het potentieel van het gebruik van gastheer-gast interacties tussen CD-Ad voor pre-targeting-toepassingen in een *in vivo* omgeving.

In **hoofdstuk 4** werd de mogelijkheid om een mismatch tussen diagnostische en therapeutische embolizatie procedures te voorkomen met behulp van de multivalente gastheer-gast interacties nader onderzocht via het gebruik van dual-isotoop beeldvorming. Hierin werden de vooraf toegediende gastvector; Ad-gefunctionaliseerde MAA-deeltjes, gelabeld met technetium-99m (^{99m}Tc -MAA-Ad) en de gastheer-vector; $\text{Cy}_{5,0,5}\text{CD}_9\text{PIBMA}_{39}$, met indium-111 (resultierend in ^{111}In - $\text{Cy}_{5,0,5}\text{CD}_9\text{PIBMA}_{39}$). [$\text{MAA-Ad-}^{111}\text{In-Cy}_{5,0,5}\text{CD}_9\text{PIBMA}_{39}$] complexen bleken stabiel in serum en dissociatie in zowel PBS als FCS lag binnen de 10 tot 20%. Voor de afzonderlijke componenten werd slechts maximaal 5% radioactiviteit dissociatie waargenomen. Dual-isotoop multiplexing onderstreepte de anatomische overlap tussen de vooraf in de lever toegediende in de lever ^{99m}Tc -MAA-Ad en de accumulatie van intraveneus toegediende ^{111}In - $\text{Cy}_{5,0,5}\text{CD}_9\text{PIBMA}_{39}$. De $14,9 \pm 6,1\%$ ID/g opname van de gastheer-vector waargenomen 2 uur na toediening, was 44 uur na toediening bijna verdubbeld tot $26,2 \pm 2,1\%$ ID/g. Ook *in vivo* bleek de co-lokalisatie van beide vectoren stabiel en waren de hepatische opname waarden opnieuw significant hoger in vergelijking tot de waarden waargenomen in controlemuizen. Als zodanig tonen de resultaten van deze studie aan dat, ondanks de chemisch complexe en harde *in vivo* omgeving, multivalente gastheer / gast-complexen tussen CD en Ad stabiel blijven tot 44 uur na toediening.

In **hoofdstuk 5** werden de multivalente supramoleculaire interacties gebruikt in een alternatieve setting om het bionanodeeltje (apo) ferritine te functionaliseren met meerdere groepen. Dis- en re-assemblage van ferritine vindt plaats door de vernietiging en vorming van multivalente waterstofbindingen en van der Waals-krachten en er werd besproken hoe deze krachten konden helpen bij het verkrijgen van controle over (multi) functionalizatie van bionanodeeltjes. Het systeem werd getest met Cy3- Cy5- en niet-gefunctionaliseerd ferritine. Ferritine werd gedemonteerd door het verstoren van de waterstofbindingen waarmee eiwit subeenheden met verschillende functionalizaties werden verkregen. Vervolgens bepaalde de stoichiometrie in het re-assemblage mengsel van de subeenheden de verhouding waarin de verschillende gefunctionaliseerde subeenheden teruggevonden

werden in het opnieuw geassembleerde (apo) ferritine, zij het met een lichte voorkeur voor de opname van niet-gefunctionaliseerde subeenheden. Bovendien konden de multi-gefunctionaliseerde (apo) ferritinedeeltjes na re-assemblage nog steeds ijzer (Fe^{II}) collecteren voor mogelijke MRI-toepassingen.

Omdat beeldvorming met fluorescentie een sleutelinstrument is voor de analyse van supramoleculaire interacties en tegelijkertijd fluorescente beeldgeleide interventies ondersteunt, werd in **hoofdstuk 6** inzicht verkregen in de relatie tussen de chemische substituenten van de cyanine 5 (Cy5) kernstructuur en de helderheid van de fluoroforen, denk hierbij aan de absorptiecoëfficiënt en kwantum yield. In termen van fluorescentie (helderheid en stabiliteit) presteerden alle Cy5-fluoroforen beter dan methyleenblauw en waren ze allen fotostabiel onder een laparoscopische Cy5 Storz-camera (belichting van 30 minuten). Verlenging van de chromatische kern met extra benzeenringen verminderde de helderheid en resulteerde in sterke niet-covalente interacties met serum eiwitten zoals albumine. Omdat de π -elektronenrijke chromatische kern van Cy5 ideaal is voor het vormen van multimeren via van der Waals- en hydrofobe krachten, werden ook de π -stackings eigenschappen van de Cy5 fluoroforen onderzocht. Hoewel de meeste Cy5 fluoroforen geen stacking lieten zien in oplossing, werden multimeren en stacking interacties waargenomen na conjugatie met ubiquitine. Gecombineerd, vraagt de geïdentificeerde directe relatie tussen de chemische substituenten en de eigenschappen van Cy5-fluoroforen aandacht bij het ontwerp van nieuwe fluorescente tracers.

In het **toekomstperspectief** werd besproken hoe supramoleculaire chemie kan worden ingezet om een zo genoemde "chemische gereedschapskist" te creëren om aan de klinische behoefte van gepersonaliseerde geneeskunde te kunnen voldoen.

LIST OF PUBLICATIONS

1. G. H. KleinJan; T. Buckle; D. M. van Willigen; M. N. van Oosterom; S. J. Spa; H. E. Kloosterboer; F. W. van Leeuwen, Fluorescent lectins for local in vivo visualization of nerves. *Molecules* **2014**, *19*, 9876-92.
2. S. J. Spa; A. Bunschoten; M. T. M. Rood; R. J. B. Peters; A. J. Koster; F. W. B. van Leeuwen, Orthogonal Functionalization of Ferritin via Supramolecular Re-Assembly. *Europ J Inorg Chem* **2015**, *2015*, 4603-4610.
3. A. Bunschoten; D. M. van Willigen; T. Buckle; N. S. van den Berg; M. M. Welling; S. J. Spa; H. J. Wester; F. W. van Leeuwen, Tailoring Fluorescent Dyes To Optimize a Hybrid RGD-Tracer. *Bioconjug Chem* **2016**, *27*, 1253-8.
4. M. T. Rood; S. J. Spa; M. M. Welling; J. B. Ten Hove; D. M. van Willigen; T. Buckle; A. H. Velders; F. W. van Leeuwen, Obtaining control of cell surface functionalizations via Pre-targeting and Supramolecular host guest interactions. *Sci Rep* **2017**, *7*, 39908.
5. T. Buckle; D. M. van Willigen; S. J. Spa; A. W. Hensbergen; S. van der Wal; C. M. de Korne; M. M. Welling; H. G. van der Poel; J. C. H. Hardwick; F. W. B. van Leeuwen, Tracers for Fluorescence-Guided Surgery: How Elongation of the Polymethine Chain in Cyanine Dyes Alters the Pharmacokinetics of a Dual-Modality c[RGDyK] Tracer. *J Nucl Med* **2018**, *59*, 986-992.
6. S. J. Spa; A. W. Hensbergen; S. van der Wal; J. Kuil; F. W. B. van Leeuwen, The influence of systematic structure alterations on the photophysical properties and conjugation characteristics of asymmetric cyanine 5 dyes. *Dyes and Pigments* **2018**, *152*, 19-28.
7. S. J. Spa; M. M. Welling; M. N. van Oosterom; D. D. D. Rietbergen; M. C. Burgmans; W. Verboom; J. Huskens; T. Buckle; F. W. B. van Leeuwen, A Supramolecular Approach for Liver Radioembolization. *Theranostics* **2018**, *8*, 2377-2386.
8. S. J. Spa; A. W. Hensbergen; S. van der Wal; J. Kuil; F. W. B. van Leeuwen, Computational and experimental data on electrostatic density and stacking tendency of asymmetric cyanine 5 dyes. *Data Brief* **2019**, *22*, 50-55.
9. M. M. Welling; S. J. Spa; D. M. van Willigen; D. D. D. Rietbergen; M. Roestenberg; T. Buckle; F. W. B. van Leeuwen, In vivo stability of supramolecular host-guest complexes monitored by dual-isotope multiplexing in a pre-targeting model of experimental liver radioembolization. *J Control Release* **2019**, *293*, 126-134

CURRICULUM VITAE

Silvia Johara Spa was born on 23 September 1998 in The Hague, The Netherlands. After finishing her VWO education in 2007 with the major Life Science & Health at the Vrije School Den Haag, she enrolled in the bachelor Molecular Science & Technology at the university of Leiden and Delft. For her bachelor internship she worked on the design of new ligands for europium and terbium complexes in the group of Prof. Dr. E. Bouwman and Dr. S. Bonnet, at the department of Metals in Catalysis, Biomimetics and Inorganic Materials at the Leiden Institute of Chemistry. To obtain knowledge on the functionalization of nanoparticles she furthermore worked at the department of Functional Materials Laboratory of the institute of chemical and bioengineering at the ETH in Zurich, Switzerland. Under the directions of Prof. Dr. Wendelin Jan Stark and Prof. Dr. Robert Grass she functionalized magnetic nanoparticles with short DNA strands and investigated if the dispersed nanoparticles could be quantified by DNA amplification.

In September 2011 she continued her studies with the research master Chemistry with the major Design & Synthesis at the Leiden University. During her studies she grew a great interest in the supramolecular chemistry and participated in supramolecular chemistry classes at the University of Amsterdam. For her twelve month master thesis internship she once more joined the department of Metals in Catalysis, Biomimetics and Inorganic Materials at the Leiden Institute of Chemistry. This time she worked on the synthesis of novel iron(II) spin-crossover complexes for surface applications. In September 2013 she obtained her masters degree.

In August 2013 she joined the Interventional Molecular Imaging group at the Department of Radiology at the Leiden University Medical Centre where she started her PhD studies under supervision of Dr. F.W.B. van Leeuwen. Here she extended her knowledge on the functionalization of (bio)nanoparticles and applied supramolecular chemistry in the field of μ -contact printing and cell-functionalization's. Thereby combining supramolecular chemistry and biochemical techniques to aid in theranostics, of which parts are described in this thesis and presented in oral presentations given at the Chains conference in Veldhoven in 2016 and 2017. In September 2017 she continued her work at the Interventional Molecular Imaging group as a post-doc.

DANKWOORD

Dan rest mij nu alleen nog te zeggen: Mensen Bedankt!

Jullie bijdrage groot en klein hebben dit proefschrift tot een succes gemaakt.

Mijn promotor *Mark van buchem*, bedankt voor het geven van deze kans. Mijn co-promotoren: *Fijs van Leeuwen*, bedankt voor je onuitputtelijke creativiteit en inspiratie en *Rob Hoeben*, bedankt voor het delen van je kennis van de virale wereld.

Mijn welgewaardeerde (ex) collega's: bedankt voor jullie inzet en kameraatschap. In het bijzonder: *Mark Rood*, voor het opzetten van ons host-guest platform. *Mick Welling*, voor het uitvoeren van de nodige muizenproeven en het helpen tot stand brengen van de desbetreffende papers. *Tessa Buckle*, voor alle tips, hulp en gezelligschap: op de werkvloer en te paard. *Fabian (Albertus Wijnand) Hensbergen*, voor het helpen met de data verzameling, voor de muziek en schnaps. *Clarize de Korne*, voor de gezellige uren achter de confocal en aan de klimmuur. *Steffen van der Wal* voor het delen van je kennis, de eindeloze doch leerzame discussies en de nodige saucijzen broodjes. *Pip Meershoek*, voor je gezelligheid, je positieve uitstraling en het veroorzaken van paars haar. *Danny van Willigen*, voor je chemische kennis en gezelligheid op het lab. *Matthias van Oosterom*, *Nynke van de Berg* en *Gijsbert Kleinjan* voor het bijbrengen van kennis in (clinical) engineering, clinical camera's en de magische (woeste) wereld van de OK. *Meta Roestenberg* en *Beatrice Winkel* voor de introductie in de wondere wereld van de parasitologie.

Niet te vergeten mijn studenten: *Devika Murly*, *Franka van der Linden* en *Luuk Lageschaar* bedankt voor jullie ongetemde inzet en hulp bij het vergaren van onmisbare data.

En natuurlijk mijn welgewaardeerde collega's van BIONT in Wageningen: Bedankt voor alle gezelligheid met in het bijzonder *Aldrik Velders*, *Jan-Bart ten Hove*, *Laura Schijven*, *Stan Willems* en *Anton Bunschoten* voor het mee denken en uitvoeren van experimenten.

Ook naast de werkomgeving hebben natuurlijk veel mensen het PhD leven vergemakkelijkt via een mooi gesprek, het delen van sport en spel of gewoon een goede lach. Al mijn goede vrienden: bedankt! Jullie weten zelf wel waarom. Alle lieve mensen van het FDA, bedankt voor het geven van de nodige positieve energie en zwierige ontspannings momenten. *Wouter Spa* en *Ada van de berg* voor de oneindige steun en luisterende oren. *Koen Taken*,

vriend en toeverlaat, waar zal ik je niet voor hoeven danken. *Jamie*, trouwe viervoeter, bedankt voor het geduldig luisteren en je onvolwaardige aandacht en liefde.